

Understanding the interfacial behaviour of bile salts, a key to their roles during fat digestion

by

Olivia Pabois

A thesis submitted in fulfilment of the requirements for the degree
of Doctor of Philosophy

Institute of Pharmaceutical Science
Faculty of Life Sciences and Medicine
King's College London, UK

December 2019 ---> **2020**

In loving memory of my grandfather

Acknowledgements

None of this would have been possible without the constant help and support of all my supervisors, Drs Cécile Dreiss, Yuri Gerelli and Isabelle Grillo.

My first thought goes to Isabelle, whose contribution to my PhD project and involvement in my professional development were fundamental; words cannot describe how grateful I am for everything she taught me, giving me in particular a solid knowledge in neutron scattering and the opportunity to develop supervisory skills. *In memoriam*.

Yuri, I have learnt so much from you. I would like to thank you for your dedication to my PhD project, for your encouragement every step of the way, for your patience (in particular, to answer repeatedly the same questions), and for contributing wholeheartedly your energy and time to help me develop a firm foundation in colloid, interface and neutron sciences. I wish you the very best for your upcoming 'adventure', back to Italy.

Cécile, I want you to know how much I value everything you have done for me, both professionally and personally. I could have never asked for a better main supervisor: despite the long distance, you have always maintained your advisory role, guiding me through my research work as much as needed, being constantly available and highly committed to my PhD; you have helped me develop as an independent researcher, giving me the chance to supervise numerous students, encouraging me to showcase my work at international events, providing me guidance on how to apply for travel grants to fund my conferences attendances and supporting – without any hesitation – my desire to carry out a research visit abroad. You have made me feel supported, valued and esteemed from day one, and you have never hesitated to go the extra mile to ensure I reach each one of my scientific and career goals. You have been a source of both inspiration and motivation to me, and I am very grateful for the chance I have had to have you as my main PhD supervisor.

Then, a special thanks goes to Prof Elliot Gilbert, who offered me the opportunity to work with him for two months at the Australian nuclear and science technology organisation (ANSTO, Australia). Elliot, many thanks for your enthusiasm and strong involvement in my project, for imparting your expertise in neutrons applied to food science, and for allowing me to expand my professional network.

I am also thankful to Dr Richard Harvey for being part of the neutron team, for his constant enthusiasm and optimism, and for all the invaluable feedback he has provided me with; Prof Peter Wilde, Dr Myriam Grundy and Dr Balazs Bajka for their contribution to my

project and, in particular, for sharing their strong expertise in food science; Dr Chris Lorenz for his collaboration – which has been essential to my work –, and for being such a great team-mate; and finally, Dr Philipp Erni and Grégory Dardelle (my M. Eng. internship supervisors at Firmenich, Switzerland) for encouraging me to embark on this PhD adventure.

I also would like to give a big thanks to all the students I worked with (Amandine Antoine-Michard, Jasmin Omar, Faizah Ahmed, Xi Zhao, Taniya Akhtar and Florian Alexis), who produced very exciting results and allowed me to make significant progress in my work.

And finally, I am very grateful:

To all the friends I made during this tough – but rewarding – journey: Marco & Fatima (*meine Schätze*) – thanks for all the joy you have brought into my life since the first day we met in German classes, and for making me survive this PhD; Amandine – I would have never thought that my intern would become such a good friend of mine, thanks for all the stomach aches we have got from laughing with each other, you are a ray of sunshine; Maria – I am very thankful for all the help, tips and support you have given me since the beginning of my PhD at King's; Ilaria – many thanks for your inestimable support (and for the Italian food overdose), *tu sei la mia ciliegina sulla torta*; Kevin – aka 'the funny German guy', thanks for enjoying each of my jokes, and for this peculiar sense of humour we both share; Dominika – thanks for your kindness and encouragement.

To those I met a long time ago now: Auranne – I am so thankful to you for helping me go through (almost) every step of my life, and for this unique relationship we have; Adélaïde – thank you from the bottom of my heart for having been by my side for so long and for being such an endlessly supportive and amazing friend; Betty & Claire – both of you are a source of joy to me and I am very lucky to have had you standing beside me for more than 15 years now; Laurence – we recently realised that we were sharing more than we thought, and I am glad this brought us closer than before, thanks for everything you have recently done for me.

To my family: my parents, who I cannot thank enough for believing in me; my sister, Angélique, who went through the same path and who I can only thank for all the advices she has given me throughout my PhD; my brother, Julien, who makes me laugh (almost) every single day; and finally, my uncle and grandmother, who have been sharing my happiness at every step of my life.

Abstract

Regulating dietary fat (lipid) digestion to tackle the ongoing obesity crisis has become a pressing issue. Bile salts (BS) are biosurfactants produced in the liver and released into the small intestine, which play key roles in lipid digestion and absorption: they facilitate enzyme adsorption to fat droplet interfaces and remove insoluble lipolysis products from the interface, carrying them to the gut mucosa for absorption. Our working hypothesis is that BS structural diversity is responsible for these contrasting functionalities.

The first objective of the thesis was to correlate BS molecular structure with their interfacial properties to shed light on the mechanisms governing their different functions in lipolysis. Two BS constituting 20% of human bile were selected, sodium taurocholate (NaTC) and sodium taurodeoxycholate (NaTDC), which differ only by one hydroxyl group but display contrasting adsorption/desorption dynamics. Their adsorption behaviour at various interfaces (from the air/water interface to the more physiologically relevant phospholipid-stabilised oil/water interface, as a better mimic of fat droplets surfaces) was assessed using a Langmuir trough, ellipsometry and the pendant drop technique, and each interfacial film structure was characterised by Brewster angle microscopy, X-ray and neutron reflectometry. BS ability to incorporate the products of lipolysis into mixed micelles in order to transport them to the gut mucosa for absorption was then investigated by studying BS micellisation with pyrene fluorescence spectroscopy and by analysing the structures of the aggregates formed (i) by BS alone, (ii) in the presence of lipolysis products, and (iii) upon solubilisation of liposomes mimicking ingested food, with small-angle X-ray and neutron scattering. Results from these surface and solution studies confirm that BS morphological richness may be key to explaining the different roles they play in the process of lipolysis.

The second objective was to examine the mechanism of BS inhibition induced by methylcellulose (MC), a selected dietary fibre and food emulsifier. The interactions between MC and the two chosen BS were investigated in water (using oscillatory shear rheology), at the MC/water interface (using the Langmuir trough set-up and ellipsometry), and at the oil/water interface of fat droplets mimicking food colloids (conducting *in vitro* lipolysis studies with optical and confocal microscopy, as well as the pH-stat method). Results demonstrate that changes in BS structure impact their interactions with MC, which, in turn, control the outcome of lipolysis.

List of grants awarded, conference presentations, and research visit abroad

Sir Eric Rideal Travel Bursary (£600), provided by the Royal Society of Chemistry (RSC) and the Society of Chemical Industry (SCI), and **King's College London (KCL) Faculty of Life Sciences and Medicine (FoLSM) Travel Grant** (£300), to give an oral presentation, **UK Colloids 2017**, July 2017, Manchester, UK

KCL Centre for Doctoral Studies (CDS) Conference Fund Grant (£300), and **KCL FoLSM Travel Grant** (£300), to give a poster presentation, **Food Colloids 2018**, April 2018, Leeds, UK

KCL CDS Conference Fund Grant (£300), to give an oral presentation, **ACIS 2019**, February 2019, Hobart, Tasmania, Australia

Sir Eric Rideal Travel Bursary (£500), and **Messel Travel Bursary** (£850), provided by the SCI, to fund my research visit, at the **Australian nuclear and science technology organisation (ANSTO)**, November-December 2019, Sydney, New South Wales, Australia

Table of contents

Introduction	1
1. Lipid digestion, with a focus on bile salts functionalities	2
1. 1. Structure and properties of bile salts	3
1. 2. The role of bile salts in lipolysis	4
1. 3. Bile salts structural diversity: a key to their contrasting functions	5
2. Regulating lipid digestion with a specific food emulsifier, methylcellulose	7
2.1. Methylcellulose, a model of dietary fibre	8
2.2. Cholesterol-lowering mechanisms of methylcellulose	8
3. Techniques of investigation	9
3. 1. Interfacial studies with the Langmuir trough	10
3. 2. Oscillatory shear rheology bulk studies	12
3. 3. Neutron and X-ray scattering techniques	14
3. 3. 1. Theoretical background on scattering techniques	14
3. 3. 1. 1. Small-angle scattering	14
3. 3. 1. 2. Specular reflectometry	18
3. 3. 2. Scattering length density, the contrast factor	21
3. 3. 3. The contrast-variation method with neutrons	21
4. Thesis objectives and methodologies	24
References	28
Chapter 1	36
Co-authors contribution to the publication	37
Abstract	38
1. Introduction	39
2. Experimental section	39
2. 1. Materials	39
2. 2. Methods	39
2. 2. 1. Langmuir trough measurements	39
2. 2. 1. 1. BS adsorption at the air/water interface	40
2. 2. 1. 2. Surface pressure - area isotherm of lipid monolayers at the air/water interface	40

2. 2. 1. 3.	BS interaction with a DPPC monolayer at the air/water interface	40
2. 2. 2.	Ellipsometry	40
2. 2. 3.	Brewster angle microscopy	40
2. 2. 4.	X-ray reflectometry	40
2. 2. 5.	Neutron reflectometry	41
2. 2. 6.	Molecular dynamics simulations	41
3.	Results	41
3. 1.	BS adsorption at the air/water interface	41
3. 1. 1.	BS adsorption/desorption dynamics	41
3. 1. 2.	BS interfacial film structure	42
3. 2.	BS interaction with a DPPC monolayer at the air/water interface	42
3. 2. 1.	Interaction between BS and lipid molecules	42
3. 2. 2.	Morphology of BS/lipid films	44
4.	Discussion	46
5.	Conclusion	47
	Corrigendum	50
	Supporting information	53
	References	63
	Chapter 2	69
	Co-worker contribution to the chapter	70
	Abstract	71
1.	Introduction	72
2.	Experimental section	75
2. 1.	Materials	75
2. 2.	Methods	75
2. 2. 1.	Interfacial tension measurements: the pendant drop technique	75
2. 2. 2.	Neutron reflectometry	76
3.	Results	79
3. 1.	BS interfacial properties	79

3. 1. 1. BS adsorption/desorption dynamics at the oil/water interface	79
3. 1. 2. BS interaction with a DPPC monolayer at the oil/water interface: interfacial morphology of BS/lipid films	81
4. Discussion	85
5. Conclusion	87
References	88
Chapter 3	93
Co-workers contribution to the chapter	94
Abstract	95
1. Introduction	96
2. Experimental section	101
2.1. Materials	101
2.2. Methods	102
2. 2. 1. Pyrene fluorescence spectroscopy	102
2. 2. 2. Neutron reflectometry	103
2. 2. 2. 1. Sample preparation	103
DPPC/TAG liposomes preparation	103
Solid-supported bilayer formation	104
2. 2. 2. 2. Instrumental configuration	105
2. 2. 2. 3. Contrast-variation method	105
2. 2. 2. 4. Data fitting	106
2. 2. 3. Small-angle X-ray and neutron scattering	107
2. 2. 3. 1. Sample preparation	107
Aggregation of BS in solution	107
Aggregation of BS with FA and/or MAG in the form of mixed micelles, in solution	107
Solubilisation of TAG-incorporating lipid vesicles into mixed micelles	111
2. 2. 3. 2. Instrumental configurations	111
Small-angle X-ray scattering	111
Small-angle neutron scattering	111

2. 2. 3. 3.	Data fitting	112
	BS micelles and mixed micelles	112
	TAG-incorporating lipid vesicles	114
2. 2. 4.	Molecular dynamics simulations	114
3.	Results	116
3. 1.	Aggregation of BS in solution	116
3. 1. 1.	Critical micellar concentration of BS	116
3. 1. 2.	Shape and size of BS micelles	117
3. 1. 3.	BS molecular organisation in micelles	125
3. 2.	Aggregation of BS with FA and/or MAG in the form of mixed micelles, in solution	126
3. 2. 1.	Shape and size of BS mixed micelles	126
3. 3.	Solubilisation of TAG-incorporating lipid vesicles into mixed micelles	134
3. 3. 1.	DPPC/TAG SLB structure	134
3. 3. 2.	Liposomes structure	139
3. 3. 3.	Impact of BS on liposomes structure	140
4.	Discussion	147
4. 1.	Bulk aggregation behaviour of BS, in the absence and presence of the products of lipolysis	147
4. 2.	Solubilising capacity of BS	150
5.	Conclusion	152
	References	154
	Chapter 4	165
	Co-authors contribution to the publication	166
	Abstract	167
1.	Introduction	167
2.	Experimental section	168
2. 1.	Materials	168
2. 2.	Methods	168
2. 2. 1.	Bulk and interfacial studies	168

2. 2. 1. 1.	Preparation of MC and MC/BS aqueous solutions	168
2. 2. 1. 2.	Rheology measurements	168
2. 2. 1. 3.	Langmuir trough measurements	169
	MC adsorption at the air/water interface	169
	BS interaction with a MC layer at the air/water interface	169
2. 2. 1. 4.	Ellipsometry	169
2. 2. 2.	<i>In vitro</i> lipolysis studies	169
2. 2. 2. 1.	Preparation of MC-stabilised emulsion	169
2. 2. 2. 2.	Simulation of the duodenal lipolysis environment	169
2. 2. 2. 3.	Optical microscopy	169
2. 2. 2. 4.	pH-stat measurements	170
3.	Results	170
3. 1.	BS interaction with MC in the bulk	170
	MC viscoelastic behaviour	170
	Effect of BS on MC viscoelastic behaviour	170
3. 2.	BS interfacial properties in the presence of MC	171
	MC adsorption dynamics at the air/water interface	171
	BS interaction with a MC layer at the air/water interface	172
3. 3.	Effect of BS structure and concentration on the duodenal digestion of an MC-stabilised emulsion	173
	Evolution of emulsion droplets microstructure	173
	Quantification of FFA release from the MC-stabilised emulsion	173
4.	Discussion	173
4. 1.	Interaction between MC and BS in the bulk and at the interface	173
4. 2.	Impact of BS/MC interactions on fat digestion	175
5.	Conclusion	176
	Supporting information	178
	References	182
	General conclusion	191

Conclusion	192
Future work	196
Appendixes	198
Appendix 1	199
Appendix 2	201
References	203

Table of figures

Introduction	1
Figure 1: Catalytic proteins involved in lipolysis and their sites of action in the human body	3
Figure 2: Structures of the main BS, which differ by the type of conjugating amino acid moiety, and the number and position of hydroxyl groups on their steroid skeleton. In humans, glyco- and tauro-conjugates form about 70% and 30% of BS mixture, respectively; cholate and chenodeoxycholate derivatives each represent 40% of it, and deoxycholates ones around 20% (reproduced from [19] by permission of The Royal Society of Chemistry). The two BS selected in this project are shown in red.	4
Figure 3: BS contrasting mechanisms of action during lipid digestion: (A) BS adsorption at the fat droplet interface, facilitating the lipase/co-lipase access to the lipid surface, thus promoting lipolysis, and (B) BS desorption from the interface and incorporation of lipolysis products into mixed micelles (reproduced from [19] by permission of The Royal Society of Chemistry).	5
Figure 4: Phase angle variation for transverse magnetic component of light (T_{m1} phase angle) during successive injections of six different BS solutions ($[BS]_{\text{solution}} = 3 \text{ mM}$) in a 2 mM bis-tris buffer (pH 7.0) containing 150 mM sodium chloride and varying calcium chloride concentrations (solid line: 0 mM; dashed line: 1 mM; dotted line: 10 mM). Each BS injection is followed by a buffer rinse and the chip is cleaned between each experiment. BS adsorption onto the C18-modified silicon oxide sensor is denoted by an increase in T_{m1} phase angle, whereas a decrease in the same parameter indicates its desorption from the hydrophobic surface (reproduced from [19] by permission of The Royal Society of Chemistry).	6
Figure 5: Structure of methylcellulose (MC)	8
Figure 6: 1,2-dipalmitoyl- <i>sn</i> -glycero-3-phosphocholine (DPPC) (—) and 1,2-dipalmitoyl- d_{62} - <i>sn</i> -glycero-3-phosphocholine-1,1,2,2- d_4 -N,N,N-trimethyl- d_9 (d_{75} -DPPC) (—) $\pi - A$ Langmuir isotherms. The phospholipids were deposited onto ultrapure water, at a low concentration (gas phase, which has a low impact on surface pressure), and compressed (at $23 \pm 2^\circ\text{C}$). $A_{\text{lift-off}}$ corresponds to the minimal surface density at which molecules start interacting and enter into the liquid-expanded (LE) state. Upon further compression, the sharper increase in surface pressure indicates the onset of a much more ordered and packed liquid-condensed (LC) monolayer. A_{collapse} and π_{collapse} are, respectively, the mean molecular area and surface pressure at which the film breaks. The different monolayer phases and related molecular organisations observed in the different regions of the isotherm are depicted in the figure. This figure has been obtained as part of our study of BS interaction with a phospholipid monolayer at the air/water interface (reproduced from Figure S10, Chapter 1, and [44]).	11
Figure 7: Schematic representation of a shear rheology measurement using a two-plate model	13
Figure 8: Schematic representation of a small-angle scattering experiment (reproduced with permission from [49]; copyright (2008) Springer Nature)	16

Figure 9: The incident wave generates scattered waves from either the nucleus (for neutrons) or electronic cloud (for X-rays) of an atom (reproduced from [52]). These re-emitted waves interfere with each other, either constructively or destructively, producing a distinctive neutron or electron scattering pattern on the detector. In this figure, these phenomena are shown using the example of a crystalline structure with fixed atom positions, into which waves are scattered from lattice planes spaced by an interplanar distance d . In the presence of constructive interferences, the scattered waves remain in phase and the path length between the two incident waves (shown in red) is equal to an integer multiple (n) of the wavelength (λ); the lower interfering wave traverses an extra length of ' $2d \sin \vartheta$ '. In the case of destructive interferences, both signals are cancelled.

16

Figure 10: Schematic representation of a scattering curve obtained with small-angle scattering, in the case of dilute (i.e., non-interacting) objects in a continuous medium. In this figure, the scattered intensity (I) is plotted as a function of the scattering vector (q) in a log-log representation. Each circle shows the typical size (q^{-1}) probed by neutrons in each q -range, as compared with the object size. At $q \rightarrow 0$, the volume of the object (and thereby its mass) can be determined. At low q , in the Guinier regime, q^{-1} is much larger than the size of the object, allowing the radius of gyration (R_g), which represents the size of the scattering object, to be obtained. In the intermediate q -range, the scattered intensity (I) has a $q^{-\alpha}$ decay, where α is related to the shape of the object (e.g., $\alpha = 1$ corresponds to a one-dimensional object, like a cylinder, 2, a two-dimensional object, like a disk, and 4, a bulky object, like a sphere; if the geometry of the object is not well defined, α will represent the object fractal dimension and will vary between 2 and 4). At high q , in the Porod regime, q^{-1} is much smaller than the size of the object, resulting in the scattered intensity being only sensitive to the interface between the homogeneous media displaying different SLD ; in this q -region, the surface area (i.e., the quantity of scattering surfaces) per unit volume of the sample, and ultimately the specific area of the object itself, can be determined.

17

Figure 11: Schematic representation of a reflectometry experiment. Both specular (reflected scattering vector \vec{k}_r) shown in blue) and off-specular (reflected scattering vector \vec{k}_r) shown in red) reflections lie in the plane of incidence (i.e., no components along the y -axis). Nonetheless, in specular reflection, the angle of reflection is equal to that of incidence, while in off-specular reflection, the angle changes; therefore, with specular reflection, perpendicular features can be resolved (the scattering vector being parallel to the z -axis (q_z)), and with off-specular reflection, structural information on the lateral direction can be obtained (the scattering vector having components along both the z - and x -axes).

19

Figure 12: Schematic representation of the contrast-matching technique applied to an emulsion droplet. A specific isotopic (or hydrogen/deuterium) solvent mixture is used to match, selectively, the oil droplet and the stabiliser layer, thereby allowing the determination of, respectively, the film thickness and the droplets specific area.

23

Figure 13: (A, B, C) Schematic representation of the contrast-matching technique applied to an air/water interface stabilised by phospholipids, in the presence of hydrogenated BS in the bulk aqueous phase (which actually corresponds to the NR experiment presented in chapter 1). (D) SLD of each component present in this experiment (lipids, subphases and BS). In this study, different subphases, characterised by different SLD , have been used to have different contrasts and highlight different parts of the system: (A) the use of D_2O with

hydrogenated phospholipid molecules (DPPC) makes both lipid and BS (NaTC and NaTDC) molecules visible; in addition, (B) with D₂O, whose *SLD* is similar to the one of deuterated phospholipid molecules (d-DPPC), the hydrogenated BS molecules are mostly seen, thereby highlighting BS location at the interface, whereas (C) with air-contrast-matched water (ACMW, a mixture of 8.1% D₂O in H₂O (V/V)), whose *SLD* is zero as air and close to the *SLD* of BS, the deuterated phospholipid molecules are highlighted, thus allowing the determination of the lipid interfacial film thickness and organisation. 24

Chapter 1 36

Figure 1: Structures of NaTC (A) and NaTDC (B). The structure of NaGDC is shown in Figure S2. 40

Figure 2: Snapshot of the simulated system made up of two DPPC monolayers (cyan (carbon) and red (oxygen) spheres) separated by 60 Å of water (translucent blue), which contains 2 NaTC molecules (purple spheres) and their sodium counterions. 42

Figure 3: Time-dependent evolution of the surface pressure (π) measured by a LT (A, B), and phase shift ($\Delta\Delta(t) = \Delta(t) - \Delta_0$) measured by ellipsometry (C, D), upon successive injections of either NaTC (A, C) or NaTDC (B, D) into the aqueous subphase (at $23 \pm 2^\circ\text{C}$). Each addition is shown by an arrow, together with the corresponding BS concentration achieved in the subphase. Each experiment was reproduced twice, and a representative measurement was selected for each experiment. 43

Figure 4: Evolution of BS film formation and organisation observed with a Brewster angle microscope, upon successive injections of BS into the aqueous subphase: NaTC, NaTDC (at $23 \pm 2^\circ\text{C}$). The scale bar of the BAM images is 50 μm . Stripes are caused by stirring-induced vibrations of the water subphase and black, circular shapes are due to dust grains. 43

Figure 5: Evolution of the electron density profile of the interfacial film along the direction perpendicular to the surface (*z*) obtained from XRR by successive injections of BS into the aqueous subphase: NaTC, NaTDC (at $23 \pm 2^\circ\text{C}$). BS concentrations below (●) 1 mM, around (●) 5 mM, and above (●) 10 mM their CMC were selected because different interfacial behaviours were observed with the LT. The electron density profile of the bare air/water interface (●) is also shown. 44

Figure 6: Time-dependent evolution of the surface pressure ($\Delta\pi(t) = \pi(t) - \pi_{\text{DPPC}}$) measured by a LT, upon successive injections of BS into the aqueous subphase: NaTC, NaTDC, NaGDC (at $23 \pm 2^\circ\text{C}$). The lipids were spread onto water at $\pi_{\text{DPPC}} = 25 \pm 2 \text{ mN/m}$. Each addition is shown by an arrow, together with the corresponding BS concentration achieved in the subphase. Each experiment was reproduced twice, and a representative measurement was selected for each BS. 44

Figure 7: Binding of NaTC and NaTDC to DPPC monolayers, from MD simulations. (A) Fraction of time that NaTC (—) and NaTDC (- - -) are adsorbed to the interface of the DPPC monolayer during the course of the simulations, with 2 (black) and 12 (red) BS. (B) The survival probability of a BS molecule at the interface of the DPPC monolayer as a function of time, for NaTC (—) and NaTDC (- - -), in the simulations with 2 (black) and 12 (red) BS. (C, D) Snapshots of the simulations with 12 NaTC (C) and 12 NaTDC (D) molecules, as they interact with the DPPC monolayers. 45

Figure 8: Interaction maps for NaTC (A, B) and NaTDC (C, D) with the head group of the DPPC molecule in a monolayer. (A, C) Interactions of the two BS for the simulated systems with 2 BS molecules. (B, D) Interactions of the two BS for the simulated systems with 12 BS molecules. Note, the atom labels used on the two axes are defined in Figure S7. 45

Figure 9: Evolution of the lipid monolayer organisation observed with a Brewster angle microscope, upon successive injections of BS into the aqueous subphase: NaTC, NaTDC (at $23 \pm 2^\circ\text{C}$). The lipids were spread onto water at $\pi_{\text{DPPC}} = 25 \pm 2 \text{ mN/m}$. Three BS concentrations are shown here, and additional ones are displayed in Supporting Information (Figure S8). The scale bar of the BAM images is $50 \mu\text{m}$. Stripes are caused by stirring-induced vibrations of the water subphase and (black or white) circular shapes are due to dust grains. The BAM image obtained with the pure DPPC monolayer can be found in Figure S8. 46

Figure 10: Evolution of the scattering length density (*SLD*) profile of the interfacial film along the direction perpendicular to the surface (*z*) obtained by successive injections of BS into the aqueous subphase: NaTC, NaTDC (at $23 \pm 2^\circ\text{C}$). The lipids were spread onto water at $\pi_{\text{DPPC}} = 25 \pm 2 \text{ mN/m}$, thus forming a pure monolayer (●). BS concentrations below (●) 1 mM, around (●) 5 mM, and above (●) 10 mM their CMC were selected because different interfacial behaviours were observed with the LT. These *SLD* profiles were recorded in ACMW (*SLD* of 0), on which a *d*₇₅-DPPC monolayer (*SLD* of $7.66 \cdot 10^{-6} \text{ \AA}^{-2}$ for the tails and $5.68 \cdot 10^{-6} \text{ \AA}^{-2}$ for the head group) was prepared; NaTC has a *SLD* of $0.95 \cdot 10^{-6} \text{ \AA}^{-2}$ and NaTDC of $0.90 \cdot 10^{-6} \text{ \AA}^{-2}$. The *SLD* profiles obtained in the other conditions of contrast are displayed in Supporting Information (Figure S12). 47

Figure S1: Structures of DPPC (A) and *d*₇₅-DPPC (B) 53

Figure S2: Structure of NaGDC 53

Figure S3: Time-dependent evolution of the surface pressure (π) measured by a LT, upon injection of BS into the aqueous subphase: NaTC, NaTDC, at varying concentrations: (—) 0.5 mM, (—) 5 mM, (—) 10 mM (at $23 \pm 2^\circ\text{C}$). Each experiment was reproduced twice, and the average measurement was selected for each BS at each concentration. 53

Figure S4: XRR signal ($R \cdot q_z^4$ representation) of ultrapure water (●) and of the interfacial film formed at the air/water interface upon successive injections of BS into the aqueous subphase: NaTC, NaTDC (at $23 \pm 2^\circ\text{C}$), as a function of the scattering vector (q_z). BS concentrations below (●) 1 mM, around (●) 5 mM, and above (●) 10 mM their CMC were selected because different interfacial behaviours were observed with the LT. 54

Figure S5: Time-dependent evolution of the surface pressure ($\Delta\pi(t) = \pi(t) - \pi_{\text{DPPC}}$) measured by a LT, upon injection of BS into the aqueous subphase: NaTC, NaTDC, at varying concentrations: (—) 0.5 mM, (—) 1 mM, (—) 5 mM, (—) 10 mM, (—) 20 mM (at $23 \pm 2^\circ\text{C}$). The lipids were spread onto water at $\pi_{\text{DPPC}} = 25 \pm 2 \text{ mN/m}$. Each experiment was reproduced twice, and the average measurement was selected for each BS at each concentration. 55

Figure S6: Time-dependent evolution of the surface pressure ($\Delta\pi(t) = \pi(t) - \pi_{\text{DPPC}}$) measured by a LT (A, B), and phase shift ($\Delta\Delta(t) = \Delta(t) - \Delta_{\text{DPPC}}$) measured by ellipsometry (C, D), upon addition of 10 mM NaTDC into the aqueous subphase, in the presence (A, C) and absence (B, D) of stirring (at $23 \pm 2^\circ\text{C}$). The lipids were spread onto water at $\pi_{\text{DPPC}} = 25 \pm 2$ mN/m, reaching $\Delta_{\text{DPPC}} = 3.20^\circ$. 55

Figure S7: Definition of the atoms labels used in the interaction maps between molecules: A. NaTC, B. NaTDC, C. DPPC. 56

Figure S8: Evolution of the lipid monolayer organisation observed with a Brewster angle microscope, upon successive injections of BS into the aqueous subphase: NaTC, NaTDC (at $23 \pm 2^\circ\text{C}$). The lipids were spread onto water at $\pi_{\text{DPPC}} = 25 \pm 2$ mN/m. The scale bar of the BAM images is 50 μm . Stripes are caused by stirring-induced vibrations of the water subphase and (black or white) circular shapes are due to dust grains. 57

Figure S9: Evolution of the lipid monolayer organisation observed with a Brewster angle microscope, upon addition of 10 mM NaTDC into the aqueous subphase, under stirring (at $23 \pm 2^\circ\text{C}$). The lipids were spread onto water at $\pi_{\text{DPPC}} = 25 \pm 2$ mN/m. The scale bar of the BAM images is 50 μm . 57

Figure S10: DPPC (—) and d_{75} -DPPC (—) $\pi - A$ Langmuir isotherms. The phospholipids were deposited onto ultrapure water, at a low concentration (gas phase), and compressed (at $23 \pm 2^\circ\text{C}$). $A_{\text{lift-off}}$ corresponds to the minimal surface density at which molecules start interacting and enter into the liquid-expanded (LE) state. Upon further compression, the sharper increase in surface pressure indicates the onset of a much more ordered and packed liquid-condensed (LC) monolayer. A_{collapse} and π_{collapse} are, respectively, the mean molecular area and surface pressure at which the film breaks. The different monolayer phases and related molecular organisations observed in the different regions of the isotherm are depicted in the figure. 58

Figure S11: NR signal ($R \cdot q_z^4$ representation) of the lipid monolayer as a function of the scattering vector (q_z) and its evolution upon successive injections of either NaTC (A, C) or NaTDC (B, D) into the aqueous subphase (at $23 \pm 2^\circ\text{C}$). The lipids were spread onto water at $\pi_{\text{DPPC}} = 25 \pm 2$ mN/m, thus forming a pure monolayer (\circ). BS concentrations below (\circ 1 mM), around (\circ 5 mM), and above (\circ 10 mM) their CMC were selected because different interfacial behaviours were observed with the LT. These NR data were recorded using ACMW, on which a monolayer of d_{75} -DPPC was prepared (A, B), and D_2O , on which a monolayer of either DPPC, for NaTC (C), or d_{75} -DPPC, for NaTDC (D), was prepared. 59

Figure S12: Evolution of the *SLD* profile of the interfacial film along the direction perpendicular to the surface (z) obtained from NR by successive injections of BS into the aqueous subphase: NaTC, NaTDC (at $23 \pm 2^\circ\text{C}$). The lipids were spread onto water at $\pi_{\text{DPPC}} = 25 \pm 2$ mN/m, thus forming a pure monolayer (\bullet). These measurements were only performed at BS concentrations below (\bullet 1 mM) and around (\bullet 5 mM) their CMC. These *SLD* profiles were recorded in D_2O (*SLD* of $6.33 \times 10^{-6} \text{ \AA}^{-2}$), on which a monolayer of either DPPC (*SLD* of $-0.41 \times 10^{-6} \text{ \AA}^{-2}$ for the tails and $1.75 \times 10^{-6} \text{ \AA}^{-2}$ for the head group), for NaTC (*SLD* of $0.95 \times 10^{-6} \text{ \AA}^{-2}$) (A), or d_{75} -DPPC (*SLD* of $7.66 \times 10^{-6} \text{ \AA}^{-2}$ for the tails and $5.68 \times 10^{-6} \text{ \AA}^{-2}$ for the head group), for NaTDC (*SLD* of $0.90 \times 10^{-6} \text{ \AA}^{-2}$) (B), was prepared. 59

Figure S13: Average lipid order parameter of the *sn*-1 tail as a function of the depth in the DPPC monolayer, for different distances from a bound BS molecule in the presence of 2 (A, C) and 12 (B, D) molecules of BS: (A, B) NaTC, (C, D) NaTDC. 61

Figure S14. Average lipid order parameter of the *sn*-2 tail as a function of the depth in the DPPC monolayer, for different distances from a bound BS molecule in the presence of 2 (A, C) and 12 (B, D) molecules of BS: (A, B) NaTC, (C, D) NaTDC. 61

Figure S15: Distributions of the monolayer thickness for each of the four simulated systems: NaTC (—), NaTDC (---), with 2 (black) and 12 (red) BS. 62

Chapter 2 69

Figure 1: Structure of DPPC 75

Figure 2: Structures of NaTC (A) and NaTDC (B) 75

Figure 3: Structure of tricaprylin 75

Figure 4: Quartz liquid/liquid cell employed for the NR experiments at the oil/water interface. Prior to pouring the aqueous and organic phases into the cell, the edges separating the two compartments were hydrophobically coated with OTS, to prevent the aqueous phase from covering these parts and thereby have a flatter (i.e., less curved) interface. Tricaprylin (used as the oil phase) was spread onto a pure 10 mM BS solution prepared in degassed D₂O (used as the aqueous phase), either directly or after deposition of a phospholipid (DPPC) monolayer at the air/water interface. Neutrons went through the aqueous phase and were reflected downwards. The presence of an inlet/outlet allows adjustment of the water level and thereby reduction of the oil/water interface curvature, which is paramount for NR measurements. 77

Figure 5: Time-dependent evolution of the interfacial tension (γ) measured with the pendant drop technique, upon formation of a tricaprylin oil drop in an aqueous phase containing different concentrations: (—) 1 mM, (—) 5 mM, (—) 10 mM, (—) 100 mM, of BS: NaTC, NaTDC (at $23 \pm 2^\circ\text{C}$). The effect of salt on BS behaviour at the oil/water interface was also studied by adding 0.15 M NaCl to a 10 mM BS aqueous solution: (—) 10 mM of BS with salt. Each experiment was reproduced at least three times, and a representative measurement was selected for each BS at each concentration. 79

Figure 6: Evolution of the interfacial tension (γ) as a function of BS concentration, measured with the pendant drop technique, upon formation of a tricaprylin oil drop in an aqueous phase containing different concentrations (1, 5, 10 and 100 mM) of BS (NaTC, NaTDC) (at $23 \pm 2^\circ\text{C}$). The interfacial tension obtained in the presence of 0.15 M NaCl with 10 mM BS is also shown, as well as that displayed by the bare oil/water (i.e., tricaprylin/D₂O) interface. The interfacial tension values shown here correspond to the values obtained after 1 hour of equilibration. These data were extracted from BS adsorption measurements (Figure 5). Each experiment was reproduced at least three times, and the average measurement was selected for each BS at each concentration. 80

Figure 7: NR signal of the oil/water (tricaprylin/D₂O) interface as a function of the scattering vector (q_z), in the presence of a phospholipid monolayer at the interface and either NaTC (●) or NaTDC (●) in the aqueous subphase (at $21 \pm 1^\circ\text{C}$). In the absence of a lipid interfacial film, a NR signal could be recorded only with NaTDC (●), the interface in the presence of NaTC alone being too diffuse to be resolved. 10 mM of BS were used in this study to mimic physiological conditions. 82

Figure 8: Bi-dimensional (time-of-flight) image of the detector obtained at the low- q_z configuration, representing the projection of the width of the oil/water (tricaprylin/D₂O) interface in the horizontal plane, in the absence (A) and presence (B, C) of a phospholipid monolayer at the interface, with either (A, C) NaTDC or (B) NaTC in the aqueous subphase (at $21 \pm 1^\circ\text{C}$). In the absence of lipid stabiliser, the interface in the presence of NaTC was too diffuse to be resolved. The colours are related to the intensity of the reflected beam at different wavelengths (represented here by the time-of-flight channel, x-axis). For a similar interfacial width (i.e., spread of the reflection along the y-axis), differences in intensity can be related to the amount of hydrogenated material adsorbed at the interface, the red showing a much denser interface compared to the blue. 83

Chapter 3

93

Figure 1: (A) The two-step aggregation model, whereby globular primary, small micelles form by back-to-back association between the steroid skeletons *via* the hydrophobic effect, and then associate with each other in the form of rod-like secondary, larger micelles *via* hydrogen bonding between hydroxyl and amino groups (reproduced with permission from [5]; copyright (2009) Elsevier); based on this mechanism, a maximum of ten molecules could self-associate hydrophobically without creating a cavity in the core. (B) The disc-shaped structure model, whereby the hydrophobic faces are oriented towards the micelles core, and the hydrophilic ones towards the aqueous solvent (reproduced with permission from [21]; copyright (1989) American Chemical Society). (C) The helical structure model, whereby molecules are stabilised *via* polar interactions, with the nonpolar moieties facing the aqueous solvent and the polar ones the micelles core, which is also filled with counterions and water molecules (reproduced with permission from [23]; copyright (1999) American Chemical Society). 97

Figure 2: Structures of NaTC (A) and NaTDC (B) 101

Figure 3: Structures of caprylic acid (C8:0 FA), monocaprylin (C8:0 MAG), tricaprylin (C8:0 TAG), oleic acid (C18:1 FA), monoolein (C18:1 MAG) and triolein (C18:1 TAG). 102

Figure 4: Structures of (A) DPPC and (B) d₆₂-DPPC 102

Figure 5: Evolution of pyrene emission fluorescence (F_{III}/F_I) in water as a function of BS concentration, at two different temperatures: NaTDC: (■) 23°C, (■) 37°C, NaTC: (●) 23°C, (●) 37°C. Solid lines are fits of the data to Equation 1. 116

Figure 6: Scattered intensity (I) as a function of the scattering vector (q) for BS aqueous solutions of either NaTC (A, C, E, G) or NaTDC (B, D, F, H), prepared at different concentrations (from 2 to 200 mM), with (A, B, C, D) and without (E, F, G, H) 0.15 M NaCl, and measured at 25°C, by SANS (A, B, E, F) and SAXS (C, D, G, H). Solids lines

correspond to fits to the data as described in the text (Equation 3). For readability purposes, curves are staggered vertically. 118

Figure 7: Evolution of (A) the volume of the object probed ($V_{Object\ probed}$), namely, the whole micelle with SAXS and the micellar core with SANS, and (B) the fraction of water in the object probed ($x_{Water\ in\ objects\ probed}$), as a function of BS concentration, with 0.15 M NaCl: NaTC: (●) SANS, (■) SAXS; NaTDC: (●) SANS, (■) SAXS. 122

Figure 8: Evolution of (A) the polar radius (R_{Pol}), (B) the equatorial radius (R_{Eq}) and (C) the eccentricity of the object probed, namely, the whole micelle with SAXS and the micellar core with SANS, as a function of BS concentration, with 0.15 M NaCl: NaTC: (●) SANS, (■) SAXS; NaTDC: (●) SANS, (■) SAXS. 123

Figure 9: Scattered intensity (I) as a function of the scattering vector (q) for aqueous solutions of BS (NaTC, NaTDC), prepared at different concentrations: (●) 10 mM, (●) 30 mM, (●) 50 mM, (●) 100 mM, (●) 200 mM, and measured at two different temperatures: (○) 25°C, (●) 37°C, without salt, with SANS. For readability purposes, curves are staggered vertically. 125

Figure 10: Structure of the micelles of BS (NaTC, NaTDC) formed at different concentrations (10 and 50 mM), in the presence of salt (0.15 M NaCl), obtained with MD simulations. At 10 mM, micelles contain 5 and 8 molecules for, respectively, NaTC and NaTDC, the remaining BS molecules being isolated in solution as unimers. At 50 mM, two aggregates, containing 12 and 13 molecules, are observed for NaTDC, while one elongated micelle containing all the BS molecules in the system is obtained for NaTC. The largest micelles found in the final snapshots of each simulation (to date) are shown in this figure. 125

Figure 11: Scattered intensity (I) as a function of the scattering vector (q) for 100 mM BS aqueous solutions of either NaTC (A, C, E, G) or NaTDC (B, D, F, H), mixed with different amounts (from 0.10% to 1.50% w/w) of either FA (A, B, C, D) or MAG (E, F, G, H), with (●) and without (x) 0.15 M NaCl, and measured at 25°C, by SANS. Two types of FA: (A, B) C8:0, (C, D) C18:1, and MAG: (E, F) C8:0, (G, H) C18:1, were employed in this study. Solids lines correspond to fits to the data as described in the text (Equation 2). 127

Figure 12: Scattered intensity (I) as a function of the scattering vector (q) for 100 mM BS aqueous solutions of either NaTC (A, C) or NaTDC (B, D), mixed with different amounts (0.25-0.25% and 1.50-1.30% w/w) of either C8:0 (A, B) or C18:1 (C, D) FA-MAG, with (●) and without (x) 0.15 M NaCl, and measured at 25°C, by SANS. Solids lines correspond to fits to the data as described in the text (Equation 2). 128

Figure 13: Evolution of (A) the volume of the BS mixed micelle core ($V_{Mixed\ micelle\ core}$), (B) the amount of charges in BS mixed micelle (charges), (C) the polar radius of the BS mixed micelle core (R_{Pol}) and (D) the equatorial radius of the BS mixed micelle core obtained by SANS, as a function of additive type, at a concentration in additive of 0.25% w/w and BS of 100 mM, with and without 0.15 M NaCl: NaTDC: (●) with salt, (■) without salt, NaTC: (●) with salt, (■) without salt. 131

Figure 14: Evolution of (A, B) the volume of the BS mixed micelle core ($V_{Mixed\ micelle\ core}$), (C, D) the amount of charges in BS mixed micelle (charges), (E, F) the polar radius of the BS mixed micelle core (R_{Pol}) and (G, H) the equatorial radius of the BS mixed micelle core obtained by SANS, as a function of additive type and

concentration, for C8:0 FA and MAG (A, C, E, G) and C18:1 FA and MAG (B, D, F, H), with a concentration in BS of 100 mM, with and without 0.15 M NaCl: NaTDC: (●) with salt, (■) without salt, NaTC: (●) with salt, (■) without salt. 132

Figure 15: NR signal ($R \cdot q_z^4$ representation) of the TAG-incorporating SLB: d₆₂-DPPC, d₆₂-DPPC/TC, d₆₂-DPPC/TO, in different aqueous phases: (○) D₂O, (◐) SiCMW, (◑) H₂O, as a function of the scattering vector (q_z). 135

Figure 16: (A) Scattering length density (SLD) profile of each SLB: d₆₂-DPPC, d₆₂-DPPC/TC, d₆₂-DPPC/TO, in three different aqueous phases: (●) D₂O, (●) SiCMW, (●) H₂O, along the direction perpendicular to the surface (z), obtained from the analysis of the reflectivity curves measured at $50 \pm 2^\circ\text{C}$. Fits of the experimental data corresponding to these profiles are shown in Figure 15. (B) Schematic representation of each SLB, showing the location and organisation of each TAG (blue molecules) in the DPPC (green molecules) bilayer. Tricaprylin lies between the two tails regions of the DPPC bilayer, with two branches perpendicular to them and one parallel, whereas triolein is incorporated into the tails regions. 137

Figure 17: Scattered intensity (I) as a function of the scattering vector (q) for the pure DPPC vesicles (●), measured at 25°C , by SANS. The connecting lines are the trend lines that best fit the data set using the vesicular model described by Gerelli *et al.* [63]; the contributions of both the uni- and multi-lamellar lipid vesicles are shown in this figure. 139

Figure 18: Scattered intensity (I) as a function of the scattering vector (q) for each TAG-incorporating lipid (DPPC, DPPC/TC, DPPC/TO) vesicle, mixed with different amounts: (●) 10 mM, (●) 30 mM, (●) 50 mM, (●) 100 mM, of BS (NaTC, NaTDC), measured at 25°C , by SANS. The scattering curve of the pure liposomes (●) is also shown for comparison. The connecting line is the trend line that best fits the data set (Equation 2). 141

Figure 19: Evolution of (A) the volume of the BS mixed micelle core ($V_{Mixed\ micelle\ core}$), (B) the amount of charges in BS mixed micelle (charges), (C) the polar radius of the BS mixed micelle core (R_{Pol}) and (D) the equatorial radius of the BS mixed micelle core obtained by SANS, as a function of liposome type, for DPPC, DPPC/TC and DPPC/TO vesicles, with either (■) 100 mM NaTC or (■) 50 mM NaTDC. Results obtained with pristine BS micelles, in the absence of liposomes, are also indicated for comparison. 143

Figure 20: Scattered intensity (I) as a function of the scattering vector (q) for each TAG-incorporating lipid (DPPC, DPPC/TC, DPPC/TO) vesicle, mixed with different amounts: (●) 10 mM, (●) 30 mM, (●) 50 mM, (●) 100 mM, of BS (NaTC, NaTDC), measured at 37°C , by SANS. The scattering curve of the pure liposomes (●) obtained at 37°C , is also shown for comparison. 145

Chapter 4 165

Figure 1: Structure of methylcellulose (MC) 168

Figure 2: Structures of sodium taurocholate (NaTC) (A) and sodium taurodeoxycholate (NaTDC) (B) 169

Figure 3: (A, B) Temperature-dependent evolution of the storage modulus (G') obtained from dynamic temperature sweeps, and (C, D) angular frequency-dependent evolution of the dynamic moduli: (●) G' , the

storage modulus, (○) G'' , the loss modulus, obtained from dynamic frequency sweeps performed at a constant temperature of 60°C, on a 1.0% w/w MC aqueous solution containing increasing amounts (1, 10, 25, 50, 100, 200, 500 mmol/kg) of BS: (A, C) NaTC, (B, D) NaTDC. The curves obtained in the absence of BS are also shown for comparison. 171

Figure 4: Evolution of MC transition temperature (T_t) (A) and dynamic moduli: (●) G' , the storage modulus, (○) G'' , the loss modulus, obtained at an angular frequency of 1 rad/s (B), as a function of the concentration in BS: NaTC, NaTDC. The transition temperature (T_t) is the temperature from which G' starts changing. These data are extracted from, respectively, (A) dynamic temperature sweeps performed over a temperature range of 20 - 80°C (Figure 3, A, B), and (B) dynamic frequency sweeps performed over an angular frequency range of 0.1 - 100 rad/s, at a constant temperature of 60°C (Figure 3, C, D). 171

Figure 5: Time-dependent evolution of (A, B) the surface pressure (π) measured in a Langmuir trough, and (C, D) phase shift ($\Delta\Delta(t) = \Delta(t) - \Delta_0$) measured by ellipsometry, upon successive injections of either (A, C) NaTC or (B, D) NaTDC into the aqueous subphase (at 23 ± 2°C). The first increase in surface pressure corresponds to the adsorption of MC at the air/water interface, which was added into water at a concentration of 0.5‰ w/w ($\pi_{MC} = 21 \pm 1$ mN/m, $\Delta\Delta_{MC} = 0.039 \pm 0.005^\circ$). Each addition of BS is shown by an arrow, together with the corresponding BS concentration achieved in the subphase. Each experiment was reproduced twice, and a representative measurement was selected for each experiment. 172

Figure 6: Evolution of the surface pressure ($\Delta\pi = \pi_{Equilibrium} - \pi_{MC}$) as a function of BS concentration, measured in a Langmuir trough, upon injection of fixed concentrations (1, 5, 10 mM) of BS (NaTC, NaTDC) into the aqueous subphase (at 23 ± 2°C). 0.5‰ w/w MC were injected into water to form a layer at the air/water interface, at $\pi_{MC} = 21 \pm 1$ mN/m. These data were extracted from individual BS injections measurements (Figure S6). Each experiment was reproduced at least twice, and the average measurement was selected for each BS at each concentration. 172

Figure 7: Time-dependent evolution of the microstructure of MC-stabilised emulsion droplets in the presence of BS: NaTC, NaTDC, used at 1 and 10 mM, under duodenal digestion conditions (at 37°C). MC-stabilised emulsion was made up of 0.5% MC and 15% sunflower oil. Both blank (without enzymes) and lipolysis (with enzymes) assays were performed to assess, respectively, the effect of BS type and concentration on the droplets stability, and of enzymes on the droplets microstructure. Microscopy observations were made at t = 5 and 60 minutes. The scale bar is 200 μm. 174

Figure 8: Time-dependent evolution of the microstructure of MC-stabilised emulsion droplets in the presence of 50 mM BS: NaTC, NaTDC, under duodenal digestion conditions (at 37°C). MC-stabilised emulsion was made up of 0.5% MC and 15% sunflower oil. The lipid droplets are stained in red (with Nile red), while MC is stained in blue (with calcofluor). Microscopy observations were made at t = 5, 15, 30 and 60 minutes, to compare the structural changes occurring during digestion; at each time point, orlistat was used to inhibit lipolysis. The scale bar is 150 μm. 174

Figure 9: (A) Cross-section confocal image of MC-stabilised emulsion droplets in the presence of 50 mM NaTC, under duodenal digestion conditions (at 37 ± 2°C). The microscopy observation was made at t = 15 minutes. (B) MC-stabilised emulsion droplets in the presence of 50 mM NaTDC, under duodenal digestion conditions (at

37°C). Insoluble lipolysis products seem to be presumably present at the fat droplet interface (see the arrow). MC-stabilised emulsion was made up of 0.5% MC and 15% sunflower oil. The lipid droplets are stained in red (with Nile red), while MC is stained in blue (with calcofluor). The scale bar is 10 μm . 175

Figure 10: (A) Proportion of FFA released (%FFA) over time from an MC-stabilised emulsion, using two different BS: NaTC, NaTDC, at two different concentrations: (\square) 10 and (\blacksquare) 50 mM, under duodenal digestion conditions (at 37°C). (B) Proportion of FFA released (%FFA) after 1 hour of digestion of an MC-stabilised emulsion, using the two BS, at 10 and 50 mM, under duodenal digestion conditions (at 37°C). Statistical significance was determined using the two-way ANOVA, followed by the Tukey post-test (**** indicates $P < 0.0001$, i.e., differences are extremely significant). MC-stabilised emulsion was made up of 0.5% MC and 15% sunflower oil. 175

Figure S1: Temperature-dependent evolution of the storage modulus (G') obtained from dynamic temperature sweeps, on MC aqueous solutions prepared at different concentrations (0.1, 0.5, 1.0, 1.5 and 2.0% w/w). G' dominates over G'' at all concentrations and temperatures; G'' was therefore omitted for clarity. 178

Figure S2: Time-dependent evolution of (A) the surface pressure (π) measured in a Langmuir trough, and (B) phase shift ($\Delta\Delta(t) = \Delta(t) - \Delta_0$) measured by ellipsometry, upon successive injections of MC: (—) $0.5 \times 10^{-1}\%$ w/w, (—) 0.25% w/w, (—) 0.5% w/w, into the aqueous subphase (at $23 \pm 2^\circ\text{C}$). 178

Figure S3: Time-dependent evolution of (A) the surface pressure (π) measured in a Langmuir trough, and (B) phase shift ($\Delta\Delta(t) = \Delta(t) - \Delta_0$) measured by ellipsometry, upon successive injections of MC: (—) $0.5 \times 10^{-2}\%$ w/w, (—) $0.25 \times 10^{-1}\%$ w/w, (—) $0.5 \times 10^{-1}\%$ w/w, into the aqueous subphase (at $23 \pm 2^\circ\text{C}$). 178

Figure S4: Time-dependent evolution of the surface pressure (π) measured in a Langmuir trough, upon injection of MC into the aqueous subphase, at varying concentrations: (—) $0.5 \times 10^{-3}\%$ w/w, (—) $0.5 \times 10^{-2}\%$ w/w, (—) $0.5 \times 10^{-1}\%$ w/w, (—) 0.5% w/w (at $23 \pm 2^\circ\text{C}$). Each experiment was reproduced twice, and the average measurement was selected for each BS at each concentration. 179

Figure S5: Time-dependent evolution of the surface pressure (π) measured in a Langmuir trough, upon successive injections of BS into the aqueous subphase: NaTC, NaTDC (at $23 \pm 2^\circ\text{C}$). The first increase in surface pressure corresponds to the adsorption of MC at the air/water interface, which was added into water at a concentration of $0.5 \times 10^{-2}\%$ w/w ($\pi_{\text{MC}} = 18 \pm 2 \text{ mN/m}$). Each addition of BS is shown by an arrow, together with the corresponding BS concentration achieved in the subphase. Each experiment was reproduced twice, and a representative measurement was selected for each experiment. 179

Figure S6: Time-dependent evolution of the surface pressure (π) measured in a Langmuir trough, upon injection of varying concentrations: 1, 5, 10 mM, of BS: NaTC, NaTDC, into the aqueous subphase (at $23 \pm 2^\circ\text{C}$). The first increase in surface pressure corresponds to the adsorption of MC at the air/water interface, which was added into water at a concentration of 0.5% w/w ($\pi_{\text{MC}} = 21 \pm 1 \text{ mN/m}$). Each experiment was reproduced at least twice, and a representative measurement was selected for each BS at each concentration. 180

Figure S7: Characterisation of MC-stabilised emulsion droplets microstructure by (A) optical (scale bar: 200 μm) and (B) confocal (scale bar: 20 μm) microscopy. MC-stabilised emulsion was made up of 0.5% MC and 15%

sunflower oil. The confocal micrograph shows the lipid droplets (stained in red with Nile red) surrounded by MC (stained in blue with calcofluor) present as a network in the bulk (B). 180

Figure S8: Impact of the different digestive fluid components: NaCl, CaCl₂ and BS (NaTC, NaTDC) (used individually), on the microstructure of MC-stabilised emulsion droplets, 60 min after mixing (at 37°C). MC-stabilised emulsion was made up of 0.5% MC and 15% sunflower oil. The scale bar is 200 µm. 181

Figure S9: Impact of the different digestive fluid components: NaCl, CaCl₂ and BS (NaTC, NaTDC) (used in combination), on the microstructure of MC-stabilised emulsion droplets, 60 min after mixing (at 37°C). MC-stabilised emulsion was made up of 0.5% MC and 15% sunflower oil. The scale bar is 200 µm. 181

Appendixes 198

Figure A1: Time-dependent evolution of the (●) resonance frequency (Δf) and (●) energy dissipation factor (ΔD) measured by quartz-crystal microbalance with dissipation monitoring (QCM-D) [1], upon formation of a SLB: DPPC, DPPC/TC, DPPC/TO, in ultrapure water, through liposomes fusion (at $50 \pm 2^\circ\text{C}$). Liposomes, followed by salt (0.5 M NaCl), were injected into the chamber, which was finally rinsed with ultrapure water to remove the lipid vesicles remaining intact at the interface and in the bulk. For readability purposes, resonance frequencies and energy dissipation factors obtained for the 3rd and 5th harmonics only are shown here. A frequency shift of around -25 Hz typically denotes the effective formation of a stable lipid membrane [2]. Each experiment was reproduced twice, and a representative measurement was selected for each SLB. 199

Table of tables

Chapter 1	36
Table 1: Calculated electron density of each component	41
Table 2: Calculated SLD of each component	41
Table S1: Evolution of the XRR parameters of the interfacial film formed at the air/water interface upon successive injections of 1, 5 and 10 mM BS into the aqueous subphase: NaTC, NaTDC. When the layer formed was very diffuse, the evolution of the air/water interfacial roughness (σ) was monitored, while a model assuming a single layer characterised by a specific roughness (σ), thickness (t), and electron density, was used to fit a more dense, well-defined film.	54
Table S2: Evolution of the NR parameters of each layer (tails and head group) of the lipid (either DPPC or d ₇₅ -DPPC) film: σ , the roughness, t , the thickness, SLD , the scattering length density and f_{water} , the amount of water, upon successive injections of 1, 5 and 10 mM BS into the aqueous subphase: NaTC, NaTDC.	60
Chapter 2	69
Table 1: Calculated SLD of each component	78
Chapter 3	93
Table 1: Calculated neutron SLD of each component	106
Table 2: Calculated electron SLD of each component	107
Table 3: Type and amount of additives used to make the mixed micelles	108
Table 4: Concentration of FA (C8:0 or C18:1) and/or MAG (C8:0 or C18:1) in the sample ($[Additive]$), volume fraction of each component in micelles (Φ_{BS} , Φ_{FA} , Φ_{MAG}), total volume fraction ($\Phi_{BS/FA/MAG} = \Phi_{BS} + \Phi_{FA} + \Phi_{MAG}$), SLD of each component (SLD_{BS} , SLD_{FA} , SLD_{MAG}), total SLD ($SLD_{BS/FA/MAG} = SLD_{BS} + SLD_{FA} + SLD_{MAG}$), for each BS studied: NaTC, NaTDC, with and without 0.15 M NaCl. These parameters were used to fit SANS2D data. While the density of both FA was known (0.91 for C8:0 FA and 0.89 for C18:1 FA), the density of both MAG was assumed to be of similar value and was fixed at 0.90 for the calculation of the volume fractions.	109
Table 5: Number (#) of BS, water, Na ⁺ & Cl ⁻ molecules in each simulated system	115
Table 6: CMC and ΔF_{max} values for each BS studied, at 23°C and 37°C	116
Table 7: Concentration of BS in the sample ($[BS]$), volume fraction of BS in micelles (Φ_{BS}), amount of charges in BS micelle, volume fraction fitted by the software ($\Phi_{software}$, also equal to $\Phi_{BS} (1 - x_{Water})$), polar (R_{Pol}) and equatorial (R_{Eq}) radii values of the (oblate) ellipsoid BS micelle, volumes of the BS micelle core ($V_{Micelle\ core}$) and micelle ($V_{Micelle}$), proportion of water in BS micelle core ($x_{Water\ in\ micelles\ core}$) and micelle ($x_{Water\ in\ micelles}$), volume	

fraction of BS micelles in solution (Φ_{Micelles}), and BS micelle aggregation number (N_{agg}), for each BS studied: NaTC, NaTDC, with and without 0.15 M NaCl. These parameters were obtained from SANS2D (SANS) and ID02 (SAXS) data fitting. In the absence of salt, only SANS data could be fitted and therefore only the parameters obtained from the SANS measurements are shown in this table; in the presence of salt, both SANS and SAXS data could be fitted, except the ones obtained at high BS concentrations (i.e., 100 and 200 mM), where strong peaks of interaction are present. 120

Table 8: Concentration of FA (C8:0 or C18:1) and/or MAG (C8:0 or C18:1) in the sample (*[Additive]*), amount of charges in BS mixed micelle, volume fraction fitted by the software (Φ_{software}), polar (R_{Pol}) and equatorial (R_{Eq}) radii values of the (oblate) ellipsoid BS mixed micelle, volume of the BS mixed micelle core ($V_{\text{Mixed micelle core}}$), for each BS studied: NaTC, NaTDC, with and without 0.15 M NaCl. These parameters were obtained from SANS2D data fitting. 129

Table 9: NR parameters of each upper and lower (tails and head group) layer of the lipid (d_{62} -DPPC, d_{62} -DPPC/TC, d_{62} -DPPC/TO) bilayer: σ , the roughness, t , the thickness, SLD , the scattering length density and f_{water} , the amount of water. The parameters of the silicon oxide (SiO_2) layer and water layer between the block and the upper head group region are also given. For d_{62} -DPPC/TC, an additional layer – corresponding to the incorporation of tricaprylin between d_{62} -DPPC tails – is present. 136

Table 10: Amount of charges in BS mixed micelle, volume fraction fitted by the software (Φ_{software}), polar (R_{Pol}) and equatorial (R_{Eq}) radii values of the (oblate) ellipsoid BS mixed micelle, volume of the BS mixed micelle core ($V_{\text{Mixed micelle core}}$), for the BS mixed micelles formed upon adding either 100 mM NaTC or 50 mM NaTDC, to the three different liposomes: DPPC, DPPC/TC, DPPC/TO. These parameters were obtained from the fitting of D33 data obtained at 25°C. 142

Introduction

As the fifth leading risk for global death, overweight and obesity are timely, global, pressing issues [1]. Since 1975, worldwide obesity levels have nearly tripled, with as much as 39% of the world's adult population being now classified as overweight and 13% as obese, resulting in the premature death of at least 2.8 million people worldwide [2]. This health crisis, which used to be predominantly associated with developed countries, is now also prevalent in lower-income countries, as a result of changes in both lifestyle and diet habits. Developing preventive and therapeutic strategies contributing to the fight against obesity-associated diseases is therefore urgently needed.

Lipid (fat) is an essential nutrient and an important source of energy, but its overconsumption is responsible for severe health conditions like chronic cardiovascular diseases and type-2-diabetes mellitus [3]. The intake of dietary fats and its effect on health have thereby become a major focus of our modern societies. Controlling the digestion of fats and optimising their absorption, and ultimately formulating novel foods with appetite-suppressing or satiety-enhancing properties [4], could go some way to addressing the current obesity crisis and related health problems [4,5]. This approach requires a fundamental mechanistic understanding of the colloidal and interfacial processes involved in lipid digestion and uptake. This understanding is also highly relevant to the formulation of lipid-based drug delivery systems administered through the oral route [6].

1. Lipid digestion, with a focus on bile salts functionalities

The process of lipid digestion, also referred to as lipolysis or lipid hydrolysis [7,8], requires two water-soluble enzymes that bind to lipophilic substrates and act at the lipid/water interface [9,10]. As a first step, the gastric lipase is released into the stomach, where it hydrolyses from 10% to 30% of dietary fats [9]. Lipid digestion, however, occurs predominantly in the small intestine and is controlled by the secretion of the co-lipase-dependent pancreatic lipase into the duodenum [9] (Figure 1). These enzymes are able to cleave short-, medium- and long-chain triacylglycerols (TAG) into more polar lipids (diacylglycerols (DAG), monoacylglycerols (MAG) and free fatty acids (FFA)) [10], which accumulate at the lipid droplet interface because

of their amphiphilicity [11]. The presence of these more surface-active products at the interface gradually hinders further enzyme adsorption onto the droplet surface [12]. Nonetheless, in the duodenum (unlike in the stomach), a specific class of naturally occurring biosurfactants, called bile salts (BS) [13], prevents this enzyme activity inhibition.

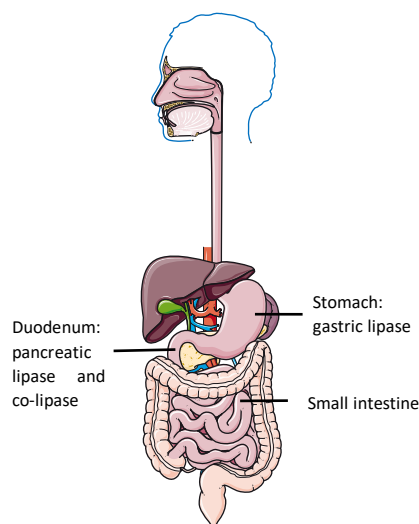


Figure 1: Catalytic proteins involved in lipolysis and their sites of action in the human body

1. 1. Structure and properties of bile salts

BS, the main components of human bile, are produced in the liver from cholesterol, stored in the gall bladder and released into the proximal small intestine (duodenum) in response to food intake. They comprise a short and flexible ionic chain linked to a rigid and slightly curved steroid skeleton (the surfactant hydrophobic "tail"), which contains hydrophilic (hydroxyl groups) and hydrophobic (methyl groups) faces [14] (Figure 2). This unconventional, planar molecular structure provides BS with atypical features, specifically in terms of bulk and interfacial behaviours. They self-assemble in solution in the form of micelles, but the structure of their aggregates and their micellisation process are still debated [15,16]. In addition, they display both a high surface activity and fast adsorption dynamics [8,17]. Their strong affinity for the interface, in particular, enables them to displace proteins from the lipid/water interface, thanks to an orogenic mechanism, whereby BS penetrate into the protein network, increasingly compressing the interfacial layer and weakening it, until it finally breaks [18].

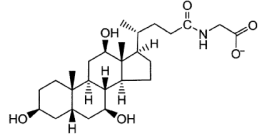
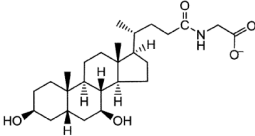
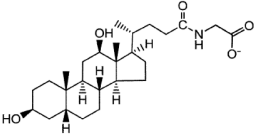
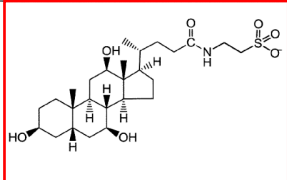
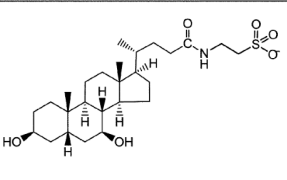
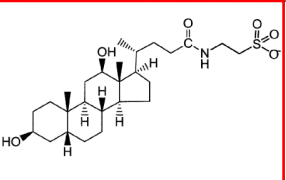
Conjugating group	Bile acid		
	Cholate	Chenodeoxycholate	Deoxycholate
Glyco-			
Tauro-			

Figure 2: Structures of the main BS, which differ by the type of conjugating amino acid moiety, and the number and position of hydroxyl groups on their steroid skeleton. In humans, glyco- and tauro-conjugates form about 70% and 30% of BS mixture, respectively; cholate and chenodeoxycholate derivatives each represent 40% of it, and deoxycholates ones around 20% (reproduced from [19] by permission of The Royal Society of Chemistry). The two BS selected in this project are shown in red.

1. 2. The role of bile salts in lipolysis

BS play a key role in promoting lipid digestion and absorption [8,17]. They are particularly crucial to avoid the inhibition of lipase activity, caused by the accumulation of hydrolysis products, because they help displace polar lipids from the lipid droplet/water interface by solubilising them into mixed micelles [13,20]. Because of their high surface activity, they also prevent the enzyme from binding to the substrate. Nevertheless, thanks to the co-lipase ability to adsorb onto a BS-dominated surface (*via* electrostatic interactions) [21], the complexation between the lipase and its co-factor [21,22] enables the reactivation of the BS-inhibited pancreatic enzyme [23].

Therefore, BS carry out two very different and vital functions in fat digestion [8,17]: 1) they promote enzyme-catalysed lipolysis, by adsorbing onto fat droplets surfaces and facilitating the access of the lipase/co-lipase complex, and 2) they remove insoluble lipolysis products from the interface, and shuttle them to the gut mucosa for absorption, by incorporating them into mixed micelles (Figure 3).

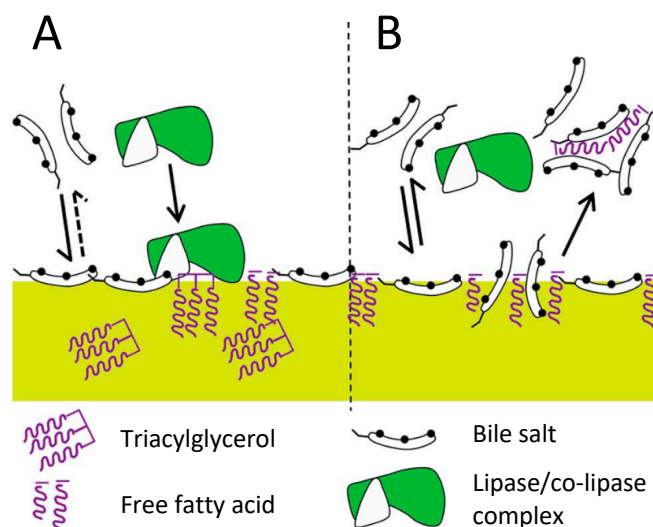


Figure 3: BS contrasting mechanisms of action during lipid digestion: (A) BS adsorption at the fat droplet interface, facilitating the lipase/co-lipase access to the lipid surface, thus promoting lipolysis, and (B) BS desorption from the interface and incorporation of lipolysis products into mixed micelles (reproduced from [19] by permission of The Royal Society of Chemistry).

1. 3. Bile salts structural diversity: a key to their contrasting functions

Although BS contrasting functionalities are well known, the underlying cause of this functional diversity still needs to be elucidated. With this prospect in mind, studies have been performed on the behaviour of BS both at the air/water interface [24] and on a hydrophobic surface [19], and the interfacial properties of *individual* BS, rather than their mixtures, or a single BS “model”, have recently been suggested to hold the key to their different roles [19]. Wilde *et al.* [19], in particular, have studied a range of BS by dual polarisation interferometry (DPI, which probes the mass of adsorbed layers onto a solid surface), focusing on the impact of small BS architectural variations on lipolysis. Their recent work [19] has brought to light clear differences in BS interfacial behaviour, mostly linked to the bile acid moiety: cholate-based BS were found to strongly adsorb onto hydrophobic surfaces (C18-modified silicon oxide sensors), in contrast to deoxycholate and chenodeoxycholate derivatives, which readily desorbed from the interface (Figure 4). These exciting new results call for further studies to elucidate how BS structure influences their interfacial behaviour and how, in turn, this impacts lipid hydrolysis.

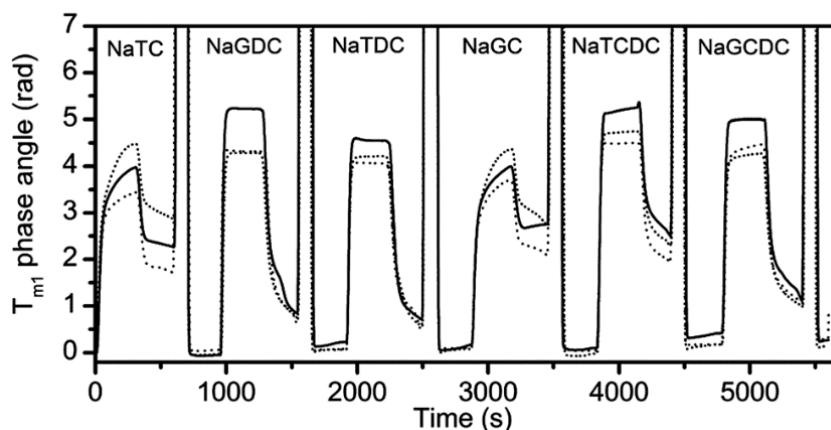


Figure 4: Phase angle variation for transverse magnetic component of light (T_{m1} phase angle) during successive injections of six different BS solutions ($[BS]_{\text{solution}} = 3 \text{ mM}$) in a 2 mM bis-tris buffer (pH 7.0) containing 150 mM sodium chloride and varying calcium chloride concentrations (solid line: 0 mM; dashed line: 1 mM; dotted line: 10 mM). Each BS injection is followed by a buffer rinse and the chip is cleaned between each experiment. BS adsorption onto the C18-modified silicon oxide sensor is denoted by an increase in T_{m1} phase angle, whereas a decrease in the same parameter indicates its desorption from the hydrophobic surface (reproduced from [19] by permission of The Royal Society of Chemistry).

The first objectives of this PhD project are therefore to determine how BS structural diversity controls their unusual interfacial properties, and to characterise the interfacial structures and mechanisms that enable them to facilitate lipid digestion, focusing on two BS, sodium taurocholate (NaTC) and sodium taurodeoxycholate (NaTDC) (Figure 2), based on their contrasting adsorption/desorption behaviour highlighted in previous work [19] (Figure 4).

To that end, we have used a wide range of interfacial techniques to assess the adsorption/desorption behaviour of these two BS and the structures they form at various interfaces:

- (i) the bare air/water interface – as a preliminary step before moving towards interfaces that better reflect the oil droplet surface (Chapter 1),
- (ii) a lipid-dense air/water interface – to represent the lipid droplet covered by phospholipid molecules found in the gut, either as endogenous molecules or food emulsifying agents (Chapter 1),
- (iii) the bare oil/water interface – to mirror the actual emulsion droplet/water interface formed upon digestion in the duodenum (Chapter 2),

- (iv) a lipid-stabilised oil/water interface – to better mimic the interfacial processes occurring during duodenal lipolysis (Chapter 2).

Due to the lack of structural characterisation of these interfaces at the molecular level, we have focused in this work on the use of X-ray and neutron reflectometry, which are techniques that have not been utilised much in the area of food science, particularly in the UK, to achieve a description of the structural organisation of each interface at the nanometre scale.

Secondly, we have focused on the solution behaviour of BS, exploring in particular the micellisation process and micellar structures relevant to the process of fat digestion (Chapter 3):

- (i) BS self-assembly on their own,
- (ii) BS aggregation in the presence of hydrolysis products found during digestion and removed by BS from the lipid droplet interface,
- (iii) BS solubilising capacity in the presence of liposomes, used as a preliminary mimic of the food colloidal structures found in the gut.

Characterising the structures of these different aggregates is an important step towards an understanding of the mechanisms underlying BS ability to incorporate lipolysis products into mixed micelles and to transport them towards the gut mucosa for absorption. Here also, we have focused on the use of small-angle neutron and X-ray scattering to obtain information on the various nanostructures formed in the bulk by BS.

2. Regulating lipid digestion with a specific food emulsifier, methylcellulose

Dietary fibres are mainly constituted of non-starch polysaccharides (including cellulose, hemicellulose, pectins and other hydrocolloids), which are resistant to hydrolysis and absorption in the small intestine, i.e., they pass the upper gastrointestinal tract and enter the colon substantially unmodified [25]; they can be found in edible plant foods, such as cereals, fruits, vegetables, beans and grains. Many human studies have shown a positive relationship between dietary fibre-rich diets and lowered obesity rates, proving in particular that dietary fibres show promise to induce weight loss and aid weight management [26]; their consumption is

therefore one potential solution for decreasing calories uptake, and ultimately stopping the rising epidemic of worldwide obesity.

2. 1. Methylcellulose, a model of dietary fibre

Due to their capacity to lower cholesterol levels after the consumption of a high-fat diet, without inducing any adverse effect [27], cellulose ethers [28,29], which play an important role in the formulation and processing of pharmaceuticals and are also widely used in food products [28], are referred to as 'dietary fibres'. With the aim of shedding light on the mechanisms underlying the hyperlipidaemia-reducing effect of these dietary fibres, methylcellulose (MC), which belongs to the large family of cellulose ethers and is approved for use in foodstuffs [30], has been selected in this work as a model emulsifying agent. MC is a non-ionic polysaccharide made up of a backbone containing repeating anhydroglucose units, where hydroxyl groups are substituted by methyl (hydrophobic) moieties [31] (Figure 5). This polysaccharide exhibits a demonstrated capability to regulate fat uptake [27], hypothetically *via* the inhibition of BS (and thus enzymes) adsorption at the fat droplet/water interface [32,33]. Our approach is thereby to better understand the processes whereby this specific lipolysis-hindering food surfactant delays fat digestion.

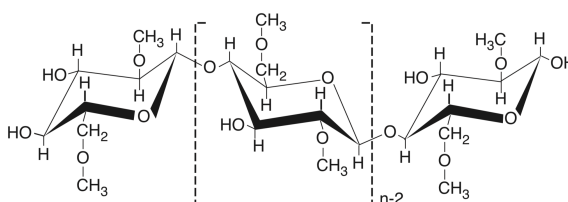


Figure 5: Structure of methylcellulose (MC)

2. 2. Cholesterol-lowering mechanisms of methylcellulose

Two models have been proposed to explain the role of MC in hindering BS activity and the observed resulting excess excretion of BS in faeces: (i) a thickening of the small intestine digesta due to MC high viscosity [34], restricting mixing, slowing down nutrients transportation and absorption by BS, and therefore reducing fat digestion [35–39]; and/or (ii) a sequestration of BS molecules in the network formed by MC, *via* hydrophobic interactions occurring both in the bulk aqueous phase and at

the fat droplet interface [32,33,40,41]. Both mechanisms could explain (i) the lengthening of the feeling of satiety *via* the activation of the “ileal brake” [42], which is induced by the accumulation of undigested fats in the distal small intestine because of BS functionalities being altered, and (ii) the reduction in hypercholesterolaemia due to the decrease in bile re-absorption in the ileum, which, in turn, increases BS synthesis from cholesterol [43]. Nevertheless, a detailed mechanistic understanding of the potential physicochemical processes delaying fat digestion in the gastrointestinal tract, is still required. In particular, there is a staggering lack of structural studies on the mechanism of BS entrapment by MC – which is the focus of this thesis.

The second objective of this PhD project is therefore to study the properties of this selected dietary fibre, MC, as a widely used food emulsifier and potential inhibitor of BS, as well as its interactions with the two BS selected.

For that purpose, we have characterised the interactions occurring between MC and BS (Chapter 4):

- (i) in the bulk aqueous phase, representative of the gut continuous aqueous medium,
- (ii) at the MC-adsorbed air/water interface, as a preliminary mimic of a fat droplet surface surrounded by MC, used as a food emulsifying agent,
- (iii) at the oil/water interface of MC-stabilised emulsion droplets, to reflect the actual lipolysis process taking place in the gastrointestinal tract.

The objectives and plan of the thesis are further described at the end of this introduction.

3. Techniques of investigation

A wide range of instruments has been employed and combined as part of this thesis. This section focuses on the main techniques of investigation: surface pressure measurements with the Langmuir trough (LT), oscillatory shear rheology and

neutron/X-ray scattering techniques. Other techniques, namely, Brewster angle microscopy, ellipsometry, pendant drop (all used as complementary interfacial methods), quartz-crystal microbalance with dissipation monitoring (which helped guide the formation of solid-supported lipid bilayers, prior to neutron reflectometry (NR) measurements), pyrene fluorescence spectroscopy (employed for the assessment of BS micellisation processes), optical/confocal microscopy and the pH-stat method (used for *in vitro* lipolysis studies), are described in the corresponding chapters.

3. 1. Interfacial studies with the Langmuir trough

Within this thesis, the Langmuir trough (LT) technique was used to study the different phases successively observed in a monolayer at the air/water interface, upon film compression. The surface pressure (π , with $\pi = \gamma_0 - \gamma$, where γ_0 is the surface tension of the bare air/water interface and γ that induced by the presence of a monolayer) is recorded as a function of the area per molecule; this measurement is known as the $\pi - A$ Langmuir isotherm. The molecular area is determined by monitoring the LT surface area and dividing it by the number of molecules present at the interface (calculated knowing the volume and concentration of material spread on top of the surface), and the surface pressure (π) by measuring the different forces acting on the plate (which is also called the 'Wilhelmy-plate' method). In this thesis, a phospholipid monolayer has been employed to mimic the lipid molecules present on fat droplet surfaces (Chapter 1); their packing was thereby studied using this technique, and the typical phases of the phospholipid film upon compression (i.e., LT surface area reduction) were analysed, as shown in Figure 6 (reproduced from Chapter 1, Figure S10). Because the surface pressure (π) is proportional to the surface tension (γ), the LT can also be used to assess the adsorption/desorption dynamics of a molecule either at the bare air/water interface or at the interface stabilised by a surface-active molecule. In this work, the interfacial properties of BS at both the pristine and phospholipid-stabilised air/water interfaces have been investigated (Chapter 1).

Surface pressure measurements with the LT can be complemented by contemporaneous Brewster angle microscopy and ellipsometry measurements,

which enable the visualisation of the lateral, morphological features of an interfacial monolayer and the assessment of the amount of material adsorbed at the interface, respectively; these two complementary techniques are further explained in the experimental section of Chapters 1 and 4. The pendant drop technique was also employed in this study to achieve further insight into BS adsorption/desorption properties at the bare oil/water interface – which is a better mimic of physiological interfaces; further information regarding the technical background of this instrument is given in the experimental section of Chapter 2.

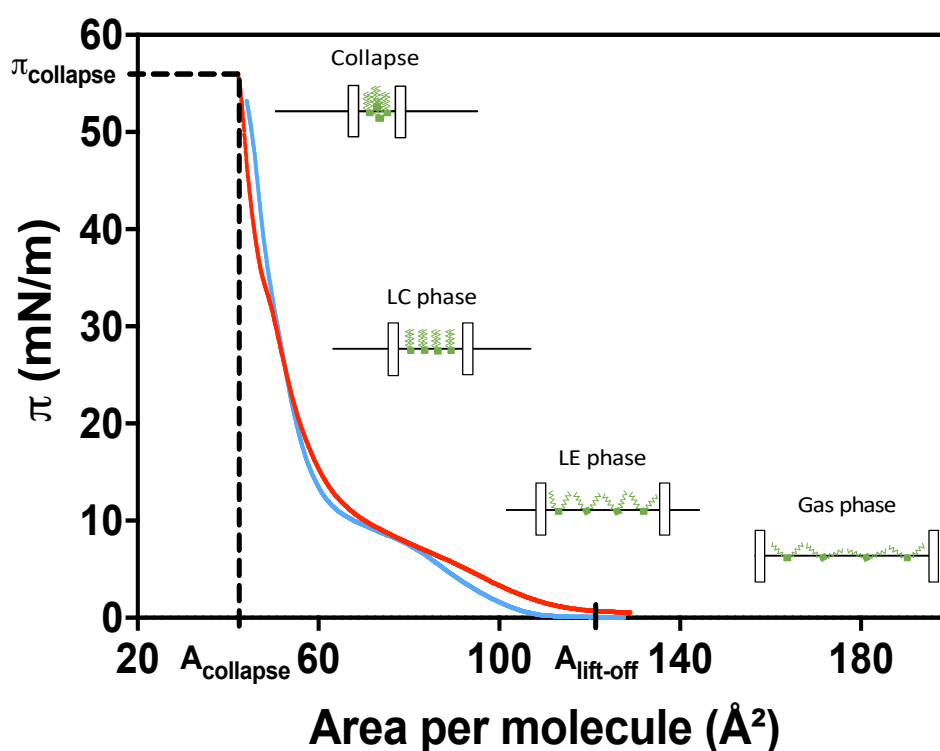


Figure 6: 1,2-dipalmitoyl-*sn*-glycero-3-phosphocholine (DPPC) (—) and 1,2-dipalmitoyl- d_{62} -*sn*-glycero-3-phosphocholine-1,1,2,2- d_4 -N,N,N-trimethyl- d_9 (d_{75} -DPPC) (—) $\pi - A$ Langmuir isotherms. The phospholipids were deposited onto ultrapure water, at a low concentration (gas phase, which has a low impact on surface pressure), and compressed (at $23 \pm 2^\circ\text{C}$). $A_{\text{lift-off}}$ corresponds to the minimal surface density at which molecules start interacting and enter into the liquid-expanded (LE) state. Upon further compression, the sharper increase in surface pressure indicates the onset of a much more ordered and packed liquid-condensed (LC) monolayer. A_{collapse} and π_{collapse} are, respectively, the mean molecular area and surface pressure at which the film breaks. The different monolayer phases and related molecular organisations observed in the different regions of the isotherm are depicted in the figure. This figure has been obtained as part of our study of BS interaction with a phospholipid monolayer at the air/water interface (reproduced from Chapter 1, Figure S10, and [44]).

3. 2. Oscillatory shear rheology bulk studies

Rheology is the study of deformation and flow of matter, *via* the measurement of its viscosity and elasticity when submitted to a force (or shear stress), which results in a deformation (or shear strain) [45,46]. Solids are 100% elastic materials, whose energy of deformation is fully recovered after removal of an applied stress, while, in liquids, this energy dissipates into the material in the form of heat and is not recovered upon stress removal, resulting in the liquid material being irreversibly deformed (i.e., flowing). Viscosity characterises the resistance of these materials to deformation.

Rheology experiments consist in shearing a sample, which is sandwiched between two plates, with the upper plate moving and the lower one remaining stationary (or *vice-versa*), and measuring the shear stress (σ), with $\sigma = F/A$, where A is the shear area and F the shear force acting on the upper plate to induce a specific shear strain (i.e., deformation) (γ , with $\gamma = s/h$, where s is the deflection path of the upper, movable plate and h the gap width between the plates), or shear strain rate (i.e., deformation rate) ($\dot{\gamma}$, with $\dot{\gamma} = \frac{1}{h} \frac{ds(t)}{dt}$) (Figure 7). These shear rheology measurements can be conducted with either continuous rotation (steady-state measurements, which generate flow curves) or rotational oscillation (dynamic or oscillatory measurements). In this thesis, a strain-controlled rheometer was employed to perform oscillatory shear rheology measurements. With this technique, an oscillatory shear strain is imposed and the resulting shear stress is measured; the phase shift (δ) between the oscillations of the applied strain and response stress varies between 0° and 90° , corresponding to, respectively, an ideal elastic deformation (instantaneous response) and ideal viscous flow (delayed response) behaviour. The complex shear modulus (G^* , with $G^* = \sigma_0/\gamma_0$, where σ_0 and γ_0 are the oscillation amplitudes of, respectively, the shear stress and shear strain), measures the material overall resistance to deformation. This parameter can be decomposed into an elastic (G') and viscous (G'') contribution. The storage (or elastic) (G') and the loss (or viscous) (G'') moduli probe, respectively, the material's elasticity (i.e., its solid-like behaviour) and viscosity (i.e., its liquid-like behaviour).

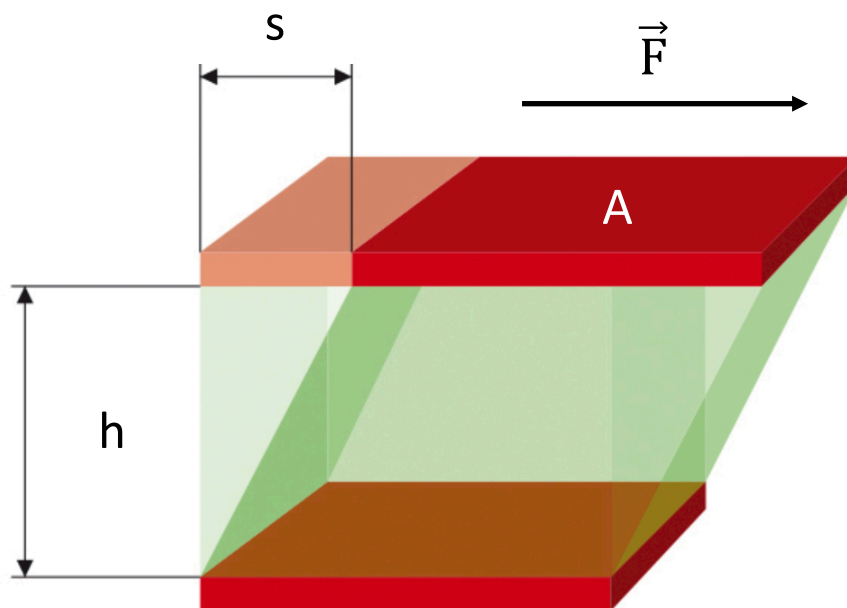


Figure 7: Schematic representation of a shear rheology measurement using a two-plate model

In this thesis, the impact of BS on the viscoelastic behaviour of MC, a polysaccharide with gelation properties, has been studied by performing oscillatory shear rheology measurements with a strain-controlled rheometer (Chapter 4). Different dynamic tests can be carried out with this technique; those performed as part of this project are explained here.

Dynamic strain amplitude sweeps, which measure the strain-dependent evolution of the viscoelastic properties (i.e., G' and G'') of a material at constant angular frequency, are first carried out to define the linear viscoelastic regime (LVR, or non-destructive deformation range), in which the storage (G') and loss (G'') moduli are independent of the applied strain. More precisely, this test enables the determination of the strain to be applied for the investigation of the rheological properties of a material as a function of temperature (dynamic temperature sweep test) or angular frequency (dynamic frequency sweep test); at this specific strain, the information obtained only depends on the properties of the material. The extent of this region also provides information on the toughness (vs. brittleness) of the material (the narrower the LVR, the more brittle the material tested).

In the case of a temperature-dependent gelation process, dynamic temperature sweeps are performed with the aim of investigating the viscoelastic behaviour of a material upon temperature-induced gel formation, following in particular changes in

the storage (G') and loss (G'') moduli. In this test, the amplitude of the strain and the angular frequency are kept constant, while a controlled temperature ramp is applied. In the sol state, very small or no elastic contribution exists ($G' < G''$); as the three-dimensional network forms, the elastic contribution increases (resulting in $G' > G''$) and both moduli level off as the system reaches equilibrium. Dynamic temperature sweeps are a particularly useful tool to determine gelation temperature.

Dynamic frequency sweeps monitor the effect of angular frequency (or rate of deformation) on the rheological properties (i.e. G' and G'') of a material, at constant strain. This type of measurements is used to determine the viscoelastic properties of a sample. A perfectly solid-like material is characterised by the frequency-independence of its storage (G') and loss (G'') moduli, with $G' > G''$ at all frequencies.

3. 3. Neutron and X-ray scattering techniques

Scattering is a class of powerful (non-destructive, in the case of neutrons) techniques, which makes use of the wave properties of either neutrons (for small-angle neutron scattering (SANS) and neutron reflectometry (NR)) or X-rays (for small-angle X-ray scattering (SAXS) and X-ray reflectometry (XRR)) to probe the structure of materials at the nanometre length scale.

3. 3. 1. **Theoretical background on scattering techniques**

3. 3. 1. 1. Small-angle scattering

Small-angle scattering allows the resolution of the nanoscale structure of materials (such as surfactants aggregates, polymers, gels, nanoparticles, proteins, among others), whose size ranges between 10 and 1,000 Å [47–51]. More specifically, this technique enables the characterisation of the objects size and shape (through the determination of its volume, radius of gyration, dimension and specific area), and also their organisation in a continuous medium (i.e., are the objects aggregated or homogeneously dispersed?). In this thesis, small-angle scattering has been used to define the self-assembled structures formed by BS micelles, in the absence and presence of the products of lipolysis, as well as the structures resulting from the BS-induced solubilisation of liposomes mimicking ingested fats (Chapter 3).

In a SANS or SAXS measurement, an incident (neutron or X-ray) beam of wavelength λ is directed at a sample and partially transmitted, absorbed and scattered, as a result of its interaction with the material (Figure 8). A detector, positioned at a distance D and covering a scattering angle 2ϑ from the sample, records the intensity of scattered radiation (I) as a function of the modulus of the scattering vector (q). Neutrons, which are scattered by the atomic nucleus, and X-rays, which interact with the atomic electron cloud, can be elastically (no loss or gain of energy upon collision) and inelastically (energy exchange with the nucleus/atom) scattered by the sample. In the case of neutrons, the scattering can be divided into two contributions: the coherent (related to the collective behaviour of different nuclei) and incoherent (related to the individual properties of a single atom) ones; in the case of X-rays, scattering is assumed to be mostly coherent. Only coherent elastic events contain relevant structural information in a small-angle scattering experiment, the incoherent component being a q -independent (i.e., flat) background. The incident beam can be described as a planar monochromatic wave characterised by an incident (\vec{k}_i) and scattered (\vec{k}_s) wave vector. The difference between these two vectors corresponds to the scattering vector ($\vec{q} = \vec{k}_s - \vec{k}_i$), whose modulus is defined as follows:

$$q = |\vec{q}| = |\vec{k}_s - \vec{k}_i| = \frac{4\pi}{\lambda} \sin \vartheta \quad (1)$$

A wide q -range can be covered either by varying the sample-to-detector distance (D), and hence the scattering angle (2ϑ), working at a fixed wavelength, or by using simultaneously a wide range of incident beam wavelengths (λ), with the time-of-flight mode, which is more often used at spallation sources and allows neutrons separation by the measurement of the speed at which neutrons with different wavelengths reach the detector.

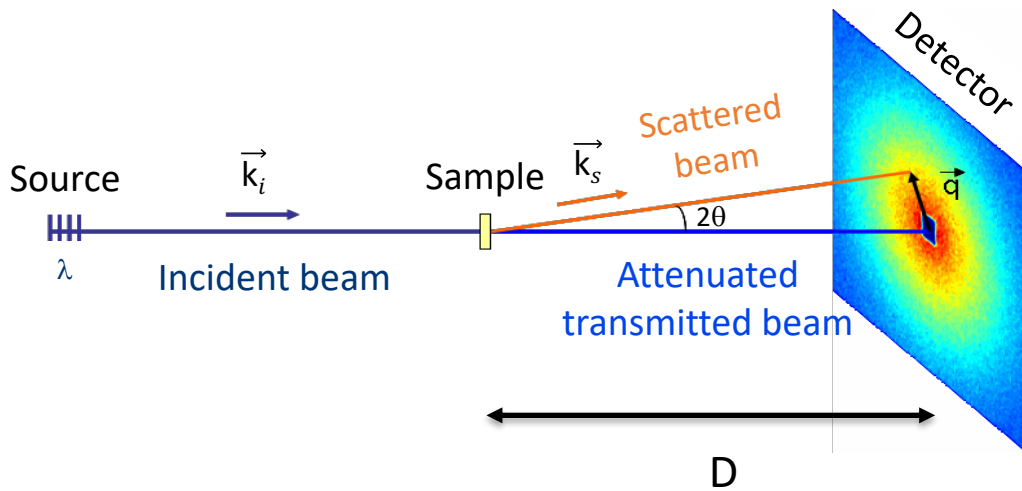


Figure 8: Schematic representation of a small-angle scattering experiment (reproduced with permission from [49]; copyright (2008) Springer Nature)

In crystalline materials, the Bragg's law of diffraction (Figure 9) is given by the following equation:

$$n\lambda = 2d \sin \vartheta \quad (2)$$

where n is an integer multiple, and d the interplanar distance between the atoms. Through this relationship, the scattering vector (q) (reciprocal space) can be linked to a characteristic distance in the sample (d) (real space) using Equation 1, as follows:

$$q = \frac{2\pi \cdot n}{d} \quad (3)$$

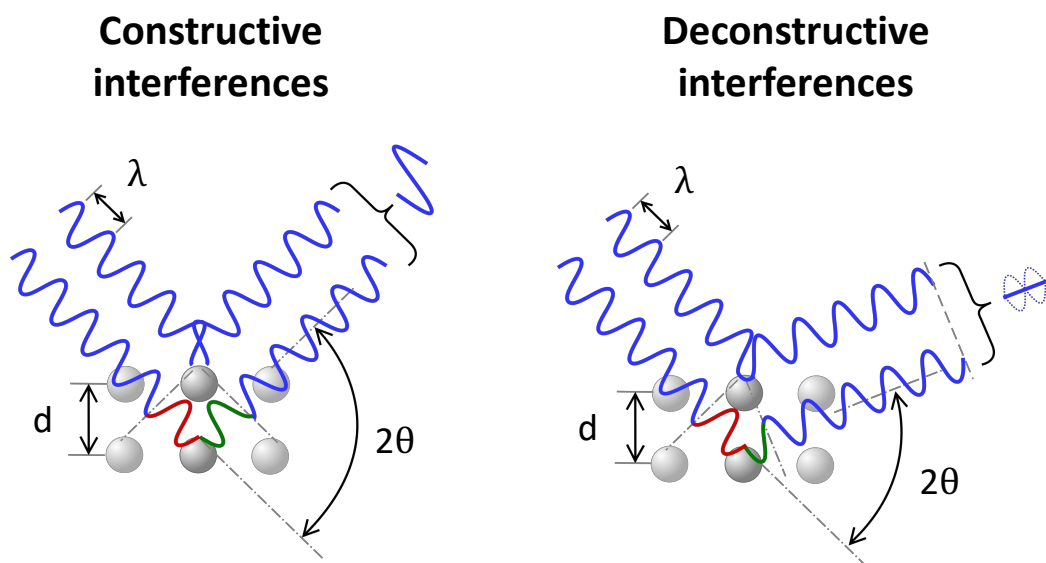


Figure 9: The incident wave generates scattered waves from either the nucleus (for neutrons) or electronic cloud (for X-rays) of an atom (reproduced from [52]). These re-emitted waves interfere with each other, either

constructively or destructively, producing a distinctive neutron or electron scattering pattern on the detector. In this figure, these phenomena are shown using the example of a crystalline structure with fixed atom positions, into which waves are scattered from lattice planes spaced by an interplanar distance d . In the presence of constructive interferences, the scattered waves remain in phase and the path length between the two incident waves (shown in red) is equal to an integer multiple (n) of the wavelength (λ); the lower interfering wave traverses an extra length of $2d \sin \vartheta'$. In the case of destructive interferences, both signals are cancelled.

This important relationship shows that, depending on the q -range probed, different length scales can be measured by varying the scattering vector: large q values enable the obtention of information at small length scales, and inversely small q values relate to large dimensions in the real space (Figure 10).

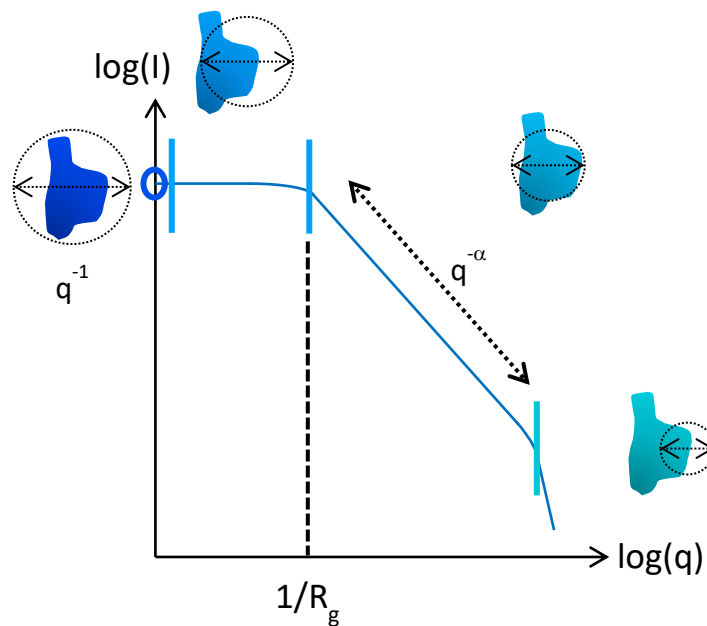


Figure 10: Schematic representation of a scattering curve obtained with small-angle scattering, in the case of dilute (i.e., non-interacting) objects in a continuous medium. In this figure, the scattered intensity (I) is plotted as a function of the scattering vector (q) in a log-log representation. Each circle shows the typical size (q^{-1}) probed by neutrons in each q -range, as compared with the object size. At $q \rightarrow 0$, the volume of the object (and thereby its mass) can be determined. At low q , in the Guinier regime, q^{-1} is much larger than the size of the object, allowing the radius of gyration (R_g), which represents the size of the scattering object, to be obtained. In the intermediate q -range, the scattered intensity (I) has a $q^{-\alpha}$ decay, where α is related to the shape of the object (e.g., $\alpha = 1$ corresponds to a one-dimensional object, like a cylinder, 2, a two-dimensional object, like a disk, and 4, a bulky object, like a sphere; if the geometry of the object is not well defined, α will represent the object fractal dimension and will vary between 2 and 4). At high q , in the Porod regime, q^{-1} is much smaller than the size of the object, resulting in the scattered intensity being only sensitive to the interface between the homogeneous media displaying different SLD ; in this q -region, the surface area (i.e., the quantity of scattering surfaces) per unit volume of the sample, and ultimately the specific area of the object itself, can be determined.

In the case of rigid centro-symmetrical objects, the scattered intensity is described by the following equation:

$$I(q) = \frac{n.N^2}{V_{Sample}} (SLD_{Object} - SLD_{Solvent})^2 V_{Object}^2 P(q) S(q) \quad (4)$$

where n is the number of objects, N the number of individual scattering species contained in each object, SLD_{Object} and $SLD_{Solvent}$ the scattering length densities (SLD) of, respectively, the object probed and the solvent, V_{Sample} and V_{Object} the volumes of, respectively, the sample and the object probed, $P(q)$ the form factor and $S(q)$ the structure factor. The SLD plays the same role as the refractive index in light scattering experiments (further explanations are given about this parameter in the “3.3.2 Scattering length density, the contrast factor” section). The form factor ($P(q)$) contains information on the correlations between the individual scattering species within the same object (i.e., intra-object contribution), and the structure factor ($S(q)$) reflects correlations between the scattering centers of mass of different objects (i.e., inter-object contribution). Consequently, the form factor characterises the size and shape of the scattering object, while the structure factor gives information on the spatial arrangement of the objects and their interactions. The inter-object contribution, and therefore the structure factor, can be reduced by dilution of the system. Various mathematical models of form factor describing most common shapes [53], as well as different analytical expressions of the structure factor [54–56], have been developed and computed in analysis programs (such as SasView [57], the software used in this work), and can therefore be used to fit experimental data.

As part of this thesis, SANS has been employed to determine the structures (i.e., their size and shape) formed upon (i) self-assembly of BS molecules, (ii) interaction of BS with components mimicking the products of lipolysis, and (iii) solubilisation of TAG-incorporating lipid vesicles by BS (Chapter 3). SAXS complementary measurements have also been carried out on BS pristine micelles to obtain a more detailed description of these self-assembled structures.

3. 3. 1. 2. Specular reflectometry

Specular reflectometry enables the probing of surfaces and buried interfaces structures in layered systems, and in particular the determination of the thickness and internal structure of thin films at various interfaces (e.g., air/liquid, liquid/liquid,

solid/air or solid/liquid). This technique resolves thicknesses ranging between 10 and 1,000 Å [50]. As part of this thesis, reflectometry has been used to characterise the molecular arrangement of BS molecules at the bare and phospholipid-stabilised air/water interfaces (Chapter 1), as well as at the pristine and phospholipid-stabilised oil/water interfaces (Chapter 2), and to determine the location and conformation of different TAG molecules in a lipid bilayer – used as a preliminary mimic of a fat droplet found in food (Chapter 3).

Reflection (as well as refraction) occurs when an incident (neutron or X-ray) beam of wavelength λ hits an interface separating two media characterised by different refractive indices (n) (Figure 11). Reflectometry records the ratio between the reflected and incident intensities, which is also called reflectivity (R), as a function of the scattering vector modulus (q). In this thesis, only specular reflection (i.e., the angle of reflection is equal to that of incidence) was measured and, in this case, the angle of reflection (ϑ_r) is equal to that of incidence (ϑ_i). In this configuration, the scattering vector (\vec{q}) is perpendicular to the interface (and therefore noted \vec{q}_z); its modulus, described as the sum of both the incident (\vec{k}_i) and reflected (\vec{k}_r) wave vectors ($q_z = |\vec{q}_z| = |\vec{k}_i + \vec{k}_r|$), is defined as in small-angle scattering experiments (Equation 1, where, in this case, $\vartheta = \vartheta_i = \vartheta_r$) and is also inversely proportional to characteristic distances of the sample in the real space (Equation 3).

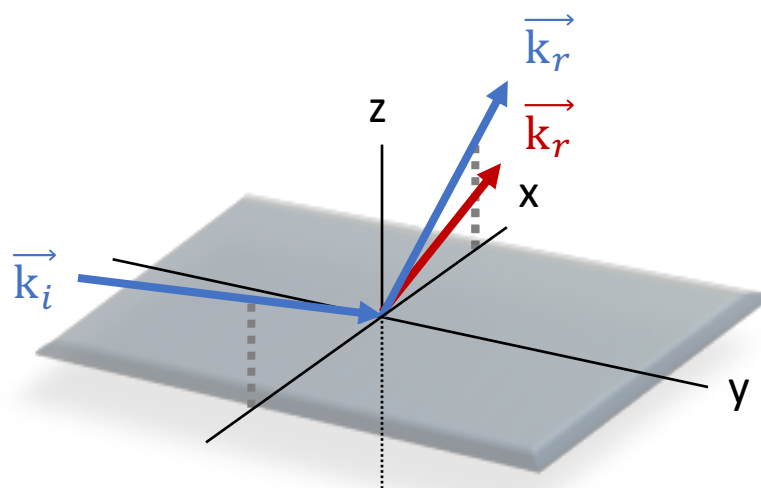


Figure 11: Schematic representation of a reflectometry experiment. Both specular (reflected scattering vector (\vec{k}_r) shown in blue) and off-specular (reflected scattering vector (\vec{k}_r) shown in red) reflections lie in the plane of incidence (i.e., no components along the y-axis). Nonetheless, in specular reflection, the angle of reflection

is equal to that of incidence, while in off-specular reflection, the angle changes; therefore, with specular reflection, perpendicular features can be resolved (the scattering vector being parallel to the z-axis (\vec{q}_z)), and with off-specular reflection, structural information can be obtained on the lateral direction (the scattering vector having components along both the z- and x-axes).

Reflectometers display either a monochromatic or time-of-flight (i.e., polychromatic, only for NR instruments) mode. For the systems studied in this thesis, the accessible q_z values ranged from 0.001 to 0.3 \AA^{-1} (for NR) and from 0.0001 to 0.4 \AA^{-1} (for XRR performed on a lab source). In both cases, the factor limiting the upper q_z value was the background level. With both types of instrument, the whole q_z -range is covered by changing the incident angle, which can be done by rotating either the sample and detector (with solid substrates) or the incidence and detector arms around a fixed sample (with free liquids). Nonetheless, contrary to time-of-flight (or polychromatic) instruments, which allow accessing the whole q_z -range using two or three configurations only (as a wide q_z -range is covered with one configuration), monochromatic instruments require many more configurations (as only one q_z value is obtained with one configuration).

The refractive index at the boundary between two media i and j ($n_{i,j}$) is known to be linked to the SLD by the following equation:

$$n_{i,j} \approx 1 - \frac{\lambda}{\pi} (SLD_j - SLD_i) \quad (5)$$

where SLD_j and SLD_i are the scattering length densities (SLD) of, respectively, the media i and j . Reflectivity is therefore determined only by the variation in SLD between the two media (or layers).

Reflectometry data analysis with data fitting softwares (such as Aurore [58], the one used in this work) enables the establishment of the SLD (for NR) or electron density (for XRR) profile of the film(s) (or layer(s)) studied along the direction perpendicular to the surface (z), which is directly related to the distribution of each molecular component in this direction. From data fitting, structural information, such as the thickness and solvation of each interfacial layer, as well as the roughness at each interface, can be obtained. It is worth noting that roughness and diffuse interfaces cannot be distinguished with specular reflectivity only.

In this work, the morphology of the films formed by BS at the bare air/water interface has been described using XRR (Chapter 1), and that formed at the pristine oil/water interface using NR (Chapter 2). The interaction of BS with phospholipid molecules present at the air/water (Chapter 1) and oil/water (Chapter 2) interfaces, has been investigated by NR. NR has also been employed to characterise the internal structure of TAG-incorporating liposomes bilayers, allowing in particular the determination of the TAG location and conformation (Chapter 3).

3. 3. 2. Scattering length density, the contrast factor

As can be seen from Equations 4 and 5, in any small-angle scattering and reflectometry experiment, the contrast term is the difference in *SLD* between the object and the solvent (for small-angle scattering) and between the two layers forming an interface (for reflectometry): with X-rays, the scattering depends on differences between the electronic structure of atoms (referred to as electron *SLD*), and for neutrons, on differences between the nuclear structure of atoms (referred to as neutron *SLD*). Because neutron and X-ray scattering techniques rely on different contrasts, their combination can be conveniently used to resolve different structural motifs in the systems studied.

The electron and neutron *SLD* of an individual scattering species (or molecule) are defined as follows:

$$\text{electron SLD} = r_e \frac{\sum x_i Z_i}{v_m} \quad (6)$$

$$\text{neutron SLD} = \frac{\sum x_i b_c^i}{v_m} \quad (7)$$

where x_i is the number of atom i in the molecule, v_m the molecular volume of the molecule, r_e the classical radius of the electron, Z_i the atomic number of the atom i , and b_c^i the coherent scattering length of the atom i (values of coherent scattering lengths are tabulated [59,60]).

3. 3. 3. The contrast-variation method with neutrons

Because the coherent scattering length (b_c) can vary significantly between isotopes – unlike the atomic number (Z) – the contrast term, which is proportional to

the scattered intensity (Equation 4) and the refractive index (Equation 5), can be easily tuned by simple isotopic substitution (assuming that it has no significant impact on the physicochemical properties of the objects probed). For instance, the coherent scattering lengths of hydrogen (H) and deuterium (D) atoms are $b_c^H = -3.74$ fm and $b_c^D = 6.67$ fm, respectively, and therefore H₂O is typically replaced by D₂O in a SANS experiment to provide contrast between the objects probed and the solvent. The method of 'contrast variation', which uses isotopic substitution, is a key advantage of neutron-based techniques (SANS and NR) over X-rays (SAXS and XRR) and light scattering, as it enables the 'highlighting' and/or 'hiding' of different parts of a system and thereby the elucidation of the structure of individual species or components in multi-component systems, either in the bulk (SANS) or at the interface (NR).

For instance, with SANS, using a specific isotopic solvent mixture (e.g., varying the hydrogen/deuterium ratio of a solvent), this strategy can be employed to create some contrast in a system in which the dispersed and continuous phases display similar *SLD*, or to match one individual scattering species of a ternary system, in order to have a binary system in terms of *SLD* and be able to determine the structure of each part of this system (e.g., contrast-matching successively the polymers and nanoparticles mixed together in a continuous phase, or the stabiliser layer and oil droplet of an emulsion in an aqueous medium) (see [61] and [62] as examples). An example of the different contrasts that can be employed in the case of an emulsion (or core/shell structure) is depicted in Figure 12.

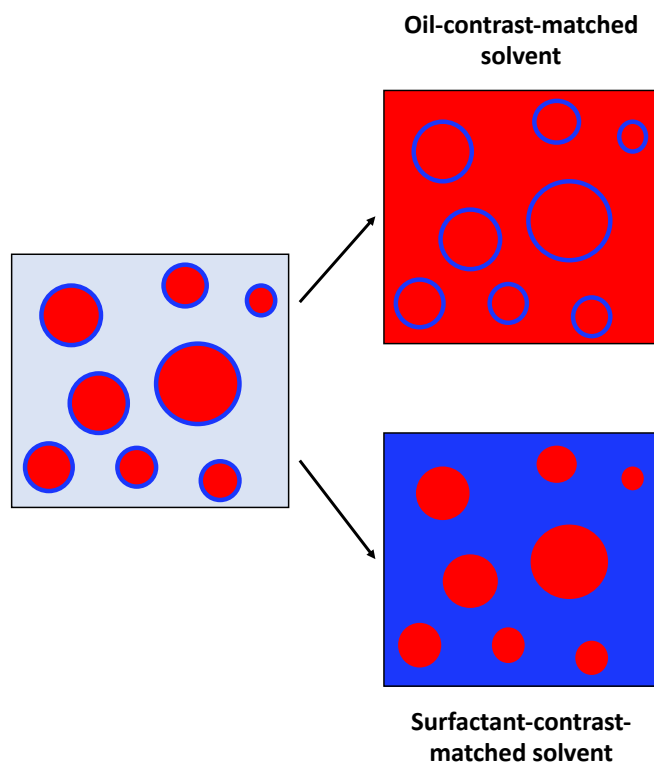


Figure 12: Schematic representation of the contrast-matching technique applied to an emulsion droplet. A specific isotopic (or hydrogen/deuterium) solvent mixture is used to match, selectively, the oil droplet and the stabiliser layer, thereby allowing the determination of, respectively, the film thickness and the droplets specific area.

With NR, hydrogen/deuterium exchange is usually used to change the *SLD* of one of the two media and/or of one of the components in a film present at the interface. For instance, a mixture of 8.1% D₂O in H₂O (V/V), also called air-contrast-matched water (ACMW), would match the *SLD* of air in the case of investigations at the air/water interface with the LT, and a mixture of 32% D₂O in H₂O (V/V), also known as silicon-contrast-matched water (SiCMW), would match the *SLD* of silicon, often used as a substrate for a solid/liquid interfacial study; deuterated molecules can also be used in the presence of D₂O, to remove their contribution to the reflectivity signal and thereby highlight hydrogenated compounds in the sample. An example of the different contrasts used in one of the NR experiments performed as part of this thesis is shown in Figure 13.

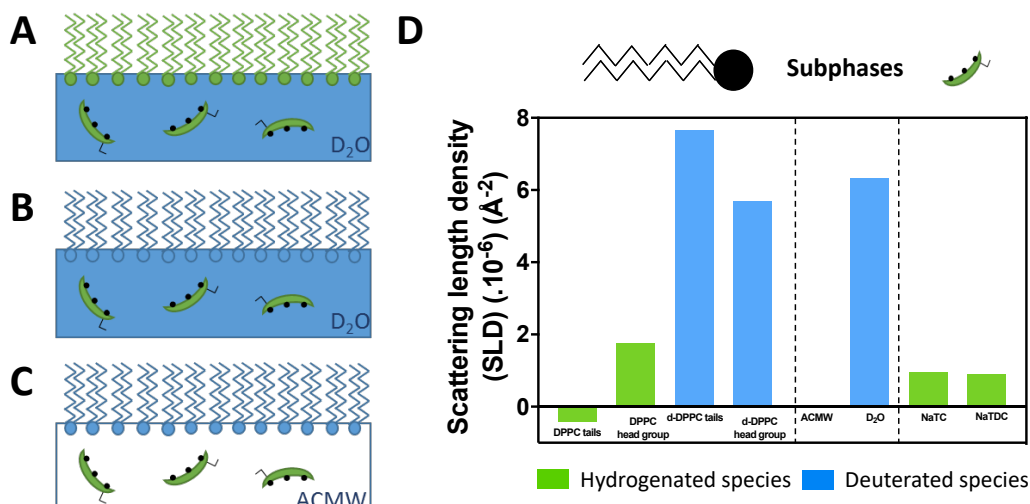


Figure 13: (A, B, C) Schematic representation of the contrast-matching technique applied to an air/water interface stabilised by phospholipids, in the presence of hydrogenated BS in the bulk aqueous phase (which actually corresponds to the NR experiment presented in Chapter 1). (D) SLD of each component present in this experiment (lipids, subphases and BS). In this study, different subphases, characterised by different SLD, have been used to have different contrasts and highlight different parts of the system: (A) the use of D₂O with hydrogenated phospholipid molecules (DPPC) makes both lipid and BS (NaTC and NaTDC) molecules visible; in addition, (B) with D₂O, whose SLD is similar to the one of deuterated phospholipid molecules (d-DPPC), the hydrogenated BS molecules are mostly seen, thereby highlighting BS location at the interface, whereas (C) with air-contrast-matched water (ACMW, a mixture of 8.1% D₂O in H₂O (V/V)), whose SLD is zero as air and close to the SLD of BS, the deuterated phospholipid molecules are highlighted, thus allowing the determination of the lipid interfacial film thickness and organisation.

4. Thesis objectives and methodologies

The aims of this PhD thesis are:

(i) to elucidate the origin of BS contrasting functionalities during fat digestion, focusing on the impact of their natural diversity on their structures and behaviour at various interfaces, and to shed light on the interfacial mechanisms that govern their different roles in the process of lipolysis,

(ii) to provide a mechanistic understanding of the processes through which MC – the selected cholesterol-lowering emulsifier – induces BS (and thus enzymes) inhibition, lipid digestion regulation and associated health benefits.

By answering these questions, this work aims to tackle very timely, practical health challenges of societal importance pertaining to the diet-gastrointestinal tract interface, and thus to provide results of particular relevance to the food industry. This

study addresses fundamental questions on the role of BS during lipolysis, from a colloid and interface science perspective, rather than a physiology and nutrition approach. The work uses a wide range of surface and solution methods, with a focus on neutron techniques, capitalising on an ILL studentship, which means that the candidate was based at the ILL for most of the PhD work. Neutron scattering, which is still under-used in the food science area, is a non-invasive physical technique allowing detailed structural information to be revealed at the nanometre scale, by making use of the wave properties of neutrons, which interact with atoms nuclei. Some theoretical background on this technique, and other techniques used in the thesis, is presented in Section 3 of this Introduction: 'Techniques of investigation'.

A plan of the thesis, with a short description of each chapter, is provided below.

Chapter 1: Molecular insights into the behaviour of bile salts at interfaces: a key to their role in lipid digestion

The digestion and absorption of dietary lipids are largely controlled by physicochemical processes occurring at the interface of emulsion droplets, as they travel along the gastrointestinal tract. Combining a range of interfacial techniques (Langmuir trough monolayers, ellipsometry and Brewster angle microscopy), we have mapped out the interfacial properties of the two selected BS, by investigating their adsorption/desorption dynamics at (i) the air/water interface, as a preliminary study towards more physiologically relevant interfaces, and (ii) the lipid/water interface, to mimic the fat droplet surface stabilised by phospholipid molecules. In order to provide a detailed molecular picture of the fat droplet interface and its evolution over time, after interaction with BS, we have employed X-ray and neutron reflectometry techniques, and also present complementary atomistic-level molecular dynamics simulations.

Chapter 2: Bile salts behaviour at the oil/water interface: molecular insight into lipid digestion

In Chapter 2, we have moved towards a more physiologically relevant oil/water interface – which reflects the actual fat droplet/water interface – and monitored the ability of BS to adsorb at this interface using the pendant drop technique. In order to achieve structural characterisation with neutron reflectometry, we have used an original oil/water liquid/liquid setup, which we have applied for the first time to a biologically relevant system, and characterised interfacial structures.

Chapter 3: Aggregates of bile salts, mixed micelles with fatty acids and monoacylglycerols, and interaction with liposomes

To gain further insight into the mechanisms through which BS promote nutrients transportation and absorption towards the gut mucosa during fat digestion, we have studied BS propensity (i) to self-assemble in water on their own, (ii) to produce mixed aggregates in the presence of the products of lipolysis (i.e., monoacylglycerols and free fatty acids), and (iii) to solubilise liposomes mimicking food ingested into the gut. We have employed small-angle X-ray and neutron scattering to obtain a structural description of each system and complemented these analyses with the characterisation of BS micellisation process with fluorescence spectroscopy, using pyrene as a probe. Additionally, we have resorted to the neutron reflectometry technique to obtain detailed information on the structural organisation of the liposomes bilayer.

Chapter 4: Interactions of bile salts with a dietary fibre, methylcellulose, and impact on lipolysis

This chapter examines the role of a dietary fibre on lipid digestion and its interactions with the two BS selected. We have investigated the impact of BS type and concentration on the bulk and interfacial properties of MC by performing oscillatory shear rheology measurements, as well as interfacial studies with the Langmuir trough and ellipsometry. We have then carried out *in vitro* lipolysis studies

on an MC-stabilised emulsion to assess how MC/BS interactions affect the process of digestion: we have used optical and confocal microscopy to probe the changes in emulsion droplets microstructures induced by BS, and the pH-stat method to monitor the proportion of free fatty acids released from the emulsion as a function of BS type and concentration.

References

- [1] EASO, Obesity statistics, (2019). <https://easo.org/media-portal/statistics/> (accessed October 22, 2019).
- [2] World Health Organization, Obesity and overweight, (2019). <http://www.who.int/mediacentre/factsheets/fs311/en/> (accessed June 26, 2019).
- [3] World Health Organization, Food & Agriculture Organization, Diet, Nutrition and the Prevention of Chronic Diseases, Geneva, 2003. http://apps.who.int/iris/bitstream/10665/42665/1/WHO_TRS_916.pdf?ua=1.
- [4] J. Mei, A. Lindqvist, L. Krabisch, J.F. Rehfeld, C. Erlanson-Albertsson, Appetite suppression through delayed fat digestion, *Physiol. Behav.* 89 (2006) 563–568. doi:10.1016/j.physbeh.2006.07.020.
- [5] D.J. McClements, Y. Li, Structured emulsion-based delivery systems: controlling the digestion and release of lipophilic food components, *Adv. Colloid Interface Sci.* 159 (2010) 213–228. doi:10.1016/j.cis.2010.06.010.
- [6] M. Wulff-Pérez, J. de Vicente, A. Martín-Rodríguez, M.J. Gálvez-Ruiz, Controlling lipolysis through steric surfactants: New insights on the controlled degradation of submicron emulsions after oral and intravenous administration, *Int. J. Pharm.* 423 (2012) 161–166. doi:10.1016/j.ijpharm.2011.12.025.
- [7] M. Golding, T.J. Wooster, The influence of emulsion structure and stability on lipid digestion, *Curr. Opin. Colloid Interface Sci.* 15 (2010) 90–101. doi:10.1016/j.cocis.2009.11.006.
- [8] P.J. Wilde, B.S. Chu, Interfacial & colloidal aspects of lipid digestion, *Adv. Colloid Interface Sci.* 165 (2011) 14–22. doi:10.1016/j.cis.2011.02.004.
- [9] M. Armand, Lipases and lipolysis in the human digestive tract: where do we

- stand?, *Curr. Opin. Clin. Nutr. Metab. Care.* 10 (2007) 156–164. doi:10.1097/MCO.0b013e3280177687.
- [10] P. Reis, K. Holmberg, H. Watzke, M.E. Leser, R. Miller, Lipases at interfaces: a review, *Adv. Colloid Interface Sci.* 147–148 (2009) 237–250. doi:10.1016/j.cis.2008.06.001.
- [11] J. Patton, M. Carey, Watching fat digestion, *Science* (80-.). 204 (1979) 145–148. doi:10.1126/science.432636.
- [12] Y. Pafumi, D. Lairon, P. Lechene de la Porte, C. Juhel, J. Storch, M. Hamosh, M. Armand, Mechanisms of inhibition of triacylglycerol hydrolysis by human gastric lipase, *J. Biol. Chem.* 277 (2002) 28070–28079. doi:10.1074/jbc.M202839200.
- [13] A.F. Hofmann, K.J. Mysels, Bile salts as biological surfactants, *Colloids and Surfaces.* 30 (1987) 145–173. doi:10.1016/0166-6622(87)80207-X.
- [14] L. Galantini, M.C. di Gregorio, M. Gubitosi, L. Travaglini, J.V. Tato, A. Jover, F. Meijide, V.H. Soto Tellini, N. V. Pavel, Bile salts and derivatives: rigid unconventional amphiphiles as dispersants, carriers and superstructure building blocks, *Curr. Opin. Colloid Interface Sci.* 20 (2015) 170–182. doi:10.1016/j.cocis.2015.08.004.
- [15] D. Madenci, S.U. Egelhaaf, Self-assembly in aqueous bile salt solutions, *Curr. Opin. Colloid Interface Sci.* 15 (2010) 109–115. doi:10.1016/j.cocis.2009.11.010.
- [16] S.R. Euston, Molecular simulation of biosurfactants with relevance to food systems, *Curr. Opin. Colloid Interface Sci.* 28 (2017) 110–119. doi:10.1016/j.cocis.2017.04.002.
- [17] J. Maldonado-Valderrama, P. Wilde, A. Macierzanka, A. Mackie, The role of bile salts in digestion, *Adv. Colloid Interface Sci.* 165 (2011) 36–46. doi:10.1016/j.cis.2010.12.002.

- [18] J. Maldonado-Valderrama, N.C. Woodward, A.P. Gunning, M.J. Ridout, F.A. Husband, A.R. Mackie, V.J. Morris, P.J. Wilde, Interfacial characterization of β -Lactoglobulin networks: displacement by bile salts, *Langmuir*. 24 (2008) 6759–6767. doi:10.1021/la800551u.
- [19] R. Parker, N.M. Rigby, M.J. Ridout, A.P. Gunning, P.J. Wilde, The adsorption–desorption behaviour and structure function relationships of bile salts, *Soft Matter*. 10 (2014) 6457–6466. doi:10.1039/c4sm01093k.
- [20] A.F. Hofmann, B. Borgström, The intraluminal phase of fat digestion in man: the lipid content of the micellar and oil phases of intestinal content obtained during fat digestion and absorption, *J. Clin. Invest.* 43 (1964) 247–257. doi:10.1172/JCI104909.
- [21] B. Borgström, C. Erlanson-Albertsson, T. Wieloch, Pancreatic colipase: chemistry and physiology., *J. Lipid Res.* 20 (1979) 805–816. <http://www.ncbi.nlm.nih.gov/pubmed/385801>.
- [22] A. Bourbon Freie, F. Ferrato, F. Carrière, M.E. Lowe, Val-407 and Ile-408 in the β 5'-loop of pancreatic lipase mediate lipase-colipase interactions in the presence of bile salt micelles, *J. Biol. Chem.* 281 (2006) 7793–7800. doi:10.1074/jbc.M512984200.
- [23] S. Labourdenne, O. Brass, M. Ivanova, A. Cagna, R. Verger, Effects of colipase and bile salts on the catalytic activity of human pancreatic lipase. A study using the oil drop tensiometer, *Biochemistry*. 36 (1997) 3423–3429. doi:10.1021/bi961331k.
- [24] J. Maldonado-Valderrama, J.L. Muros-Cobos, J.A. Holgado-Terriza, M.A. Cabrerizo-Vílchez, Bile salts at the air-water interface: adsorption and desorption, *Colloids Surfaces B Biointerfaces*. 120 (2014) 176–183. doi:10.1016/j.colsurfb.2014.05.014.
- [25] C. Agostoni, J.-L. Bresson, S. Fairweather-Tait, A. Flynn, I. Golly, H. Korhonen, P. Lagiou, M. Løvik, R. Marchelli, A. Martin, B. Moseley, M. Neuhäuser-

- Berthold, H. Przyrembel, S. Salminen, Y. Sanz, S.J.J. Strain, S. Strobel, I. Tetens, D. Tomé, H. van Loveren, H. Verhagen, Scientific opinion on dietary reference values for carbohydrates and dietary fibre, *EFSA J.* 8 (2010) 1–1462. doi:10.2903/j.efsa.2010.1462.
- [26] J.L. Slavin, Dietary fiber and body weight, *Nutrition.* 21 (2005) 411–418. doi:10.1016/j.nut.2004.08.018.
- [27] C. Agostoni, J.-L. Bresson, S. Fairweather-Tait, A. Flynn, I. Golly, H. Korhonen, P. Lagiou, M. Løvik, R. Marchelli, A. Martin, B. Moseley, M. Neuhäuser-Berthold, H. Przyrembel, S. Salminen, Y. Sanz, S.J.J. Strain, S. Strobel, I. Tetens, D. Tomé, H. van Loveren, H. Verhagen, Scientific opinion on the substantiation of health claims related to hydroxypropyl methylcellulose (HPMC) and maintenance of normal bowel function (ID 812), reduction of post-prandial glycaemic responses (ID 814), maintenance of normal blood cholesterol concentrations (ID 815) and increase in satiety leading to a reduction in energy intake (ID 2933) pursuant to Article 13(1) of Regulation (EC) No 1924/2006, *EFSA J.* 8 (2010) 1739. doi:10.2903/j.efsa.2010.1739.
- [28] The Dow Chemical Company, METHOCEL cellulose ethers - Technical handbook, (2002) 1–32.
- [29] The Dow Chemical Company, Chemistry of METHOCEL™: cellulose ethers - a technical review, METHOCEL™ - Tech. Bull. (2013) 1–16. http://msdssearch.dow.com/PublishedLiteratureDOWCOM/dh_08e5/0901b803808e5f58.pdf?filepath=dowwolff/pdfs/noreg/198-02289.pdf&fromPage=GetDoc.
- [30] M. Younes, P. Aggett, F. Aguilar, R. Crebelli, A. Di Domenico, B. Dusemund, M. Filipič, M. Jose Frutos, P. Galtier, D. Gott, U. Gundert-Remy, G. Georg Kuhnle, C. Lambré, J. Leblanc, I.T. Lillegaard, P. Moldeus, A. Mortensen, A. Oskarsson, I. Stankovic, P. Tobback, I. Waalkens-Berendsen, M. Wright, A. Tard, S. Tasiopoulou, R.A. Woutersen, Re-evaluation of celluloses E 460(i), E 460(ii), E 461, E 462, E 463, E 464, E 465, E 466, E 468 and E 469 as food additives, *EFSA*

J. 16 (2018) 1–104. doi:10.2903/j.efsa.2018.5047.

- [31] P.L. Nasatto, F. Pignon, J.L.M. Silveira, M.E.R. Duarte, M.D. Nosedá, M. Rinaudo, Methylcellulose, a cellulose derivative with original physical properties and extended applications, *Polymers (Basel)*. 7 (2015) 777–803. doi:10.3390/polym7050777.
- [32] A. Torcello-Gómez, T.J. Foster, Interactions between cellulose ethers and a bile salt in the control of lipid digestion of lipid-based systems, *Carbohydr. Polym.* 113 (2014) 53–61. doi:10.1016/j.carbpol.2014.06.070.
- [33] A. Torcello-Gómez, C. Fernández Fraguas, M.J. Ridout, N.C. Woodward, P.J. Wilde, T.J. Foster, Effect of substituent pattern and molecular weight of cellulose ethers on interactions with different bile salts, *Food Funct.* 6 (2015) 730–739. doi:10.1039/c5fo00099h.
- [34] C. Reppas, J.H. Meyer, P.J. Sirois, J.B. Dressman, Effect of hydroxypropylmethylcellulose on gastrointestinal transit and luminal viscosity in dogs, *Gastroenterology*. 100 (1991) 1217–1223. doi:10.1016/0016-5085(91)70007-K.
- [35] K.C. Maki, M.L. Carson, W.H. Kerr Anderson, J. Geohas, M.S. Reeves, M. V. Farmer, M. Turowski, M. Miller, V.N. Kaden, M.R. Dicklin, T.M. Rains, Lipid-altering effects of different formulations of hydroxypropylmethylcellulose, *J. Clin. Lipidol.* 3 (2009) 159–166. doi:10.1016/j.jacl.2009.04.053.
- [36] C. Reppas, S.Z. Swidan, S.W. Tobey, M. Turowski, J.B. Dressman, Hydroxypropylmethylcellulose significantly lowers blood cholesterol in mildly hypercholesterolemic human subjects, *Eur. J. Clin. Nutr.* 63 (2009) 71–77. doi:10.1038/sj.ejcn.1602903.
- [37] G.E. Bartley, W. Yokoyama, S.A. Young, W.H.K. Anderson, S.-C. Hung, D.R. Albers, M.L. Langhorst, H. Kim, Hypocholesterolemic effects of hydroxypropyl methylcellulose are mediated by altered gene expression in hepatic bile and cholesterol pathways of male hamsters, *J. Nutr.* 140 (2010) 1255–1260.

doi:10.3945/jn.109.118349.

- [38] T. van der Gronde, A. Hartog, C. van Hees, H. Pellikaan, T. Pieters, Systematic review of the mechanisms and evidence behind the hypocholesterolaemic effects of HPMC, pectin and chitosan in animal trials, *Food Chem.* 199 (2016) 746–759. doi:10.1016/j.foodchem.2015.12.050.
- [39] T.P. Carr, D.D. Gallaher, C.-H. Yang, C.A. Hassel, Increased intestinal contents viscosity reduces cholesterol absorption efficiency in hamsters fed hydroxypropyl methylcellulose, *J. Nutr.* 126 (1996) 1463–1469. doi:10.1093/jn/126.5.1463.
- [40] V.M. Pizones Ruiz-Henestrosa, F.A. Bellesi, N.A. Camino, A.M.R. Pilosof, The impact of HPMC structure in the modulation of in vitro lipolysis: the role of bile salts, *Food Hydrocoll.* 62 (2017) 251–261. doi:10.1016/j.foodhyd.2016.08.002.
- [41] A.M.R. Pilosof, Potential impact of interfacial composition of proteins and polysaccharides stabilized emulsions on the modulation of lipolysis. The role of bile salts., *Food Hydrocoll.* 68 (2017) 178–185. doi:10.1016/j.foodhyd.2016.08.030.
- [42] P.W.J. Maljaars, H.P.F. Peters, D.J. Mela, A.A.M. Masclee, Ileal brake: A sensible food target for appetite control. A review, *Physiol. Behav.* 95 (2008) 271–281. doi:10.1016/j.physbeh.2008.07.018.
- [43] P. Gunness, M.J. Gidley, Mechanisms underlying the cholesterol-lowering properties of soluble dietary fibre polysaccharides, *Food Funct.* 1 (2010) 149–155. doi:10.1039/c0fo00080a.
- [44] O. Pabois, C.D. Lorenz, R.D. Harvey, I. Grillo, M.M.-L. Grundy, P.J. Wilde, Y. Gerelli, C.A. Dreiss, Molecular insights into the behaviour of bile salts at interfaces: a key to their role in lipid digestion, *J. Colloid Interface Sci.* 556 (2019) 266–277. doi:10.1016/j.jcis.2019.08.010.
- [45] H.A. Barnes, J.F. Hutton, K. Walters, *An introduction to rheology*, 1st ed.,

Elsevier Science, Oxford, 1989.

- [46] R.G. Larson, *The structure and rheology of complex fluids*, 1st ed., Oxford University Press Inc., New York, 1999.
- [47] A. Guinier, G. Fournet, *Structure of matter series: small-angle scattering of X-rays*, 1st ed., John Wiley & Sons, Inc., New York, 1955.
- [48] T. Zemb, P. Linder, eds., *Neutron, X-rays and light. Scattering methods applied to soft condensed matter.*, 1st ed., North Holland, Amsterdam, 2002.
- [49] I. Grillo, *Small-angle neutron scattering and applications in soft condensed matter*, in: R. Borsali, R. Pecora (Eds.), *Soft Matter Charact. Vol. 2*, 1st ed., Springer Science+Business Media, LLC., New York, 2008: pp. 723–782.
- [50] A.J. Jackson, *Introduction to small-angle neutron scattering and neutron reflectometry*, NIST Cent. Neutron Res. (2008) 1–24. ftp://ftp.ncnr.nist.gov/pub/sans/kline/Tutorials/P85_vs_Temp_NG3_2008.zip (accessed November 16, 2019).
- [51] F. Cousin, *Small angle neutron scattering*, in: M. Ceretti, W. Paulus, M.-H. Mathon, C. Ritter (Eds.), *JDN 21 - Neutrons Mater. Energy Appl. Neutrons Scatt. Tech. to Mater. Energy*, EPJ Web of Conferences, Sète, 2015: p. 01004. doi:10.1051/epjconf/201510401004.
- [52] Wikipedia, *Bragg's law*, Wikipedia, Free Encycl. (2019) 1. https://en.wikipedia.org/w/index.php?title=Bragg%27s_law&oldid=921744939 (accessed November 18, 2019).
- [53] J.S. Pedersen, *Analysis of small-angle scattering data from colloids and polymer solutions: modeling and least-squares fitting*, *Adv. Colloid Interface Sci.* 70 (1997) 171–210. doi:10.1016/S0001-8686(97)00312-6.
- [54] J.K. Percus, G.J. Yevick, *Analysis of classical statistical mechanics by means of collective coordinates*, *Phys. Rev.* 110 (1958) 1–13. doi:10.1103/PhysRev.110.1.

- [55] J.B. Hayter, J. Penfold, An analytic structure factor for macroion solutions, *Mol. Phys.* 42 (1981) 109–118. doi:10.1080/00268978100100091.
- [56] J.-P. Hansen, J.B. Hayter, A rescaled MSA structure factor for dilute charged colloidal dispersions, *Mol. Phys.* 46 (1982) 651–656. doi:10.1080/00268978200101471.
- [57] SasView for small angle scattering analysis, (2018). www.sasview.org (accessed August 22, 2018).
- [58] Y. Gerelli, Aurore: new software for neutron reflectivity data analysis, *J. Appl. Crystallogr.* 49 (2016) 330–339. doi:10.1107/S1600576716000108.
- [59] L. Koester, H. Rauch, E. Seymann, Neutron scattering lengths: a survey of experimental data and methods, *At. Data Nucl. Data Tables.* 49 (1991) 65–120. doi:10.1016/0092-640X(91)90012-S.
- [60] V.F. Sears, Neutron scattering lengths and cross sections, *Neutron News.* 3 (1992) 26–37. doi:10.1080/10448639208218770.
- [61] F. Boué, F. Cousin, J. Gummel, J. Oberdisse, G. Carrot, A. El Harrak, Small angle scattering from soft matter - application to complex mixed systems, *Comptes Rendus Phys.* 8 (2007) 821–844. doi:10.1016/j.crhy.2007.10.013.
- [62] A. Bumajdad, J. Eastoe, S. Nave, D.C. Steytler, R.K. Heenan, I. Grillo, Compositions of Mixed Surfactant Layers in Microemulsions Determined by Small-Angle Neutron Scattering, *Langmuir.* 19 (2003) 2560–2567. doi:10.1021/la026586f.

Chapter 1

Molecular insights into the behaviour of
bile salts at interfaces: a key to their
role in lipid digestion

Co-authors contribution to the publication

Dr Christian D. Lorenz (Department of Physics, King's College London, UK) carried out the molecular dynamics simulations.

Dr Richard D. Harvey (Institut für Pharmazie, Martin-Luther-Universität Halle-Wittenberg, Germany), Dr Myriam M.-L. Grundy (School of Agriculture, Policy and Development, University of Reading, UK) and Prof Peter J. Wilde (Quadram Institute Bioscience, UK) provided advices and feedback as to the experimental work and manuscript.

Dr Cécile A. Dreiss (Institute of Pharmaceutical Science, King's College London, UK), Dr Yuri Gerelli (Institut Laue-Langevin, France) and Dr Isabelle Grillo (Institut Laue-Langevin, France) supervised the project.



Contents lists available at ScienceDirect

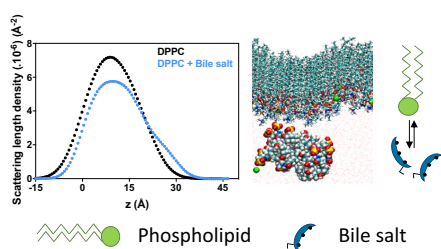
Journal of Colloid and Interface Science

journal homepage: www.elsevier.com/locate/jcis

Regular Article

Molecular insights into the behaviour of bile salts at interfaces: a key to their role in lipid digestion [☆]Olivia Pabois ^{a,b}, Christian D. Lorenz ^c, Richard D. Harvey ^d, Isabelle Grillo ^a, Myriam M.-L. Grundy ^e, Peter J. Wilde ^f, Yuri Gerelli ^{a,*}, Cécile A. Dreiss ^{b,*}^a Institut Laue-Langevin, Grenoble 38000, France^b Institute of Pharmaceutical Science, King's College London, London SE1 9NH, United Kingdom^c Department of Physics, King's College London, London WC2R 2LS, United Kingdom^d Institut für Pharmazie, Martin-Luther-Universität Halle-Wittenberg, Halle (Saale) 06099, Germany^e School of Agriculture, Policy and Development, University of Reading, Reading RG6 6AR, United Kingdom^f Quadram Institute Bioscience, Norwich Research Park, Norwich NR4 7UA, United Kingdom

GRAPHICAL ABSTRACT



ARTICLE INFO

Article history:

Received 4 April 2019

Revised 21 June 2019

Accepted 3 August 2019

Available online 5 August 2019

Keywords:

Bile salts

Lipid digestion

Interfacial properties

DPPC monolayer

Neutron reflectometry

ABSTRACT

Hypotheses: Understanding the mechanisms underlying lipolysis is crucial to address the ongoing obesity crisis and associated cardiometabolic disorders. Bile salts (BS), biosurfactants present in the small intestine, play key roles in lipid digestion and absorption. It is hypothesised that their contrasting functionalities – adsorption at oil/water interfaces and shuttling of lipolysis products away from these interfaces – are linked to their structural diversity. We investigate the interfacial films formed by two BS, sodium taurocholate (NaTC) and sodium taurodeoxycholate (NaTDC), differing by the presence or absence of a hydroxyl group on their steroid skeleton.

Experiments: Their adsorption behaviour at the air/water interface and interaction with a phospholipid monolayer – used to mimic a fat droplet interface – were assessed by surface pressure measurements and ellipsometry, while interfacial morphologies were characterised in the lateral and perpendicular directions by Brewster angle microscopy, X-ray and neutron reflectometry, and molecular dynamics simulations.

Findings: Our results provide a comprehensive molecular-level understanding of the mechanisms governing BS interfacial behaviour. NaTC shows a higher affinity for the air/water and lipid/water interfaces,

[☆] Shortly after acceptance of this manuscript, our long-term colleague, ILL staff scientist, Isabelle Grillo tragically passed away. We wish to dedicate this manuscript to her memory.

* Corresponding authors at: Institut Max von Laue – Paul Langevin, 71 avenue des Martyrs, 38000 Grenoble, France (Y. Gerelli). King's College London, Institute of Pharmaceutical Science, Franklin-Wilkins Building, 150 Stamford Street, SE1 9NH London, United Kingdom (C.A. Dreiss).

E-mail addresses: olivia.pabois@kcl.ac.uk (O. Pabois), chris.lorenz@kcl.ac.uk (C.D. Lorenz), richard.harvey@pharmazie.uni-halle.de (R.D. Harvey), grillo@ill.fr (I. Grillo), m.m.grundy@reading.ac.uk (M.M.-L. Grundy), peter.wilde@quadram.ac.uk (P.J. Wilde), gerelli@ill.fr (Y. Gerelli), cecile.dreiss@kcl.ac.uk (C.A. Dreiss).

<https://doi.org/10.1016/j.jcis.2019.08.010>

0021-9797/© 2019 Elsevier Inc. All rights reserved.

and may therefore favour enzyme adsorption, whereas NaTDC exhibits a higher propensity for desorption from these interfaces, and may thus more effectively displace hydrolysis products from the interface, through dynamic exchange.

© 2019 Elsevier Inc. All rights reserved.

1. Introduction

Over the past few years, changes in both lifestyle and eating habits have resulted in a global increase in obesity prevalence. More specifically, since 1975, worldwide obesity levels have nearly tripled [1]. Dietary fats (lipids) are an excellent source of energy, which is essential for many physiological functions, but its excessive consumption (particularly of saturated fats) contributes towards a large number of chronic cardiovascular illnesses [2]. There is, therefore, an urgent need to develop preventive and therapeutic strategies to tackle this ongoing health crisis. One proposed strategy towards regulating the digestion of lipids consists of using novel foods with appetite-suppressing or satiety-enhancing properties [3]. This approach requires a detailed understanding of the mechanisms involved in fat digestion.

The process of lipid digestion [4,5], also called lipolysis or lipid hydrolysis, requires two water-soluble enzymes (i.e., gastric and pancreatic lipases) that bind to fat droplets and act at the lipid/water interface [6,7]. Dietary triacylglycerols are mostly hydrolysed in the small intestine by co-lipase-dependent pancreatic lipase; products of the lipolysis (diacylglycerols, monoacylglycerols and free fatty acids) accumulate at the lipid droplet interface because of their amphiphilicity [7,8]. As a result, they would gradually hinder further enzyme adsorption onto the droplet surface [7,9], if this was not prevented by the presence of bile salts (BS).

BS, produced in the liver and stored in the gall bladder, play key roles in promoting lipid digestion and absorption [5,10,11]. Comprising a short and flexible ionic chain linked to a steroid skeleton [12], they display an unusual planar polarity [13], adsorb at interfaces and facilitate the adsorption of the co-lipase-dependent pancreatic lipase onto a BS-dominated surface [14–17]. In addition, BS prevent lipase inhibition caused by the accumulation of hydrolysis products by removing polar lipids from the fat droplet surface, solubilising them into mixed micelles [10]. Therefore, BS play two very different roles in fat digestion [5,11]: on the one hand, they promote enzyme-catalysed lipolysis by facilitating the adsorption of the lipase/co-lipase complex at the lipid/water interface, and on the other, they desorb insoluble lipolysis products from the interface, shuttling them into mixed micelles to the gut mucosa, where they are absorbed.

While BS contrasting functionalities have been known for some time, their origin is not well understood. For this reason, the characterisation of their behaviour at both the air/water [18] and lipid/water [19] interfaces has recently begun to garner interest. A recent study [19], in particular, has linked differences in BS interfacial properties to their structure, specifically the bile acid moiety: cholate-based BS were found to strongly adsorb onto hydrophobic surfaces (C18-modified silicon oxide sensors), while deoxycholate and chenodeoxycholate derivatives readily desorbed from the interface. Further studies are thus needed to elucidate how BS structure influences their interfacial behaviour and how, in turn, this correlates to their different roles in lipolysis.

This work reports a detailed investigation of the interfacial properties of two selected BS, sodium taurocholate (NaTC) and sodium taurodeoxycholate (NaTDC) (Fig. 1), using a range of complementary techniques. These two BS differ in the structure of their bile acid region (NaTC has an additional hydroxyl group (Fig. 1)), and have previously been shown to display contrasting interfacial

behaviour [19]. In this work, we investigate the adsorption/desorption dynamics of BS at the bare air/water interface, using a Langmuir trough (LT) and ellipsometer, and characterise the structure of the interfacial films on a range of length scales, using Brewster angle microscopy (BAM) and X-ray reflectometry (XRR). As a first step towards a more physiologically relevant oil/water interface, we then explore the interaction of BS with a lipid monolayer (1,2-dipalmitoyl-*sn*-glycero-3-phosphocholine, DPPC) (Fig. S1A) deposited at the air/water interface, which mimics the phospholipids present on the surface of lipid droplets [5,9,11,20–22], either as endogenous lipids secreted in the gastrointestinal tract [4,10] or as emulsifying agents present in foodstuffs [23,24]. This study provides a molecular-level characterisation of the interfacial films, using neutron reflectometry (NR) combined to molecular dynamics (MD) simulations, bringing an unprecedented insight into the different roles played by BS during lipid digestion.

2. Experimental section

2.1. Materials

DPPC (Fig. S1A) and 1,2-dipalmitoyl-*d*₆₂-*sn*-glycero-3-phosphocholine-1,1,2,2-*d*₄-N,N,N-trimethyl-*d*₉ (*d*₇₅-DPPC) (Fig. S1B) were provided by Avanti Polar Lipids, Inc. (Alabaster, AL, USA), and chloroform (CHCl₃) by Fisher Scientific (Loughborough, UK). NaTC (P97.0% TLC) (Fig. 1A), NaTDC (P95.0% TLC) (Fig. 1B), sodium glycodeoxycholate (NaGDC, P97.0% HPLC) (Fig. S2) and ethanol (EtOH, P99.8% GC) were all purchased from Sigma-Aldrich (Gillingham, UK). Ultrapure water, or MilliQ-grade water (H₂O, 18.2 MΩ cm, Merck Millipore, Molsheim, France), was used in all experiments, except for the NR measurements, where deuterium oxide (D₂O, P99.9%), provided by Euriso-top SAS (St. Aubin, France), and air-contrast-matched water (ACMW, 8.1% D₂O / 91.9% H₂O by volume) were employed. All reagents were used as supplied.

2.2. Methods

2.2.1. Langmuir trough (LT) measurements

Interfacial tension measurements were performed using two different set-ups. The first set-up was employed to carry out measurements at a fixed area and with stirring, in a 50-mm-diameter perfluoroalkoxy petri dish (19.6 cm² surface area and 20 mL volume of subphase), which was placed over a magnetic stirring plate and used as a trough to study both BS adsorption at the air/water interface and BS interaction with a DPPC monolayer. The second set-up was a classic polytetrafluoroethylene trough (Nima 611D, Nima Technology Ltd, Coventry, UK) of 30 × 20 × 0.5 cm (length × width × depth), with a 300 mL volume of subphase, and was used to measure the surface pressure – area ($\pi - A$) isotherm of a lipid monolayer at the air/water interface. All experiments were carried out at a constant temperature of 23 ± 2 °C (room temperature). The surface pressure (π) was measured by a Wilhelmy plate, made of chromatographic paper (Whatman International Ltd, Maidstone, UK) of 2.3 × 1.0 cm (length × width) and attached to a calibrated Nima PS4 microbalance.

Prior to any measurement, the trough was thoroughly cleaned with EtOH and CHCl₃ to remove organic impurities, and then filled with ultrapure water (subphase). Surface-active contaminants,

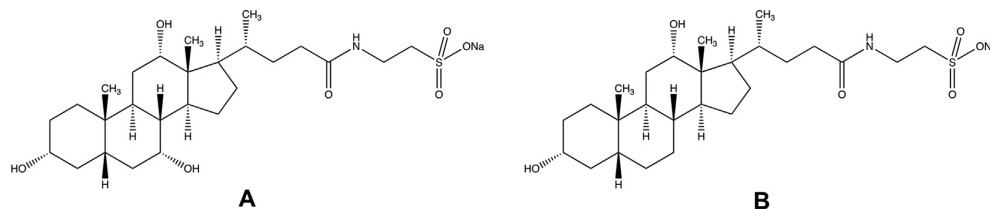


Fig. 1. Structures of NaTC (A) and NaTDC (B). The structure of NaGDC is shown in Fig. S2.

dust and bubbles were all removed from the subphase by suction with a pump. The subphase was considered as clean when changes in surface pressure did not exceed ± 0.2 mN/m over approximately two minutes with the petri dish, or when compressed over the entire compression range (64–567 cm²) with the LT.

2.2.1.1. BS adsorption at the air/water interface. Using a 1 mL syringe (Becton Dickinson, Madrid, Spain) fitted with a 19 G \times 1 1/2 in. needle (Becton Dickinson, Dublin, Ireland), a defined amount of pure BS solution in ultrapure water was injected into the subphase of the petri dish, under constant stirring. Surface pressure (π) was measured over time, until it reached a plateau. Each experiment was repeated twice; either a representative curve or an average measurement is shown.

2.2.1.2. Surface pressure – area ($\pi - A$) isotherm of lipid monolayers at the air/water interface. A 1 mg/mL solution of hydrogenated (DPPC) or deuterated (d₇₅-DPPC) lipid was prepared in pure CHCl₃. For each isotherm, a specific amount (45 μ L for DPPC, 60 μ L for d₇₅-DPPC) was deposited dropwise onto the aqueous surface, using a 50 μ L syringe (Hamilton Company, Bonaduz, Switzerland), with the barrier opened at its maximum. After solvent evaporation and monolayer equilibration (ca. 10 min), the phospholipid film was compressed at a rate of 35 cm²/min. Changes in surface pressure (π) were recorded as a function of the area per molecule until the lipid monomolecular layer had reached its collapse point, at its collapse surface pressure (π_{collapse}). The average of three isotherms is shown for each lipid.

2.2.1.3. BS interaction with a DPPC monolayer at the air/water interface. A DPPC monolayer was first formed onto the clean water surface in the petri dish set-up, at the target surface pressure ($\pi_{\text{DPPC}} = 25 \pm 2$ mN/m). After solvent evaporation and film equilibration (ca. 1 h), stirring was started (at low speed), and a defined amount of pure BS solution in ultrapure water was injected beneath the phospholipid monolayer. The corresponding changes in surface pressure ($\Delta\pi$, with $\Delta\pi(t) = \pi(t) - \pi_{\text{DPPC}}$) were recorded over time. Each experiment was repeated twice; either a representative curve or the average measurement is shown.

2.2.2. Ellipsometry

BS adsorption at the air/water interface and interaction with the DPPC monolayer at the air/water interface were further investigated by ellipsometry (Beaglehole Instruments, Wellington, New Zealand). Time-dependent measurements were performed with a 632.8-nm-wavelength laser hitting the surface at an incident angle of 50°. In this configuration, changes in the polarisation of light reflected by the interface are measured, over the 1 mm² area and 1 μ m depth probed by the laser beam; these changes can be correlated to the amount of material adsorbed at this interface over time. The polarisation state of the incident light is composed of an *s*- and *p*-component (where the *s*-component is oscillating par-

allel to the sample surface, and the *p*-one parallel to the plane of incidence). The ratio of the reflectivity of these two components (r_s for the *s*-component and r_p for the *p*-component) characterises the polarisation change and is expressed by the following equation:

$$\frac{r_p}{r_s} = \tan \Psi \cdot e^{i\Delta} \quad (1)$$

where Ψ is the amplitude change and Δ the phase shift. In the thin film limit at the air/water interface (i.e., film thickness \ll laser wavelength), Δ is much more sensitive to changes in the amount adsorbed at the interface than Ψ [25]. Therefore, the time-dependent changes in phase shift (ΔA) were measured, with $\Delta A(t) = \Delta(t) - \Delta(t_0)$, where $\Delta(t_0)$ is the phase shift at the beginning of a given experiment, namely, the phase shift of the bare air/water interface (Δ_0) for BS adsorption at the air/water interface, or that of the pure DPPC monolayer (Δ_{DPPC}) for BS interaction with this film at the air/water interface. The instrument was mounted on top of the LT to measure, simultaneously, the surface pressure and phase shift changes for the same sample. Data were acquired at a rate of 0.2 Hz, using the Igor Pro software. Each experiment was repeated twice; a representative measurement of each is shown.

2.2.3. Brewster angle microscopy (BAM)

Surface pressure measurements with the LT were complemented by contemporaneous BAM measurements, which enabled the visualisation of the spatial structure of the interfacial layer. Brewster angle micrographs were obtained using a Nanofilm EP3 instrument equipped with a 532-nm-wavelength laser and a 10 \times objective lens (Accurion GmbH, Göttingen, Germany), and mounted on top of the LT. The angles of the laser and camera were identical and fixed to the value of the Brewster angle for the pure air/water interface ($\alpha = 53.1^\circ$ at this wavelength, with $\tan \alpha = \frac{n_1}{n_2}$, where n_i is the refractive index of each medium at the interface). At this specific angle, the *p*-polarised light is fully transmitted from the air/water interface, thus giving a black image, while in the presence of material at the interface, the optical properties of the interface vary, thus resulting in the appearance of brighter zones due to the reflection of some *p*-polarised light. Images were captured by the built-in charge-coupled device camera, using the EP3View software, which was also employed to subtract the background.

2.2.4. X-ray reflectometry (XRR)

XRR experiments were performed using an Emyrean diffractometer (Malvern Analytical S.A.S., Limeil-Brevannes, France). The instrument was configured with an incoming monochromatic X-ray beam of wavelength $\lambda = 1.54$ Å (Cu α source), and the angle of incidence (θ_i , equal to that of detection) was varied between 0 and 5°, thus allowing values of the scattering vector perpendicular to the surface (q_z , with $q_z = \frac{4\pi}{\lambda} \sin \theta_i$) ranging from 0 to 0.35 Å⁻¹ to be obtained. Reflectivity (R), which is the ratio between the

reflected and incident intensities, was measured as a function of q_z in this range.

Because X-rays are not sensitive enough to distinguish between organic molecules, XRR measurements were only carried out on the pure BS films adsorbed at the air/water interface. BS concentrations below, around, and above their critical micelle concentration (CMC) (i.e., 1, 5 and 10 mM) were selected because different interfacial behaviours were observed with the LT. XRR experiments were performed in ultrapure water, as the contrast with BS was high enough (Table 1).

XRR curves were analysed with the Aurore software [26] following two different modelling approaches: when the layer formed at the air/water interface by BS molecules was very diffuse, the evolution of the air/water interfacial roughness (σ) was monitored and the thickness (t) calculated as follows: $t = 2.35 \cdot \sigma$, while a model assuming a single layer characterised by a specific thickness (t), electron density and σ , was used to fit a more dense, well-defined film. The result of the XRR data analysis is the electron density profile along the direction perpendicular to the surface (z), which is directly related to the distribution of each molecular component in this direction.

2.2.5. Neutron reflectometry (NR)

NR measurements were performed on FIGARO, the ILL time-of-flight neutron reflectometer [27]. This instrument uses an incoming polychromatic neutron beam with wavelengths (λ) ranging from 2 to 20 Å, with a 7% $d\lambda/\lambda$ resolution. In order to cover a similar q_z range as the one obtained with XRR, two different incident angles, $\theta_1 = 0.622^\circ$ and $\theta_2 = 3.780^\circ$, were employed on FIGARO; q_z values ranging from 0.01 to 0.25 Å⁻¹ were thus accessible. As for XRR, R was measured as a function of q_z in this range.

The same BS concentrations as those used for XRR experiments were employed. Contrast-variation, which enables highlighting different components by simple isotopic deuteration, was performed by spreading the same phospholipid monolayer onto the surface of two subphases differing by their D₂O/H₂O ratio: pure D₂O and 8.1% D₂O / 91.9% H₂O ratio, corresponding to ACMW (air-contrast-matched water), with a scattering length density (SLD) of zero matching air. Either a non-labelled (DPPC) or deuterated (d₇₅-DPPC) lipid monolayer was formed onto the clean water surface (either D₂O or ACMW). In this way, different parts of the system were highlighted: the DPPC/D₂O system made both BS and lipid molecules visible, while the use of deuterated lipids (d₇₅-DPPC) in D₂O and ACMW highlighted, respectively, BS location and changes in lipid interfacial film thickness and organisation (Table 2).

Prior to analysis, NR data were converted to reflectivity curves $R(q_z)$ using the COSMOS software application available for the ILL reflectometers [28]. Data analysis was performed with the Aurore software [26] and a global fitting procedure was applied for compatible data sets. The modelling approach used is the same as the one reported by Campbell *et al.* [29]. Briefly, the thin film present at the interface was divided into two layers, each characterised by a specific t , SLD, amount of water (f_{water}) and σ . Because of the instrumental geometry used, the first (upper) layer in the model corresponds to the lipids acyl chains, while the second (lower) one is ascribed to the head groups region in contact

Table 1
Calculated electron density of each component.

Component		Electron density ($\times 10^6$) (Å ⁻²)
Subphase	H ₂ O	9.47
BS	NaTC	12.05
	NaTDC	12.16

Table 2
Calculated SLD of each component.

Component		SLD ($\times 10^6$) (Å ⁻²)
DPPC	h ₆₂ -tails	-0.41
	h ₁₈ -head group	1.75
d ₇₅ -DPPC	d ₆₂ -tails	7.66
	d ₁₃ -head group	5.68
Subphase	ACMW	0
	D ₂ O	6.33
BS	NaTC	0.95
	NaTDC	0.90

with the aqueous subphase. As for XRR, the result of the NR data analysis is the SLD profile along z .

2.2.6. Molecular dynamics (MD) simulations

MD simulations were carried out to investigate the molecular-scale mechanisms governing the interaction of BS with DPPC monolayers. In doing so, each simulation system contained two DPPC monolayers, each made up of 64 lipid molecules that were separated by 60 Å of water. The monolayers were constructed such that the area per lipid was 42.5 Å², using the CHARMM-GUI membrane builder [30–32]. BS molecules and their counterions were inserted into the aqueous phase. Two different systems containing 2 and 12 BS molecules were studied for each BS (NaTC and NaTDC). Fig. 2 shows a snapshot of the simulated system containing 2 NaTC molecules between the two DPPC monolayers. The empty space in the z -dimension between the two monolayers was sufficiently large to prevent interactions from occurring between the two monolayers through the periodic boundary in the z -dimension.

The same simulation protocol was followed for each system. First, an energy minimisation was performed on each of the monolayer systems using 100,000 steps as the maximum number of force/energy evaluations. Then, the minimised configurations were equilibrated at 300 K using the NVT ensemble, in which a Langevin thermostat [33] was applied, for 400 ps. Then, a production simulation was carried out for 100 ns at 300 K using the NVT ensemble with a Nosé-Hoover thermostat [34].

All of the simulations presented in this manuscript used the LAMMPS simulation package [35]. The inter- and intra-molecular interactions of the BS, sodium counterions and DPPC molecules were described with the CHARMM force field [36–38]. The TIP3P water model [39] in its modified form, which is commonly used with the CHARMM force field [40], was used to describe the interactions involving water molecules. The van der Waals interactions were cut off at 10 Å whilst the electrostatic interactions were cut off at 12 Å. The PPPM method [41] was used to compute long-range Coulombic interactions. A timestep of 2 fs was used in all simulations to ensure stable integration of Newton's equations of motion with the velocity Verlet algorithm whilst all hydrogen-containing bonds were constrained using the SHAKE algorithm [42].

3. Results

3.1. BS adsorption at the air/water interface

3.1.1. BS adsorption/desorption dynamics

The capacity of NaTC and NaTDC to adsorb at the air/water interface was assessed with a LT, by monitoring the evolution of the surface pressure (π) over time after injection, into the water subphase, of either three successive amounts of BS (1, 5 and 10 mM) (Fig. 3, A, B), or fixed BS concentrations (0.5, 5 or 10 mM) over longer periods of time (Fig. S3). These BS concentrations were selected to be below (0.5 or 1 mM), around

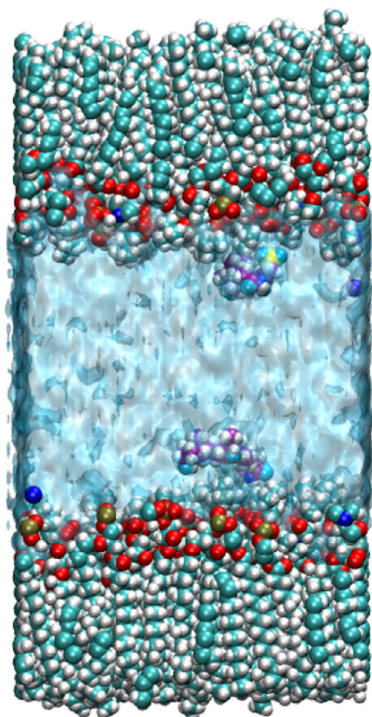


Fig. 2. Snapshot of the simulated system made up of two DPPC monolayers (cyan (carbon) and red (oxygen) spheres) separated by 60 Å of water (translucent blue), which contains 2 NaTC molecules (purple spheres) and their sodium counterions. (For interpretation of the references to colour in this figure legend, the reader is referred to the web version of this article.)

(5 mM), and above (10 mM) their CMC, which is 4–7 mM for NaTC (gradual micellisation process) and 2 mM for NaTDC (data not shown) [43].

Independently of the type of BS, the addition of a 1 mM BS solution into the aqueous subphase leads to an instantaneous increase in surface pressure, which stabilises after a few hours. A higher surface pressure is reached for NaTDC ($\pi = 21 \pm 1$ mN/m) (Fig. 3B), compared to NaTC ($\pi = 11 \pm 0.1$ mN/m) (Fig. 3A). Above 5 mM, the behaviour of the two BS differs: while surface pressure does not change further with additional injections of NaTDC, which is fully micellised ($\pi = 21 \pm 2$ mN/m at both 5 and 10 mM) (Fig. 3B), the addition of 5 mM NaTC results in an increase to $\pi = 21 \pm 3$ mN/m, which remains relatively stable at 10 mM ($\pi = 20 \pm 1$ mN/m) (Fig. 3A). These different patterns can be related to the higher concentration of NaTC needed to reach an aggregated state.

Similar values are obtained for both BS with individual injections of fixed concentrations (Fig. S3): a surface pressure of $\pi = 14 \pm 0.2$ mN/m is reached at 0.5 mM, while injections of higher concentrations of BS, 5 and 10 mM, result in an increase to $\pi = 23 \pm 1$ mN/m. These results are consistent with surface pressure values at the air/water interface reported elsewhere [11,18,22]. Slight differences in the kinetics of adsorption can be explained by different stirring conditions of the different set-ups.

Ellipsometry performed at the same time gives information on the amount of material adsorbed at the interface [25], by monitoring the phase shift ($\Delta\Delta$) (Fig. 3C and D). For both BS, the phase shift increases upon injection of 1 mM BS and rapidly reaches a near

plateau at $\Delta\Delta = 0.024 \pm 0.003^\circ$ and $\Delta\Delta = 0.031 \pm 0.005^\circ$ for NaTC and NaTDC, respectively (Fig. 3C and D). At higher concentrations, again, the behaviour of the two BS diverges: while the addition of NaTC induces a further increase in phase shift (stabilising at $\Delta\Delta = 0.029 \pm 0.004^\circ$, at 10 mM) (Fig. 3C), the injection of 5 and 10 mM NaTDC leads to a gradual decrease to $\Delta\Delta = 0.023 \pm 0.004^\circ$ and $\Delta\Delta = 0.020 \pm 0.004^\circ$, respectively (Fig. 3D).

3.1.2. BS interfacial film structure

A molecular-level characterisation of the BS films was obtained in the lateral (BAM, Fig. 4) and perpendicular (XRR, Figs. 5 and S3, Table S1) directions, with resolutions of ca. 1000 nm (BAM) and < 1 nm (XRR).

At the Brewster angle of the bare air/water interface, no light is reflected from the interface, giving a dark background. Upon successive additions of NaTC into the water subphase, the image becomes uniformly brighter, showing the formation of a homogeneous layer in the lateral direction, with a refractive index different from water (Fig. 4). Instead, successive injections of NaTDC result in small, numerous brighter islands on the water surface, characterised by a specific refractive index.

The successive additions of NaTC into the water subphase lead to the formation of a very diffuse layer, whose interfacial roughness (and thus thickness) increases with the amount of BS (from $\sigma = 4$ Å (or $t = 9$ Å) in the absence of NaTC, to $\sigma = 5, 6$ and 6 Å (or $t = 12, 14$ and 14 Å) in the presence of, respectively, 1, 5 and 10 mM) (Figs. 5 and S4, Table S1). NaTDC forms a significantly thicker film at the air/water interface at 1 mM ($t = 33$ Å), while the addition of further NaTDC molecules results in a significant thinning of the layer ($t = 24$ Å at 5 mM); at 10 mM, the film becomes too diffuse to be fitted using a single-layer model (at this high concentration, NaTDC forms a layer with an interfacial roughness of $\sigma = 5$ Å (or $t = 12$ Å), a value very similar to those obtained for the NaTC adsorbed layer).

3.2. BS interaction with a DPPC monolayer at the air/water interface

3.2.1. Interaction between BS and lipid molecules

First, the optimal lipid density, or monolayer surface pressure, leading to the most efficient adsorption of BS within the liquid-condensed phase, where the lipid monolayer is uniform and compacted ($25 < \pi < 45$ mN/m), was determined. BS molecules were injected into the water subphase below lipid monolayers prepared at different surface pressures ($\pi_{\text{DPPC}} = 25, 35, 45$ mN/m), and the least packed and ordered lipid film within the liquid-condensed phase ($\pi_{\text{DPPC}} = 25$ mN/m) was selected, as it showed the highest extent of BS adsorption (data not shown). Following this, three BS (NaTC, NaTDC and NaGDC) were injected into the water subphase below the DPPC monolayer ($\pi_{\text{DPPC}} = 25 \pm 2$ mN/m), either by increasing BS concentration stepwise (10 successive injections, each spaced by one hour from the next) (Fig. 6), or by adding a fixed concentration (0.5, 1, 5, 10 or 20 mM) and monitoring over longer times ($t > 2.5$ h) (Fig. S5). The results are shown as a change in surface pressure: $\Delta\pi(t)$, with $\Delta\pi(t) = \pi(t) - \pi_{\text{DPPC}}$, where π_{DPPC} is the initial DPPC monolayer surface pressure.

The surface pressure evolution is strikingly similar for NaTDC and NaGDC (which bears a different amino acid group – glyco, instead of tauro –, but the same steroid backbone), and differs for NaTC (Fig. 6). In the case of NaTC, three different regions are observed: at low concentrations (1–2 mM), the surface pressure rises up to a plateau, at $\Delta\pi = 19 \pm 2$ mN/m; subsequent additions of BS (3–6 mM) induce a much weaker increase, followed by a decrease above 7–8 mM. Instead, the first addition (1 mM) of either NaTDC or NaGDC induces a sharp increase in surface pressure ($\Delta\pi = 27 \pm 1$ mN/m), which stays relatively constant around 2–3 mM, and then steeply drops above 4 mM.

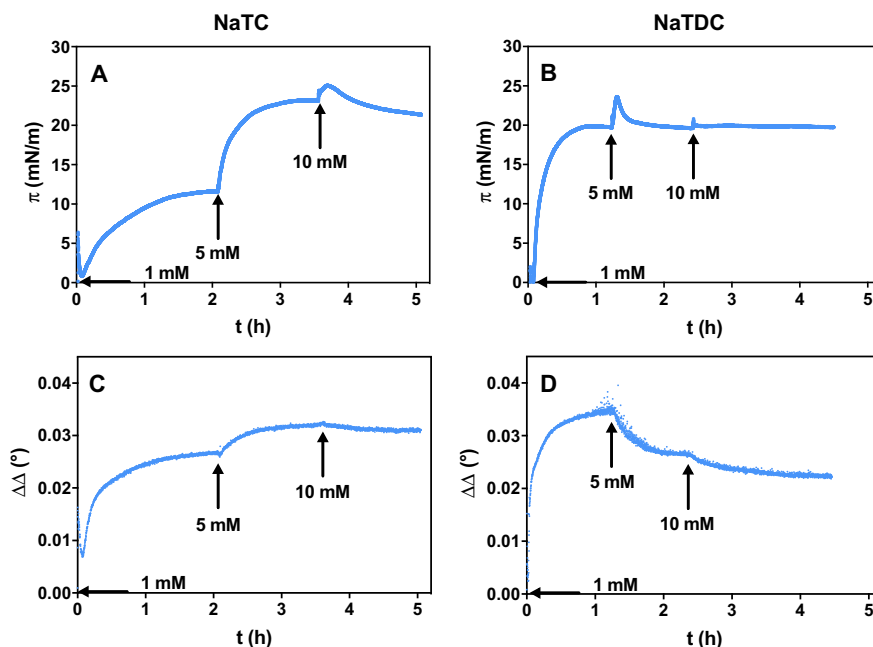


Fig. 3. Time-dependent evolution of the surface pressure (π) measured by a LT (A and B), and phase shift ($\Delta\Delta(t) = \Delta(t) - \Delta_0$) measured by ellipsometry (C and D), upon successive injections of either NaTC (A and C) or NaTDC (B and D) into the aqueous subphase (at $23 \pm 2^\circ\text{C}$). Each addition is shown by an arrow, together with the corresponding BS concentration achieved in the subphase. Each experiment was reproduced twice, and a representative measurement was selected for each experiment.

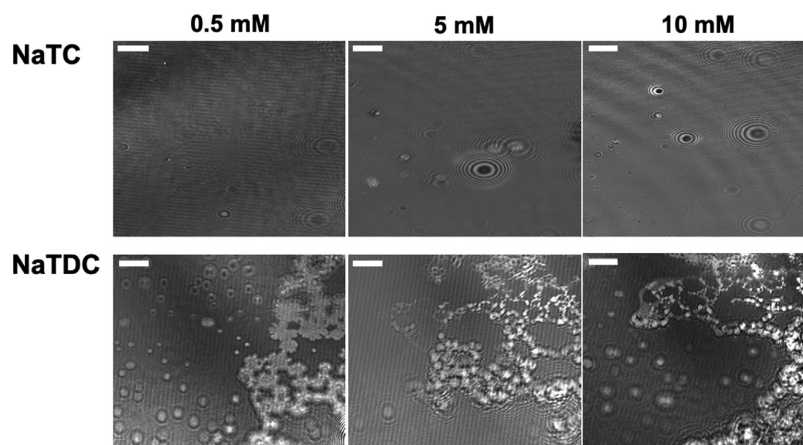


Fig. 4. Evolution of BS film formation and organisation observed with a Brewster angle microscope, upon successive injections of BS into the aqueous subphase: NaTC, NaTDC (at $23 \pm 2^\circ\text{C}$). The scale bar of the BAM images is 50 μm . Stripes are caused by stirring-induced vibrations of the water subphase and black, circular shapes are due to dust grains.

The interaction of NaTC and NaTDC with the DPPC film monitored over longer times (Fig. S5) also shows a concentration-dependent adsorption pattern: up to a threshold concentration, which depends on the BS used (10 mM for NaTC and 1 mM for NaTDC), the surface pressure increases to stabilise at $\Delta\pi = 23 \pm 1 \text{ mN/m}$; at higher concentrations of BS, injection into the subphase results in a small peak surface pressure increase, which then stabilises at a lower value ($\Delta\pi = 11 \pm 3 \text{ mN/m}$). The

transient peaks observed with the LT upon injection of BS (particularly marked for NaTDC) (Figs. 6, S5, and S6A and B) were also found with ellipsometry (Fig. S6C and D), and both in the presence (Fig. S6A and C) and absence (Fig. S6B and D) of stirring; they were therefore attributed to transient adsorption/desorption processes.

From the MD trajectories, the interaction of NaTC and NaTDC with an ordered DPPC monolayer was studied (Fig. 7). Fig. 7A shows the fraction of time that a BS molecule is bound to the

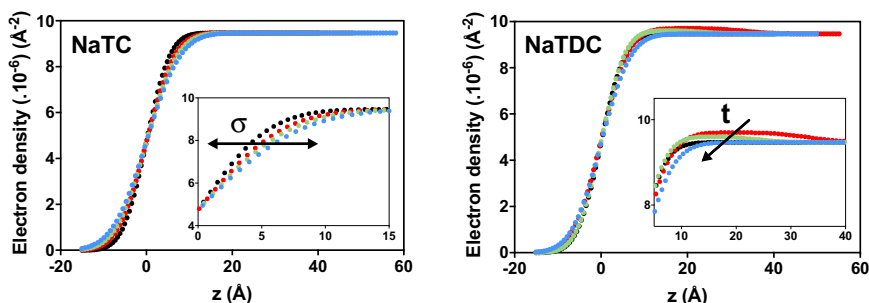


Fig. 5. Evolution of the electron density profile of the interfacial film along the direction perpendicular to the surface (z) obtained from XRR by successive injections of BS into the aqueous subphase: NaTC, NaTDC (at 23 ± 2 °C). BS concentrations below (\bullet 1 mM), around (\bullet 5 mM), and above (\bullet 10 mM) their CMC were selected because different interfacial behaviours were observed with the LT. The electron density profile of the bare air/water interface (\bullet) is also shown.

monolayer, over the course of the trajectory of each simulation. The results show that, for both NaTC and NaTDC, BS molecules as

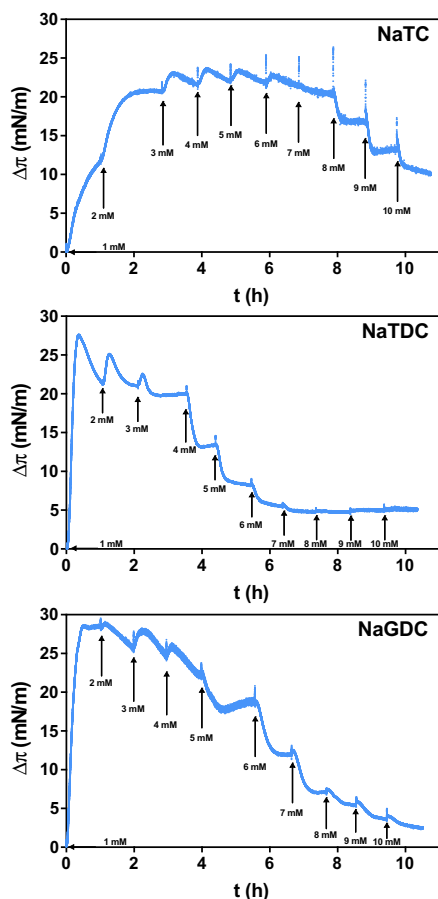


Fig. 6. Time-dependent evolution of the surface pressure ($\Delta\pi(t) = \pi(t) - \pi_{DPPC}$) measured by a LT, upon successive injections of BS into the aqueous subphase: NaTC, NaTDC, NaGDC (at 23 ± 2 °C). The lipids were spread onto water at $\pi_{DPPC} = 25 \pm 2$ mN/m. Each addition is shown by an arrow, together with the corresponding BS concentration achieved in the subphase. Each experiment was reproduced twice, and a representative measurement was selected for each BS.

unimers (i.e., below the CMC) spend more time at the lipid interface (30% and 40% of the time for NaTC and NaTDC, respectively) than they do when in aggregates (i.e., above the CMC); in the aggregated state, they are both found to adsorb onto the monolayer interface approximately 20% of the time. Fig. 7B shows the probability that any given NaTC or NaTDC molecule stays bound to the DPPC monolayer for a certain amount of time. NaTC molecules have nearly identical probabilities of staying bound to the interface for a given amount of time when they are isolated and aggregated. However, NaTDC molecules are significantly more likely to remain bound for longer times when they are present as unimers than when aggregated.

In order to understand these differences, the pairs of atoms that are most commonly found to interact on the BS molecule and the DPPC head group moiety were measured. Fig. 8 shows the probability that a heavy atom on the BS is bound to a heavy atom in the phosphatidylcholine head group (the labels on either axis are defined in Supporting Information, Fig. S7). In all cases, the most common interaction between the BS and the DPPC head group is through the sulfate group of the BS (S, O5 (O4), O6 (O5), O7 (O6) for NaTC (NaTDC)) and the choline head group of the lipid (N, C11, C12, C13, C14, C15). In the aggregated state (Fig. 8B and D), the oxygen at the opposite end of the BS molecule (O1) was found to commonly interact with the choline head group as well, whereas it was not nearly as common with isolated BS molecules (Fig. 8A and C).

While BS seem to most commonly interact with the DPPC choline head group, they also interact with its phosphate group. In the systems with isolated NaTC (Fig. 8A) and NaTDC (Fig. 8C), BS molecules were found to make contact with the phosphate group (P, O11, O12, O13, O14) for approximately 5% of the time that they are bound. In the aggregated state, the amount of time that they bind to the phosphate group decreases for both NaTC (Fig. 8B) and NaTDC (Fig. 8D). However, the decrease is more significant for NaTDC (1% of the time), as compared to NaTC (3%).

3.2.2. Morphology of BS/lipid films

Next, structural changes induced by the two BS on the DPPC monolayer were monitored by BAM (Figs. 9, S8 and S9) and NR (Figs. 10, S11 and S12, Table S2).

BAM images show that the injection of NaTC does not affect the lipid film structure (Figs. 9 and S8), while, instead, the addition of NaTDC above 9 mM leads to a patterning of the surface, revealing the presence of different packing phases in the monolayer (Figs. 9, S8 and S9).

Using NR, the internal structure of the lipid film at the sub-nanometre length scale was obtained using contrast variation, by selective deuteration of the lipids (DPPC and d_{75} -DPPC) and solvent

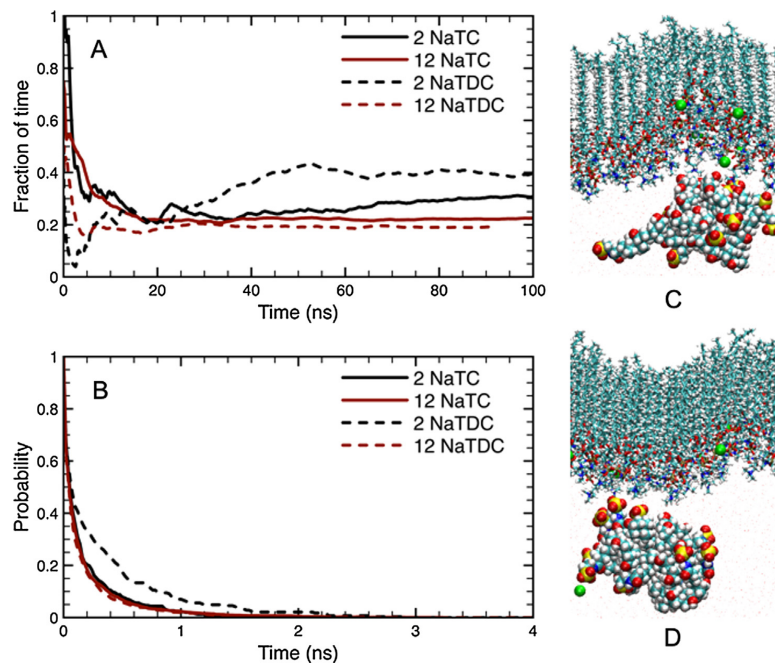


Fig. 7. Binding of NaTC and NaTDC to DPPC monolayers, from MD simulations. (A) Fraction of time that NaTC (—) and NaTDC (---) are adsorbed to the interface of the DPPC monolayer during the course of the simulations, with 2 (black) and 12 (red) BS. (B) The survival probability of a BS molecule at the interface of the DPPC monolayer as a function of time, for NaTC (—) and NaTDC (---), in the simulations with 2 (black) and 12 (red) BS. (C, D) Snapshots of the simulations with 12 NaTC (C) and 12 NaTDC (D) molecules, as they interact with the DPPC monolayers. (For interpretation of the references to colour in this figure legend, the reader is referred to the web version of this article.)

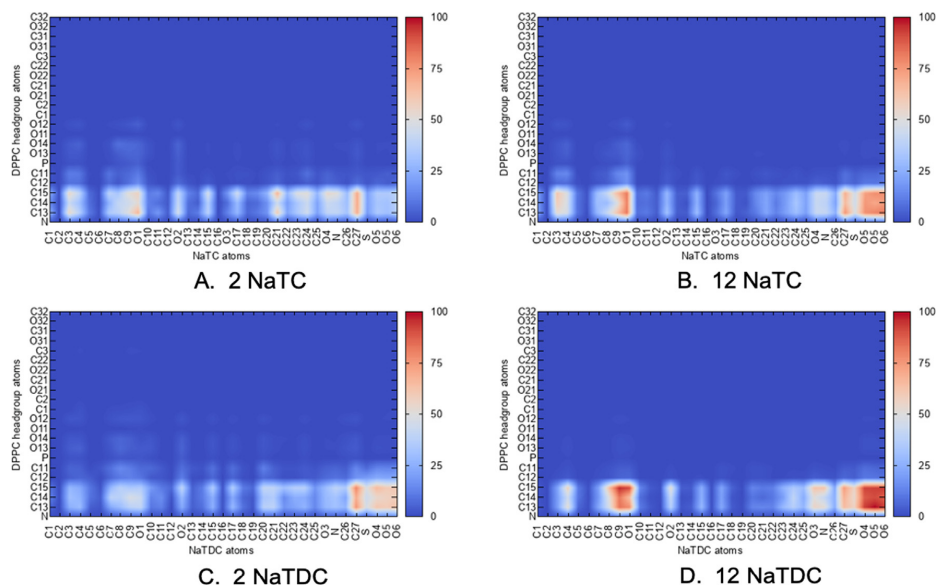


Fig. 8. Interaction maps for NaTC (A and B) and NaTDC (C and D) with the head group of the DPPC molecule in a monolayer. (A and C) Interactions of the two BS for the simulated systems with 2 BS molecules. (B and D) Interactions of the two BS for the simulated systems with 12 BS molecules. Note, the atom labels used on the two axis are defined in Fig. S7.

(H₂O/D₂O and D₂O). We verified that DPPC (Fig. S1A) and d₇₅-DPPC (Fig. S1B) exhibited a similar $\pi - A$ isotherm, and thus a similar packing state at the same surface pressure (Fig. S10); measurements were consistent with literature values for DPPC [44] and d₇₅-DPPC [45].

The proportions of lipid, water and BS in the interfacial film were modelled by assuming that only air could penetrate the tails, while both water and BS could go into the head group region, but not into the tails (further detail on the fitting process can be found in Supporting Information). Based on these assumptions, the head group region of the pure lipid monolayer (in the absence of BS) was found to comprise of 90% lipids and 10% water (Figs. 10, S11 and S12, Table S2). For both BS, successive additions of either NaTC or NaTDC under this lipid film lead to a gradual decrease in the *SLD* of the tails layer, thus indicating a transition from a condensed, uniform phospholipid film to a less compacted and more disorganised one. This observation is in agreement with results from atomic force microscopy, using DPPC and a mixture of NaTC and NaGDC [20]. In concurrence with the results obtained with all of the other techniques, the injection of the two BS into the water subphase generates different structures at the lipid/water interface. With NaTC, two concentration regimes can be distinguished: at low concentration (1 mM), BS molecules adsorb significantly at the interface, reaching a 1:1 BS/DPPC molar ratio, while at higher concentrations, the BS/DPPC molar ratio decreases sharply (to 0.1:1, at 5 mM), until there is no BS at the lipid/water interface at 10 mM. In addition, at this very high BS concentration (10 mM), the proportion of DPPC at the air/water interface decreases to 70%, showing a less compacted film. In contrast, the injection of NaTDC results in a net decrease in the amount of DPPC at the interface, from 90% (without BS) to approximately 40% (with BS), independently of the BS concentration. Moreover, in contrast to NaTC, a BS/DPPC molar ratio of 0:1 was obtained for NaTDC at all BS concentrations, indicating that NaTDC molecules do not penetrate the head group layer.

4. Discussion

The aim of this work was to study and compare the interfacial properties of two BS to understand the impact of their molecular structure on the specific roles they play in lipolysis. For this pur-

pose, their adsorption at an air/water interface and their interaction with a phospholipid monolayer – mimicking the physiological components present at the interface of fat droplets – were characterised. The two BS, differing in the structure of their bile acid moiety (NaTC has an additional hydroxyl group (Fig. 1)), were selected based on previously reported distinct adsorption/desorption dynamics on hydrophobic surfaces [19].

First, BS adsorption properties at the air/water interface were evaluated. Surface pressure measurements show that the injection of BS results in an instantaneous increase in surface pressure, independently of the type of BS, reflecting a very fast adsorption process (Fig. 3A, B, and S3). These rapid dynamics have been observed previously [11,18,22], and are attributed to the planar structure and large surface area of these molecules [46–48]. This unusual flat configuration also explains the relatively low surface pressure ($\pi = 21\text{--}23$ mN/m) obtained after equilibration (Fig. 3A, B, and S3). In comparison, traditional surfactants typically reach values around $\pi = 40\text{--}50$ mN/m. Ellipsometry (Fig. 3C and D) and XRR (Fig. 5, Table S1) measurements reveal different adsorption/desorption behaviour for the two BS. Successive injections of NaTC result in an increase in surface pressure (Fig. 3A), phase shift (Fig. 3C) and interfacial roughness (Fig. 5, Table S1), which all correlate with a higher amount of material adsorbed at the interface [25]. The combination of the three techniques (LT, ellipsometry and XRR) thus confirms that NaTC adsorbs at the interface, until it forms a stable film. In addition, BAM (Fig. 4) and XRR (Fig. 5, Table S1) measurements indicate that the layers formed by NaTC are laterally homogeneous, but diffuse in the perpendicular direction. In contrast, successive additions of NaTDC induce a decrease in phase shift above 5 mM (Fig. 3D), in other words, the desorption of material, while the surface pressure remains constant (Fig. 3B). In conjunction with the ellipsometry measurements, the characterisation of NaTDC adsorbed layer by XRR (Fig. 5, Table S1) shows that, at low concentrations (1 mM), NaTDC adsorbs readily at the air/water interface, forming a relatively thick film, while the addition of further BS (5 mM) leads to a decrease in layer thickness, until a very diffuse film is formed (at 10 mM), thus demonstrating that NaTDC partially leaves the interface as its concentration in the bulk increases. The discrepancy between the stabilisation of the surface pressure, which suggests a stabilisation of the film, and the decrease in both phase shift and film thickness, which implies the desorption of material, can be explained by the formation of

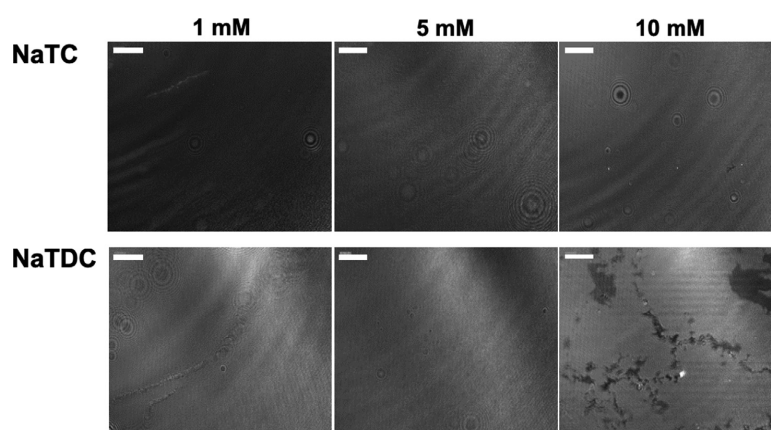


Fig. 9. Evolution of the lipid monolayer organisation observed with a Brewster angle microscope, upon successive injections of BS into the aqueous subphase: NaTC, NaTDC (at 23 ± 2 °C). The lipids were spread onto water at $\pi_{\text{DPPC}} = 25 \pm 2$ mN/m. Three BS concentrations are shown here, and additional ones are displayed in Supporting Information (Fig. S8). The scale bar of the BAM images is 50 μm . Stripes are caused by stirring-induced vibrations of the water subphase and (black or white) circular shapes are due to dust grains. The BAM image obtained with the pure DPPC monolayer can be found in Fig. S8.

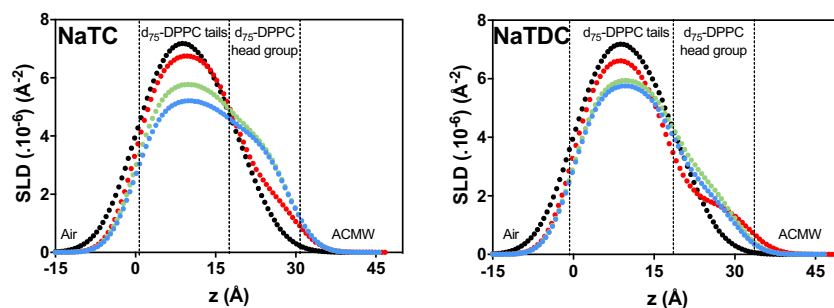


Fig. 10. Evolution of the scattering length density (SLD) profile of the interfacial film along the direction perpendicular to the surface (z) obtained from NR by successive injections of BS into the aqueous subphase: NaTC, NaTDC (at 23 ± 2 °C). The lipids were spread onto water at $\pi_{\text{DPPC}} = 25 \pm 2$ mN/m, thus forming a pure monolayer (●). BS concentrations below (●) 1 mM, around (●) 5 mM, and above (●) 10 mM their CMC were selected because different interfacial behaviours were observed with the LT. These SLD profiles were recorded in ACMW (SLD of 0), on which a d_{75} -DPPC monolayer (SLD of $7.66 \times 10^{-6} \text{ \AA}^{-2}$ for the tails and $5.68 \times 10^{-6} \text{ \AA}^{-2}$ for the head group) was prepared; NaTC has a SLD of $0.95 \times 10^{-6} \text{ \AA}^{-2}$ and NaTDC of $0.90 \times 10^{-6} \text{ \AA}^{-2}$. The SLD profiles obtained in the other conditions of contrast are displayed in Supporting Information (Fig. S12).

buried layers beneath the monolayer at the air/water interface. Any event occurring in these sublayers (either adsorption or desorption) would not affect surface pressure [21,49–51]. Moreover, unlike NaTC, which produces a laterally uniform film at the air/water interface, the adsorption of NaTDC leads to irregular patterns in BAM images, reflecting the formation of islands on the water surface (Fig. 4). Based on these results, it is clear that the small structural difference between the two BS affects their adsorption behaviour at the air/water interface, with NaTC being more prone to remain at the interface, despite its lower hydrophobicity [52].

In the second part, the interaction of BS with a DPPC monolayer was studied, mimicking the interfacial processes taking place when a hydrosoluble BS molecule approaches a fat droplet.

Successive injections of NaTC (1–6 mM) below this monolayer induce an increase in surface pressure (Fig. 6), suggesting adsorption of the BS. This observation is confirmed by NR, which shows that NaTC adsorbs into the lipid head group region, at a 1:1 BS/DPPC molar ratio at 1 mM (Figs. 10 and S12, Table S2). MD simulations indicate that NaTC primarily interacts with the choline head group of DPPC, and does occasionally penetrate deeper into the lipid membrane, to the level of the phosphate group (Fig. 8A, B and S6A, C). Above ca. 7 mM, however, a decrease in surface pressure is measured, which could suggest the desorption of NaTC from the interface or, alternatively, the displacement of DPPC molecules into the subphase, through their incorporation into mixed micelles (Fig. 6). BAM images show that the interfacial layer remains homogeneous, suggesting the absence of any lateral disorganisation (which could occur by the removal of DPPC molecules) (Figs. 9 and S8). NR data at these concentrations show a transition to a less compacted and more disordered DPPC film, as well as a decrease in the amount of NaTC in the lipid layer (from 1:1 BS/DPPC at 1 mM to 0.1:1 at 5 mM and 0:1 at 10 mM) (Figs. 10 and S12, Table S2). The apparent discrepancy between BAM and NR results can be explained by the rather low lateral resolution of the Brewster angle microscope. Overall, these results clearly imply that, at high concentrations, NaTC desorbs from the interface and removes some DPPC molecules in the process. This change in behaviour (from adsorption to desorption) corresponds to the onset of micellisation (4–7 mM for NaTC). The results of MD simulations corroborate these observations, showing a higher probability of NaTC molecules to interact with the lipid film in their non-aggregated state, compared to their micellised state (Fig. 7).

In contrast to NaTC, the addition of NaTDC leads to a decrease in surface pressure at quite low concentrations (ca. 3 mM), which could be due to either BS molecules desorbing from the interface

or DPPC molecules being displaced by BS (Fig. 6). This behaviour suggests a lower affinity for the lipid/water interface. A similar surface pressure trend is exhibited by both NaTDC and NaGDC, stressing the importance of the steroid backbone in dictating behaviour, rather than the conjugated amino acid. NR measurements reveal that NaTDC molecules, unlike NaTC, do not penetrate deeply into the DPPC head group layer, a key difference between the two BS (Figs. 10 and S12, Table S2). NaTDC induces, instead, a diffuse layer beneath the DPPC head group, at the head group/water interface. MD simulations show a drop in interaction with the monolayer upon aggregation of BS (Fig. 7), which, for NaTDC, occurs at very low concentrations (2 mM). NaTDC interacts with the choline head group of DPPC, and is generally oriented such that the length of the molecule is parallel to the monolayer interface (Fig. 8C, D, and S7B, C). As for NaTC, the addition of increasing amounts of NaTDC loosens the packing of the DPPC monolayer (Figs. 10 and S12, Table S2). The major difference between the two BS is the strong desorption of DPPC molecules from the interface induced by NaTDC (to approximately 40%, at all concentrations), resulting in the formation of fluid domains (Figs. 10 and S12, Table S2). The addition of NaTDC was seen to induce the formation of domains with distinct organisations (i.e., lipid packing states), clearly detected by BAM above 9 mM (Figs. 9, S8 and S9). The lack of domains at lower concentrations may be because these domains are, in size, smaller than the lateral resolution of the Brewster angle microscope. These observations taken together suggest, for NaTDC, a lipid-solubilising effect, leading to the formation of mixed micelles in the bulk.

Overall, the combination of all these experiments clearly suggests different roles during lipolysis for the two BS studied: cholate-based BS (NaTC) have a higher affinity for the interface and may thus be more prone to adsorb at the lipid/water interface, thus facilitating lipase and co-lipase adsorption, while deoxycholate derivatives (NaTDC and NaGDC) have a higher propensity to desorb and are thus more likely to be involved in removing insoluble hydrolysis products from the interface, by solubilising them into mixed micelles. These findings thus confirm that a very small difference in BS structure on the steroid backbone has a major impact on their adsorption/desorption behaviour and may be a key to the significance – often overlooked – of BS structural diversity.

5. Conclusion

In this work, we compared the adsorption dynamics and film morphology of two BS, NaTC and NaTDC, at the air/water interface

and under a phospholipid monolayer, in order to shed light on their specific roles in lipid digestion.

Both BS injected under a DPPC monolayer were found to disrupt lipid packing. However, NaTC penetrated more deeply into the lipid head group region, compared to NaTDC. In addition, NaTC remained adsorbed at the interface over a wider concentration range. Instead, NaTDC was shown to displace DPPC molecules through dynamic exchange. These findings support our hypothesis that NaTC may be more efficient at facilitating the adsorption and activity of co-lipase-dependent pancreatic lipase, while NaTDC may be more prone to remove insoluble lipolysis products from the interface, through their incorporation into mixed micelles. This hypothesis will need to be further explored in future work by enzymatic absorption studies.

The contrasting interfacial behaviour displayed by the two BS was also found to correlate with their bulk aggregation processes: the adsorption of NaTC at interfaces over a wider range of concentrations correlates with a later onset of micellisation (4–7 mM), while desorption of NaTDC occurring at low concentrations correlates with a lower CMC value (ca. 2 mM). Therefore, BS adsorption/desorption processes at the interface are linked to processes taking place in the bulk, which, in turn, are dictated by the chemical structure.

To our knowledge, this is the first time that the interaction between BS and a lipid monolayer – mimicking the phospholipids molecules present on the surface of a fat droplet – has been characterised at the nanometre scale. Our NR studies and MD simulations establish a molecular-level description of the BS and lipid films, which is a key-step towards a better understanding of the lipolysis process and addressing the current challenges of excessive fat uptake and associated health conditions. This work will be complemented by additional NR work on lipid bilayers and at the oil/water interface (in preparation), and with bulk studies on mixed micelles of BS and the products of lipolysis, by small-angle neutron scattering and MD simulations, as well as *in vitro* lipolysis experiments.

Declaration of Competing Interest

None.

Acknowledgements

The authors acknowledge the ILL for the provision of a PhD studentship (OP) and award of beam time on FIGARO (doi: 10.5291/ILL-DATA.9-10-1488). The Partnership for Soft Condensed Matter (PSCM) is acknowledged for access to sample preparation facilities and the use of the LT, ellipsometer, Brewster angle microscope and X-ray reflectometer. OP thanks Kelly Vandra for her kind help with LT experiments, as well as Pierre Lloria and Andrea Tummino for the support provided during the acquisition of BAM images and ellipsometry measurements. Arthur Bernardeau was involved in preliminary work on MD simulations during a summer internship. Via CDL's membership of the UK's HEC Materials Chemistry Consortium, which is funded by EPSRC (EP/L000202/1, EP/R029431/1), this work used the ARCHER UK National Supercomputing Service (<http://www.archer.ac.uk>) and the UK Materials and Molecular Modelling Hub (MMM Hub) for computational resources, which is partially funded by EPSRC (EP/P020194/1) to carry out the MD simulations reported in this manuscript. PJW and MM-LG gratefully acknowledge the support of the Biotechnology and Biological Sciences Research Council (BBSRC) through the BBSRC Institute Strategic Programme Food Innovation and Health BB/R012512/1 and its constituent project BBS/E/F/000PR10345.

Appendix A. Supplementary material

Supplementary data to this article can be found online at <https://doi.org/10.1016/j.jcis.2019.08.010>.

References

- [1] World Health Organization, Obesity and Overweight, 2018, <http://www.who.int/mediacentre/factsheets/fs311/en/> (accessed August 21, 2018).
- [2] World Health Organization, Food & Agriculture Organization, Diet, Nutrition and the Prevention of Chronic Diseases, Geneva, 2003, http://apps.who.int/iris/bitstream/10665/42665/1/WHO_TRS_916.pdf?ua=1.
- [3] J. Mei, A. Lindqvist, L. Krabisch, J.F. Rehfeld, C. Erlanson-Albertsson, Appetite suppression through delayed fat digestion, *Physiol. Behav.* 89 (2006) 563–568, <https://doi.org/10.1016/j.physbeh.2006.07.020>.
- [4] M. Golding, T.J. Wooster, The influence of emulsion structure and stability on lipid digestion, *Curr. Opin. Colloid Interface Sci.* 15 (2010) 90–101, <https://doi.org/10.1016/j.cocis.2009.11.006>.
- [5] P.J. Wilde, B.S. Chu, Interfacial & colloidal aspects of lipid digestion, *Adv. Colloid Interface Sci.* 165 (2011) 14–22, <https://doi.org/10.1016/j.cis.2011.02.004>.
- [6] M. Armand, Lipases and lipolysis in the human digestive tract: where do we stand?, *Curr. Opin. Clin. Nutr. Metab. Care.* 10 (2007) 156–164, <https://doi.org/10.1097/MCO.0b013e3280177687>.
- [7] P. Reis, K. Holmberg, H. Watzke, M.E. Leser, R. Miller, Lipases at interfaces: a review, *Adv. Colloid Interface Sci.* 147–148 (2009) 237–250, <https://doi.org/10.1016/j.cis.2008.06.001>.
- [8] J. Patton, M. Carey, Watching fat digestion, *Science* 204 (4389) (1979) 145–148, <https://doi.org/10.1126/science.432636>.
- [9] Y. Pafumi, D. Lairon, P. Lechene de la Porte, C. Juhel, J. Storch, M. Hamosh, M. Armand, Mechanisms of inhibition of triacylglycerol hydrolysis by human gastric lipase, *J. Biol. Chem.* 277 (2002) 28070–28079, <https://doi.org/10.1074/jbc.M202839200>.
- [10] A.F. Hofmann, K.J. Mysels, Bile salts as biological surfactants, *Colloids Surf.* 30 (1987) 145–173, [https://doi.org/10.1016/0166-6622\(87\)80207-X](https://doi.org/10.1016/0166-6622(87)80207-X).
- [11] J. Maldonado-Valderrama, P. Wilde, A. Macierzanka, A. Mackie, The role of bile salts in digestion, *Adv. Colloid Interface Sci.* 165 (2011) 36–46, <https://doi.org/10.1016/j.cis.2010.12.002>.
- [12] L. Galantini, M.C. di Gregorio, M. Gubitosi, L. Travaglini, J. Vázquez Tato, A. Jover, F. Mejjide, V.H. Soto Tellini, N.V. Pavel, Bile salts and derivatives: rigid unconventional amphiphiles as dispersants, carriers and superstructure building blocks, *Curr. Opin. Colloid Interface Sci.* 20 (2015) 170–182, <https://doi.org/10.1016/j.cocis.2015.08.004>.
- [13] D. Madenci, S.U. Egelhaaf, Self-assembly in aqueous bile salt solutions, *Curr. Opin. Colloid Interface Sci.* 15 (2010) 109–115, <https://doi.org/10.1016/j.cocis.2009.11.010>.
- [14] B. Borgström, C. Erlanson-Albertsson, T. Wieloch, Pancreatic colipase: chemistry and physiology, *J. Lipid Res.* 20 (1979) 805–816, <http://www.ncbi.nlm.nih.gov/pubmed/385801>.
- [15] C. Erlanson-Albertsson, The interaction between pancreatic lipase and colipase: a protein-protein interaction regulated by a lipid, *FEBS Lett.* 162 (1983) 225–229, [https://doi.org/10.1016/0014-5793\(83\)80760-1](https://doi.org/10.1016/0014-5793(83)80760-1).
- [16] A. Bourbon Freie, F. Ferrato, F. Carrière, M.E. Lowe, Val-407 and Ile-408 in the $\beta 5$ -loop of pancreatic lipase mediate lipase-colipase interactions in the presence of bile salt micelles, *J. Biol. Chem.* 281 (2006) 7793–7800, <https://doi.org/10.1074/jbc.M512984200>.
- [17] S. Labourenne, O. Brass, M. Ivanova, A. Cagna, R. Verger, Effects of colipase and bile salts on the catalytic activity of human pancreatic lipase. A study using the oil drop tensiometer, *Biochemistry* 36 (1997) 3423–3429, <https://doi.org/10.1021/bi961331k>.
- [18] J. Maldonado-Valderrama, J.L. Muros-Cobos, J.A. Holgado-Terriza, M.A. Cabrero-Vilchez, Bile salts at the air-water interface: adsorption and desorption, *Colloids Surf. B Biointerf.* 120 (2014) 176–183, <https://doi.org/10.1016/j.colsurfb.2014.05.014>.
- [19] R. Parker, N.M. Rigby, M.J. Ridout, A.P. Gunning, P.J. Wilde, The adsorption-desorption behaviour and structure function relationships of bile salts, *Soft Matter* 10 (2014) 6457–6466, <https://doi.org/10.1039/c4sm01093k>.
- [20] B.-S. Chu, A.P. Gunning, G.T. Rich, M.J. Ridout, R.M. Faulks, M.S.J. Wickham, V.J. Morris, P.J. Wilde, Adsorption of bile salts and pancreatic colipase and lipase onto digalactosyldiacylglycerol and dipalmitoylphosphatidylcholine monolayers, *Langmuir* 26 (2010) 9782–9793, <https://doi.org/10.1021/la100044e>.
- [21] A. Bénarouche, L. Sams, C. Bourlieu, V. Vié, V. Point, J.F. Cavalier, F. Carrière, Studying gastric lipase adsorption onto phospholipid monolayers by surface tensiometry, ellipsometry, and atomic force microscopy, in: M.H. Gelb (Ed.), *Methods Enzymol. - Enzymol. Membr. Interface Interfacial Enzymol. Protein-Membrane Bind.*, 1st ed., Elsevier Inc., San Diego, 2017, pp. 255–278, <https://doi.org/10.1016/bs.mie.2016.09.039>.
- [22] J. Maldonado-Valderrama, N.C. Woodward, A.P. Gunning, M.J. Ridout, F.A. Husband, A.R. Mackie, V.J. Morris, P.J. Wilde, Interfacial characterization of β -lactoglobulin networks: displacement by bile salts, *Langmuir* 24 (2008) 6759–6767, <https://doi.org/10.1021/la800551u>.

- [23] H. Singh, A. Ye, D. Horne, Structuring food emulsions in the gastrointestinal tract to modify lipid digestion, *Prog. Lipid Res.* 48 (2009) 92–100, <https://doi.org/10.1016/j.plipres.2008.12.001>.
- [24] D.G. Dalgleish, Food emulsions - their structures and structure-forming properties, *Food Hydrocoll.* 20 (2006) 415–422, <https://doi.org/10.1016/j.foodhyd.2005.10.009>.
- [25] H. Motschmann, R. Teppner, Ellipsometry in interface science, in: D. Möbius, R. Miller (Eds.), *Stud. Interface Sci. - Nov. Methods to Study Interfacial Layers*, 1st ed., Elsevier Science B. V, Amsterdam, 2001, pp. 1–42.
- [26] Y. Gerelli, Aurore: new software for neutron reflectivity data analysis, *J. Appl. Crystallogr.* 49 (2016) 330–339, <https://doi.org/10.1107/S1600576716000108>.
- [27] R.A. Campbell, H.P. Wacklin, I. Sutton, R. Cubitt, G. Fragneto, FIGARO: the new horizontal neutron reflectometer at the ILL, *Eur. Phys. J. Plus.* 126 (2011) 1–22, <https://doi.org/10.1140/epjp/i2011-11107-8>.
- [28] Institut Laue-Langevin, The COSMOS software application available for the ILL reflectometers, 2018, <https://www.ill.eu/fr/users-en/instruments/instruments-list/d17/more/cosmos/> (accessed August 23, 2018).
- [29] R.A. Campbell, Y. Saaka, Y. Shao, Y. Gerelli, R. Cubitt, E. Nazaruk, D. Matyszewska, M.J. Lawrence, Structure of surfactant and phospholipid monolayers at the air/water interface modeled from neutron reflectivity data, *J. Colloid Interface Sci.* 531 (2018) 98–108, <https://doi.org/10.1016/j.jcis.2018.07.022>.
- [30] S. Jo, T. Kim, V.G. Iyer, W. Im, CHARMM-GUI: a web-based graphical user interface for CHARMM, *J. Comput. Chem.* 29 (2008) 1859–1865, <https://doi.org/10.1002/jcc.20945>.
- [31] E.L. Wu, X. Cheng, S. Jo, H. Rui, K.C. Song, E.M. Dávila-Contreras, Y. Qi, J. Lee, V. Monje-Galvan, R.M. Venable, J.B. Klauda, W. Im, CHARMM-GUI Membrane Builder toward realistic biological membrane simulations, *J. Comput. Chem.* 35 (2014) 1997–2004, <https://doi.org/10.1002/jcc.23702>.
- [32] J. Lee, X. Cheng, J.M. Swails, M.S. Yeom, P.K. Eastman, J.A. Lemkul, S. Wei, J. Buckner, J.C. Jeong, Y. Qi, S. Jo, V.S. Pande, D.A. Case, C.L. Brooks III, A.D. MacKerell Jr., J.B. Klauda, W. Im, CHARMM-GUI input generator for NAMD, GROMACS, AMBER, OpenMM, and CHARMM/OpenMM simulations using the CHARMM36 additive force field, *J. Chem. Theory Comput.* 12 (2016) 405–413, <https://doi.org/10.1021/acs.jctc.5b00935>.
- [33] T. Schneider, E. Stoll, Molecular-dynamics study of a three-dimensional one-component model for distortive phase transitions, *Phys. Rev. B* 17 (1978) 1302–1322, <https://doi.org/10.1103/PhysRevB.17.1302>.
- [34] W.G. Hoover, Canonical dynamics: equilibrium phase-space distributions, *Phys. Rev. A* 31 (1985) 1695–1697, <https://doi.org/10.1103/PhysRevA.31.1695>.
- [35] S. Plimpton, Fast parallel algorithms for short-range molecular dynamics, *J. Comput. Phys.* 117 (1995) 1–19, <https://doi.org/10.1006/jcph.1995.1039>.
- [36] K. Vanommeslaeghe, E. Hatcher, C. Acharya, S. Kundu, S. Zhong, J. Shim, E. Darian, O. Guvench, P. Lopes, I. Vorobyov, A.D. MacKerell Jr., CHARMM general force field: a force field for drug-like molecules compatible with the CHARMM all-atom additive biological force fields, *J. Comput. Chem.* 31 (2010) 671–690, <https://doi.org/10.1002/jcc.21367>.
- [37] J.B. Klauda, R.M. Venable, J.A. Freites, J.W. O'Connor, D.J. Tobias, C. Mondragon-Ramirez, I. Vorobyov, A.D. MacKerell Jr., R.W. Pastor, Update of the CHARMM all-atom additive force field for lipids: validation on six lipid types, *J. Phys. Chem. B* 114 (2010) 7830–7843, <https://doi.org/10.1021/jp101759q>.
- [38] R.W. Pastor, A.D. MacKerell Jr., Development of the CHARMM force field for lipids, *J. Phys. Chem. Lett.* 2 (2011) 1526–1532, <https://doi.org/10.1021/jz200167q>.
- [39] W.L. Jorgensen, J. Chandrasekhar, J.D. Madura, R.W. Impey, M.L. Klein, Comparison of simple potential functions for simulating liquid water, *J. Chem. Phys.* 79 (1983) 926–935, <https://doi.org/10.1063/1.445869>.
- [40] W.E. Reiher, *Theoretical Studies Of Hydrogen Bonding*, Harvard University, 1985.
- [41] T. Darden, D. York, L. Pedersen, Particle mesh Ewald: an N-log(N) method for Ewald sums in large systems, *J. Chem. Phys.* 98 (1993) 10089–10092, <https://doi.org/10.1063/1.464397>.
- [42] J.-P. Ryckaert, G. Ciccotti, H.J. Berendsen, Numerical integration of the cartesian equations of motion of a system with constraints: molecular dynamics of n-alkanes, *J. Comput. Phys.* 23 (1977) 327–341, [https://doi.org/10.1016/0021-9991\(77\)90098-5](https://doi.org/10.1016/0021-9991(77)90098-5).
- [43] K. Matsuoka, M. Maeda, Y. Moroi, Micelle formation of sodium glyco- and taurocholates and sodium glyco- and taurodeoxycholates and solubilization of cholesterol into their micelles, *Colloids Surf. B Biointerf.* 32 (2003) 87–95, [https://doi.org/10.1016/S0927-7765\(03\)00148-6](https://doi.org/10.1016/S0927-7765(03)00148-6).
- [44] K. Sabatini, J.-P. Mattila, P.K.J. Kinnunen, Interfacial behavior of cholesterol, ergosterol, and lanosterol in mixtures with DPPC and DMPC, *Biophys. J.* 95 (2008) 2340–2355, <https://doi.org/10.1529/biophysj.108.132076>.
- [45] V. Rondelli, G. Fragneto, S. Motta, E. Del Favero, L. Cantù, Reflectivity from floating bilayers: can we keep the structural asymmetry?, *J. Phys. Conf. Ser.* 340 (2012) 1–10, <https://doi.org/10.1088/1742-6596/340/1/012083>.
- [46] A. Tiss, S. Ransac, H. Lengsfeld, P. Hadváry, A. Cagna, R. Verger, Surface behaviour of bile salts and tetrahydrolipstatin at air/water and oil/water interfaces, *Chem. Phys. Lipids* 111 (2001) 73–85, [https://doi.org/10.1016/S0009-3084\(01\)00149-9](https://doi.org/10.1016/S0009-3084(01)00149-9).
- [47] N. Matubayasi, M. Kanzaki, S. Sugiyama, A. Matuzawa, Thermodynamic study of gaseous adsorbed films of sodium taurocholate at the air/water interface, *Langmuir* 12 (1996) 1860–1862, <https://doi.org/10.1021/la950832o>.
- [48] N. Matubayasi, S. Sugiyama, M. Kanzaki, A. Matuzawa, Thermodynamic studies of the adsorbed films and micelles of sodium taurodeoxycholate, *J. Colloid Interface Sci.* 196 (1997) 123–127, <https://doi.org/10.1006/jcis.1997.5213>.
- [49] D.E. Graham, M.C. Phillips, Proteins at liquid interfaces. III. Molecular structures of adsorbed films, *J. Colloid Interface Sci.* 70 (1979) 427–439, [https://doi.org/10.1016/0021-9797\(79\)90050-X](https://doi.org/10.1016/0021-9797(79)90050-X).
- [50] V.M. Bolanos-García, A. Renault, S. Beaufils, Surface rheology and adsorption kinetics reveal the relative amphiphilicity, interfacial activity, and stability of human exchangeable apolipoproteins, *Biophys. J.* 94 (2008) 1735–1745, <https://doi.org/10.1529/biophysj.107.115220>.
- [51] D.J.F. Taylor, R.K. Thomas, J.D. Hines, K. Humphreys, J. Penfold, The adsorption of oppositely charged polyelectrolyte/surfactant mixtures at the air/water interface: neutron reflection from dodecyl trimethylammonium bromide/sodium poly(styrene sulfonate) and sodium dodecyl sulfate/poly(vinyl pyridinium chloride), *Langmuir* 18 (2002) 9783–9791, <https://doi.org/10.1021/la020503d>.
- [52] M.J. Armstrong, M.C. Carey, The hydrophobic-hydrophilic balance of bile salts. Inverse correlation between reverse-phase high performance liquid chromatographic mobilities and micellar cholesterol-solubilizing capacities, *J. Lipid Res.* 23 (1982) 70–80.

Corrigendum

Corrigendum to 'Molecular insights into the behaviour of bile salts at interfaces: a key to their role in lipid digestion' [Journal of Colloid and Interface Science, 556 (2019) 266-277].

Olivia Pabois^{a, b}, Christian D. Lorenz^c, Richard D. Harvey^d, Isabelle Grillo^a, Myriam M.-L. Grundy^e, Peter J. Wilde^f, Yuri Gerelli^{a*}, Cécile A. Dreiss^{b*}

^a Institut Laue-Langevin, Grenoble 38000, France

^b School of Cancer and Pharmaceutical Sciences, Institute of Pharmaceutical Science, King's College London, London SE1 9NH, United-Kingdom

^c Department of Physics, King's College London, London WC2R 2LS, United-Kingdom

^d Institut für Pharmazie, Martin-Luther-Universität Halle-Wittenberg, Halle (Saale) 06099, Germany

^e School of Agriculture, Policy and Development, University of Reading, Reading RG6 6AR, United-Kingdom

^f Quadram Institute Bioscience, Norwich Research Park, Norwich NR4 7UA, United-Kingdom

The authors regret inverting the symbols colours in Figures 5 and 10. Amended captions are shown below. The authors would like to apologise for any inconvenience caused.

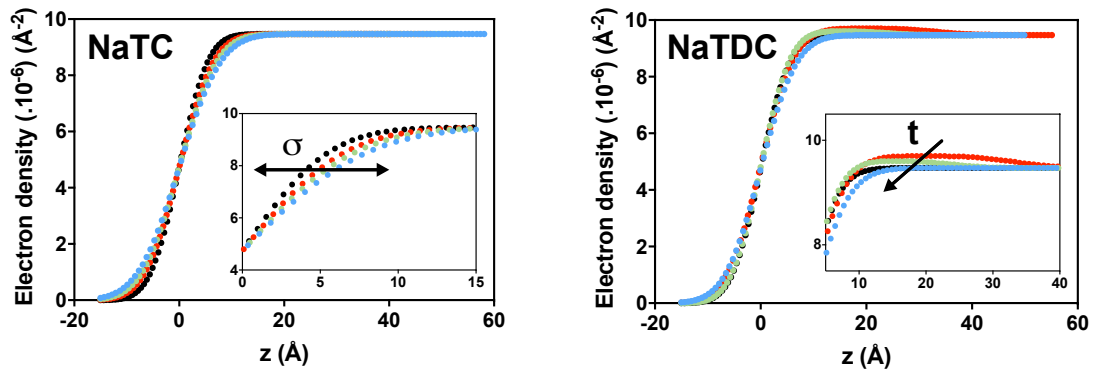


Figure 5: Evolution of the electron density profile of the interfacial film along the direction perpendicular to the surface (z) obtained from XRR by successive injections of BS into the aqueous subphase: NaTC, NaTDC (at $23 \pm 2^\circ\text{C}$). BS concentrations below (\bullet) 1 mM), around (\bullet) 5 mM), and above (\bullet) 10 mM) their CMC were selected because different interfacial behaviours were observed with the LT. The electron density profile of the bare air/water interface (\bullet) is also shown.

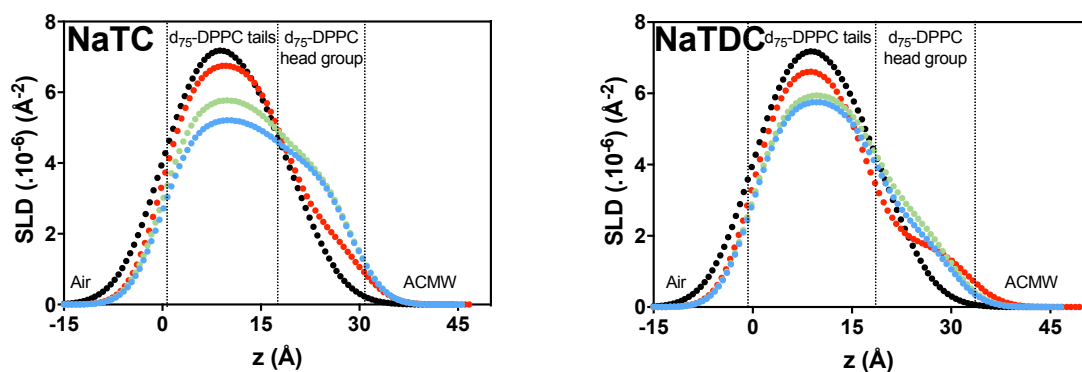


Figure 10: Evolution of the scattering length density (SLD) profile of the interfacial film along the direction perpendicular to the surface (z) obtained by successive injections of BS into the aqueous subphase: NaTC, NaTDC (at $23 \pm 2^\circ\text{C}$). The lipids were spread onto water at $\pi_{\text{DPPC}} = 25 \pm 2 \text{ mN/m}$, thus forming a pure monolayer (\bullet). BS concentrations below (\bullet) 1 mM), around (\bullet) 5 mM), and above (\bullet) 10 mM) their CMC were selected because different interfacial behaviours were observed with the LT. These SLD profiles were recorded in ACMW (SLD of 0), on which a d_{75} -DPPC monolayer (SLD of $7.66 \cdot 10^{-6} \text{ \AA}^{-2}$ for the tails and $5.68 \cdot 10^{-6} \text{ \AA}^{-2}$ for the head group) was prepared; NaTC has a SLD of $0.95 \cdot 10^{-6} \text{ \AA}^{-2}$ and NaTDC of $0.90 \cdot 10^{-6} \text{ \AA}^{-2}$. The SLD profiles obtained in the other conditions of contrast are displayed in Supporting Information (Figure S12).

DOI of original article: [10.1016/j.jcis.2019.08.010](https://doi.org/10.1016/j.jcis.2019.08.010)

Cécile A. Dreiss:

King's College London

School of Cancer & Pharmaceutical Sciences

Franklin-Wilkins Building

150 Stamford Street

SE1 9NH London, UK

Tel: +44 (0)207 848 3766

Yuri Gerelli:

Institut Max von Laue - Paul Langevin

71 avenue des Martyrs

38000 Grenoble, France

Tel: +33 (0)4 76 20 70 68

cecile.dreiss@kcl.ac.uk; gerelli@ill.fr

Supporting information

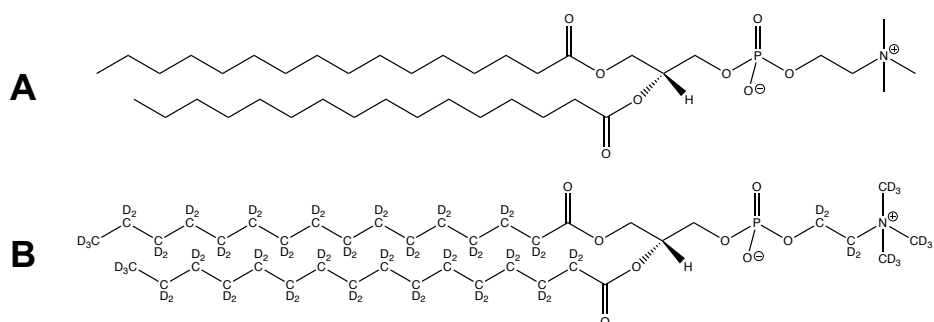


Figure S1: Structures of DPPC (A) and d_{75} -DPPC (B)

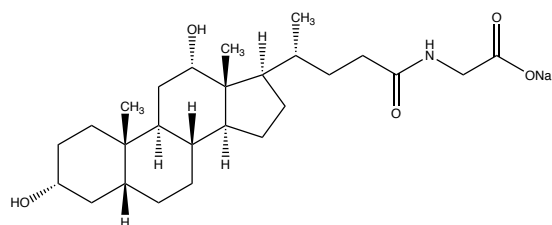


Figure S2: Structure of NaGDC

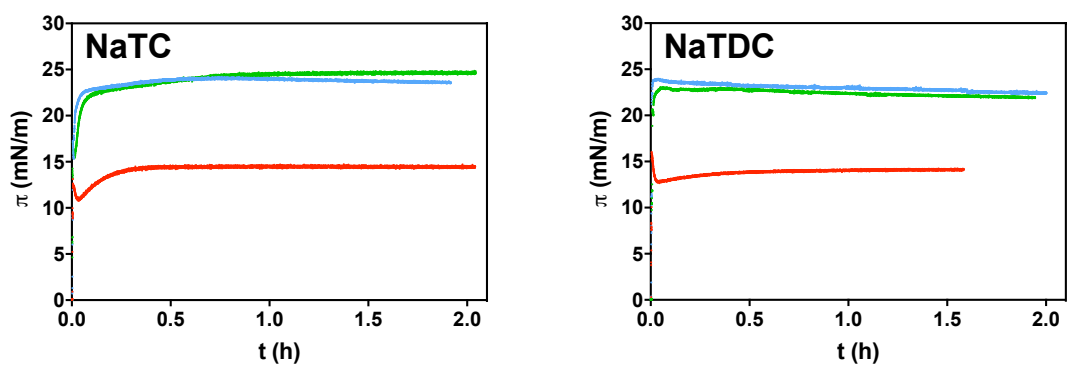


Figure S3: Time-dependent evolution of the surface pressure (π) measured by a LT, upon injection of BS into the aqueous subphase: NaTC, NaTDC, at varying concentrations: (—) 0.5 mM, (—) 5 mM, (—) 10 mM (at $23 \pm 2^\circ\text{C}$). Each experiment was reproduced twice, and the average measurement was selected for each BS at each concentration.

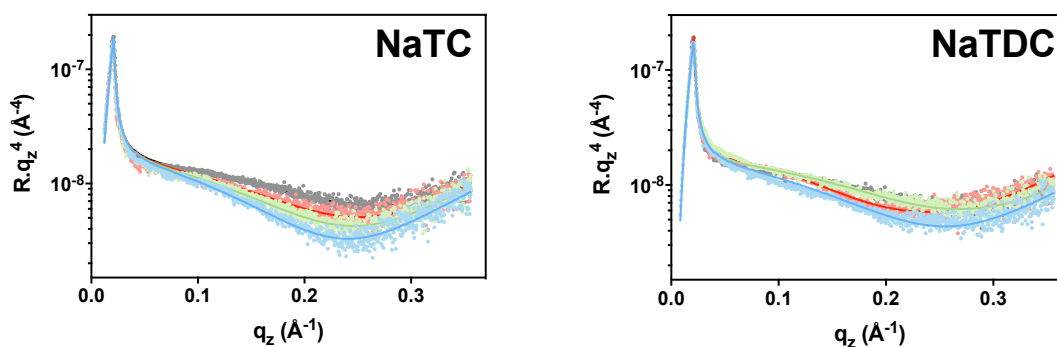


Figure S4: XRR signal ($R \cdot q_z^4$ representation) of ultrapure water (●) and of the interfacial film formed at the air/water interface upon successive injections of BS into the aqueous subphase: NaTC, NaTDC (at $23 \pm 2^\circ\text{C}$), as a function of the scattering vector (q_z). BS concentrations below (●) 1 mM, around (●) 5 mM, and above (●) 10 mM) their CMC were selected because different interfacial behaviours were observed with the LT.

NaTC	Water	[NaTC] (mM)		
		1	5	10
σ (Å)	4	5	6	6
t (Å)	-	-	-	-
Electron density ($\times 10^6$) (Å ⁻²)	-	-	-	-

NaTDC	Water	[NaTDC] (mM)		
		1	5	10
σ (Å)	4	5	4	5
t (Å)	-	33	24	-
Electron density ($\times 10^6$) (Å ⁻²)	-	9.7	9.6	-

Table S1: Evolution of the XRR parameters of the interfacial film formed at the air/water interface upon successive injections of 1, 5 and 10 mM BS into the aqueous subphase: NaTC, NaTDC. When the layer formed was very diffuse, the evolution of the air/water interfacial roughness (σ) was monitored, while a model assuming a single layer characterised by a specific roughness (σ), thickness (t), and electron density, was used to fit a more dense, well-defined film.

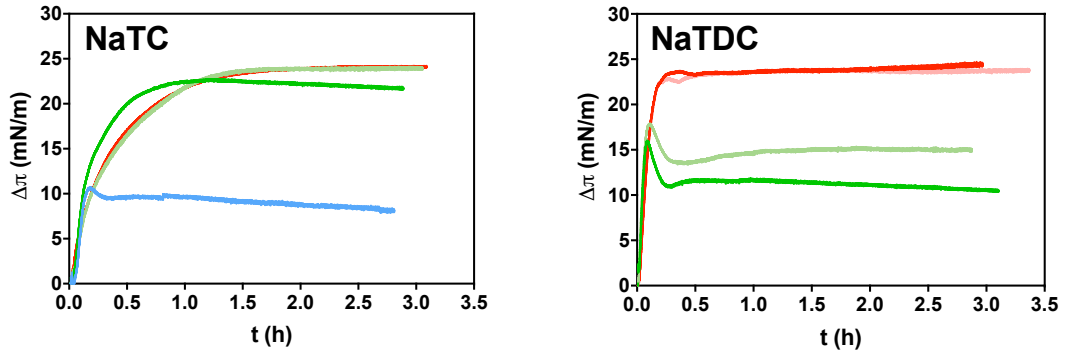


Figure S5: Time-dependent evolution of the surface pressure ($\Delta\pi(t) = \pi(t) - \pi_{\text{DPPC}}$) measured by a LT, upon injection of BS into the aqueous subphase: NaTC, NaTDC, at varying concentrations: (—) 0.5 mM, (—) 1 mM, (—) 5 mM, (—) 10 mM, (—) 20 mM (at $23 \pm 2^\circ\text{C}$). The lipids were spread onto water at $\pi_{\text{DPPC}} = 25 \pm 2 \text{ mN/m}$. Each experiment was reproduced twice, and the average measurement was selected for each BS at each concentration.

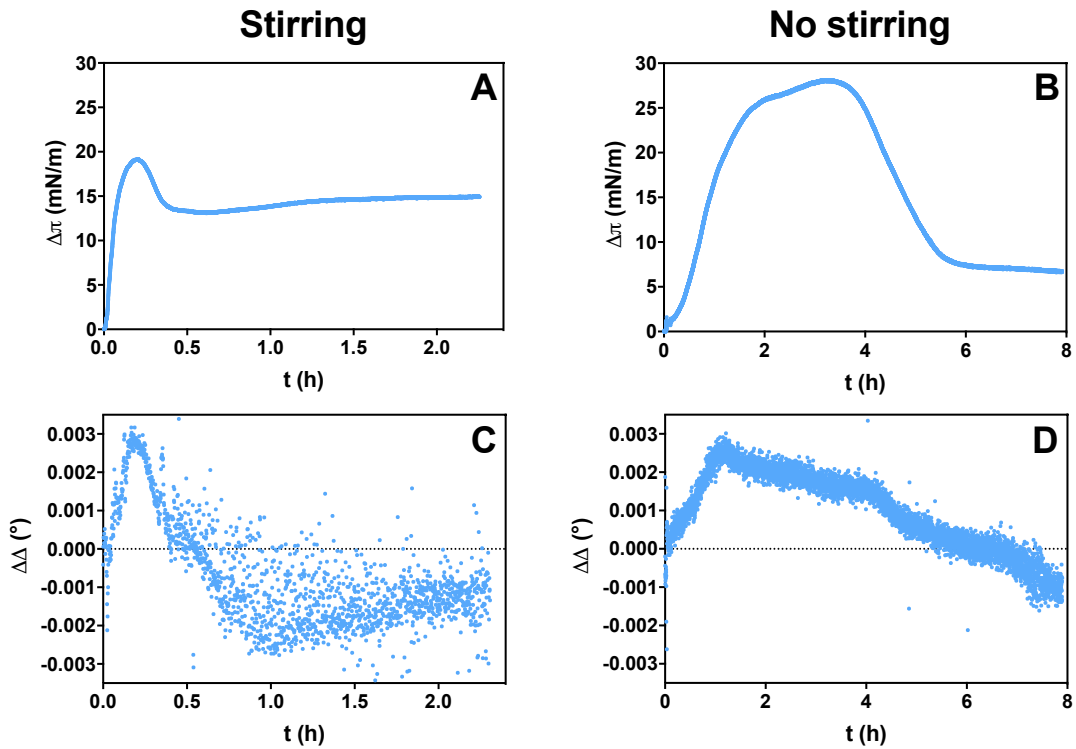
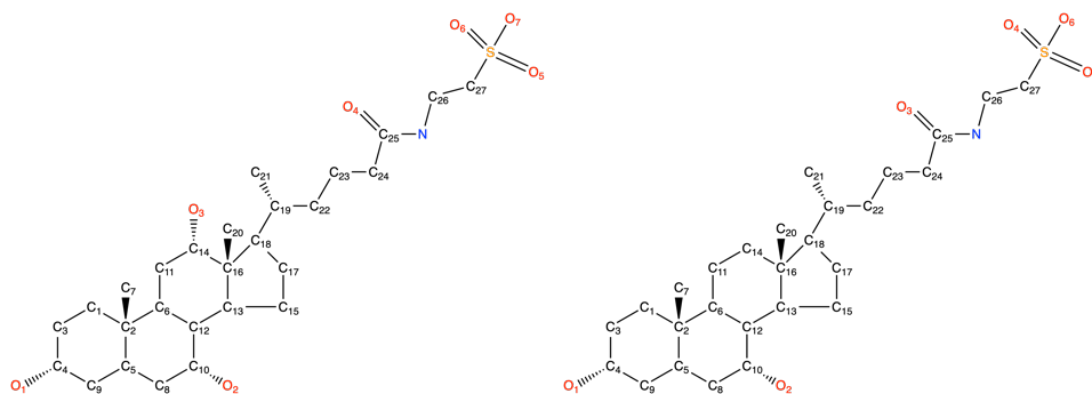
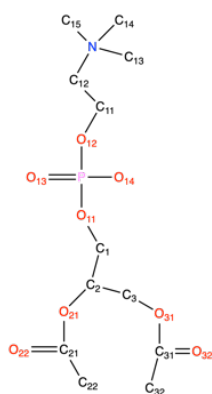


Figure S6: Time-dependent evolution of the surface pressure ($\Delta\pi(t) = \pi(t) - \pi_{\text{DPPC}}$) measured by a LT (A, B), and phase shift ($\Delta\Delta(t) = \Delta(t) - \Delta_{\text{DPPC}}$) measured by ellipsometry (C, D), upon addition of 10 mM NaTDC into the aqueous subphase, in the presence (A, C) and absence (B, D) of stirring (at $23 \pm 2^\circ\text{C}$). The lipids were spread onto water at $\pi_{\text{DPPC}} = 25 \pm 2 \text{ mN/m}$, reaching $\Delta_{\text{DPPC}} = 3.20^\circ$.



A. NaTC

B. NaTDC



C. DPPC

Figure S7: Definition of the atoms labels used in the interaction maps between molecules: A. NaTC, B. NaTDC, C. DPPC.

In order to characterise the interactions between the BS and DPPC monolayers, we have determined the interaction maps between the two molecules. In order to present these in a tractable manner, atom names were used in the manuscript for the heavy atoms in each BS and within the head group portion of the DPPC molecule. In Figure S7, we show the definition of these atom labels in terms of the chemical structure of each molecule.

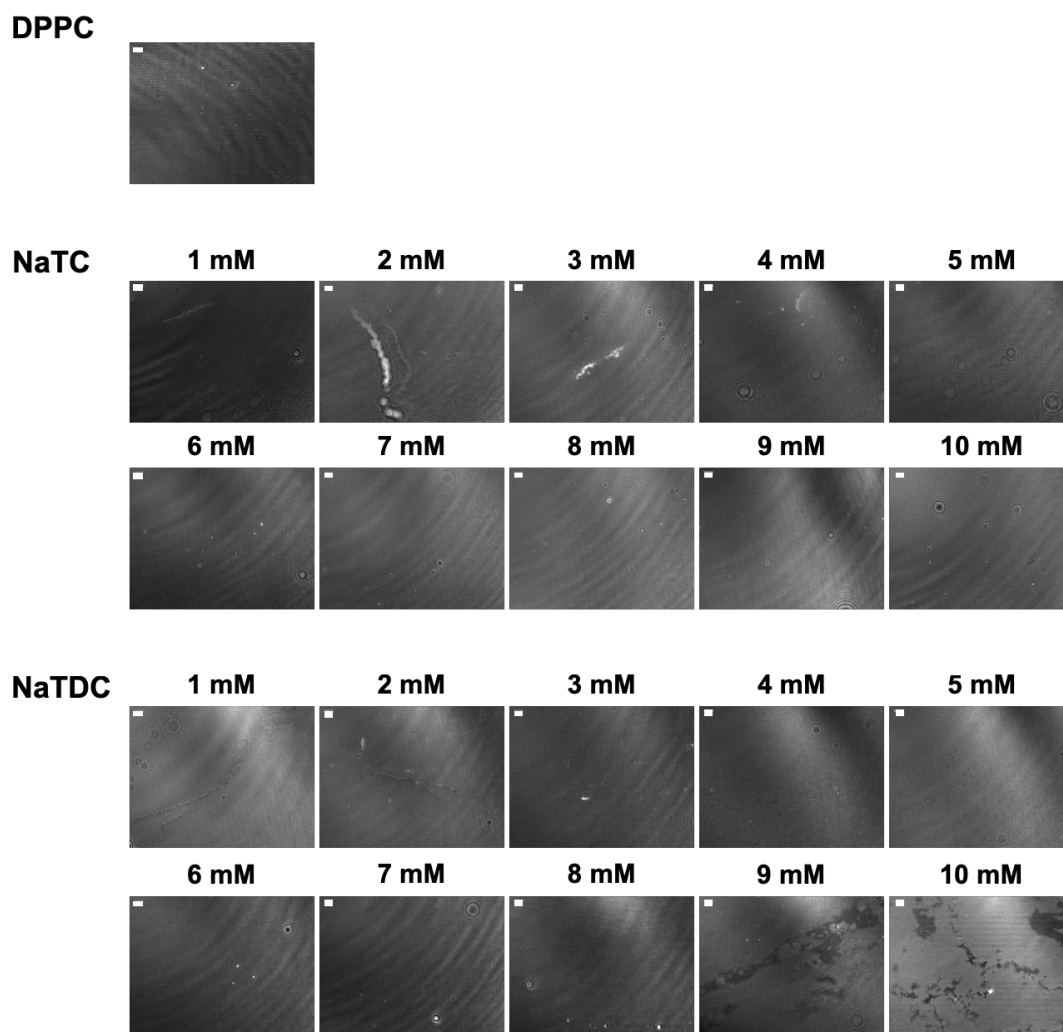


Figure S8: Evolution of the lipid monolayer organisation observed with a Brewster angle microscope, upon successive injections of BS into the aqueous subphase: NaTC, NaTDC (at $23 \pm 2^\circ\text{C}$). The lipids were spread onto water at $\pi_{\text{DPPC}} = 25 \pm 2 \text{ mN/m}$. The scale bar of the BAM images is $50 \mu\text{m}$. Stripes are caused by stirring-induced vibrations of the water subphase and (black or white) circular shapes are due to dust grains.

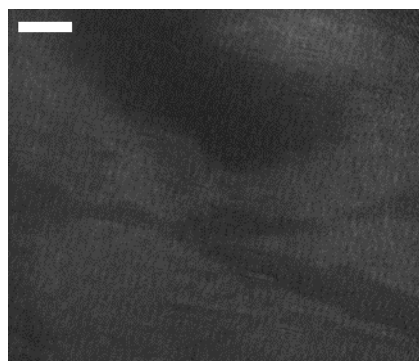


Figure S9: Evolution of the lipid monolayer organisation observed with a Brewster angle microscope, upon addition of 10 mM NaTDC into the aqueous subphase, under stirring (at $23 \pm 2^\circ\text{C}$). The lipids were spread onto water at $\pi_{\text{DPPC}} = 25 \pm 2 \text{ mN/m}$. The scale bar of the BAM images is $50 \mu\text{m}$.

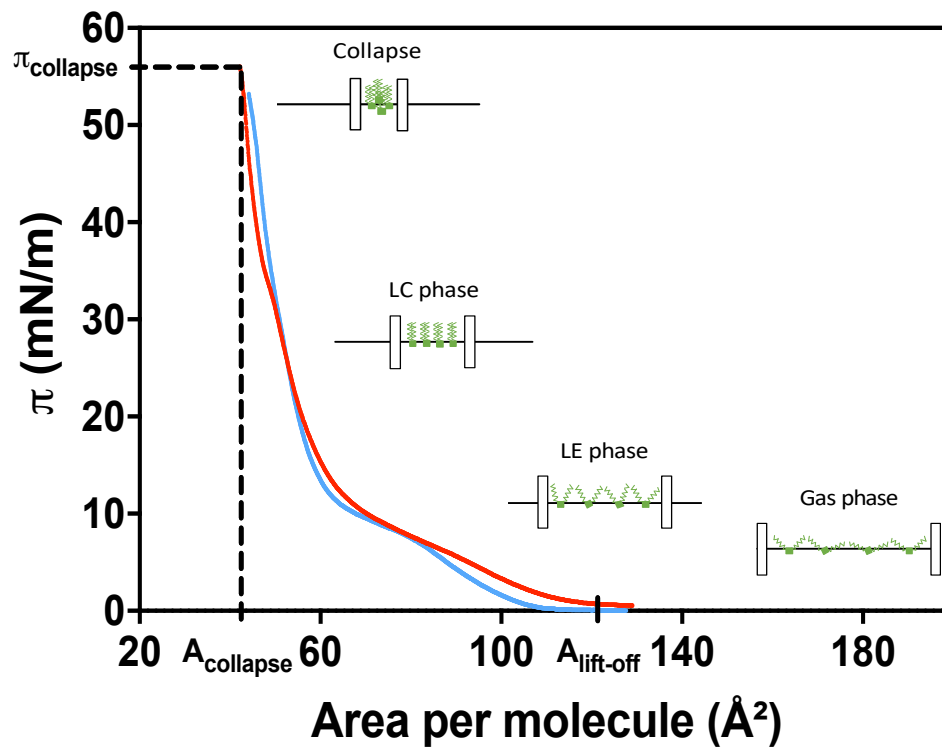


Figure S10: DPPC (—) and d_{75} -DPPC (—) $\pi - A$ Langmuir isotherms. The phospholipids were deposited onto ultrapure water, at a low concentration (gas phase), and compressed (at $23 \pm 2^\circ\text{C}$). $A_{\text{lift-off}}$ corresponds to the minimal surface density at which molecules start interacting and enter into the liquid-expanded (LE) state. Upon further compression, the sharper increase in surface pressure indicates the onset of a much more ordered and packed liquid-condensed (LC) monolayer. A_{collapse} and π_{collapse} are, respectively, the mean molecular area and surface pressure at which the film breaks. The different monolayer phases and related molecular organisations observed in the different regions of the isotherm are depicted in the figure.

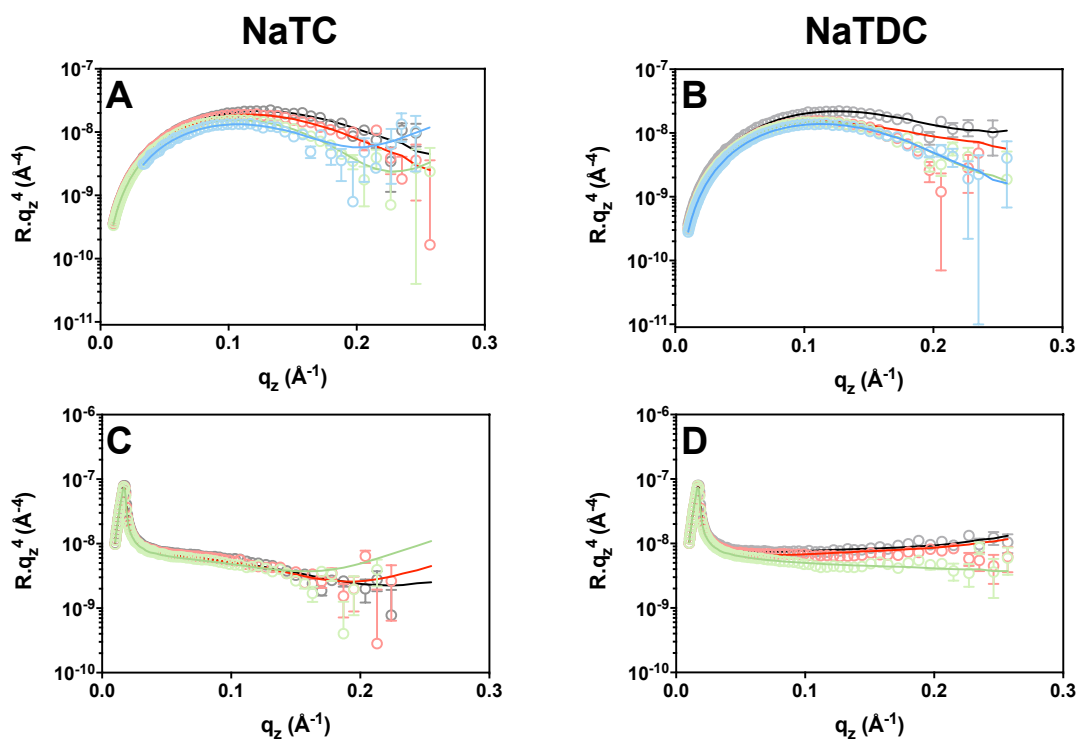


Figure S11: NR signal ($R \cdot q_z^4$ representation) of the lipid monolayer as a function of the scattering vector (q_z) and its evolution upon successive injections of either NaTC (A, C) or NaTDC (B, D) into the aqueous subphase (at $23 \pm 2^\circ\text{C}$). The lipids were spread onto water at $\pi_{\text{DPPC}} = 25 \pm 2$ mN/m, thus forming a pure monolayer (\circ). BS concentrations below (\circ 1 mM), around (\circ 5 mM), and above (\circ 10 mM) their CMC were selected because different interfacial behaviours were observed with the LT. These NR data were recorded using ACMW, on which a monolayer of d_{75} -DPPC was prepared (A, B), and D_2O , on which a monolayer of either DPPC, for NaTC (C), or d_{75} -DPPC, for NaTDC (D), was prepared.

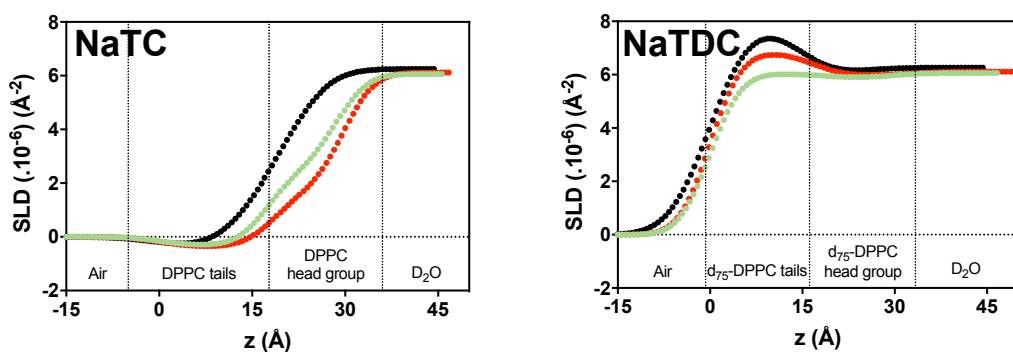


Figure S12: Evolution of the SLD profile of the interfacial film along the direction perpendicular to the surface (z) obtained from NR by successive injections of BS into the aqueous subphase: NaTC, NaTDC (at $23 \pm 2^\circ\text{C}$). The lipids were spread onto water at $\pi_{\text{DPPC}} = 25 \pm 2$ mN/m, thus forming a pure monolayer (\bullet). These measurements were only performed at BS concentrations below (\bullet 1 mM) and around (\bullet 5 mM) their CMC. These SLD profiles were recorded in D_2O (SLD of $6.33 \times 10^{-6} \text{ \AA}^{-2}$), on which a monolayer of either DPPC (SLD of $-0.41 \times 10^{-6} \text{ \AA}^{-2}$ for the tails and $1.75 \times 10^{-6} \text{ \AA}^{-2}$ for the head group), for NaTC (SLD of $0.95 \times 10^{-6} \text{ \AA}^{-2}$) (A), or d_{75} -DPPC (SLD of $7.66 \times 10^{-6} \text{ \AA}^{-2}$ for the tails and $5.68 \times 10^{-6} \text{ \AA}^{-2}$ for the head group), for NaTDC (SLD of $0.90 \times 10^{-6} \text{ \AA}^{-2}$) (B), was prepared.

NaTC		d ₇₅ -DPPC	[NaTC] (mM)			DPPC	[NaTC] (mM)	
			1	5	10		1	5
	σ (Å)	5	4	4	4	5	4	4
Tails	t (Å)	14	18	17	17	14	18	17
	SLD ($\times 10^6$) (Å ⁻²)	8.1	6.9	5.9	5.3	-0.4	-0.4	-0.3
	f_{water}	0	0	0	0	0	0	0
Head group	t (Å)	7	11	11	11	7	11	11
	SLD ($\times 10^6$) (Å ⁻²)	5.7	2.2	4.0	4.0	1.7	1.7	2.5
	f_{water}	0.1	0	0	0	0.1	0	0

NaTDC		d ₇₅ -DPPC	[NaTDC] (mM)		
			1	5	10
	σ (Å)	5	4	4	4
Tails	t (Å)	14	17	18	18
	SLD ($\times 10^6$) (Å ⁻²)	8.1	6.8	6.0	5.8
	f_{water}	0	0	0	0
Head group	t (Å)	7	16	11	11
	SLD ($\times 10^6$) (Å ⁻²)	5.7	5.7	5.7	2.3
	f_{water}	0.1	0.7	0.5	0

Table S2: Evolution of the NR parameters of each layer (tails and head group) of the lipid (either DPPC or d₇₅-DPPC) film: σ , the roughness, t , the thickness, SLD , the scattering length density and f_{water} , the amount of water, upon successive injections of 1, 5 and 10 mM BS into the aqueous subphase: NaTC, NaTDC.

Method of determination of the proportion of each component in each lipid film layer:

The proportion of each component (air, water, DPPC or BS) in each layer (lipid tails or head group) was determined using the following equation:

$$SLD_{layer} = \sum_i f_i \cdot SLD_i \quad (S1)$$

where i represents each component present in the corresponding layer, SLD_{layer} the SLD of the corresponding layer fitted by the software, f_i and SLD_i , respectively, the proportion and SLD of the component i in the corresponding layer.

In the case of our study, and based on our assumptions (i.e., only air goes into the tails region, only water and BS go into the head group region), the SLD of the tails and head group layers are described as follows:

$$SLD_{tails\ layer} = f_{air} \cdot SLD_{air} + f_{tails} \cdot SLD_{tails} = f_{tails} \cdot SLD_{tails}, \text{ given that } SLD_{air} = 0 \quad (S2)$$

$$SLD_{head\ group\ layer} = f_{water} \cdot SLD_{water} + f_{BS} \cdot SLD_{BS} + f_{head\ group} \cdot SLD_{head\ group} \quad (S3)$$

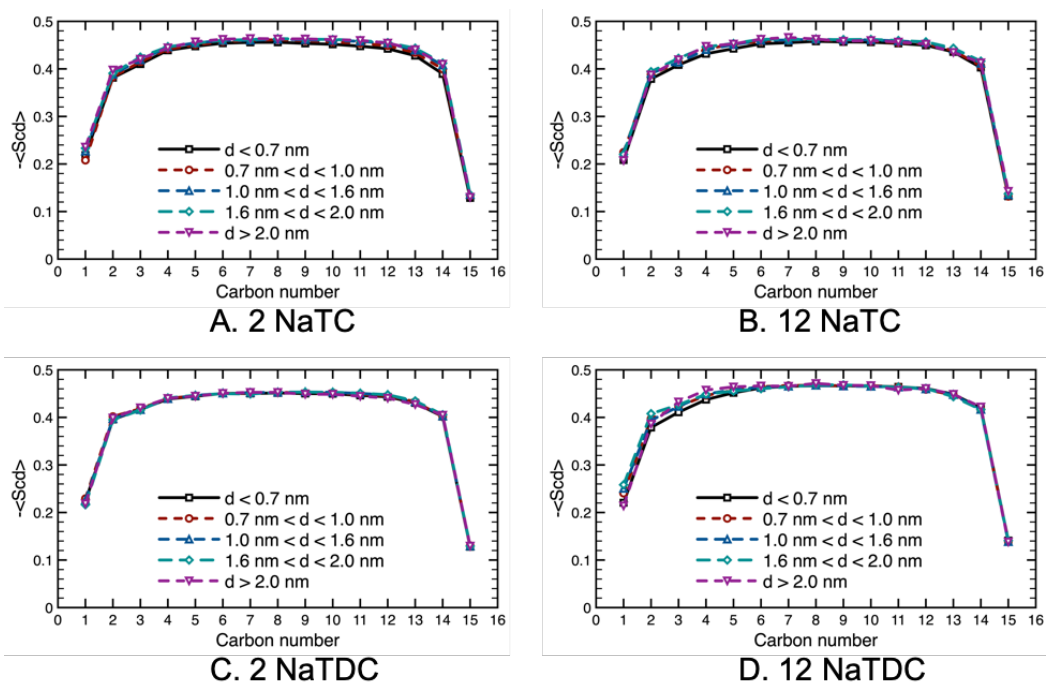


Figure S13: Average lipid order parameter of the *sn*-1 tail as a function of the depth in the DPPC monolayer, for different distances from a bound BS molecule in the presence of 2 (A, C) and 12 (B, D) molecules of BS: (A, B) NaTC, (C, D) NaTDC.

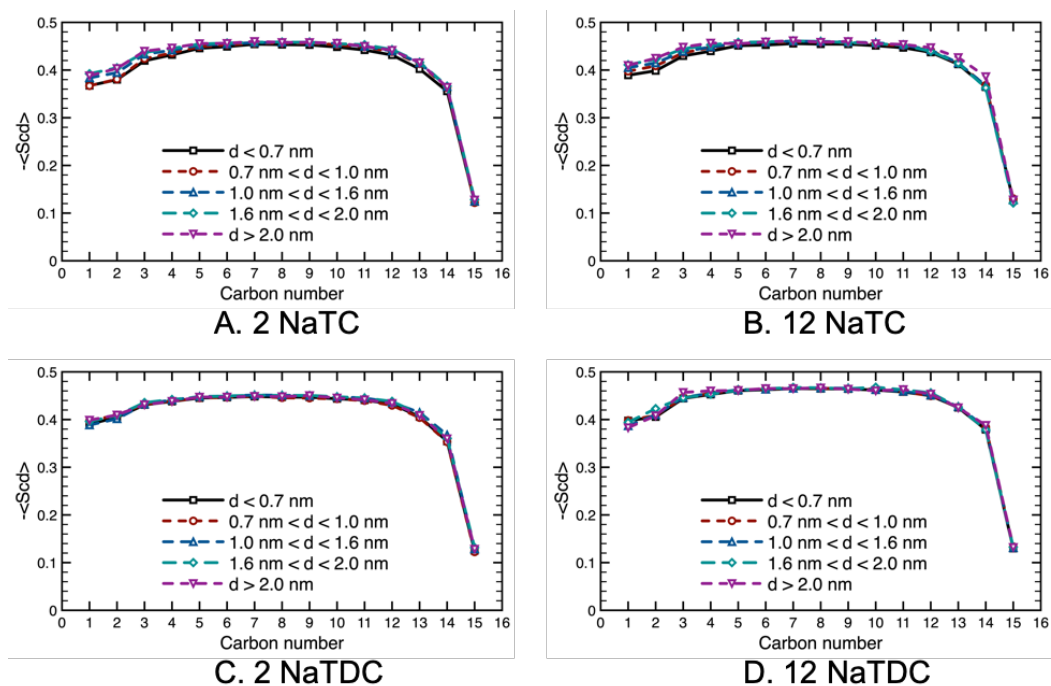


Figure S14: Average lipid order parameter of the *sn*-2 tail as a function of the depth in the DPPC monolayer, for different distances from a bound BS molecule in the presence of 2 (A, C) and 12 (B, D) molecules of BS: (A, B) NaTC, (C, D) NaTDC.

In each system, we have investigated the lipid order parameter of each lipid tail and then grouped them according to the distance that the lipid is from a bound BS molecule. We have plotted the lipid parameters as a function of the carbon number in the *sn*-1 (Figure S13) and *sn*-2 (Figure S14) tails in each system. As can be seen, there is very little effect on the order of the monolayers caused by the bound BS, independent of which type of BS is studied. If there is any difference at all, it is a very slight disordering of the lipid film near the ester group of the lipids (carbons 1 and 2) at small distances from the BS molecule.

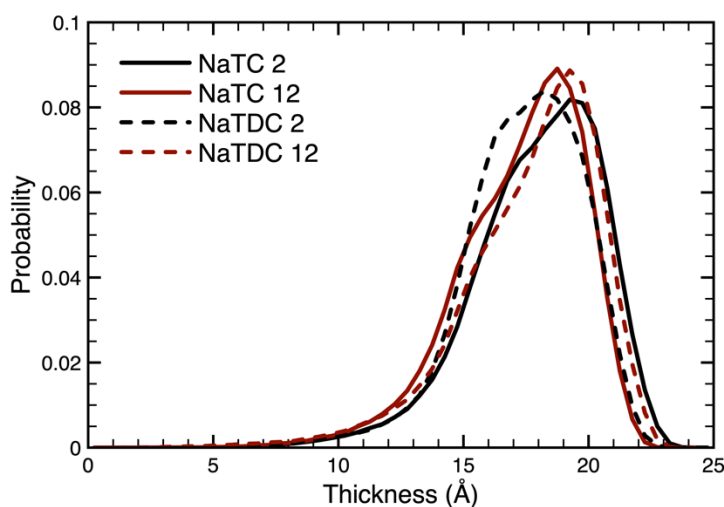


Figure S15: Distributions of the monolayer thickness for each of the four simulated systems: NaTC (—), NaTDC (---), with 2 (black) and 12 (red) BS.

We have also investigated the thickness of the monolayers in the systems we have simulated. Once again, we see very little difference in the thickness of the monolayers whether there are 2 or 12 BS molecules interacting with the monolayers (Figure S15).

References

- [1] World Health Organization, Obesity and Overweight, (2018). <http://www.who.int/mediacentre/factsheets/fs311/en/> (accessed August 21, 2018).
- [2] World Health Organization, Food & Agriculture Organization, Diet, Nutrition and the Prevention of Chronic Diseases, Geneva, 2003. http://apps.who.int/iris/bitstream/10665/42665/1/WHO_TRS_916.pdf?ua=1.
- [3] J. Mei, A. Lindqvist, L. Krabisch, J.F. Rehfeld, C. Erlanson-Albertsson, Appetite suppression through delayed fat digestion, *Physiol. Behav.* 89 (2006) 563–568. doi:10.1016/j.physbeh.2006.07.020.
- [4] M. Golding, T.J. Wooster, The influence of emulsion structure and stability on lipid digestion, *Curr. Opin. Colloid Interface Sci.* 15 (2010) 90–101. doi:10.1016/j.cocis.2009.11.006.
- [5] P.J. Wilde, B.S. Chu, Interfacial & colloidal aspects of lipid digestion, *Adv. Colloid Interface Sci.* 165 (2011) 14–22. doi:10.1016/j.cis.2011.02.004.
- [6] M. Armand, Lipases and lipolysis in the human digestive tract: where do we stand?, *Curr. Opin. Clin. Nutr. Metab. Care.* 10 (2007) 156–164. doi:10.1097/MCO.0b013e3280177687.
- [7] P. Reis, K. Holmberg, H. Watzke, M.E. Leser, R. Miller, Lipases at interfaces: a review, *Adv. Colloid Interface Sci.* 147–148 (2009) 237–250. doi:10.1016/j.cis.2008.06.001.
- [8] J.S. Patton, M.C. Carey, Watching fat digestion, *Science* (80-.). 204 (1979) 145–148. doi:10.1126/science.432636.
- [9] Y. Pafumi, D. Lairon, P. Lechene de la Porte, C. Juhel, J. Storch, M. Hamosh, M. Armand, Mechanisms of inhibition of triacylglycerol hydrolysis by human gastric lipase, *J. Biol. Chem.* 277 (2002) 28070–28079. doi:10.1074/jbc.M202839200.
- [10] A.F. Hofmann, K.J. Mysels, Bile salts as biological surfactants, *Colloids and Surfaces.* 30 (1987) 145–173. doi:10.1016/0166-6622(87)80207-X.
- [11] J. Maldonado-Valderrama, P. Wilde, A. Macierzanka, A. Mackie, The role of bile

- salts in digestion, *Adv. Colloid Interface Sci.* 165 (2011) 36–46. doi:10.1016/j.cis.2010.12.002.
- [12] L. Galantini, M.C. di Gregorio, M. Gubitosi, L. Travaglini, J. Vázquez Tato, A. Jover, F. Mejjide, V.H. Soto Tellini, N. V. Pavel, Bile salts and derivatives: rigid unconventional amphiphiles as dispersants, carriers and superstructure building blocks, *Curr. Opin. Colloid Interface Sci.* 20 (2015) 170–182. doi:10.1016/j.cocis.2015.08.004.
- [13] D. Madenci, S.U. Egelhaaf, Self-assembly in aqueous bile salt solutions, *Curr. Opin. Colloid Interface Sci.* 15 (2010) 109–115. doi:10.1016/j.cocis.2009.11.010.
- [14] B. Borgström, C. Erlanson-Albertsson, T. Wieloch, Pancreatic colipase: chemistry and physiology., *J. Lipid Res.* 20 (1979) 805–816. <http://www.ncbi.nlm.nih.gov/pubmed/385801>.
- [15] C. Erlanson-Albertsson, The interaction between pancreatic lipase and colipase: a protein-protein interaction regulated by a lipid, *FEBS Lett.* 162 (1983) 225–229. doi:10.1016/0014-5793(83)80760-1.
- [16] A. Bourbon Freie, F. Ferrato, F. Carrière, M.E. Lowe, Val-407 and Ile-408 in the $\beta 5'$ -loop of pancreatic lipase mediate lipase-colipase interactions in the presence of bile salt micelles, *J. Biol. Chem.* 281 (2006) 7793–7800. doi:10.1074/jbc.M512984200.
- [17] S. Labourdenne, O. Brass, M. Ivanova, A. Cagna, R. Verger, Effects of colipase and bile salts on the catalytic activity of human pancreatic lipase. A study using the oil drop tensiometer, *Biochemistry.* 36 (1997) 3423–3429. doi:10.1021/bi961331k.
- [18] J. Maldonado-Valderrama, J.L. Muros-Cobos, J.A. Holgado-Terriza, M.A. Cabrerizo-Vílchez, Bile salts at the air-water interface: adsorption and desorption, *Colloids Surfaces B Biointerfaces.* 120 (2014) 176–183. doi:10.1016/j.colsurfb.2014.05.014.
- [19] R. Parker, N.M. Rigby, M.J. Ridout, A.P. Gunning, P.J. Wilde, The adsorption–desorption behaviour and structure function relationships of bile salts, *Soft Matter.* 10 (2014) 6457–6466. doi:10.1039/c4sm01093k.
- [20] B.-S. Chu, A.P. Gunning, G.T. Rich, M.J. Ridout, R.M. Faulks, M.S.J. Wickham,

- V.J. Morris, P.J. Wilde, Adsorption of bile salts and pancreatic colipase and lipase onto digalactosyldiacylglycerol and dipalmitoylphosphatidylcholine monolayers, *Langmuir*. 26 (2010) 9782–9793. doi:10.1021/la1000446.
- [21] A. Bénarouche, L. Sams, C. Bourlieu, V. Vié, V. Point, J.F. Cavalier, F. Carrière, Studying gastric lipase adsorption onto phospholipid monolayers by surface tensiometry, ellipsometry, and atomic force microscopy, in: M.H. Gelb (Ed.), *Methods Enzymol. - Enzymol. Membr. Interface Interfacial Enzymol. Protein-Membrane Bind.*, 1st ed., Elsevier Inc., San Diego, 2017: pp. 255–278. doi:10.1016/bs.mie.2016.09.039.
- [22] J. Maldonado-Valderrama, N.C. Woodward, A.P. Gunning, M.J. Ridout, F.A. Husband, A.R. Mackie, V.J. Morris, P.J. Wilde, Interfacial characterization of β -lactoglobulin networks: displacement by bile salts, *Langmuir*. 24 (2008) 6759–6767. doi:10.1021/la800551u.
- [23] H. Singh, A. Ye, D. Horne, Structuring food emulsions in the gastrointestinal tract to modify lipid digestion, *Prog. Lipid Res.* 48 (2009) 92–100. doi:10.1016/j.plipres.2008.12.001.
- [24] D.G. Dalgleish, Food emulsions - their structures and structure-forming properties, *Food Hydrocoll.* 20 (2006) 415–422. doi:10.1016/j.foodhyd.2005.10.009.
- [25] H. Motschmann, R. Teppner, Ellipsometry in interface science, in: D. Möbius, R. Miller (Eds.), *Stud. Interface Sci. - Nov. Methods to Study Interfacial Layers*, 1st ed., Elsevier Science B. V., Amsterdam, 2001: pp. 1–42.
- [26] Y. Gerelli, Aurore: new software for neutron reflectivity data analysis, *J. Appl. Crystallogr.* 49 (2016) 330–339. doi:10.1107/S1600576716000108.
- [27] R.A. Campbell, H.P. Wacklin, I. Sutton, R. Cubitt, G. Fragneto, FIGARO: the new horizontal neutron reflectometer at the ILL, *Eur. Phys. J. Plus.* 126 (2011) 1–22. doi:10.1140/epjp/i2011-11107-8.
- [28] Institut Laue-Langevin, The COSMOS software application available for the ILL reflectometers, (2018). <https://www.ill.eu/fr/users-en/instruments/instruments-list/d17/more/cosmos/> (accessed August 23, 2018).
- [29] R.A. Campbell, Y. Saaka, Y. Shao, Y. Gerelli, R. Cubitt, E. Nazaruk, D.

- Matyszewska, M.J. Lawrence, Structure of surfactant and phospholipid monolayers at the air/water interface modeled from neutron reflectivity data, *J. Colloid Interface Sci.* 531 (2018) 98–108. doi:10.1016/j.jcis.2018.07.022.
- [30] S. Jo, T. Kim, V.G. Iyer, W. Im, CHARMM-GUI: a web-based graphical user interface for CHARMM, *J. Comput. Chem.* 29 (2008) 1859–1865. doi:10.1002/jcc.20945.
- [31] E.L. Wu, X. Cheng, S. Jo, H. Rui, K.C. Song, E.M. Dávila-Contreras, Y. Qi, J. Lee, V. Monje-Galvan, R.M. Venable, J.B. Klauda, W. Im, CHARMM-GUI Membrane Builder toward realistic biological membrane simulations, *J. Comput. Chem.* 35 (2014) 1997–2004. doi:10.1002/jcc.23702.
- [32] J. Lee, X. Cheng, J.M. Swails, M.S. Yeom, P.K. Eastman, J.A. Lemkul, S. Wei, J. Buckner, J.C. Jeong, Y. Qi, S. Jo, V.S. Pande, D.A. Case, C.L. Brooks III, A.D. MacKerell Jr., J.B. Klauda, W. Im, CHARMM-GUI input generator for NAMD, GROMACS, AMBER, OpenMM, and CHARMM/OpenMM simulations using the CHARMM36 additive force field, *J. Chem. Theory Comput.* 12 (2016) 405–413. doi:10.1021/acs.jctc.5b00935.
- [33] T. Schneider, E. Stoll, Molecular-dynamics study of a three-dimensional one-component model for distortive phase transitions, *Phys. Rev. B.* 17 (1978) 1302–1322. doi:10.1103/PhysRevB.17.1302.
- [34] W.G. Hoover, Canonical dynamics: equilibrium phase-space distributions, *Phys. Rev. A.* 31 (1985) 1695–1697. doi:10.1103/PhysRevA.31.1695.
- [35] S. Plimpton, Fast parallel algorithms for short-range molecular dynamics, *J. Comput. Phys.* 117 (1995) 1–19. doi:10.1006/jcph.1995.1039.
- [36] K. Vanommeslaeghe, E. Hatcher, C. Acharya, S. Kundu, S. Zhong, J. Shim, E. Darian, O. Guvench, P. Lopes, I. Vorobyov, A.D. MacKerell, Jr., CHARMM general force field: a force field for drug-like molecules compatible with the CHARMM all-atom additive biological force fields, *J. Comput. Chem.* 31 (2010) 671–690. doi:10.1002/jcc.21367.
- [37] J.B. Klauda, R.M. Venable, J.A. Freites, J.W. O'Connor, D.J. Tobias, C. Mondragon-Ramirez, I. Vorobyov, A.D. MacKerell, Jr., R.W. Pastor, Update of the CHARMM all-atom additive force field for lipids: validation on six lipid types, *J. Phys. Chem. B.* 114 (2010) 7830–7843. doi:10.1021/jp101759q.

- [38] R.W. Pastor, A.D. MacKerell, Jr., Development of the CHARMM force field for lipids, *J. Phys. Chem. Lett.* 2 (2011) 1526–1532. doi:10.1021/jz200167q.
- [39] W.L. Jorgensen, J. Chandrasekhar, J.D. Madura, R.W. Impey, M.L. Klein, Comparison of simple potential functions for simulating liquid water, *J. Chem. Phys.* 79 (1983) 926–935. doi:10.1063/1.445869.
- [40] W.E. Reiher, *Theoretical studies of hydrogen bonding*, Harvard University, 1985.
- [41] T. Darden, D. York, L. Pedersen, Particle mesh Ewald: an N·log(N) method for Ewald sums in large systems, *J. Chem. Phys.* 98 (1993) 10089–10092. doi:10.1063/1.464397.
- [42] J.-P. Ryckaert, G. Ciccotti, H.J.. Berendsen, Numerical integration of the cartesian equations of motion of a system with constraints: molecular dynamics of n-alkanes, *J. Comput. Phys.* 23 (1977) 327–341. doi:10.1016/0021-9991(77)90098-5.
- [43] K. Matsuoka, M. Maeda, Y. Moroi, Micelle formation of sodium glyco- and taurocholates and sodium glyco- and taurodeoxycholates and solubilization of cholesterol into their micelles, *Colloids Surfaces B Biointerfaces.* 32 (2003) 87–95. doi:10.1016/S0927-7765(03)00148-6.
- [44] K. Sabatini, J.-P. Mattila, P.K.J. Kinnunen, Interfacial behavior of cholesterol, ergosterol, and lanosterol in mixtures with DPPC and DMPC, *Biophys. J.* 95 (2008) 2340–2355. doi:10.1529/biophysj.108.132076.
- [45] V. Rondelli, G. Fragneto, S. Motta, E. Del Favero, L. Cantù, Reflectivity from floating bilayers: can we keep the structural asymmetry?, *J. Phys. Conf. Ser.* 340 (2012) 1–10. doi:10.1088/1742-6596/340/1/012083.
- [46] A. Tiss, S. Ransac, H. Lengsfeld, P. Hadvary, A. Cagna, R. Verger, Surface behaviour of bile salts and tetrahydrolipstatin at air/water and oil/water interfaces, *Chem. Phys. Lipids.* 111 (2001) 73–85. doi:10.1016/S0009-3084(01)00149-9.
- [47] N. Matubayasi, M. Kanzaki, S. Sugiyama, A. Matuzawa, Thermodynamic study of gaseous adsorbed films of sodium taurocholate at the air/water interface, *Langmuir.* 12 (1996) 1860–1862. doi:10.1021/la950832o.
- [48] N. Matubayasi, S. Sugiyama, M. Kanzaki, A. Matuzawa, Thermodynamic

- studies of the adsorbed films and micelles of sodium taurodeoxycholate, *J. Colloid Interface Sci.* 196 (1997) 123–127. doi:10.1006/jcis.1997.5213.
- [49] D.E. Graham, M.C. Phillips, Proteins at liquid interfaces. III. Molecular structures of adsorbed films, *J. Colloid Interface Sci.* 70 (1979) 427–439. doi:10.1016/0021-9797(79)90050-X.
- [50] V.M. Bolanos-Garcia, A. Renault, S. Beaufils, Surface rheology and adsorption kinetics reveal the relative amphiphilicity, interfacial activity, and stability of human exchangeable apolipoproteins, *Biophys. J.* 94 (2008) 1735–1745. doi:10.1529/biophysj.107.115220.
- [51] D.J.F. Taylor, R.K. Thomas, J.D. Hines, K. Humphreys, J. Penfold, The adsorption of oppositely charged polyelectrolyte/surfactant mixtures at the air/water interface: neutron reflection from dodecyl trimethylammonium bromide/sodium poly(styrene sulfonate) and sodium dodecyl sulfate/poly(vinyl pyridinium chloride), *Langmuir.* 18 (2002) 9783–9791. doi:10.1021/la020503d.
- [52] M.J. Armstrong, M.C. Carey, The hydrophobic-hydrophilic balance of bile salts. Inverse correlation between reverse-phase high performance liquid chromatographic mobilities and micellar cholesterol-solubilizing capacities., *J. Lipid Res.* 23 (1982) 70–80. <http://www.ncbi.nlm.nih.gov/pubmed/7057113>.

Chapter 2

Bile salts behaviour at the oil/water
interface: molecular insight into lipid
digestion

Co-worker contribution to the chapter

Florian Alexis (M. Eng. student, Ecole Nationale Supérieure de Chimie de Lille, France) carried out the pendant drop measurements, under my supervision.

Abstract

Hypotheses. Bile salts (BS), present in the small intestine, carry out two different and vital functionalities in the process of lipid digestion and absorption: they facilitate the adsorption of digestive enzymes onto the surface of fat droplets and displace lipolysis products from the lipid/water interface, for transportation towards the gut mucosa. BS contrasting roles are thought to be due to differences in interfacial properties, hypothetically attributed to slight variations in bile acid portion. Two BS, sodium taurocholate (NaTC) and sodium taurodeoxycholate (NaTDC), which differ by the presence of an additional hydroxyl group on NaTC steroid backbone, were selected and their properties at the physiologically relevant oil/water interface compared.

Experiments. BS adsorption dynamics at the surface of a lipid droplet were investigated using the pendant drop technique. Changes in interfacial structure were characterised with a first-of-its-kind neutron reflectometry (NR) measurement at the oil/water interface, in the absence and presence of a phospholipid monolayer at the interface, employing a liquid/liquid setup applied for the first time to a biologically relevant system.

Findings. Our results demonstrate that NaTDC is more efficient at stabilising the bare oil/water interface than NaTC and highlight different interfacial behaviours for NaTC and NaTDC in the presence of a phospholipid interfacial film. These preliminary results pave the way for the use of NR measurements enabling the spatio-temporal resolution of relevant interfaces and bringing new insights in the food colloid area.

1. Introduction

Recent investigations carried out on a hydrophobic surface [1], as well as studies at the air/water interface, either bare [2,3] (Chapter 1), or with a deposited lipid monolayer [3] (Chapter 1), have demonstrated that slight structural differences in BS bile acid moiety (more specifically, the number and position of hydroxyl groups) may be at the origin of their distinct functions in fat digestion. Our results of the very first measurement on a lipid/air interface with neutron reflectometry (NR) [3] (Chapter 1), in particular, have revealed that cholate-based BS have a higher affinity for this interface and may therefore help enzyme adsorption, whereas deoxycholate derivatives are more likely to desorb lipid molecules from the interface, through dynamic exchange, and may thus be involved in the removal of lipolysis products from the interface, *via* their solubilisation into mixed micelles.

Nevertheless, very few experiments [4–6] have been carried out at the more physiologically relevant oil/water interface – which is a better mimic of the fat droplet/water interface that would be present in the gut, either stabilised with food emulsifiers or with endogenous surfactants – and there is, to date, no structural characterisation of this interface at the molecular level. The main reason behind this knowledge gap lays in the restricted number of techniques that are able to provide information at relevant length scales on this interface. Following our preliminary study at the bare and lipid-stabilised air/water interfaces [3] (Chapter 1), the objective of the work presented here is to bring new understanding on the interfacial phenomena underlying fat digestion, by examining the oil/water interface in the presence of BS molecules, using a combination of techniques, including the very powerful NR technique.

NR is a tool of choice to explore interfaces and describe molecular ordering and morphology at the nanometre scale. Nevertheless, resolving the structure of liquid/liquid interfaces, such as oil/water, with NR is quite challenging because of the neutron beam being drastically attenuated by its passage through either the organic or aqueous phase. This attenuation problem can be slightly reduced by using heavy water (D₂O) instead of H₂O as incoming medium for the neutron beam, or highly reduced by replacing the organic oil with a fluorinated one and using it as incoming

medium [7]. This second option was not suitable for our experiments since it would have affected the oil properties and made the oil/water interface irrelevant to food science. Few techniques and setups, all presenting both advantages and drawbacks, have been reported over the past years to perform NR measurements at the oil/water interface: condensation of a micrometre-thick volatile oil film onto an aqueous subphase surface [8–10]; entrapment of a thin, uniform oil layer between a hydrophobically-modified silicon substrate and a bulk aqueous subphase, using the spin-freeze-thaw approach [11]; spreading of a thin aqueous film onto a highly hydrophilic quartz block, subsequently placed in contact with a denser oil subphase [12]; deposition of an oil phase on top of a hydrophilic sapphire substrate-containing aqueous subphase [13,14]; spreading of an oil phase onto an aqueous subphase, using a quartz cell [15]. As part of the work presented here, NR experiments were carried out using the liquid/liquid cell developed very recently by Scoppola [15]. To the best of our knowledge, this is the first time that this liquid/liquid setup has been applied to a food colloid system, mimicking in particular the fat droplet/water surface of an emulsion. While this work is quite explorative and still early work, it provides evidence of the feasibility of the study as well as some early analysis, which opens the way to more work in the food colloid area.

In this study, we investigated the behaviour of BS at the oil/water interface, in the absence and presence of a lipid monolayer (1,2-dipalmitoyl-*sn*-glycero-3-phosphocholine, DPPC) (Figure 1), representative of food emulsion droplets surfaces, which are often stabilised by phospholipids [4,16–20] (either found in the gut as endogenous lipids secreted in the gastrointestinal tract [21,22], or as emulsifying agents present in foodstuffs [23,24]). Two BS, sodium taurocholate (NaTC) and sodium taurodeoxycholate (NaTDC) (Figure 2), were employed as their distinct bile acid structures (NaTC has an additional hydroxyl group) are hypothesised to explain their different interfacial properties and therefore the different roles they exhibit during lipolysis [1,3] (Chapter 1). Using tricaprylin as the oil phase (Figure 3), we monitored BS adsorption dynamics at this physiologically relevant interface with the pendant drop technique and characterised their impact on the interface morphology with NR. This study not only provides further insights into the different functionalities

of BS during lipolysis, but also paves the way for the implementation of biologically relevant experiments with the NR technique.

2. Experimental section

2.1. Materials

DPPC (Figure 1) was provided by Avanti Polar Lipids, Inc. (Alabaster, AL, USA), Hellmanex III by Hellma (Paris, France), and chloroform (CHCl_3) by Fisher Scientific (Loughborough, UK). NaTC (P97.0% TLC) (Figure 2A), NaTDC (P95.0% TLC) (Figure 2B), tricaprylin (C8:0 TAG, P99.0%) (Figure 3), octadecyltrichlorosilane (OTS, P90.0%), hexadecane (P99.0%) and ethanol (EtOH, P99.8% GC) were all purchased from Sigma-Aldrich (Gillingham, UK). Deuterium oxide (D_2O , P99.9%), bought from Euriso-top SAS (St. Aubin, France), was used in all experiments. All reagents were used as supplied.

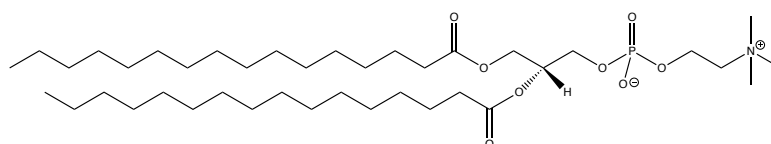


Figure 1: Structure of DPPC

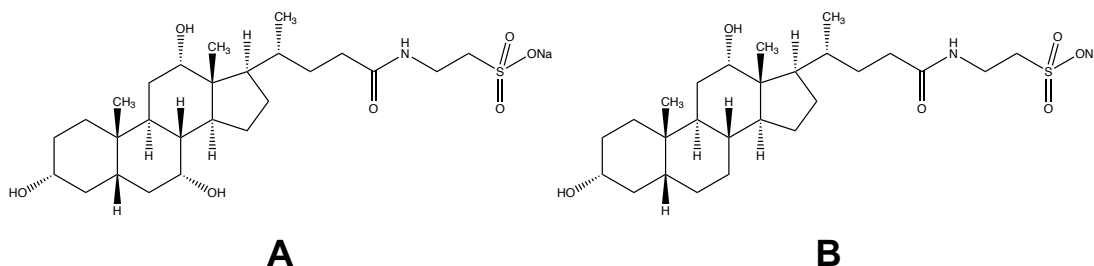


Figure 2: Structures of NaTC (A) and NaTDC (B)

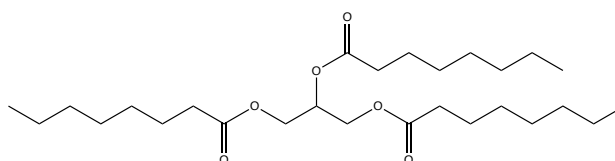


Figure 3: Structure of tricaprylin

2.2. Methods

2.2.1. Interfacial tension measurements: the pendant drop technique

Interfacial tension measurements were performed in a high-precision optical glass cuvette (5 mL volume of aqueous phase) to study BS interfacial adsorption at the bare oil/water interface. All experiments were carried out at a temperature of $23 \pm 2^\circ\text{C}$

(room temperature). Prior to any measurement, the cuvette was thoroughly cleaned with Hellmanex III, water, EtOH and CHCl₃, successively, to remove organic impurities, then dried with nitrogen gas, and finally filled with a BS-containing aqueous phase. Because of the low density of tricaprylin (used as the oil phase), the BS solutions used were prepared in D₂O instead of H₂O in order to minimize the droplet size. The surface tension of the covered surface (γ) was measured by forming a rising (or inverted pendant) tricaprylin drop in a BS-containing aqueous phase, with a 0.72-mm-outer diameter J-shaped needle, and fitting its shape to the Young-Laplace equation with the Drop Shape Analysis 10 software of the pendant drop instrument (EasyDrop Standard, KRÜSS GmbH, Hamburg, Germany). Interfacial tension (γ) was recorded over time, until it reached a plateau. Each experiment was repeated at least three times; either a representative curve or an average measurement is shown.

2.2.2. Neutron reflectometry (NR)

NR measurements were performed using the unique “reflection down” option available on FIGARO, the ILL time-of-flight neutron reflectometer [25]. This instrument uses an incoming polychromatic neutron beam with wavelengths (λ) ranging from 2 to 20 Å, with a 7% $\Delta\lambda/\lambda$ resolution. In order to cover values of the scattering vector perpendicular to the surface (q_z , with $q_z = \frac{4\pi}{\lambda} \sin \vartheta_i$) ranging from 0.009 to 0.1 Å⁻¹, two different incident angles (ϑ_i), $\theta_1 = 0.626^\circ$ and $\theta_2 = 1.397^\circ$, were used. Reflectivity (R), which is the ratio between the reflected and incident intensities, was measured as a function of q_z in this range.

The quartz liquid/liquid cell (22.75 cm² surface area and 65 mL volume of subphase) developed by Scoppola [15] was employed in these experiments; the cell is made up of two adjacent compartments, the lower part being used for the aqueous phase and the upper one for the organic phase (Figure 4). Prior to any measurement, the cell was treated by UV/Ozone to remove organic impurities, and the edges separating the two compartments were hydrophobically coated with OTS (prepared in hexadecane at a concentration of 1 mM) (1-hour treatment) to “pin” the interface to this section and thus have an almost flat oil/water interface (the meniscus, very pronounced

without coating, was reduced to its minimum). Having a non-curved interface is paramount for the reflection to be the same in every different part of the interface. Finally, hexadecane and EtOH were sequentially spread onto the edges for cleaning (10-minute treatment each), before drying the cell under nitrogen.

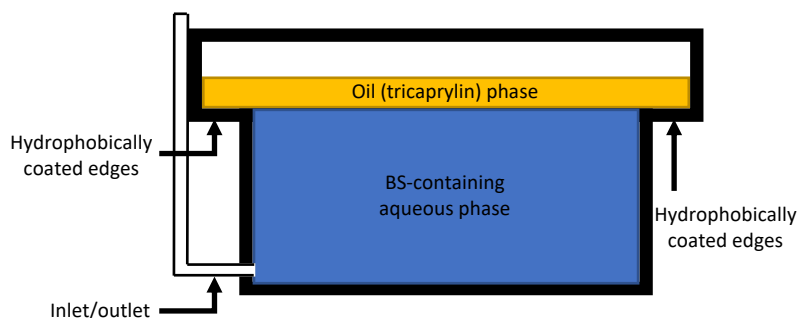


Figure 4: Quartz liquid/liquid cell employed for the NR experiments at the oil/water interface. Prior to pouring the aqueous and organic phases into the cell, the edges separating the two compartments were hydrophobically coated with OTS, to prevent the aqueous phase from covering these parts and thereby have a flatter (i.e., less curved) interface. Tricaprylin (used as the oil phase) was spread onto a pure 10 mM BS solution prepared in degassed D₂O (used as the aqueous phase), either directly or after deposition of a phospholipid (DPPC) monolayer at the air/water interface. Neutrons went through the aqueous phase and were reflected downwards. The presence of an inlet/outlet allows adjustment of the water level and thereby reduction of the oil/water interface curvature, which is paramount for NR measurements.

10 mM of pure BS solution prepared in degassed D₂O were poured into the cell, prior to spreading tricaprylin (the oil phase) onto the aqueous phase either directly, or after deposition of a 1 mg/mL phospholipid (DPPC) monolayer (5 μ L) at the air/water interface. This BS concentration was selected as being representative of physiological conditions, and this amount of DPPC was used to form a homogeneous film onto the aqueous subphase.

Because of the technical limitations imposed by the liquid/liquid NR setup, the contrast-variation method could not be applied in this case. A single contrast configuration, namely, pure D₂O as aqueous phase, hydrogenated tricaprylin as oil phase and non-labelled DPPC as lipid monolayer, was used; in this way, the attenuation of the incoming and reflected neutron beams, set up to cross the aqueous phase, was reduced, although still important. Because of the scattering length density (SLD) values characterising the sample components (Table 1), compositional changes were difficult to be monitored, while changes in thickness or width of the interface could be qualitatively assessed.

Table 1: Calculated *SLD* of each component

Component		SLD ($\cdot 10^{-6}$) (\AA^{-2})
Oil phase	Tricaprylin	0.33
Aqueous phase	D ₂ O	6.33
DPPC	h ₆₂ -tails	-0.41
	h ₁₈ -head group	1.75
BS	NaTC	0.95
	NaTDC	0.90

To perform qualitative analysis, bi-dimensional raw data were compared to the corresponding mono-dimensional reflectivity curves $R(q_z)$ obtained using the COSMOS software application available for the ILL reflectometers [26]. Quantitative data analysis (i.e., data fitting), which would allow quantifying the amount of material (i.e., lipid, BS and water) adsorbed at the interface, is still ongoing.

3. Results

3.1. BS interfacial properties

3.1.1. BS adsorption/desorption dynamics at the oil/water interface

The capacity of NaTC and NaTDC to adsorb at the oil/water interface was assessed using the pendant drop technique, by monitoring the time-dependent evolution of the interfacial tension (γ) of a tricaprylin (oil) drop formed in aqueous solutions containing different amounts of BS (1, 5, 10 and 100 mM) (Figures 5 and 6). These BS concentrations were selected to cover a wide range of concentrations around the critical micellar concentration (CMC): below, around, above, and well above the CMC, which is 4 – 7 mM for NaTC (gradual micellisation process) and 2 mM for NaTDC (Figure 5 of Chapter 3) [27]. The effect of salt on BS adsorption behaviour was also assessed, using 0.15 M NaCl at one BS concentration (10 mM). The interfacial tension value displayed by the bare oil/water (i.e., tricaprylin/D₂O) interface is 28 ± 0.3 mN/m; this value is consistent with those reported in the literature [28,29].

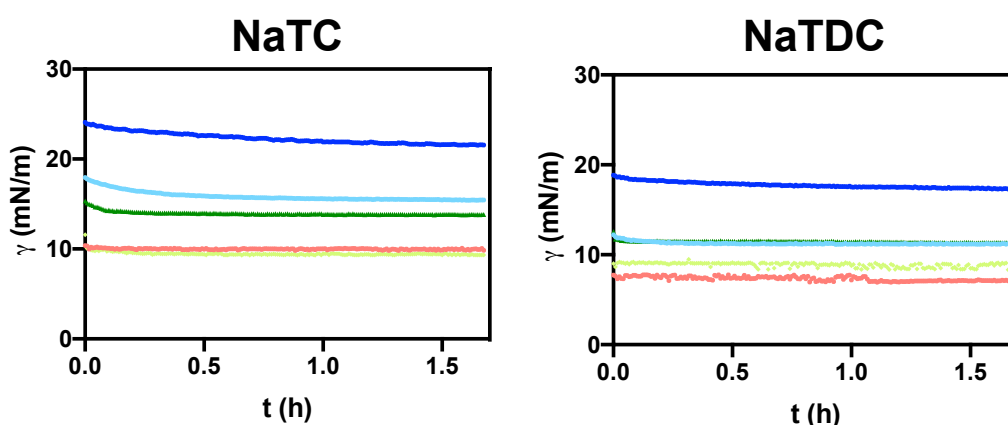


Figure 5: Time-dependent evolution of the interfacial tension (γ) measured with the pendant drop technique, upon formation of a tricaprylin oil drop in an aqueous phase containing different concentrations: (—) 1 mM, (—) 5 mM, (—) 10 mM, (—) 10 mM, of BS: NaTC, NaTDC (at $23 \pm 2^\circ\text{C}$). The effect of salt on BS behaviour at the oil/water interface was also studied by adding 0.15 M NaCl to a 10 mM BS aqueous solution: (—) 10 mM of BS with salt. Each experiment was reproduced at least three times, and a representative measurement was selected for each BS at each concentration.

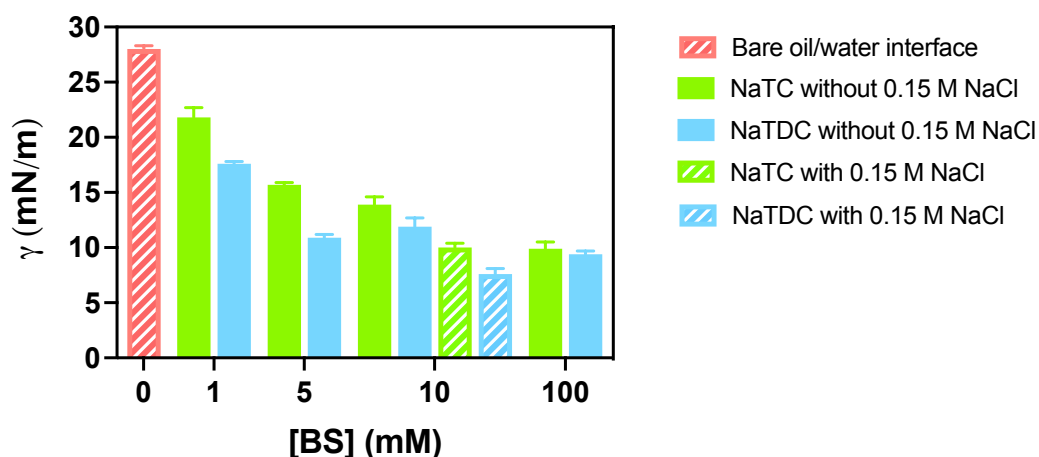


Figure 6: Evolution of the interfacial tension (γ) as a function of BS concentration, measured with the pendant drop technique, upon formation of a tricaprylin oil drop in an aqueous phase containing different concentrations (1, 5, 10 and 100 mM) of BS (NaTC, NaTDC) (at $23 \pm 2^\circ\text{C}$). The interfacial tension obtained in the presence of 0.15 M NaCl with 10 mM BS is also shown, as well as that displayed by the bare oil/water (i.e., tricaprylin/ D_2O) interface. The interfacial tension values shown here correspond to the values obtained after 1 hour of equilibration. These data were extracted from BS adsorption measurements (Figure 5). Each experiment was reproduced at least three times, and the average measurement was selected for each BS at each concentration.

Independently of the type of BS and concentration, the interfacial tension decreases directly after formation of the tricaprylin (oil) drop in the BS-containing aqueous phase, and then progressively stabilises at an equilibrium value – more rapidly at higher BS concentrations (Figure 5). The interfacial tension values reached at equilibrium are summarised in Figure 6. At 1, 5 and 10 mM, lower surface tensions are reached with NaTDC ($\gamma = 18 \pm 0.2$ mN/m at 1 mM; $\gamma = 11 \pm 0.3$ mN/m at 5 mM; $\gamma = 12 \pm 1$ mN/m at 10 mM), compared with NaTC ($\gamma = 22 \pm 1$ mN/m at 1 mM; $\gamma = 16 \pm 0.2$ mN/m at 5 mM; $\gamma = 14 \pm 1$ mN/m at 10 mM); however, at 100 mM – a concentration well above both BS CMC and where, therefore, an excess of BS micelles is present in the bulk –, the two BS attain very similar interfacial tension values ($\gamma = 10 \pm 1$ and 9 ± 0.3 mN/m for NaTC and NaTDC, respectively). NaTC induces a gradual decrease in surface tension with increasing concentration. Instead, NaTDC causes a reduction from 1 to 5 mM, beyond which the surface tension remains relatively constant around an average value up to 100 mM. These distinct patterns can be related to the difference in BS micellisation processes: indeed, at 5, 10 and 100 mM (which are all above the CMC of NaTDC (2 mM)), NaTDC presents a similar state of aggregation, which may thus lead to similar adsorption behaviour. The additional

decrease in interfacial tension values well above NaTC CMC (100 mM) has already been observed elsewhere [5] and reveals the adsorption of further BS molecules even well after the onset of formation of micelles in the bulk.

The addition of 0.15 M NaCl to each BS aqueous solution induces a marked decrease in interfacial tension, with the lowest value being reached by NaTDC (from $\gamma = 12 \pm 1$ mN/m without salt, to $\gamma = 8 \pm 0.5$ mN/m with salt), as compared to NaTC (from $\gamma = 14 \pm 1$ mN/m without salt, to $\gamma = 10 \pm 0.4$ mN/m with salt); this more efficient adsorption of BS molecules at the bare oil/water interface in the presence of salt can be attributed to the screening of the repulsive interactions occurring between BS molecules, therefore facilitating the formation of a denser layer at the interface. These results are consistent with surface tension values at the oil/water interface reported elsewhere [4,5].

3.1.2. BS interaction with a DPPC monolayer at the oil/water interface: interfacial morphology of BS/lipid films

The changes in interfacial structure induced by BS were then investigated with NR, using 10 mM BS only – a concentration mimicking fed state conditions –, in the absence and presence of a phospholipid (DPPC) monolayer at the oil/water interface (Figures 7 and 8).

Prior to performing NR experiments with the liquid/liquid setup [15], an attempt was made using the spin-freeze-thaw method [11], which consists in (i) spreading a thin layer of oil onto a hydrophobically-spin coated silicon (or sapphire) block, (ii) freezing the oil, and (iii) placing the oil-coated substrate in contact with a bulk aqueous phase, thus allowing oil thawing. The advantage of this setup is the reduction in transmitted signal loss, due to the neutron beam passing through a silicon (or sapphire) block and thin deuterated oil film, which both have a high transmission coefficient. However, in this study, the oil coating was found to be unstable because of the too low hydrophobicity of the oil used (tricaprylin), thereby preventing this setup from being employed.

The main drawback of the liquid/liquid experiments with NR is the signal-to-noise ratio, due to the neutron beam having to go through a strongly attenuating

liquid phase (transmission for neutrons with 4 Å wavelength is around 50% for 5 cm of D₂O, while it is basically 0% for hydrogenated oil or H₂O). The use of the liquid/liquid cell was possible because of FIGARO's high flux and unique "reflection down" option, which allows the neutrons to cross the deuterated aqueous subphase and, consequently, the beam to not be excessively attenuated.

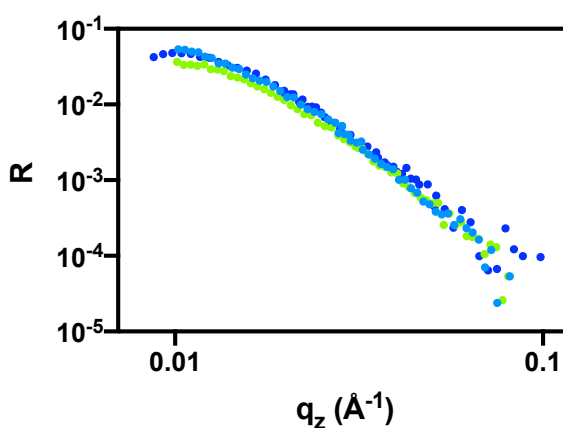


Figure 7: NR signal of the oil/water (tricaprylin/D₂O) interface as a function of the scattering vector (q_z), in the presence of a phospholipid monolayer at the interface and either NaTC (●) or NaTDC (●) in the aqueous subphase (at $21 \pm 1^\circ\text{C}$). In the absence of a lipid interfacial film, a NR signal could be recorded only with NaTDC (●), the interface in the presence of NaTC alone being too diffuse to be resolved. 10 mM of BS were used in this study to mimic physiological conditions.

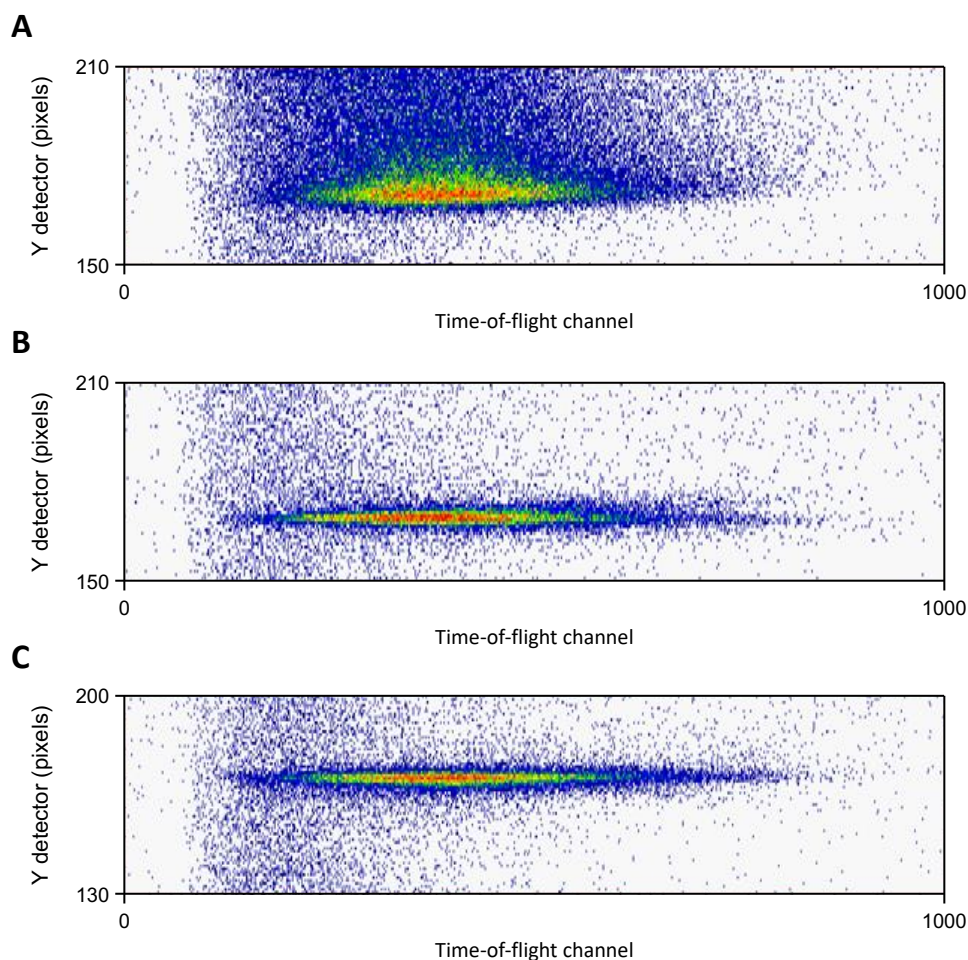


Figure 8: Bi-dimensional (time-of-flight) image of the detector obtained at the low- q_z configuration, representing the projection of the width of the oil/water (tricaprylin/ D_2O) interface in the horizontal plane, in the absence (A) and presence (B, C) of a phospholipid monolayer at the interface, with either (A, C) NaTDC or (B) NaTC in the aqueous subphase (at $21 \pm 1^\circ\text{C}$). In the absence of lipid stabiliser, the interface in the presence of NaTC was too diffuse to be resolved. The colours are related to the intensity of the reflected beam at different wavelengths (represented here by the time-of-flight channel, x-axis). For a similar interfacial width (i.e., spread of the reflection along the y-axis), differences in intensity can be related to the amount of hydrogenated material adsorbed at the interface, the red showing a much denser interface compared to the blue.

Preliminary analysis demonstrated that, in the absence of a stabiliser, the bare oil/water interface was too diffuse to be resolved (probably because of the too high hydrophilicity of the oil used, tricaprylin) (data not shown). The deposition of a phospholipid (DPPC) monolayer at the air/water interface, prior to spreading the oil on top of the water surface, was nonetheless found to notably enhance the reflectivity signal, as can be seen in the bi-dimensional detector images reported (Figures 8B and 8C). While the bare oil/water interface in the presence of NaTDC in

the aqueous subphase was found to be diffuse, but sufficiently defined to be measured (Figure 8A), the interface with NaTC was too diffuse (i.e., not stabilised enough) to be measured (data cannot be shown because the interface could not be found with the neutron beam). Several attempts to improve the oil/water interface stabilisation in the presence of NaTC were carried out: while the use of a higher amount of BS (20 mM, instead of 10 mM) and the addition of salt (0.15 M NaCl) were unsuccessful, the deposition of a DPPC monolayer at the air/water interface, before spreading tricaprylin (the oil phase) onto the aqueous subphase, allowed the stabilisation of the oil/water interface, thereby making it visible to neutrons in the presence of both BS (Figures 8B and 8C). Nevertheless, the presence of BS was seen to result in a broader interface, as compared to the bare lipid-stabilised oil/water interface (data not shown). The reflectivity signals obtained with NaTDC in both the presence and absence of a phospholipid film at the oil/water interface were found to be relatively similar (Figure 7), while the corresponding bi-dimensional detector images show that the interface is much broader in the absence of lipids (Figures 8A and 8C), which indicates the better stabilisation of the interface with the lipid monolayer. The comparison of the results obtained with NaTC and NaTDC, in the presence of a lipid film at the interface, shows that NaTC gives a lower reflectivity signal at low- q_z (or along the time-of-flight channel) and a similar intensity at high- q_z (Figure 7). By evaluating bi-dimensional images, the broadness of the interface was found to be slightly larger in the case of NaTC (Figure 8B), as compared to NaTDC (Figure 8C). No conclusion can be drawn yet from the $R(q_z)$ curves. This qualitative data analysis is currently being complemented with data fitting to quantify the amount of materials (including lipids, BS and water) adsorbed at the interface. It is worth noticing that a larger q_z -range could not be covered because of the decay of the signal-to-noise ratio; this limited the maximum structural resolution achievable, which was not sufficient to resolve the structure of the film forming at the interface. In addition, the difference in the low- q_z region between NaTC and NaTDC is at the moment difficult to interpret.

4. Discussion

The objective of the work presented in this short chapter was to study and compare the interfacial properties of two BS to understand the impact of their molecular structure on the specific roles they play in lipolysis. For this purpose, their adsorption at an oil/water interface, in the absence and presence of a phospholipid monolayer – further stabilising the interface and mimicking the physiological components present at the interface of fat droplets –, was characterised. The two BS used in this project, which differ in the structure of their bile acid moiety (NaTC has an additional hydroxyl group (Figure 2)), were selected based on previously reported distinct adsorption/desorption dynamics at interfaces [1,3] (Chapter 1).

The study of BS properties at the oil/water interface reveals a very rapid, and concentration-dependent kinetics of adsorption (Figure 5), which has already been observed at both the air/water [2–4,16] (Chapter 1) and oil/water [4,5] interfaces. As already suggested for their behaviour at the air/water interface [3,6,30,31] (Chapter 1), these adsorption dynamics can be explained by their flat conformation, allowing them to occupy a large surface area. Interfacial tension measurements also show different extents of adsorption for the two BS, with NaTDC exhibiting lower interfacial tensions and thereby a higher affinity for the interface, which correlates with its higher hydrophobicity [32] (Figure 6). This better ability of NaTDC to stabilise the oil/water interface was also visible in the NR experiments: in the absence of a stabiliser, in this case DPPC, NaTDC induced a well-defined (and therefore measurable) oil/water interface (Figure 8A), while the interface in the presence of NaTC was too diffuse to be measured. The addition of a phospholipid monolayer at the oil/water interface improved the interface stabilisation for both BS, therefore making the measurement possible with both BS (Figures 8B and 8C). However, in the presence of both BS in the aqueous subphase, the bi-dimensional detector signal of the lipid-stabilised interface was found to be broader, as compared to the bare interface, which demonstrates that BS may create some interfacial disorder (data not shown); such a disorganisation may be due to either the adsorption of BS molecules at the lipid/water interface, or the removal of lipid molecules from the interface by BS. Additionally, bi-dimensional raw data showed a broader signal for NaTC (Figure

8B), as compared with NaTDC (Figure 8C); this result – although difficult to interpret qualitatively – clearly demonstrates a difference in terms of interfacial behaviour between the two structurally distinct BS, which is consistent with our findings at the air/water interface [3] (Chapter 1) and supports our working hypothesis that NaTC may facilitate pancreatic lipase/co-lipase adsorption at the fat droplet interface, whereas NaTDC may be more likely to be involved in lipolysis products displacement from the interface. All these observations and suggestions remain, however, qualitative, and will need to be confirmed by quantitative data analysis.

5. Conclusion

In this work, we evaluated the adsorption/desorption behaviour of two structurally distinct BS, NaTC and NaTDC, at the physiologically relevant oil/water interface, in the absence and presence of a phospholipid monolayer, in order to further understand the origin of their contrasting functionalities during lipolysis.

Preliminary qualitative data analysis revealed that NaTDC – the more hydrophobic BS – has a better stabilising capacity at the bare oil/water interface than NaTC, and that the two BS exhibit different behaviours in the presence of a lipid film at the oil/water interface. These results thereby suggest that BS morphological richness – which has been vastly neglected until now – is key to explaining the different roles they play in the process of lipolysis.

As far as we know, this is the first-ever study that has investigated the behaviour of BS at the physiologically relevant phospholipid-stabilised oil/water interface, at the nanometre scale; this promising NR experiment at the oil/water interface has been made possible thanks to the newly developed NR liquid/liquid setup, which has been used for the first time to mimic a food-related system, more precisely the fat droplet/water interface of ingested lipids. The analysis of the NR data presented in this chapter is ongoing and will provide a molecular-level description of the oil/water interface in the presence of BS. Future work will also involve performing enzymatic absorption studies with both the pH-stat method (which allows the monitoring of free fatty acid release) and NR.

References

- [1] R. Parker, N.M. Rigby, M.J. Ridout, A.P. Gunning, P.J. Wilde, The adsorption–desorption behaviour and structure function relationships of bile salts, *Soft Matter*. 10 (2014) 6457–6466. doi:10.1039/c4sm01093k.
- [2] J. Maldonado-Valderrama, J.L. Muros-Cobos, J.A. Holgado-Terriza, M.A. Cabrerizo-Vílchez, Bile salts at the air-water interface: adsorption and desorption, *Colloids Surfaces B Biointerfaces*. 120 (2014) 176–183. doi:10.1016/j.colsurfb.2014.05.014.
- [3] O. Pabois, C.D. Lorenz, R.D. Harvey, I. Grillo, M.M.-L. Grundy, P.J. Wilde, Y. Gerelli, C.A. Dreiss, Molecular insights into the behaviour of bile salts at interfaces: a key to their role in lipid digestion, *J. Colloid Interface Sci.* 556 (2019) 266–277. doi:10.1016/j.jcis.2019.08.010.
- [4] J. Maldonado-Valderrama, N.C. Woodward, A.P. Gunning, M.J. Ridout, F.A. Husband, A.R. Mackie, V.J. Morris, P.J. Wilde, Interfacial characterization of β -Lactoglobulin networks: displacement by bile salts, *Langmuir*. 24 (2008) 6759–6767. doi:10.1021/la800551u.
- [5] A. Torcello-Gómez, A.B. Jódar-Reyes, J. Maldonado-Valderrama, A. Martín-Rodríguez, Effect of emulsifier type against the action of bile salts at oil–water interfaces, *Food Res. Int.* 48 (2012) 140–147. doi:10.1016/j.foodres.2012.03.007.
- [6] A. Tiss, S. Ransac, H. Lengsfeld, P. Hadvàry, A. Cagna, R. Verger, Surface behaviour of bile salts and tetrahydrolipstatin at air/water and oil/water interfaces, *Chem. Phys. Lipids*. 111 (2001) 73–85. doi:10.1016/S0009-3084(01)00149-9.
- [7] E. Scoppola, S. Micciulla, L. Kuhrts, A. Maestro, R.A. Campbell, O. V. Konovalov, G. Fragneto, E. Schneck, Reflectometry reveals accumulation of surfactant impurities at bare oil/water interfaces, *Molecules*. 24 (2019) 4113–4129. doi:10.3390/molecules24224113.

- [8] L.T. Lee, D. Langevin, B. Farnoux, Neutron reflectivity of an oil-water interface, *Phys. Rev. Lett.* 67 (1991) 2678–2681. doi:10.1103/PhysRevLett.67.2678.
- [9] T. Cosgrove, J.S. Phipps, R.M. Richardson, Neutron reflection from a liquid/liquid interface, *Colloids and Surfaces.* 62 (1992) 199–206. doi:10.1016/0166-6622(92)80002-J.
- [10] J.S. Phipps, R.M. Richardson, T. Cosgrove, A. Eaglesham, Neutron reflection studies of copolymers at the hexane/water interface, *Langmuir.* 9 (1993) 3530–3537. doi:10.1021/la00036a031.
- [11] A. Zarbakhsh, J. Bowers, J.R.P. Webster, A new approach for measuring neutron reflection from a liquid/liquid interface, *Meas. Sci. Technol.* 10 (1999) 738–743. doi:10.1088/0957-0233/10/8/309.
- [12] J. Strutwolf, A.L. Barker, M. Gonsalves, D.J. Caruana, P.R. Unwin, D.E. Williams, J.R.P. Webster, Probing liquid/liquid interfaces using neutron reflection measurements and scanning electrochemical microscopy, *J. Electroanal. Chem.* 483 (2000) 163–173. doi:10.1016/S0022-0728(00)00027-9.
- [13] L. Besnard, M. Protat, F. Malloggi, J. Daillant, F. Cousin, N. Pantoustier, P. Guenoun, P. Perrin, Breaking of the Bancroft rule for multiple emulsions stabilized by a single stimuable polymer, *Soft Matter.* 10 (2014) 7073–7087. doi:10.1039/C4SM00596A.
- [14] M. Protat, N. Bodin-Thomazo, F. Malloggi, J. Daillant, R.A. Campbell, G. Fragneto, E.B. Watkins, P. Perrin, N. Pantoustier, P. Guenoun, Neutron reflectivity measurements at the oil/water interface for the study of stimuli-responsive emulsions, *Eur. Phys. J. E.* 41 (2018) 85. doi:10.1140/epje/i2018-11693-8.
- [15] E. Scoppola, Solvent extraction: a study of the liquid/liquid interface with ligands combining X-ray and neutron reflectivity measurements, Université de Montpellier, 2015. <https://tel.archives-ouvertes.fr/tel-02049227>.

- [16] J. Maldonado-Valderrama, P. Wilde, A. Macierzanka, A. Mackie, The role of bile salts in digestion, *Adv. Colloid Interface Sci.* 165 (2011) 36–46. doi:10.1016/j.cis.2010.12.002.
- [17] B.-S. Chu, A.P. Gunning, G.T. Rich, M.J. Ridout, R.M. Faulks, M.S.J. Wickham, V.J. Morris, P.J. Wilde, Adsorption of bile salts and pancreatic colipase and lipase onto digalactosyldiacylglycerol and dipalmitoylphosphatidylcholine monolayers, *Langmuir*. 26 (2010) 9782–9793. doi:10.1021/la1000446.
- [18] A. Bénarouche, L. Sams, C. Bourlieu, V. Vié, V. Point, J.F. Cavalier, F. Carrière, Studying gastric lipase adsorption onto phospholipid monolayers by surface tensiometry, ellipsometry, and atomic force microscopy, in: M.H. Gelb (Ed.), *Methods Enzymol. - Enzymol. Membr. Interface Interfacial Enzymol. Protein-Membrane Bind.*, 1st ed., Elsevier Inc., San Diego, 2017: pp. 255–278. doi:10.1016/bs.mie.2016.09.039.
- [19] P.J. Wilde, B.S. Chu, Interfacial & colloidal aspects of lipid digestion, *Adv. Colloid Interface Sci.* 165 (2011) 14–22. doi:10.1016/j.cis.2011.02.004.
- [20] Y. Pafumi, D. Lairon, P. Lechene de la Porte, C. Juhel, J. Storch, M. Hamosh, M. Armand, Mechanisms of inhibition of triacylglycerol hydrolysis by human gastric lipase, *J. Biol. Chem.* 277 (2002) 28070–28079. doi:10.1074/jbc.M202839200.
- [21] M. Golding, T.J. Wooster, The influence of emulsion structure and stability on lipid digestion, *Curr. Opin. Colloid Interface Sci.* 15 (2010) 90–101. doi:10.1016/j.cocis.2009.11.006.
- [22] A.F. Hofmann, K.J. Mysels, Bile salts as biological surfactants, *Colloids and Surfaces*. 30 (1987) 145–173. doi:10.1016/0166-6622(87)80207-X.
- [23] H. Singh, A. Ye, D. Horne, Structuring food emulsions in the gastrointestinal tract to modify lipid digestion, *Prog. Lipid Res.* 48 (2009) 92–100. doi:10.1016/j.plipres.2008.12.001.

- [24] D.G. Dalgleish, Food emulsions - their structures and structure-forming properties, *Food Hydrocoll.* 20 (2006) 415–422. doi:10.1016/j.foodhyd.2005.10.009.
- [25] R.A. Campbell, H.P. Wacklin, I. Sutton, R. Cubitt, G. Fragneto, FIGARO: the new horizontal neutron reflectometer at the ILL, *Eur. Phys. J. Plus.* 126 (2011) 1–22. doi:10.1140/epjp/i2011-11107-8.
- [26] Institut Laue-Langevin, The COSMOS software application available for the ILL reflectometers, (2018). <https://www.ill.eu/fr/users-en/instruments/instruments-list/d17/more/cosmos/> (accessed August 23, 2018).
- [27] K. Matsuoka, M. Maeda, Y. Moroi, Micelle formation of sodium glyco- and taurocholates and sodium glyco- and taurodeoxycholates and solubilization of cholesterol into their micelles, *Colloids Surfaces B Biointerfaces.* 32 (2003) 87–95. doi:10.1016/S0927-7765(03)00148-6.
- [28] E.N. Jaynes, M.A. Flood, Protein films at oil-water interfaces: interfacial tension measurements by the static drop method, *J. Dispers. Sci. Technol.* 6 (1985) 55–68. doi:10.1080/01932698508943933.
- [29] M.S. Manga, T.N. Hunter, O.J. Cayre, D.W. York, M.D. Reichert, S.L. Anna, L.M. Walker, R.A. Williams, S.R. Biggs, Measurements of submicron particle adsorption and particle film elasticity at oil–water interfaces, *Langmuir.* 32 (2016) 4125–4133. doi:10.1021/acs.langmuir.5b04586.
- [30] N. Matubayasi, M. Kanzaki, S. Sugiyama, A. Matuzawa, Thermodynamic study of gaseous adsorbed films of sodium taurocholate at the air/water interface, *Langmuir.* 12 (1996) 1860–1862. doi:10.1021/la950832o.
- [31] N. Matubayasi, S. Sugiyama, M. Kanzaki, A. Matuzawa, Thermodynamic studies of the adsorbed films and micelles of sodium taurodeoxycholate, *J. Colloid Interface Sci.* 196 (1997) 123–127. doi:10.1006/jcis.1997.5213.

- [32] M.J. Armstrong, M.C. Carey, The hydrophobic-hydrophilic balance of bile salts. Inverse correlation between reverse-phase high performance liquid chromatographic mobilities and micellar cholesterol-solubilizing capacities., *J. Lipid Res.* 23 (1982) 70–80. <http://www.ncbi.nlm.nih.gov/pubmed/7057113>.

Chapter 3

Aggregates of bile salts, mixed micelles
with fatty acids and monoacylglycerols,
and interaction with liposomes

Co-workers contribution to the chapter

Dr Christian D. Lorenz (Department of Physics, King's College London, UK) carried out the molecular dynamics simulations.

Dr Michael Sztucki (European Synchrotron Radiation Facility, France), Dr Sylvain Prévost and Nico Carl (Institut Laue-Langevin, France) performed the small-angle X-ray scattering measurements.

Abstract

Hypotheses. Bile salts (BS) are biosurfactants released into the small intestine, which play key roles in lipid digestion and absorption; specifically, they promote the adsorption of enzymes onto fat droplets, and the removal and shuttling of lipolysis products. Slight variations in their structure are hypothesised to explain their different aggregation behaviour and therefore underlie their contrasting functionalities in lipid digestion.

Experiments. The micellisation of two BS, sodium taurocholate (NaTC) and sodium taurodeoxycholate (NaTDC), which differ by one hydroxyl group on their steroid skeleton, was assessed by fluorescence spectroscopy, using pyrene as a probe, and the micellar structure (i.e., size and shape) of aggregates formed in the absence and presence of the products of lipolysis – fatty acids and monoacylglycerols – was resolved by combining small-angle X-ray/neutron scattering (SAXS, SANS) with molecular dynamics simulations. Triacylglycerol-incorporating liposomes – mimicking ingested lipids – were formulated, and their structure analysed with neutron reflectometry and SANS, prior to assessing BS ability to solubilise them into mixed aggregates, with SANS.

Findings. Our results demonstrate that BS micelles exhibit an ellipsoidal shape, comprising a hydrophobic core and a more hydrophilic shell, with NaTDC forming more spherical aggregates with higher aggregation numbers ($N_{\text{agg}} = 7 - 11$), and aggregating at a lower critical micelle concentration (CMC = 2 mM), than NaTC ($N_{\text{agg}} = 2 - 4$; CMC = 4 – 7 mM). Similar observations are made for BS mixed micelles. Structural studies with liposomes show that the addition of BS induces their disruption into mixed micelles, with NaTDC exhibiting a higher solubilising capacity than NaTC.

1. Introduction

The interfacial studies carried out both at the air/water (Chapter 1) [1] and oil/water (Chapter 2) interfaces, in the absence and presence of a phospholipid monolayer, suggest that the distinct roles performed by bile salts (BS) during lipolysis arise from their architectural diversity, in particular the very minor variations (i.e., the position and number of hydroxyl groups) on their bile acid portion [1,2]. Characterising BS behaviour in solution and the impact of their molecular structure is therefore key to establishing the source of BS different functionalities in the gut.

BS are unconventional surface-active materials made up of a short and flexible ionic chain linked to a rigid and slightly curved steroid skeleton (the hydrophobic “tail”) (with a concave/convex structure), which contains weakly separated hydrophilic (hydroxyl groups) and hydrophobic (methyl groups) faces [3]. This unusual planar polarity enables them to self-assemble in solution in the form of micelles, whose mechanism of formation and structure are, to date, still under debate, despite extensive investigations [4,5]. Two models, both involving the hydrophobic effect and intermolecular hydrogen bonding, have been proposed to describe their self-organisation process: (i) a two-step mechanism, whereby primary, small micelles form, and subsequently associate with each other into secondary, larger micelles [6,7]; (ii) a continuous self-association process, following which BS aggregates grow in size upon addition of unimers [8,9] (Figure 1). These models have been suggested to result in various shapes and sizes for BS micelles, from globular [9–15] and rod-like [10,16–20], to disc-shaped [21] and helical [22–24] structures. These discrepancies across the existing body of literature call for further structural characterisations to provide a clear molecular-level picture of BS complex aggregates, whose knowledge is crucial to understanding BS physicochemical and biological properties.

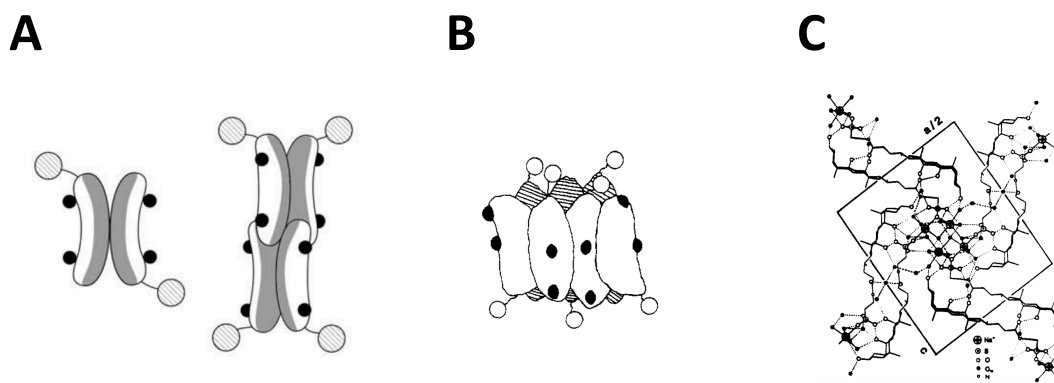


Figure 1: (A) The two-step aggregation model, whereby globular primary, small micelles form by back-to-back association between the steroid skeletons *via* the hydrophobic effect, and then associate with each other in the form of rod-like secondary, larger micelles *via* hydrogen bonding between hydroxyl and amino groups (reproduced with permission from [5]; copyright (2009) Elsevier); based on this mechanism, a maximum of ten molecules could self-associate hydrophobically without creating a cavity in the core. (B) The disc-shaped structure model, whereby the hydrophobic faces are oriented towards the micelles core, and the hydrophilic ones towards the aqueous solvent (reproduced with permission from [21]; copyright (1989) American Chemical Society). (C) The helical structure model, whereby molecules are stabilised *via* polar interactions, with the nonpolar moieties facing the aqueous solvent and the polar ones the micelles core, which is also filled with counterions and water molecules (reproduced with permission from [23]; copyright (1999) American Chemical Society).

BS are also known to combine with dietary materials resulting from the lipolysis process in the small intestine (e.g., phospholipids and triacylglycerols (TAG) hydrolysis products, like monoacylglycerols (MAG) and fatty acids (FA)), generating a very wide range of phases, depending on the composition of the lipid/BS/water system (see the lecithin/sodium cholate/water [25], monoolein/sodium cholate/water [26] and monoolein/sodium taurocholate/water [27] ternary phase diagrams, as examples). In this study, the area of interest is the region of high-water content, which reflects the actual duodenal composition, where lipids and BS are highly diluted in the gastrointestinal tract. While the phase diagram of the highly hydrated lipid/BS system [28–30], and more precisely the presence of mixed vesicles, mixed micelles and coexistence phases [26,31,32], is perfectly established, the mechanism of vesicle/micelle transition, in particular the localisation and organisation of both compounds in each phase, remains largely unknown. A range of structural studies has been carried out mainly with the aim of assessing the effect of dilution on lipid/BS mixed micelles and demonstrated a micelle-to-vesicle transition, driven by the differences in both solubility and spontaneous curvature between BS

and lipids. Systems studied have included for instance lecithin/sodium taurocholate and lecithin/sodium taurodeoxycholate using small-angle neutron scattering (SANS) and dynamic light scattering [33], lecithin/sodium glycocholate using SANS [34], monoolein/sodium taurocholate using quasielastic light scattering and electron microscopy [35], monoolein/chenodeoxycholate and monoolein/cholate using SANS [36]. Upon dilution, BS molecules – which, unlike lipids, are largely soluble in aqueous media – tend to leave the mixed lipid/BS micelles to maintain their bulk unimer concentration; since lipids display a lower spontaneous curvature than BS, the resulting increase in lipid/BS molar ratio in the micelles subsequently causes a globular-to-cylindrical shape transition. Based on SANS measurements, for all lipophilic components (e.g., phospholipids like 1,2-dipalmitoyl-*sn*-glycero-3-phosphocholine (DPPC) [37] or MAG like monoolein [36]), a common cylindrical structure has been suggested for the aggregates, with the lipids being inserted radially (with their head group at the micellar interface and their tails in the micellar core) and the BS lying flat between the lipids head groups, with their hydrophilic part facing the aqueous solvent; BS can be found in the whole micelle, but are hypothesised to be mainly located in the end caps of the cylinder [38]. As soon as the amount of BS molecules is no longer sufficient to maintain the cylinder body, the mixed aggregates transform into BS-incorporating lipid vesicles. The same effect (i.e., micelle elongation, followed by vesicle formation) is observed upon increasing the lipid/BS molar ratio [39]. Some work has also been performed on the vesicle-to-micelle reverse pathway occurring upon solubilisation of lipid vesicles into mixed micelles by BS – which is the focus of this study –, and the same (but reversed) sequence of structures was observed upon addition of increasing amounts of BS to liposomes (e.g., egg phosphatidylcholine/sodium cholate using cryo-transmission electron microscopy and turbidity analysis [40], DPPC/sodium deoxycholate using SANS and dynamic light scattering [41], DPPC/sodium taurocholate using turbidity analysis and differential scattering calorimetry [42], DPPC/sodium cholate and DPPC/sodium deoxycholate using isothermal and differential scanning calorimetry, dynamic light scattering and SANS [28]). This ability of BS to induce micellar solubilisation – which is a crucial step in the transportation of nutrients towards the gut mucosa where they are absorbed [43] – also derives from their amphiphilic

character. Although the physicochemical process taking place during the formation of mixed vesicles (induced by BS removal from mixed micelles, upon dilution, keeping the lipid/BS molar ratio constant) is mostly understood, the mechanism responsible for their dissolution into mixed micelles (upon addition of BS to liposomes, decreasing the lipid/BS molar ratio) remains quite unclear. In particular, structural characterisations aiming at determining the interaction mechanism between BS and liposomes, as well as the localisation and organisation of both BS and lipids in globular mixed micelles, are still required.

The processes occurring during transport and absorption of lipids are quite complex and still not fully elucidated; more importantly, to the best of our knowledge, no relationships have been established yet between BS architecture, their solubilising property and the structure of the resulting dietary mixed micelles. Consequently, further studies on BS self-assembly behaviour and interaction with components found in the gut are necessary to clarify how BS structure governs their peculiar aggregation properties in the bulk and how, in turn, this may explain their contrasting biological roles during lipolysis, in particular their capacity to incorporate lipolytic products into mixed micelles for absorption in the gut.

The work presented in this chapter reports a structural investigation of the aggregation properties of two selected BS, sodium taurocholate (NaTC) and sodium taurodeoxycholate (NaTDC) (Figure 2), in the absence and presence of the predominant digestion products (FA and/or MAG). Additionally, lipid vesicles, made up of DPPC and TAG, were employed as a mimic of colloidal structures found in the gastrointestinal tract – TAG being the major type of dietary fats –, to assess BS solubilising capacity. After studying BS micellisation process with fluorescence spectroscopy, using pyrene as a probe, we characterised the structure of BS neat and mixed micelles by combining small-angle neutron and X-ray scattering (SANS, SAXS) techniques. Complementary molecular dynamics (MD) simulations were also performed (by Dr Christian D. Lorenz) and preliminary results are shown here. Thereafter, we determined the location and organisation of TAG in the phospholipid bilayer using neutron reflectometry (NR), as well as the liposomes structure in the bulk aqueous phase using SANS, and we monitored with SANS the fate of liposomes upon interaction with BS, probing in particular the formation of equilibrium

structures in the bulk, such as mixed micelles. For this study, caprylic (C8:0) and oleic (C18:1) acids were employed as FA, monocaprylin (C8:0) and monoolein (C18:1) as MAG, and tricaprylin (C8:0) and triolein (C18:1) as TAG, to evaluate the effect of both chain length and saturation on digestion. All the aforementioned equilibrium studies provide a basis for defining the likely colloidal structures formed upon digestion of TAG.

2. Experimental section

2.1. Materials

NaTC (P97.0% TLC) (Figure 2A), NaTDC (P95.0% TLC) (Figure 2B), pyrene (Puriss. P.a., for fluorescence, P99.0% GC), caprylic acid (C8:0 FA, P99.0%) (Figure 3), oleic acid (C18:1 FA, P99.0% GC) (Figure 3), monocaprylin (C8:0 MAG, P99.0%) (Figure 3), monoolein (C18:1 MAG, P99.0%) (Figure 3), sodium chloride (NaCl, P99.8%), tricaprylin (C8:0 TAG, P99.0%) (Figure 3), triolein (C18:1 TAG, P99.0%) (Figure 3), ethanol (EtOH, P99.8% GC) and acetone (AcOH, P99.5%) were all purchased from Sigma-Aldrich (Gillingham, UK). DPPC (Figure 4A) and 1,2-dipalmitoyl-*d*₆₂-*sn*-glycero-3-phosphocholine (*d*₆₂-DPPC) (Figure 4B) were provided by Avanti Polar Lipids, Inc. (Alabaster, AL, USA), and chloroform (CHCl₃) by Fisher Scientific (Loughborough, UK). Ultrapure water, or MilliQ-grade water (H₂O, 18.2 MΩ·cm, Merck Millipore, Molsheim, France), was used in all experiments, except for the SANS measurements, where deuterium oxide (D₂O, P99.9%), provided by Euriso-top SAS (St. Aubin, France), was employed, and for NR experiments, where both D₂O and silicon-contrast-matched water (SiCMW, 38% D₂O / 62% H₂O by volume) were used. All reagents were used as supplied.

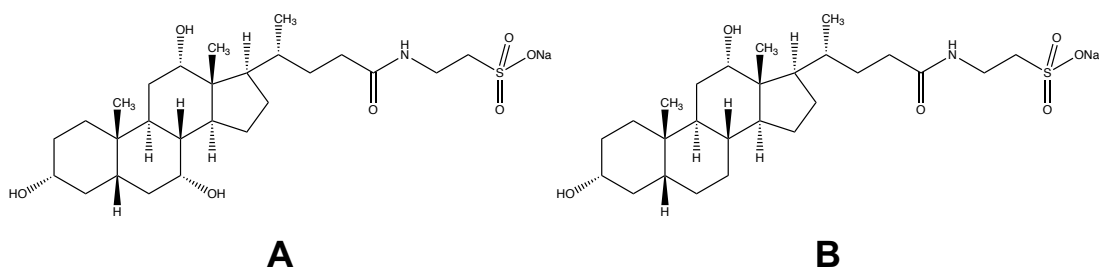


Figure 2: Structures of NaTC (A) and NaTDC (B)

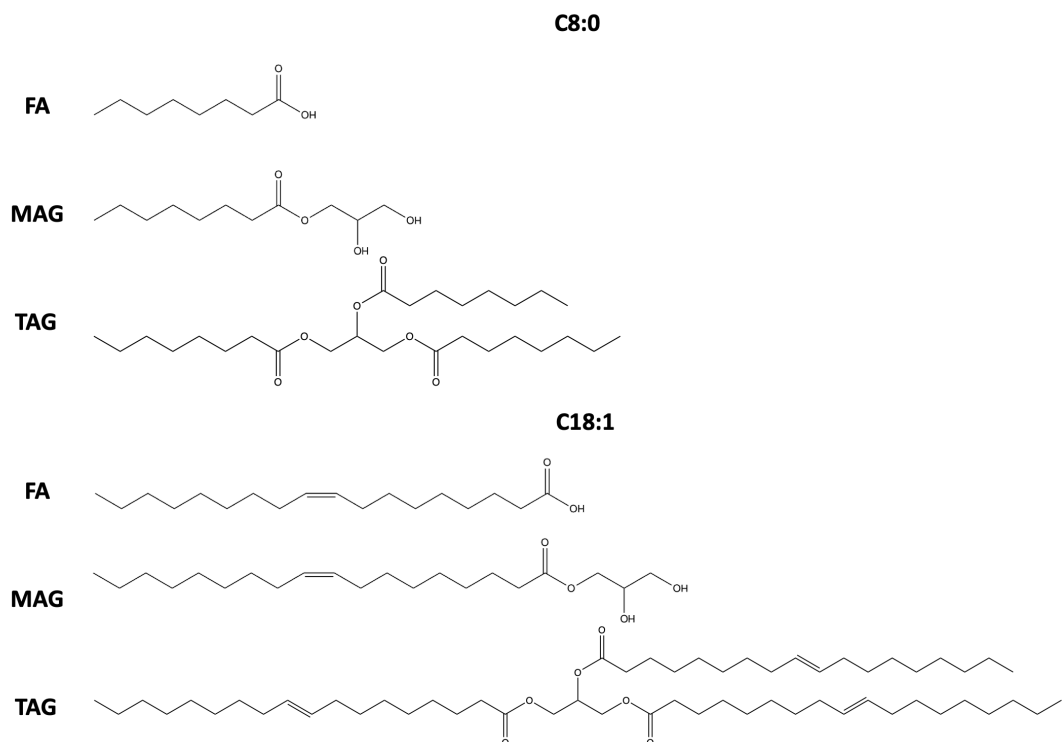


Figure 3: Structures of caprylic acid (C8:0 FA), monocaprylin (C8:0 MAG), tricaprylin (C8:0 TAG), oleic acid (C18:1 FA), monoolein (C18:1 MAG) and triolein (C18:1 TAG).

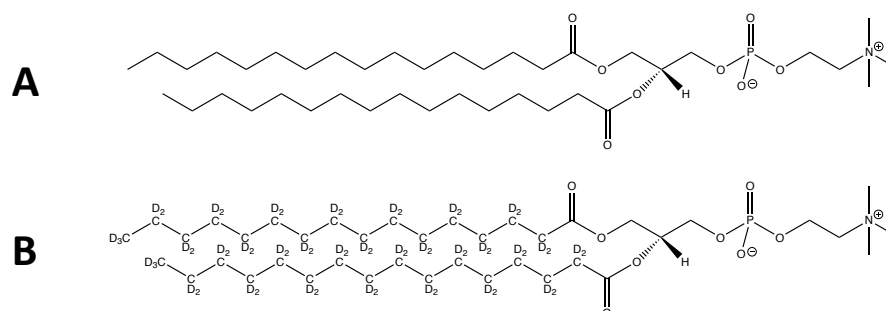


Figure 4: Structures of (A) DPPC and (B) d_{62} -DPPC

2.2. Methods

2.2.1. Pyrene fluorescence spectroscopy

The critical micellar concentration (CMC) of NaTC and NaTDC was determined by fluorescence spectroscopy, using pyrene as a probe. This method is based on the dependence of pyrene fluorescence intensity on the solvent environment [44]. In the absence of micelles (below the CMC), pyrene is surrounded by polar molecules of water and the ratio of the third to the first vibrational peaks (F_{III}/F_I , with $F_{III}/F_I = I_{III}/I_I$, where I_I and I_{III} are the intensities at wavelengths (λ) of $\lambda = 373$ and 383 nm,

respectively) is low. Above the CMC, pyrene partitions into the micelles and F_{III}/F_I increases because of the less polar environment.

Pyrene fluorescence emission (0.5 μ M of pyrene, varying amounts of BS) was measured on a Cary Eclipse fluorescence spectrophotometer (Agilent Technologies UK Ltd, Stockport, UK), using 114F-QS quartz cells (Hellma Analytics, Müllheim, Germany), with excitation at 310 nm, recorded both at 23 and 37°C. The F_{III}/F_I intensity ratio was fitted using the following equation:

$$F_{III}/F_I = F_0 + \frac{K \cdot \Delta F_{max}}{K \cdot e^{-[BS]} \cdot c \cdot \Delta F_{max}} \quad (1)$$

where F_0 is the fluorescence emission intensity of pyrene in water, F_{max} the maximum fluorescence emission intensity of pyrene in the micellar aggregates, $\Delta F_{max} = F_{max} - F_0$ the maximum change in F_{III}/F_I , and K and c two constants [45]. The fluorescence from BS in the absence of pyrene was also measured and subtracted from the measurements. The CMC is taken here as the concentration value at which F_{III}/F_I starts to level off.

2.2.2. Neutron reflectometry (NR)

2.2.2.1. Sample preparation

DPPC/TAG liposomes preparation. Chain-deuterated lipids (d_{62} -DPPC) were dissolved in CHCl_3 , with or without C8:0 (tricaprylin) or C18:1 (triolein) TAG, and the organic solvent was removed by using a rotavapor (at 474 mPa, at 40°C), and by then placing the samples under *vacuum* overnight (at 10 mPa, at 50°C). The solubility limit of each TAG in DPPC vesicles being around 14% for tricaprylin [46,47] and 3% for triolein [46,48,49], TAG concentrations of, respectively, 12% and 2% (slightly below the threshold values) were employed. The dried lipid film was dispersed into degassed D_2O at a DPPC concentration of 2 mg/mL, and then agitated for 15 minutes. Thereafter, the hydrated lipid suspension was subjected to 5 cycles of 3-minute freezing (in liquid nitrogen) and 3-minute thawing, before tip-sonicating the aqueous solution at a frequency of 20 kHz and amplitude of 30% (alternating between 2 seconds of pulse and 3 seconds of pause), for 30 minutes (SONOPULS HD 3100 ultrasonic homogeniser, microtip model: MS 73, BANDELIN electronic GmbH & Co.

KG, Berlin, Germany), and centrifuging it at 11,000 rpm for 30 minutes, to remove titanium fragments. The liposomes suspension was finally extruded 11 times through 50-nm-pore size polycarbonate membranes (Avanti Mini-Extruder, Avanti Polar Lipids, Inc., Alabaster, AL, USA). These hydration and extrusion procedures were carried out at $50^{\circ}\text{C} \pm 2$, well above the temperature of the main gel-to-fluid phase transition of d_{62} -DPPC, i.e., $T_{d_{62}\text{-DPPC phase transition}} = 37^{\circ}\text{C}$, which is around 5°C lower than $T_{\text{DPPC phase transition}}$ [50]. The phase transition temperatures of tricaprylin-incorporating (or DPPC/TC) and triolein-incorporating (or DPPC/TO) DPPC vesicles were preliminarily determined by micro-differential scanning calorimetry and were found to be lower than the DPPC one (i.e., $T_{\text{DPPC}} = 41^{\circ}\text{C}$, $T_{\text{DPPC/tricaprylin}} = 39^{\circ}\text{C}$ and $T_{\text{DPPC/triolein}} = 40^{\circ}\text{C}$) (data not shown).

Solid-supported lipid bilayer (SLB) formation. Lipid bilayers were deposited onto silicon substrates ($80 \times 50 \text{ cm}^2$ surface) that were previously enclosed in laminar flow solid/liquid cells. The protocol for the vesicle fusion deposition of SLB was defined thanks to preliminary quartz-crystal microbalance with dissipation monitoring (QCM-D) measurements, which enable the quantification of the mass adsorbed on a solid surface (further detail on the method and results obtained can be found in Appendix 1 (Figure A1)).

Prior to any measurement, the flow cells were thoroughly cleaned through bath sonication in EtOH, and the silicon blocks in CHCl_3 , AcOH and EtOH, sequentially, before rinsing both extensively with ultrapure water and drying them under nitrogen. The silicon substrates were then treated by UV/Ozone to further remove organic impurities and have more hydrophilic surfaces. Once assembled, the cells were prefilled with degassed D_2O for alignment and pre-characterisation purposes. The solid/liquid cells were connected to a liquid chromatography pump, which allowed for easy exchange of the buffer solutions.

Liposomes were injected by hand into the flow cells at a temperature of $50^{\circ}\text{C} \pm 2$ (well above $T_{d_{62}\text{-DPPC phase transition}} = 37^{\circ}\text{C}$ [50]). Salt (0.5 M NaCl) was then flushed into the solid/liquid cells, to induce the rupture and fusion of surface-adsorbed lipid vesicles and, ultimately, bilayer formation. Finally, the chamber was rinsed with D_2O to remove the liposomes remaining intact on the solid surface and in the bulk phase.

2.2.2.2. Instrumental configuration

NR measurements were performed on the INTER time-of-flight neutron reflectometer at ISIS neutron source (Didcot, UK) [51]. This instrument uses an incoming polychromatic neutron beam with wavelengths (λ) ranging from 1.8 to 17 Å, with a 3% $\Delta\lambda/\lambda$ resolution. Two different incident angles (ϑ_i , with $\theta_1 = 0.7^\circ$ and $\theta_2 = 2.3^\circ$) were employed to obtain values of the scattering vector perpendicular to the surface (q_z , with $q_z = \frac{4\pi}{\lambda} \sin \vartheta_i$) ranging from 0.01 to 0.3 Å⁻¹. Reflectivity (R), which is the ratio between the reflected and incident intensities, was measured as a function of q_z in this range.

2.2.2.3. Contrast-variation method

Contrast-variation, which is a method by which different regions of a sample are highlighted using isotopic substitution (commonly, hydrogen-deuterium substitution for NR experiments), was performed by using three aqueous phases differing by their D₂O/H₂O ratio: pure D₂O, pure H₂O and 38% D₂O / 62% H₂O (V/V) mixture, corresponding to SiCMW (silicon-contrast-matched water), with a scattering length density (SLD) of 2.07×10^{-6} Å⁻² matching the silicon substrate. Combining these aqueous phases with the different bilayers compositions (d₆₂-DPPC, d₆₂-DPPC/TC or d₆₂-DPPC/TO) allowed us to highlight different parts of the systems: the d₆₂-DPPC/SiCMW system made both TAG and lipid molecules visible, while the use of deuterated lipids (d₆₂-DPPC) in D₂O and H₂O highlighted, respectively, TAG location and changes in lipid interfacial bilayer thickness and organisation (Table 1). Prior to any measurement, the bare silicon substrates were characterised in D₂O and H₂O.

Table 1: Calculated neutron *SLD* of each component

Component	Neutron SLD ($\times 10^6$) (\AA^{-2})	
Solid substrate	Silicon (Si)	2.07
	Silicon oxide (SiO ₂)	3.41
d₆₂-DPPC	d ₆₂ -tails	6.71
	h ₁₈ -head group	1.88 ^a
DPPC	h ₈₀ -DPPC	0.25
Aqueous phase	D ₂ O	6.33
	SiCMW	2.07
	H ₂ O	-0.56
BS	NaTC	0.95
	NaTDC	0.90
FA	Caprylic acid (C8:0)	0.19
	Oleic acid (C18:1)	0.08
MAG	Monocaprylin (C8:0)	0.35
	Monoolein (C18:1)	0.20
TAG	Tricaprylin (C8:0)	0.33
	Triolein (C18:1)	0.15

^a The *SLD* value reported for the head group does not include any contribution from water hydration.

2.2.2.4. Data fitting

Prior to analysis, NR data were converted to reflectivity curves $R(q_z)$ using the manipulation and analysis toolkit for instrument data (MANTID) software application available for the ISIS reflectometers [52]. Data analysis was performed with the Aurore software [53] and a global fitting procedure was applied for compatible data sets. The modelling approach used is the same as the one reported by Gerelli [54]. Briefly, the SLB was divided into four layers, each characterised by a specific thickness (t), *SLD*, amount of water (f_{water}) and interfacial roughness (σ). Because of the instrumental geometry used, the first two (upper) layers in the model correspond to, respectively, the head groups (in contact with silicon oxide (SiO₂)) and the tails regions of the inner leaflet, while the second two (lower) ones are ascribed to, respectively, the tails and head groups (in contact with the aqueous phase) of the outer leaflet (see supplementary material in reference [54]). The result of the NR data analysis is a *SLD* profile along the direction perpendicular to the surface (z), which is directly related to the distribution of each molecular component in this direction.

2.2.3. Small-angle X-ray and neutron scattering (SAXS, SANS)

In any small-angle scattering experiment, the contrast term is the difference in scattering length density (*SLD*) between the object and the solvent: with small-angle X-ray scattering (SAXS), the scattering arises from the electron density (referred to as electron *SLD*), whereas for small-angle neutron scattering (SANS), it arises from the nuclear scattering length (referred to as neutron *SLD*). The combination of these two techniques, which are sensitive to different contrasts, enables the resolution of different structural motifs in the systems studied.

2.2.3.1. Sample preparation

Aggregation of BS in solution. SAXS and SANS measurements were carried out on a range of BS aqueous solutions (with concentrations ranging between 2 and 200 mM), at 25°C, using ID02 and SANS2D, respectively. Measurements were also performed at 37°C on D33 to assess the effect of temperature on BS micelles structure. The aqueous solutions of BS were prepared with and without salt (0.15 M NaCl), in either D₂O (SANS) or H₂O (SAXS) (Tables 1 and 2). The salt screens out the inter-micellar electrostatic interactions.

Table 2: Calculated electron *SLD* of each component

Component		Electron SLD ($\times 10^{-6}$) (\AA^{-2})
Solvent	H ₂ O	9.47
BS	NaTC	12.05
	NaTDC	12.16

Aggregation of BS with FA and/or MAG in the form of mixed micelles, in solution. BS/FA, BS/MAG and BS/FA/MAG mixed micelles were prepared by vortex-mixing, and then solubilising the different components with a tip sonicator (BANDELIN electronic GmbH & Co. KG, Berlin, Germany) for 30 s, at an amplitude of 30% and frequency of 20 kHz. Based on solubility tests (data not shown), FA (caprylic acid (C8:0) and oleic acid (C18:1)) and MAG (monocaprylin (C8:0) and monoolein (C18:1)) were employed at concentrations both close to and far away from their solubility limit in the BS micelles, which was higher for NaTDC (Table 3). Each mixed micelle (BS/FA, BS/MAG and BS/FA/MAG) comprised 100 mM BS (well above BS CMC), to maximise the scattering. All micelles were prepared with and without salt (0.15 M NaCl) in D₂O, to

provide a significant contrast (Table 1), and were measured at 25°C, with SANS (SANS2D) only. The parameters used to fit SANS2D data are shown in Table 4.

Table 3: Type and amount of additives used to make the mixed micelles

	Additive	[Additive] (% w/w)
FA	Caprylic acid (C8:0)	0.25
		1.50
	Oleic acid (C18:1)	0.10
		0.25
MAG	Monocaprylin (C8:0)	0.25
		1.30
	Monoolein (C18:1)	0.10
		0.25
FA – MAG	Caprylic acid – Monocaprylin (C8:0)	1.30 – 1.50
	Oleic acid – Monoolein (C18:1)	0.25 – 0.25

Table 4: Concentration of FA (C8:0 or C18:1) and/or MAG (C8:0 or C18:1) in the sample ($[Additive]$), volume fraction of each component in micelles (Φ_{BS} , Φ_{FA} , Φ_{MAG}), total volume fraction ($\Phi_{BS/FA/MAG} = \Phi_{BS} + \Phi_{FA} + \Phi_{MAG}$), SLD of each component (SLD_{BS} , SLD_{FA} , SLD_{MAG}), total SLD ($SLD_{BS/FA/MAG} = \frac{1}{\Phi_{BS/FA/MAG}} (\Phi_{BS} SLD_{BS} + \Phi_{FA} SLD_{FA} + \Phi_{MAG} SLD_{MAG})$), for each BS studied: NaTC, NaTDC, with and without 0.15 M NaCl. These parameters were used to fit SANS2D data. While the density of both FA was known (0.91 for C8:0 FA and 0.89 for C18:1 FA), the density of both MAG was assumed to be of similar value and was fixed at 0.90 for the calculation of the volume fractions.

NaTC		[Additive] (% w/w)	Φ_{BS}		Φ_{FA}	Φ_{MAG}	$\Phi_{BS/FA/MAG}$		$SLD_{BS/FA/MAG}$ ($\cdot 10^{-6}$) (\AA^{-2})	
			No salt	Salt			No salt	Salt	No salt	Salt
			FA	C8:0	0.25	0.0392	0.0400	0.0031	-	0.0422
1.50	0.0386	0.0395			0.0160	-	0.0546	0.0555	0.73	0.73
C18:1	0.10	0.0393		0.0401	0.0011	-	0.0404	0.0412	0.93	0.93
	0.25	0.0392		0.0400	0.0031	-	0.0423	0.0431	0.89	0.89
MAG	C8:0	0.25	0.0392	0.0400	-	0.0029	0.0421	0.0429	0.91	0.91
		1.30	0.0387	0.0395	-	0.0142	0.0530	0.0538	0.79	0.79
	C18:1	0.10	0.0393	0.0401	-	0.0011	0.0404	0.0412	0.93	0.93
		0.25	0.0392	0.0400	-	0.0027	0.0418	0.0427	0.90	0.90
FA – MAG	C8:0	1.30 – 1.50	0.0381	0.0389	0.0143	0.0162	0.0685	0.0694	0.65	0.65
	C18:1	0.25 – 0.25	0.0391	0.0399	0.0029	0.0027	0.0446	0.0455	0.85	0.85

NaTDC

		[Additive] (% w/w)	Φ_{BS}		Φ_{FA}	Φ_{MAG}	$\Phi_{BS/FA/MAG}$		$SLD_{BS/FA/MAG}$ ($\cdot 10^{-6}$) (\AA^{-2})	
			No salt	Salt			No salt	Salt	No salt	Salt
FA	C8:0	0.25	0.0387	0.0391	0.0033	-	0.0420	0.0424	0.84	0.84
		1.50	0.0382	0.0386	0.0166	-	0.0548	0.0552	0.68	0.69
	C18:1	0.10	0.0388	0.0392	0.0013	-	0.0401	0.0405	0.87	0.87
		0.25	0.0387	0.0391	0.0029	-	0.0416	0.0420	0.84	0.84
MAG	C8:0	0.25	0.0387	0.0391	-	0.0027	0.0414	0.0418	0.86	0.86
		1.30	0.0382	0.0386	-	0.0145	0.0527	0.0531	0.75	0.75
	C18:1	0.10	0.0388	0.0392	-	0.0011	0.0399	0.0403	0.88	0.88
		0.25	0.0387	0.0391	-	0.0027	0.0414	0.0418	0.86	0.86
FA – MAG	C8:0	1.30 – 1.50	0.0368	0.0376	0.0141	0.0164	0.0673	0.0681	0.62	0.62
	C18:1	0.25 – 0.25	0.0378	0.0386	0.0027	0.0035	0.0440	0.0448	0.79	0.80

Solubilisation of TAG-incorporating lipid vesicles into mixed micelles. Each TAG-incorporating liposome (DPPC, DPPC/TC and DPPC/TO) was prepared following the protocol described in the “Neutron reflectometry (NR)” method section, using hydrogenated lipids (DPPC) instead of chain-deuterated ones (d_{62} -DPPC). These liposomes were then mixed with specific amounts of pure BS aqueous solutions, with at least 12 hours of equilibration. All samples were made in D_2O to provide a significant contrast (Table 1) and were measured at both 25 and 37°C, with SANS (D33) only.

2.2.3.2. Instrumental configurations

Small-angle X-ray scattering (SAXS). SAXS measurements were performed on the high brilliance ID02 beamline, at the European Synchrotron Radiation Facility (ESRF, Grenoble, France) [55], using a 2-mm-inner diameter flow-through quartz capillary, thermostated by a Peltier module.

The instrument, equipped with a charge-coupled device-based Rayonix MX-170HS detector, was configured with an incoming monochromatic X-ray beam of wavelength $\lambda = 1 \text{ \AA}$ (12.46 keV X-ray energy) and resolution $\Delta\lambda/\lambda = 0.015\%$. Two fixed sample-to-detector distances (1 and 2 m) were used, thus allowing values of the scattering vector (q , with $q = \frac{4\pi}{\lambda} \sin \vartheta$, with 2ϑ the scattering angle) ranging from 0.015 to 0.8 \AA^{-1} to be obtained.

Data were corrected for the dark current, flat field, incoming flux and transmitted beam measured simultaneously with scattering. Ten measurements were averaged after verifying that no change due to radiation damage occurred. Contribution of the solvent-filled capillary was subtracted. The absolute scale was determined using the plateau intensity level of water (at $1.63 \times 10^{-2} \text{ cm}^{-1}$, at 298 K).

Small-angle neutron scattering (SANS). SANS measurements were performed on the time-of-flight SANS2D instrument, at ISIS (Didcot, UK) [56] (for BS micelles and mixed micelles), and on the D33 spectrometer [57], at the Institut Laue-Langevin (ILL, Grenoble, France) (for BS micelles and TAG-incorporating liposomes), using 1 mm path-length quartz cells (Hellma Analytics, Müllheim, Germany) thermostated with a circulating water bath.

SANS2D data were acquired with a polychromatic incident beam of wavelength (λ) ranging between 2 and 14 Å, and with a fixed instrument setup of 4 m, thus yielding a q -range of 0.015 to 1 Å⁻¹; D33 data were recorded with a monochromatic neutron beam with an incident wavelength of $\lambda = 6$ Å (with a 10% $\Delta\lambda/\lambda$ resolution) and three fixed sample-to-detector distances ($D = 2, 5$ and 12 m), as well as with $\lambda = 13$ Å and $D = 12$ m, thus obtaining q values ranging from $1.5 \cdot 10^{-3}$ to 0.47 Å⁻¹.

Raw data were radially averaged and corrected from the scattering of the empty cell and the D₂O background. Detector efficiency corrections and data normalisation to an appropriate standard were done using the MANTID (available for the ISIS diffractometers [52]) and the large array manipulation program (LAMP, available for the ILL spectrometers [58]) software applications.

2.2.3.3. Data fitting

BS micelles and mixed micelles. Data analysis was performed with the SasView software [59]. The intensity $I(q)$ scattered from BS micelles and mixed micelles was fitted to an oblate ellipsoid model combined with a Hayter-Penfold structure factor, according to the following equation:

$$I(q) = \Phi_{Micelles} (SLD_{Micelle} - SLD_{Water})^2 P_{Ellipsoid}(q) S_{H-P}(q) \quad (2)$$

where $\Phi_{Micelles}$ is the micellar volume fraction, $SLD_{Micelle}$ and SLD_{Water} the SLD of the BS micelle or mixed micelle and water, respectively, $P_{Ellipsoid}(q)$ the form factor for ellipsoids, and $S_{H-P}(q)$ the Hayter-Penfold structure factor, which describes the interactions between charged micelles [60,61]. The polydispersity of micellar radii was fixed at 0.2 in the software, assuming a lognormal distribution. Making the hypothesis that all the additives (FA or/and MAG) molecules contribute to the formation of mixed aggregates, the volume fractions of the additives (Φ_{FA} and Φ_{MAG}) were calculated considering the absence of free monomers, and the SLD of the objects measured with SANS was fixed to $SLD_{BS/FA/MAG}$, with $SLD_{BS/FA/MAG} = \frac{1}{\Phi_{BS/FA/MAG}}$ ($\Phi_{BS} SLD_{BS} + \Phi_{FA} SLD_{FA} + \Phi_{MAG} SLD_{MAG}$), where Φ_{BS} , Φ_{FA} and Φ_{MAG} are the volume fractions of, respectively, BS, FA and MAG, SLD_{BS} , SLD_{FA} and SLD_{MAG} the SLD of, respectively, BS, FA and MAG, $\Phi_{BS/FA/MAG}$ and $SLD_{BS/FA/MAG}$ the total volume fraction and total SLD , respectively (Table 4). The composition of the BS mixed micelles

formed upon addition of BS to liposomes being unknown, the SLD of the objects probed by SANS was fixed to the one of BS; this assumption is reasonable since in the 'ideal' case where all the lipids, TAG and BS are incorporated into the mixed aggregates (which is not the case here as the systems contain other structures than mixed micelles), the minimum value of SLD obtained would be $0.69 \times 10^{-6} \text{ \AA}^{-2}$, which is relatively similar to that of BS ($0.95 \times 10^{-6} \text{ \AA}^{-2}$ for NaTC, and $0.90 \times 10^{-6} \text{ \AA}^{-2}$ for NaTDC). All the known parameters (i.e., SLD of the objects measured and solvent, salt concentration) were fixed to minimise the variation on the fitted parameters; an error of ± 0.0005 on the volume fraction parameter returned by the software (referred to as $\Phi_{software}$) and of ± 2 on the fitted radii (R_{Pol} , R_{Eq}) and charges parameters was found.

In the case of BS micelles, the previous equation (Equation 2) is equivalent to the following one:

$$I(q) = \Phi_{BS} (1 - x_{Water}) (SLD_{BS} - SLD_{Water})^2 P_{Ellipsoid}(q) S_{H-P}(q) \quad (3)$$

where Φ_{BS} is the volume fraction of BS in the micelles, x_{Water} the volume fraction of water in the micelles, and SLD_{BS} and SLD_{Water} the SLD of BS and water, respectively. Further explanations about how this equation was established can be found in Appendix 2.

The volume of each BS micelle or mixed micelle ($V_{Micelle}$) was calculated as follows:

$$V_{Micelle} = \frac{4}{3} \pi R_{Pol} R_{Eq}^2 \quad (4)$$

where R_{Pol} and R_{Eq} are the polar and equatorial radii of the (oblate) ellipsoid micelle. For SANS measurements, we found (see results section) that $V_{Micelle}$ corresponds to the volume of the micellar core only, rather than the whole micelle, as neutrons are not sensitive to the hydrated hydrophilic shell.

Using SAXS data, the aggregation number (N_{agg}) of BS micelles was determined from:

$$N_{agg} = \frac{V_{BS}^{Micelle}}{v_{mBS}}, \text{ with } V_{BS}^{Micelle} = \frac{4}{3} \pi R_{Pol} R_{Eq}^2 (1 - x_{Water}) \quad (5)$$

where $V_{BS}^{Micelle}$ is the volume occupied by BS in the hydrated micelle and $v_{m\ BS}$ the molecular volume of each BS ($v_{m\ NaTC} = 0.680\text{ nm}^3$ [62] and $v_{m\ NaTDC} = 0.658\text{ nm}^3$ [19]).

The eccentricity of each BS micelle was calculated as follows:

$$\text{Eccentricity} = \sqrt{1 - \frac{R_{Pol}^2}{R_{Eq}^2}} \quad (6)$$

Therefore, the eccentricity of an ellipsoid varies between 0 and 1, and that of a sphere is 0.

TAG-incorporating lipid vesicles. The intensity $I(q)$ scattered from pure liposomes was fitted to a model that takes into account two vesicle populations, namely, uni-lamellar and multi-lamellar vesicles. Further explanations about the equation used for data fitting can be found in reference [63], where this model is described in detail. The uni-lamellar lipid vesicles contribution takes into account a core/shell structure, whose polydispersity is described by a Schultz distribution, while the multi-lamellar lipid vesicles contribution corresponds to a core, surrounded by multiple lipid bilayer shells, each spaced by an aqueous solvent layer; in the case of multi-lamellar liposomes, the polydispersity is attributed to the variable number of bilayers (or shells) and polydispersity of the solvent layer thickness, also described by a Schultz distribution. The features of the individual bilayers (*SLD*, thickness and hydration) were described by the same set of parameters for uni- and multi-lamellar vesicles.

2.2.4. Molecular dynamics (MD) simulations

All-atom molecular dynamics (MD) simulations were carried out to investigate the molecular-scale mechanisms governing the self-assembly of NaTC and NaTDC in a 0.15 M NaCl aqueous solution. Two different concentrations (10 and 50 mM) were employed for each BS. Table 5 summarises the number of BS, water, Na^+ and Cl^- molecules included in each of the four simulated systems. The number of BS was chosen so that there is at least twice the number of BS molecules in the simulation as had been reported as the average aggregation number (N_{agg}) from the experimental investigations.

Table 5: Number (#) of BS, water, Na⁺ & Cl⁻ molecules in each simulated system

	[BS] (mM)	# BS	# water	# Na ⁺	# Cl ⁻
NaTC	10	12	62709	190	178
	50	25	25009	96	71
NaTDC	10	12	62717	190	178
	50	25	25433	96	71

Each of these systems was initially built with the BS molecules and the salt ions randomly distributed in the simulation box using the CHARMM-GUI multicomponent assembler. After the initial systems were assembled, the same simulation protocol was followed for each system. First, a steepest descent energy minimisation was performed on each of the systems using a maximum of 5000 minimisation steps and an energy tolerance of 1000 kJ/mol. Then, the minimised configurations were equilibrated at 303.15 K using the NVT (constant number, volume and temperature) ensemble, in which a Nosé-Hoover thermostat was applied, for 25 ps. Finally, a production simulation was carried out for 150 ns at 300 K using the NPT (constant number, pressure and temperature) ensemble with a Nosé-Hoover thermostat at 303.15 K and a Parrinello-Rahman barostat at 1 bar.

All of the simulations presented in this manuscript used the GROMACS simulation 2008 package. The inter- and intra-molecular interactions of the BS, sodium (Na⁺) and chlorine (Cl⁻) ions were described with the CHARMM force field [64]. The TIP3P water model [65] in its modified form, which is commonly used with the CHARMM force field [66], was used to describe the interactions involving water molecules. The van der Waals interactions were cut off at 10 Å, whilst the electrostatic interactions were cut off at 12 Å. The PME method was used to compute long-range Coulombic interactions. A timestep of 2 fs was used in all simulations to ensure stable integration of Newton's equations of motion with the velocity Verlet algorithm, whilst all hydrogen-containing bonds were constrained using the LINCS algorithm.

3. Results

3.1. Aggregation of BS in solution

3.1.1. Critical micellar concentration (CMC) of BS

The micellisation of NaTC and NaTDC in water was studied by fluorescence spectroscopy, using pyrene as a probe, by monitoring the evolution of F_{III}/F_I as a function of BS concentration, at two different temperatures (Figure 5, Table 6).

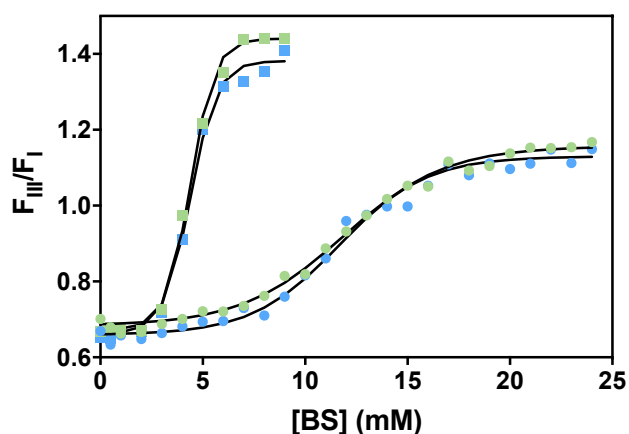


Figure 5: Evolution of pyrene emission fluorescence (F_{III}/F_I) in water as a function of BS concentration, at two different temperatures: NaTDC: (■) 23°C, (■) 37°C, NaTC: (●) 23°C, (●) 37°C. Solid lines are fits of the data to Equation 1.

	CMC (mM)		ΔF_{max}	
	23°C	37°C	23°C	37°C
NaTC	4 – 7	4 – 6	0.47	0.45
NaTDC	2	2	0.79	0.75

Table 6: CMC and ΔF_{max} values for each BS studied, at 23°C and 37°C

For each BS, three regions, corresponding to distinct aggregation states, can be distinguished: at low concentrations, BS are in the form of free unimers and pyrene emission is low; as BS concentration increases, they start aggregating; at high concentrations, a plateau, characteristic of the presence of micelles, is reached. The two BS, however, present very distinct profiles (Figure 5): NaTC shows a smooth, gradual rise in F_{III}/F_I , in contrast to NaTDC, with which a sharp and more pronounced increase is observed at low BS concentrations, as reported elsewhere [67–69]. These contrasting profiles are associated to different values of the CMC and ΔF_{max} , which are insensitive to temperature (in agreement with the literature, which indicates a

weak effect on BS CMC in this temperatures range [70]): NaTC has a much higher CMC than NaTDC, but a much lower ΔF_{max} (Table 6, Equation 1). The CMC values are consistent with literature data obtained using the same technique (NaTC: CMC = 3 – 5 mM; NaTDC: CMC = 2.9 mM) [69]. ΔF_{max} (or $F_{max} - F_0$, the maximum change in pyrene emission fluorescence) characterises the polarity of the environment probed by pyrene: the higher this parameter, the higher the hydrophobicity. The higher value of ΔF_{max} obtained with NaTDC ($\Delta F_{max} = 0.79$, at 23°C) thus shows that pyrene probes a more hydrophobic environment when inside NaTDC micelles, compared to NaTC ($\Delta F_{max} = 0.47$, at 23°C); this may be linked to the extent of hydration of the micelles (which would be lower for NaTDC), or the lower polarity of NaTDC, which bears one less hydroxyl group.

3.1.2. Shape and size of BS micelles

The structure of NaTC and NaTDC micelles was characterised as a function of BS concentration, in the absence and presence of salt (0.15 M NaCl), using both SANS and SAXS. Various models were used to fit the data (including sphere and cylinder models), and the model that provided the best fit to the scattering data was the oblate ellipsoid model combined with a Hayter-Penfold structure factor (Figures 6, 7, 8 and 9, Table 7).

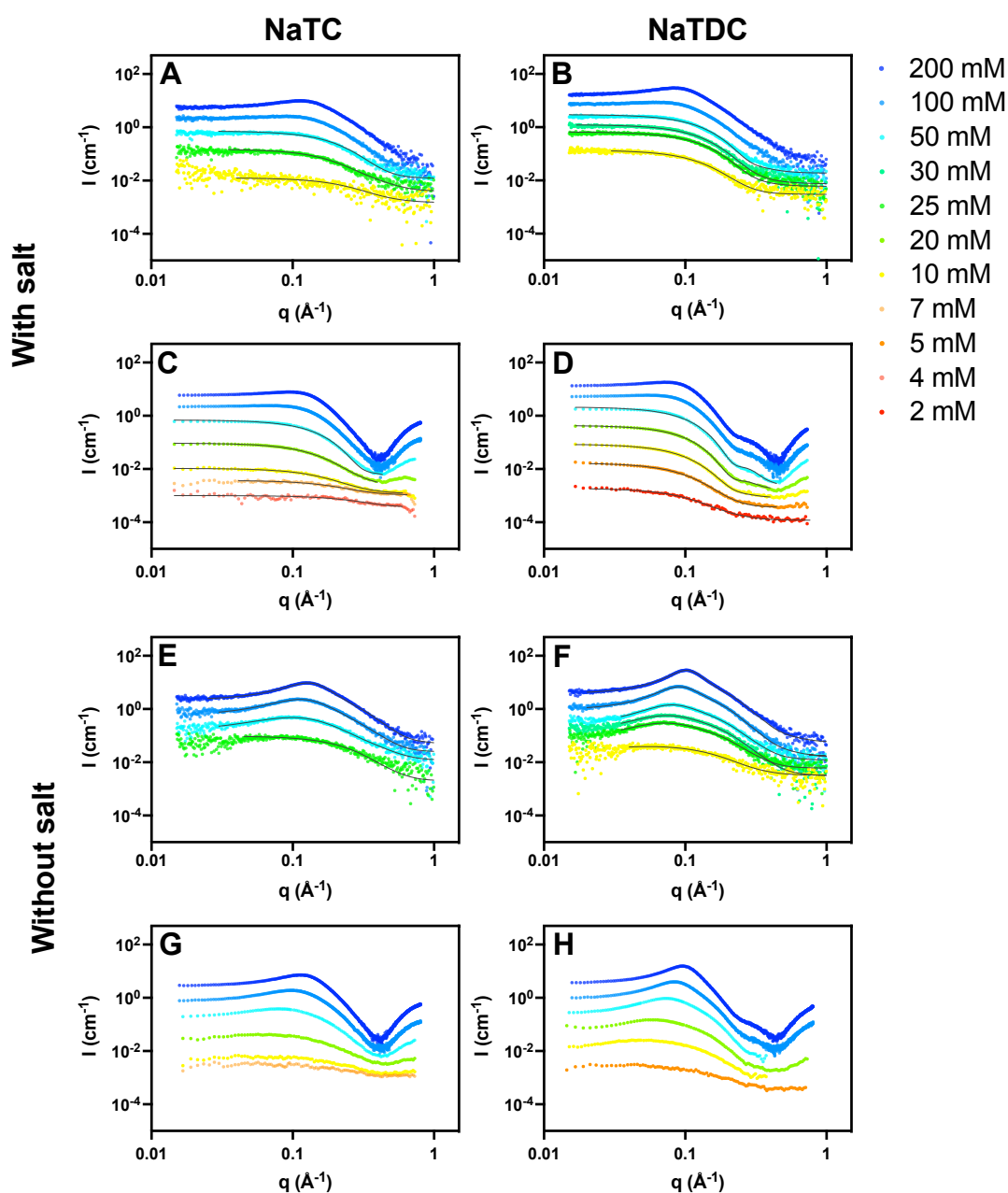


Figure 6: Scattered intensity (I) as a function of the scattering vector (q) for BS aqueous solutions of either NaTC (A, C, E, G) or NaTDC (B, D, F, H), prepared at different concentrations (from 2 to 200 mM), with (A, B, C, D) and without (E, F, G, H) 0.15 M NaCl, and measured at 25°C, by SANS (A, B, E, F) and SAXS (C, D, G, H). Solids lines correspond to fits to the data as described in the text (Equation 3). For readability purposes, curves are staggered vertically.

Due to the small micellar sizes, weak scattering was obtained ($I(0) < 100 \text{ cm}^{-1}$) for both BS (Figure 6). In the absence of salt, the two BS exhibit a peak characteristic of electrostatic interactions (Figures 6, E, F, G, H). In the presence of 0.15 M NaCl, this peak disappears due to the screening of charges, except at the highest concentrations of BS, 100 and 200 mM (Figures 6, A, B, C, D); we therefore neglected

the structure factor in the analysis of the data showing no peak of interaction (i.e., in the presence of salt, except with 100 and 200 mM BS). SAXS data obtained in the presence of interaction (i.e., at all BS concentrations in the absence of salt, and at 100 and 200 mM in the presence of salt) and SANS data obtained in the presence of salt at 100 and 200 mM BS could not be fitted.

Table 7: Concentration of BS in the sample ($[BS]$), volume fraction of BS in micelles (Φ_{BS}), amount of charges in BS micelle, volume fraction fitted by the software ($\Phi_{software}$, also equal to Φ_{BS} ($1 - x_{Water}$)), polar (R_{Pol}) and equatorial (R_{Eq}) radii values of the (oblate) ellipsoid BS micelle, volumes of the BS micelle core ($V_{Micelle\ core}$) and micelle ($V_{Micelle}$), proportion of water in BS micelle core ($x_{Water\ in\ micelles\ core}$) and micelle ($x_{Water\ in\ micelles}$), volume fraction of BS micelles in solution ($\Phi_{Micelles}$), and BS micelle aggregation number (N_{agg}), for each BS studied: NaTC, NaTDC, with and without 0.15 M NaCl. These parameters were obtained from SANS2D (SANS) and ID02 (SAXS) data fitting. In the absence of salt, only SANS data could be fitted and therefore only the parameters obtained from the SANS measurements are shown in this table; in the presence of salt, both SANS and SAXS data could be fitted, except the ones obtained at high BS concentrations (i.e., 100 and 200 mM), where strong peaks of interaction are present.

Without salt

NaTC

[BS] (mM)	Φ_{BS}	Charges (e)	$\Phi_{Software}$	R_{Pol} (Å)	R_{Eq} (Å)	$V_{Micelle\ core}$ (nm ³)	$x_{Water\ in\ the\ core}$
25	0.0086	-	0.0080	4	10	2	0.1
50	0.0189	4	0.0181	3	14	3	0.04
100	0.0394	7	0.0351	5	14	4	0.1
200	0.0804	10	0.0614	5	16	6	0.2

NaTDC

[BS] (mM)	Φ_{BS}	Charges (e)	$\Phi_{Software}$	R_{Pol} (Å)	R_{Eq} (Å)	$V_{Micelle\ core}$ (nm ³)	$x_{Water\ in\ the\ core}$
10	0.0032	3	0.0027	5	14	4	0.2
25	0.0091	7	0.0076	6	16	6	0.2
30	0.0111	7	0.0093	7	16	7	0.2
50	0.0190	10	0.0154	7	17	8	0.2
100	0.0387	15	0.0310	8	18	11	0.2
200	0.0783	19	0.0626	8	21	14	0.2

With salt

NaTC

[BS] (mM)	Φ_{BS}	Charges (e)		$\Phi_{Software}$		R_{Pol} (Å)		R_{Eq} (Å)		$V_{Micelle\ core}$ (nm ³)	$V_{Micelle}$ (nm ³)	$x_{Water\ in\ the\ core}$	$x_{Water\ in\ micelles}$	$\Phi_{Micelles}$	N_{agg}
		SANS	SAXS	SANS	SAXS	SANS	SAXS	SANS	SAXS	SANS	SAXS	SANS	SAXS	SAXS	SAXS
4	0.0008		-		0.0005		4		8		1		0.4	0.0013	1
7	0.0021		-		0.0007		3		11		1		0.7	0.0060	1
10	0.0033	-	-	0.0031	0.0008	3	4	9	14	1	3	0.1	0.8	0.0135	1
20	0.0074		-		0.0017		7		16		7		0.8	0.0321	2
25	0.0094	-		0.0083		3		13		2		0.1			
50	0.0197	-	-	0.0146	0.0047	5	11	12	15	3	10	0.3	0.8	0.0826	4

NaTDC

[BS] (mM)	Φ_{BS}	Charges (e)		$\Phi_{Software}$		R_{Pol} (Å)		R_{Eq} (Å)		$V_{Micelle\ core}$ (nm ³)	$V_{Micelle}$ (nm ³)	$x_{Water\ in\ the\ core}$	$x_{Water\ in\ micelles}$	$\Phi_{Micelles}$	N_{agg}
		SANS	SAXS	SANS	SAXS	SANS	SAXS	SANS	SAXS	SANS	SAXS	SANS	SAXS	SAXS	SAXS
2	0.0004		-		0.0001		6		22		13		0.7	0.0011	7
5	0.0016	/	-	/	0.0004	/	11	/	23	/	24	/	0.8	0.0062	9
10	0.0036	-	-	0.0028	0.0007	8	14	19	23	12	30	0.2	0.8	0.0181	9
20	0.0075		-		0.0017		18		21		32		0.8	0.0332	11
25	0.0095	-		0.0069		9		18		12		0.3			
30	0.0115	-		0.0082		9		18		13		0.3			
50	0.0194	-	-	0.0140	0.0045	11	21	17	19	13	31	0.3	0.8	0.0833	11

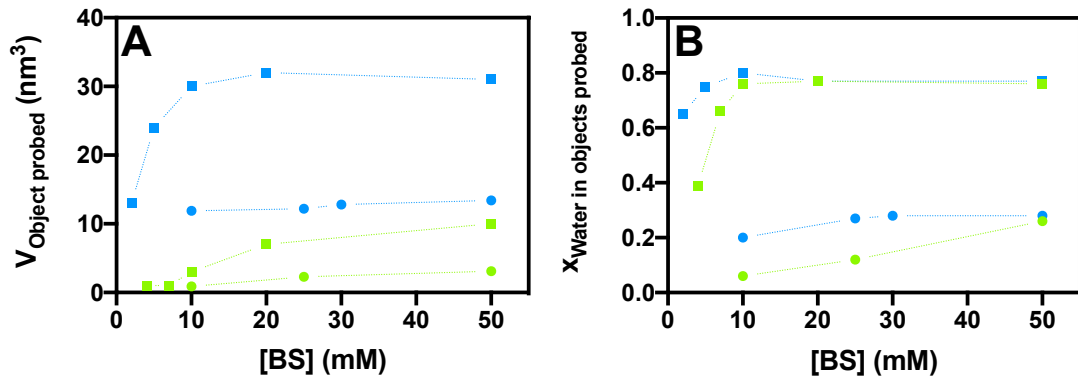


Figure 7: Evolution of (A) the volume of the object probed ($V_{Object\ probed}$), namely, the whole micelle with SAXS and the micellar core with SANS, and (B) the fraction of water in the object probed ($x_{Water\ in\ objects\ probed}$), as a function of BS concentration, with 0.15 M NaCl: NaTC: (●) SANS, (■) SAXS; NaTDC: (●) SANS, (■) SAXS.

In the presence of salt, BS aggregates were found to be larger when measured with SAXS, compared with SANS (particularly NaTDC aggregates), thus suggesting that the micelles exhibit a core/shell structure, where the corona is not resolved by neutrons due to a too low contrast (or SLD difference) between the shell and D_2O (e.g., with 50 mM NaTC, the volume ($V_{Object\ probed}$) obtained from SAXS is 10 nm^3 compared to 3 nm^3 with SANS; with NaTDC, it is 31 nm^3 with SAXS vs. 13 nm^3 with SANS) (Figure 7A, Table 7). This hypothesis is confirmed by the higher extent of hydration ($x_{Water\ in\ objects\ probed}$) obtained from SAXS, which probes the whole micellar structure, and therefore the very hydrated hydrophilic shell, which is invisible to SANS (Figure 7B, Table 7). Based on this assumption, the aggregation number (N_{agg}) and volume ($V_{Micelle}$) of each BS micelle, as well as the amount of water in the micelles ($x_{Water\ in\ micelles}$) and the micellar volume fraction ($\Phi_{Micelles}$), can only be determined from the SAXS data. From SANS fits, the volume of the core ($V_{Micelle\ core}$) and the extent of hydration in the core ($x_{Water\ in\ the\ core}$) were obtained.

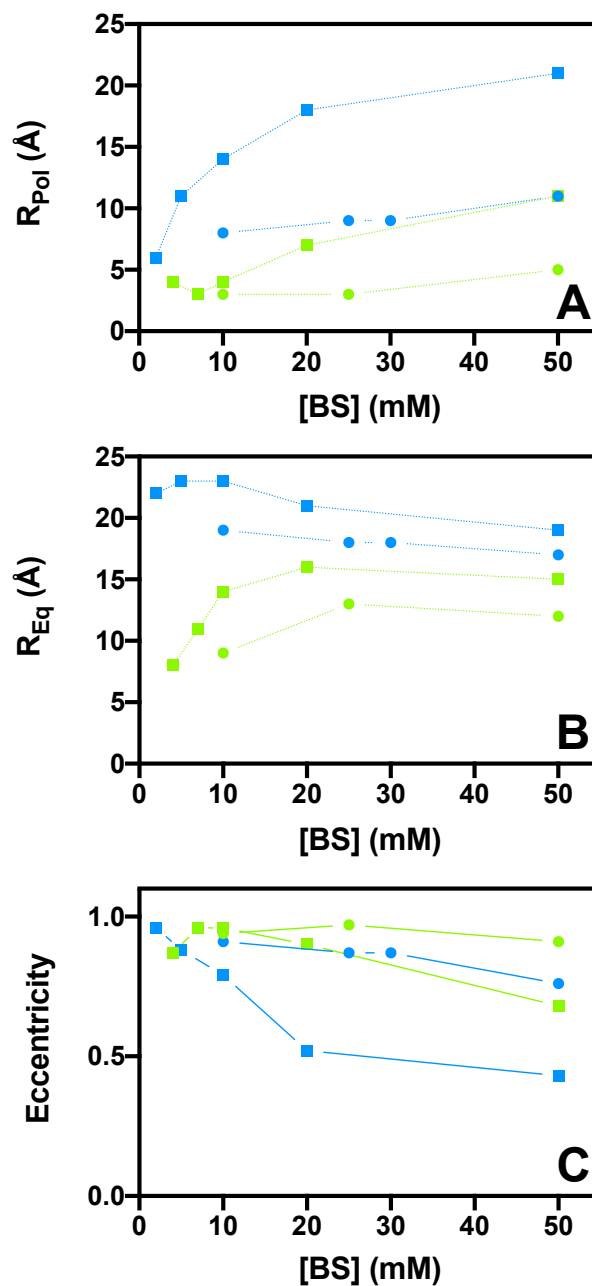


Figure 8: Evolution of (A) the polar radius (R_{Pol}), (B) the equatorial radius (R_{Eq}) and (C) the eccentricity of the object probed, namely, the whole micelle with SAXS and the micellar core with SANS, as a function of BS concentration, with 0.15 M NaCl: NaTC: (●) SANS, (■) SAXS; NaTDC: (●) SANS, (■) SAXS.

Both in the absence and presence of salt, much smaller micelles ($V_{Micelle\ core}$, $V_{Micelle}$, N_{agg}) are obtained with NaTC, compared to NaTDC (e.g., $N_{agg} = 4$ for NaTC, vs. $N_{agg} = 11$ for NaTDC, with 50 mM BS, in the presence of salt) (Figure 7A, Table 7). This is consistent with values from the literature (NaTC: $N_{agg} = 3 - 7$, NaTDC: $N_{agg} = 12 - 19$) [2,5]. Such small micellar sizes are obtained because of BS peculiar molecular

structure, which limits the hydrophobic contacts they can make and thus prevents an efficient packing.

Additionally, for both BS, in both salt conditions, an increase in BS concentration leads to an increase in micellar size ($V_{\text{Micelle core}}$, V_{Micelle} , N_{agg}) (e.g., N_{agg} increases from 1 to 4 for NaTC and from 9 to 11 for NaTDC, when BS concentration increases from 10 to 50 mM, in the presence of salt) (Figure 7A, Table 7), suggesting that BS molecules keep self-assembling into larger structures above their CMC. Interestingly, the ellipsoids formed by NaTDC grow exclusively in the direction of their polar radius (R_{Pol}) (from around 11 Å to 21 Å, from 2 to 50 mM BS, with salt, from SAXS data) (Figure 8A), with their equatorial radius (R_{Eq}) not evolving much (staying around 20 Å, from SAXS data) (Figure 8B), resulting, at high concentrations, in a more isotropic shape (e.g., at 50 mM BS, $R_{\text{Pol}} = 21$ Å and $R_{\text{Eq}} = 19$ Å, with salt, from SAXS data), compared to lower concentrations. Instead, micelles formed by NaTC increase in size *via* both their polar and equatorial radii (R_{Pol} increases from around 4 Å to 11 Å, and R_{Eq} from around 8 Å to 15 Å, from 4 to 50 mM BS, with salt, from SAXS data) (Figures 8, A, B), thus preserving their anisotropic shape. The radii values obtained in this study are in the range of BS dimensions, the molecule being approximately 20 Å long and 7 Å wide [71]. Overall, upon increasing BS concentration to 50 mM, the micelle eccentricity decreases from around 1 to 0.7 and 0.4 for, respectively, NaTC and NaTDC, thereby indicating a transition from ellipsoidal to more spherical shapes, particularly with NaTDC (Figure 8C). SANS data show a similar evolution in micellar sizes, although occurring to a much lower extent (Figures 8, A, B, C). Similar observations were made elsewhere, with NaTDC micelles measured in tris buffer with SAXS [12].

The addition of salt results in a significant increase in size ($V_{\text{Micelle core}}$) for NaTDC (e.g., with $V_{\text{Micelle core}}$ increasing from 8 nm³ to 13 nm³, at 50 mM), whereas the aggregates formed by NaTC display a similar, significantly smaller volume both in the absence and presence of salt (e.g., $V_{\text{Micelle core}} = 3$ nm³ at 50 mM) (Table 7). The fact that the self-aggregation of BS molecules is facilitated by the addition of salt, particularly for NaTDC, can be explained by the complete screening of BS repulsive

charges (except at the highest concentrations studied, 100 and 200 mM, where interactions are still present).

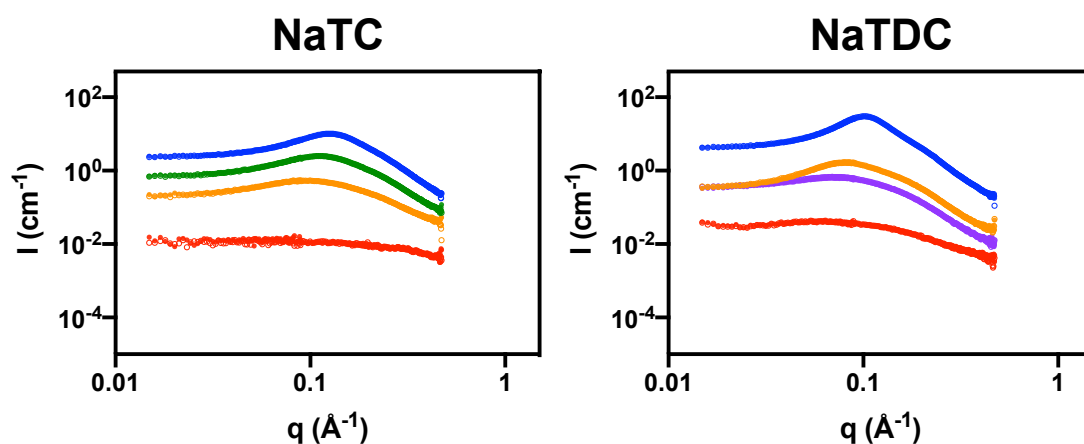


Figure 9: Scattered intensity (I) as a function of the scattering vector (q) for aqueous solutions of BS (NaTC, NaTDC), prepared at different concentrations: (●) 10 mM, (●) 30 mM, (●) 50 mM, (●) 100 mM, (●) 200 mM, and measured at two different temperatures: (○) 25°C, (●) 37°C, without salt, with SANS. For readability purposes, curves are staggered vertically.

Measurements were also performed at 37°C, in the absence of salt, and this increase in temperature was found to have no impact on BS micellar structure, independently of BS type and concentration (Figure 9).

3.1.3. BS molecular organisation in micelles

Preliminary MD simulations were performed by Dr Christian D. Lorenz in order to obtain further insight into the molecular arrangement of each BS in their micellar aggregates, at 10 and 50 mM, in the presence of salt (0.15 M NaCl) (Figure 10).

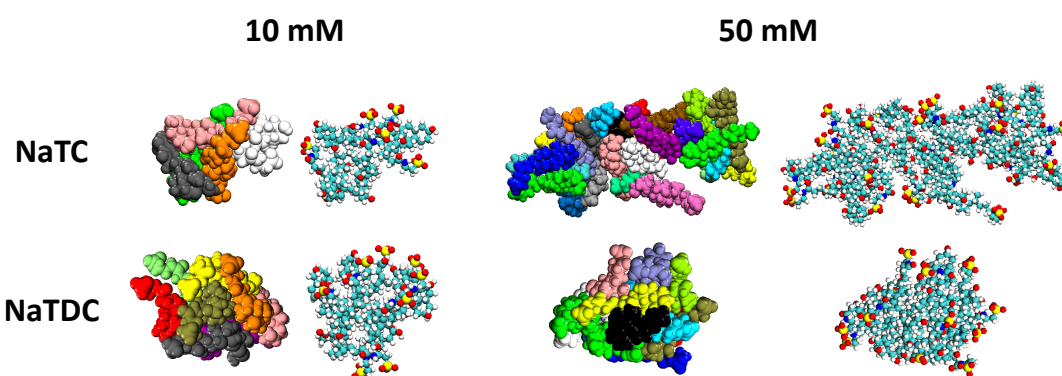


Figure 10: Structure of the micelles of BS (NaTC, NaTDC) formed at different concentrations (10 and 50 mM), in the presence of salt (0.15 M NaCl), obtained with MD simulations. At 10 mM, micelles contain 5 and 8 molecules

for, respectively, NaTC and NaTDC, the remaining BS molecules being isolated in solution as unimers. At 50 mM, two aggregates, containing 12 and 13 molecules, are observed for NaTDC, while one elongated micelle containing all the BS molecules in the system is obtained for NaTC. The largest micelles found in the final snapshots of each simulation (to date) are shown in this figure.

Results show that, for both BS, BS molecules interact *via* the hydrophobic face of their steroid backbone, thus forming an inner hydrophobic core, while their ionic chain and hydroxyl groups are in contact with the water solvent. The snapshots presented here also demonstrate the non-spherical shape of these aggregates, as well as the more marked elongation and more ellipsoid-shaped structure of NaTC upon increasing BS concentration from 10 to 50 mM, as compared with NaTDC, in agreement with the SANS and SAXS data. Nonetheless, contrary to scattering measurements, these computer simulations seem to show larger micellar sizes for NaTC at high BS concentration (50 mM). Further analysis of these MD simulations (over a range of BS concentrations) will confirm these preliminary results.

3.2 Aggregation of BS with FA and/or MAG in the form of mixed micelles, in solution

3.2.1 Shape and size of BS mixed micelles

The scattering from BS micelles in the presence of FA and MAG, typical products obtained from the lipolysis of TAG, was fitted with the same model as that used for BS neat micelles (Figures 11, 12, 13 and 14, Table 8).

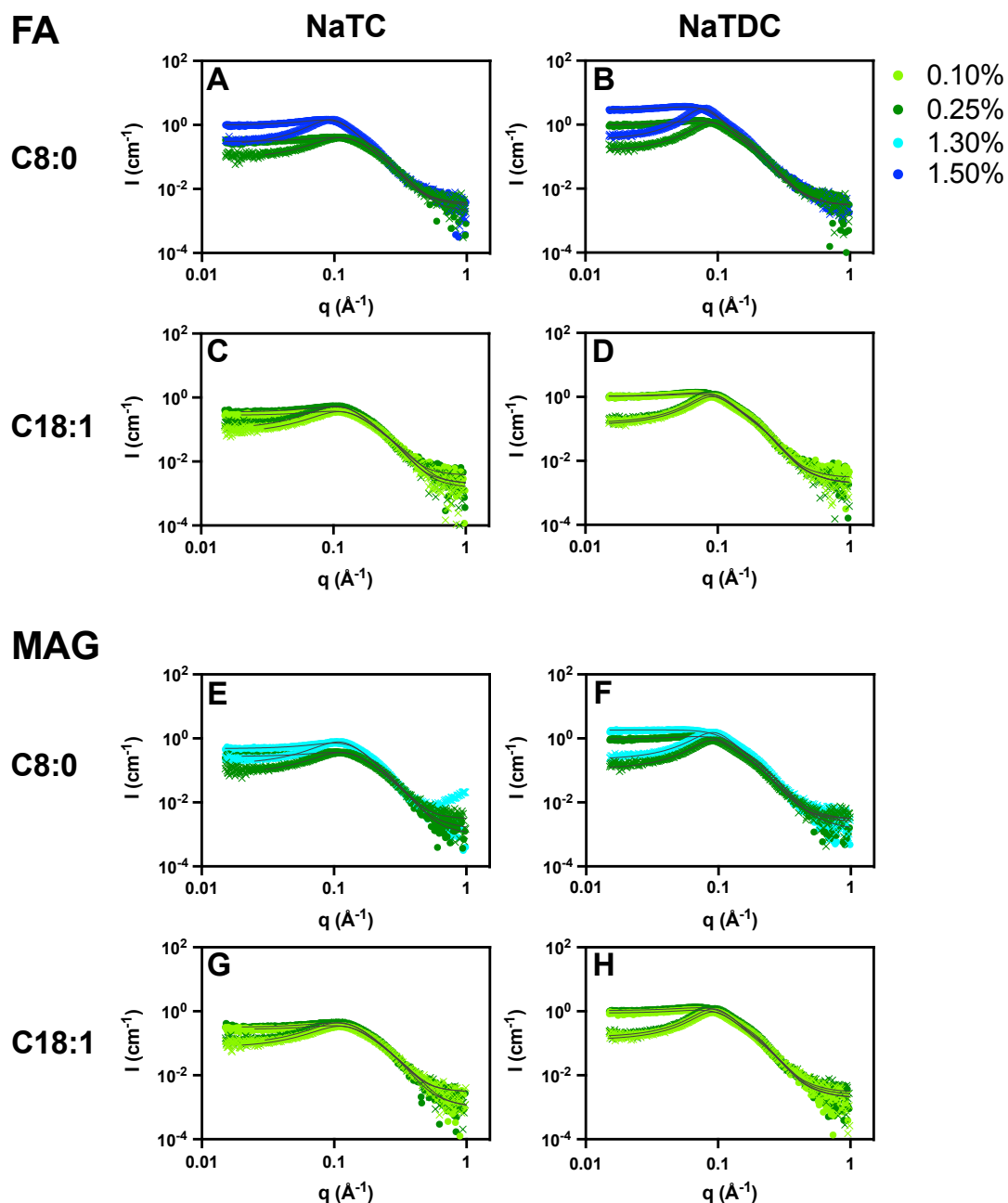


Figure 11: Scattered intensity (I) as a function of the scattering vector (q) for 100 mM BS aqueous solutions of either NaTC (A, C, E, G) or NaTDC (B, D, F, H), mixed with different amounts (from 0.10% to 1.50% w/w) of either FA (A, B, C, D) or MAG (E, F, G, H), with (●) and without (x) 0.15 M NaCl, and measured at 25°C, by SANS. Two types of FA: (A, B) C8:0, (C, D) C18:1, and MAG: (E, F) C8:0, (G, H) C18:1, were employed in this study. Solid lines correspond to fits to the data as described in the text (Equation 2).

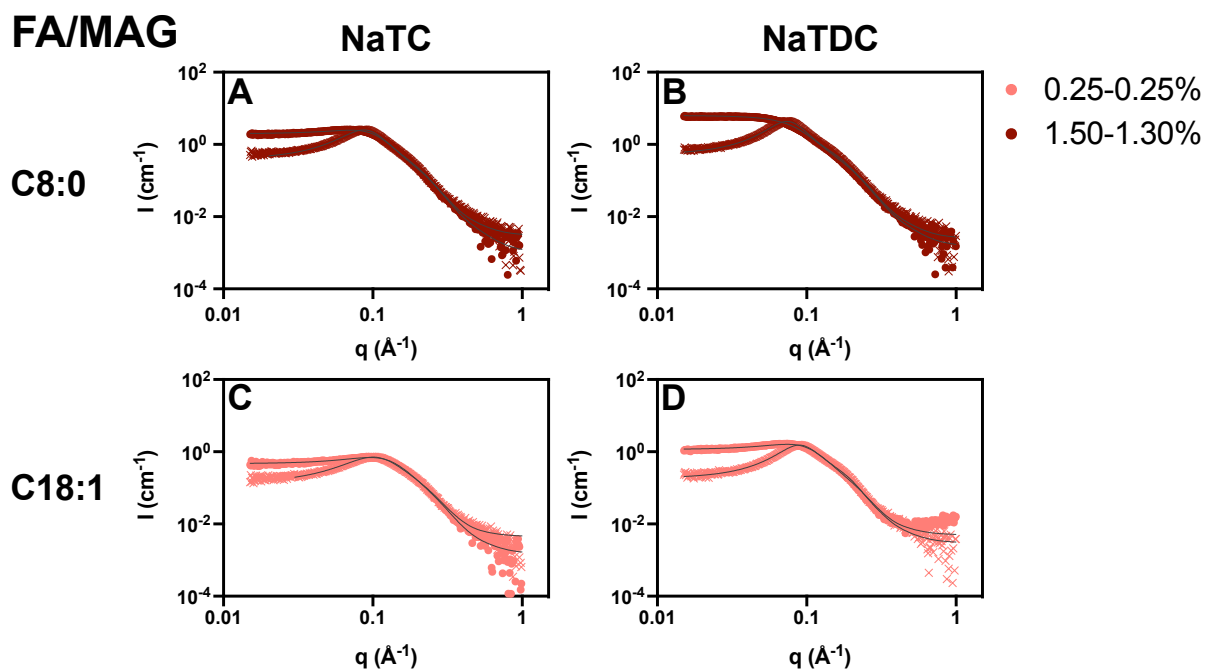


Figure 12: Scattered intensity (I) as a function of the scattering vector (q) for 100 mM BS aqueous solutions of either NaTC (A, C) or NaTDC (B, D), mixed with different amounts (0.25-0.25% and 1.50-1.30% w/w) of either C8:0 (A, B) or C18:1 (C, D) FA-MAG, with (●) and without (x) 0.15 M NaCl, and measured at 25°C, by SANS. Solids lines correspond to fits to the data as described in the text (Equation 2).

Similarly to BS micelles, the low scattering signals ($I(0) < 100 \text{ cm}^{-1}$) and the peaks of interaction, which disappear for most of them in the presence of salt (0.15 M NaCl), suggest that the mixed aggregates formed are relatively small and interact with each other, unless the electrostatic interactions are screened by the addition of a sufficient amount of salt (Figures 11 and 12).

Table 8: Concentration of FA (C8:0 or C18:1) and/or MAG (C8:0 or C18:1) in the sample (*[Additive]*), amount of charges in BS mixed micelle, volume fraction fitted by the software ($\Phi_{software}$), polar (R_{pol}) and equatorial (R_{Eq}) radii values of the (oblate) ellipsoid BS mixed micelle, volume of the BS mixed micelle core ($V_{Mixed\ micelle\ core}$), for each BS studied: NaTC, NaTDC, with and without 0.15 M NaCl. These parameters were obtained from SANS2D data fitting.

NaTC		[Additive] (% w/w)	Charges (e)		$\Phi_{Software}$		R_{Pol} (Å)		R_{Eq} (Å)		$V_{Mixed\ micelle\ core}$ (nm ³)	
			No salt	Salt	No salt	Salt	No salt	Salt	No salt	Salt	No salt	Salt
FA	C8:0	0.25	8	12	0.0321	0.0347	6	5	15	16	5	6
		1.50	13	23	0.0456	0.0471	8	10	20	31	14	41
	C18:1	0.10	8	12	0.0290	0.0327	6	5	14	16	5	6
		0.25	9	16	0.0322	0.0332	7	7	15	16	7	8
MAG	C8:0	0.25	8	12	0.0309	0.0319	6	6	14	15	5	6
		1.30	9	15	0.0422	0.0418	7	7	16	17	8	9
	C18:1	0.10	8	12	0.0286	0.0314	6	5	14	16	5	6
		0.25	8	14	0.0305	0.0312	7	7	15	16	6	7
FA - MAG	C8:0	1.30 - 1.50	14	21	0.0585	0.0577	9	9	23	26	20	24
	C18:1	0.25 - 0.25	9	17	0.0351	0.0360	8	8	17	17	9	9

NaTDC

	[Additive] (% w/w)	Charges (e)		Φ_{Software}		$R_{\text{Pol}} (\text{\AA})$		$R_{\text{Eq}} (\text{\AA})$		$V_{\text{Mixed micelle core}} (\text{nm}^3)$		
		No salt	Salt	No salt	Salt	No salt	Salt	No salt	Salt	No salt	Salt	
FA	C8:0	0.25	17	30	0.0356	0.0359	8	8	20	24	13	18
		1.50	23	36	0.0473	0.0510	10	10	24	31	26	41
	C18:1	0.10	16	22	0.0331	0.0351	8	8	18	23	12	18
		0.25	17	26	0.0356	0.0377	9	8	19	23	13	18
MAG	C8:0	0.25	16	23	0.0294	0.0339	8	8	18	23	11	17
		1.30	15	13	0.0445	0.0435	8	8	21	25	15	21
	C18:1	0.10	16	24	0.0334	0.0327	8	8	19	22	11	16
		0.25	16	22	0.0370	0.0369	9	8	19	23	13	18
FA - MAG	C8:0	1.30 - 1.50	19	15	0.0600	0.0581	10	10	28	35	32	50
	C18:1	0.25 - 0.25	18	28	0.0388	0.0393	10	9	19	23	15	21

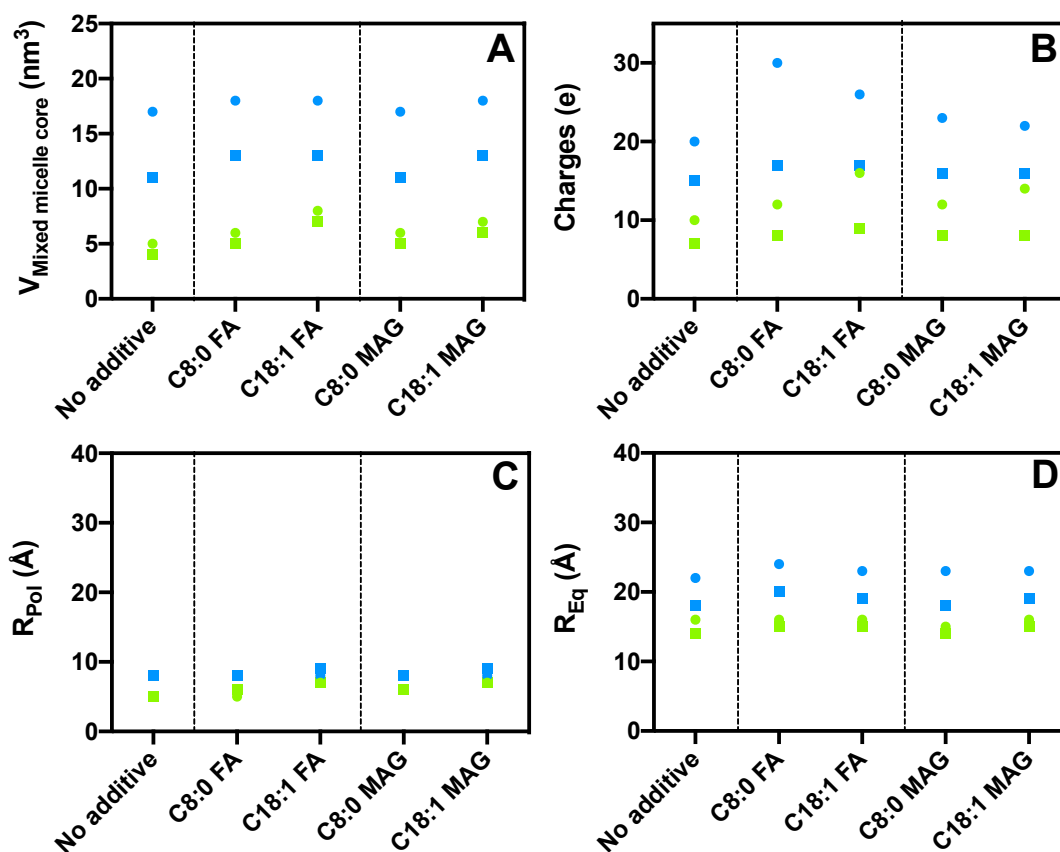


Figure 13: Evolution of (A) the volume of the BS mixed micelle core ($V_{Mixed\ micelle\ core}$), (B) the amount of charges in BS mixed micelle (charges), (C) the polar radius of the BS mixed micelle core (R_{Pol}) and (D) the equatorial radius of the BS mixed micelle core (R_{Eq}) obtained by SANS, as a function of additive type, at a concentration in additive of 0.25% w/w and BS of 100 mM, with and without 0.15 M NaCl: NaTDC: (●) with salt, (■) without salt, NaTC: (●) with salt, (■) without salt.

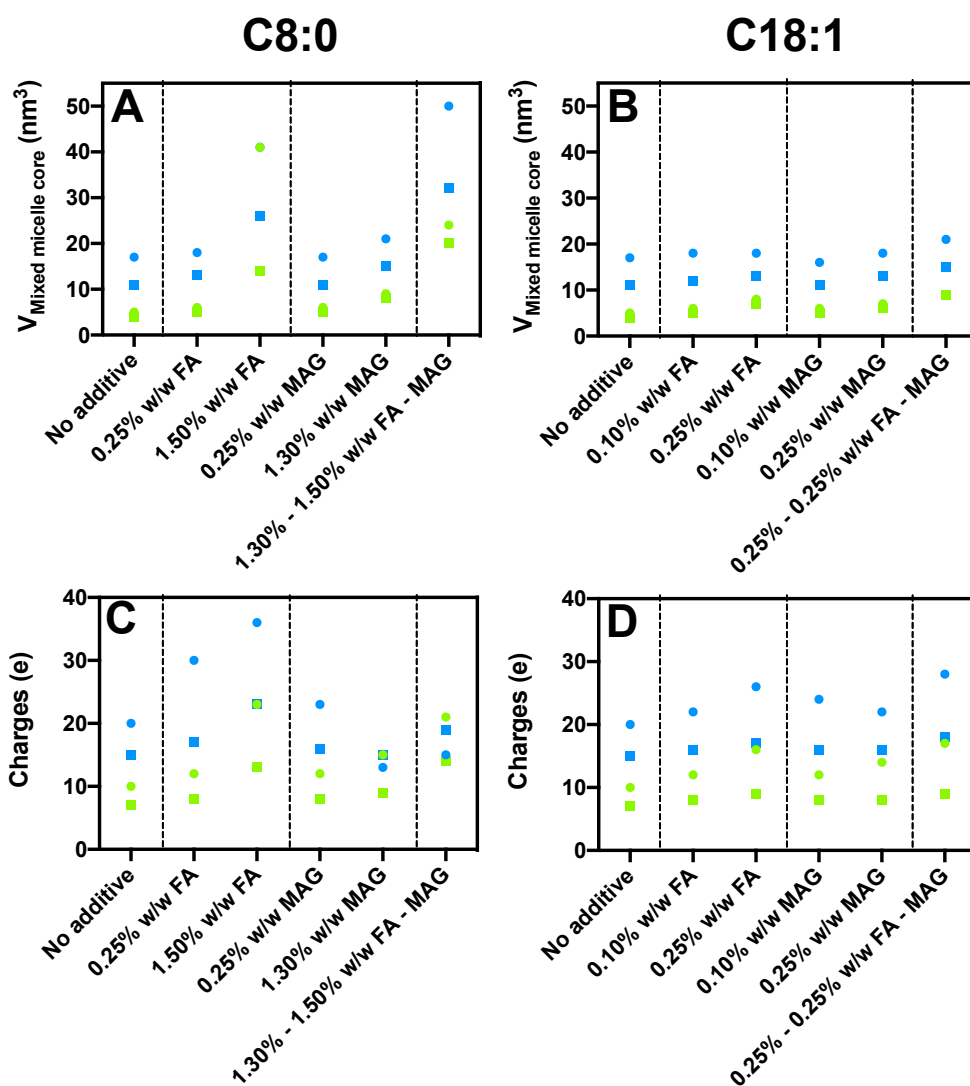
When comparing the results obtained with the same concentration of additive (0.25% w/w), NaTDC was found to form larger mixed micelles (Figures 13, A, C, D, Table 8), bearing a higher amount of charge (Figure 13B, Table 8), compared to NaTC, independently of the ionic strength and type of additive (C8:0 or C18:1 FA or MAG).

As expected, the addition of salt causes an increase in micellar size and charge number under all conditions, and to a relatively higher extent for NaTDC, as compared to NaTC. As for BS micelles, the more efficient aggregation process can be attributed to the screening effect induced by the presence of NaCl.

Furthermore, both the type of additive (FA vs. MAG) and the chain length and saturation (C8:0 vs. C18:1) affect the micellar structure. In the presence of oleic acid

and monoolein (C18:1), BS mixed aggregates display higher core volumes and amounts of charge than with, respectively, caprylic acid and monocaprylin (C8:0), except for NaTDC with salt, where lower charge numbers are obtained. The expected increase in micellar size with increasing lipid chain length has already been observed elsewhere, upon addition of both FA and MAG to BS/phospholipids mixed micelles [72]. The addition of MAG to BS aqueous solution results in slightly smaller and less charged micelles, as compared with mixtures of FA and BS; this difference in charge number is particularly visible for the mixed aggregates formed by NaTDC, in the presence of salt.

The main differences in micellar sizes between NaTC vs. NaTDC, with vs. without salt, C8:0 vs. C18:1 additives, and FA vs. MAG, are in the equatorial radius (R_{Eq}) (Figure 13D, Table 8), while the polar radius (R_{Pol}) does not change much (Figure 13C, Table 8).



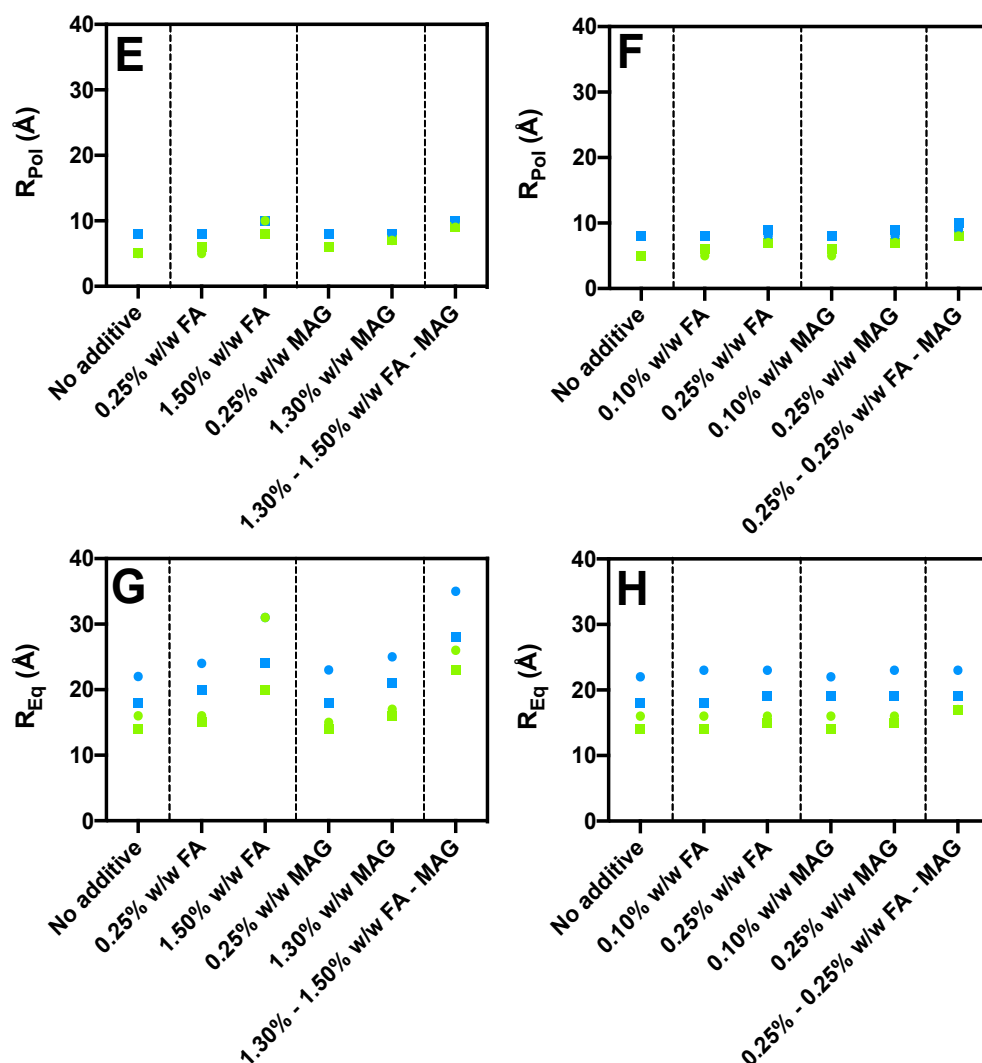


Figure 14: Evolution of (A, B) the volume of the BS mixed micelle core ($V_{Mixed\ micelle\ core}$), (C, D) the amount of charges in BS mixed micelle (charges), (E, F) the polar radius of the BS mixed micelle core (R_{Pol}) and (G, H) the equatorial radius of the BS mixed micelle core (R_{Eq}), obtained by SANS, as a function of additive type and concentration, for C8:0 FA and MAG (A, C, E, G) and C18:1 FA and MAG (B, D, F, H), with a concentration in BS of 100 mM, with and without 0.15 M NaCl: NaTDC: (●) with salt, (■) without salt, NaTC: (●) with salt, (■) without salt.

Independently of the ionic strength and BS type, upon increasing the concentration of additive (from 0% w/w to 0.25% and 1.50% w/w for C8:0 FA, to 0.25% and 1.30% w/w for C8:0 MAG, and to 0.10% and 0.25% w/w for C18:1 FA and MAG), the mixed micelles increase in size, and to a higher extent with C8:0 additives (Figure 14A, Table 8), as compared to C18:1 (Figure 14B, Table 8), – particularly for FA. Such a difference can be explained by the higher amount of additives used with C8:0 FA and MAG, as they can be solubilised to a larger extent. The number of charges held by the mixed micelles was also found to increase with the quantity of additive

for every FA and MAG type, except with NaTDC/MAG, for which a decrease is observed (Figures 14, C, D, Table 8).

NaTDC generally forms larger and more charged aggregates than NaTC. However, in the presence of high amounts of C8:0 MAG and FA/MAG, NaTDC mixed micelles bear a lower amount of charges than NaTC.

Upon the addition of salt, both the size and charge number of the mixed aggregates increase under all conditions, except in the presence of NaTDC with high quantities of C8:0 MAG or FA/MAG. The fact that the same results are not observed with C18:1 MAG and FA/MAG can be due to the too low concentrations employed.

As previously observed, differences in micellar sizes between the different additive concentrations, NaTC vs. NaTDC, and with vs. without salt, are linked to differences in equatorial radius (R_{Eq}) (Figures 14, G, H, Table 8), while the polar radius (R_{Pol}) remains quite constant (Figures 14, E, F, Table 8).

3.3. Solubilisation of TAG-incorporating lipid vesicles into mixed micelles

Prior to evaluating the effect of the two BS (NaTC and NaTDC) on TAG-containing liposomes with SANS, the bilayer structure of each lipid vesicle (in particular, the localisation and organisation of each TAG in the lipid bilayer) was analysed with NR, and the liposomes structure in the bulk aqueous phase with SANS.

3.3.1. DPPC/TAG SLB structure

Using NR, the internal morphology of each TAG-incorporating lipid bilayer (d_{62} -DPPC, d_{62} -DPPC/TC and d_{62} -DPPC/TO) was characterised at the sub-nanometre length scale with contrast variation, by selective deuteration of the solvent (H_2O , H_2O/D_2O and D_2O) (Figures 15 and 16, Table 9).

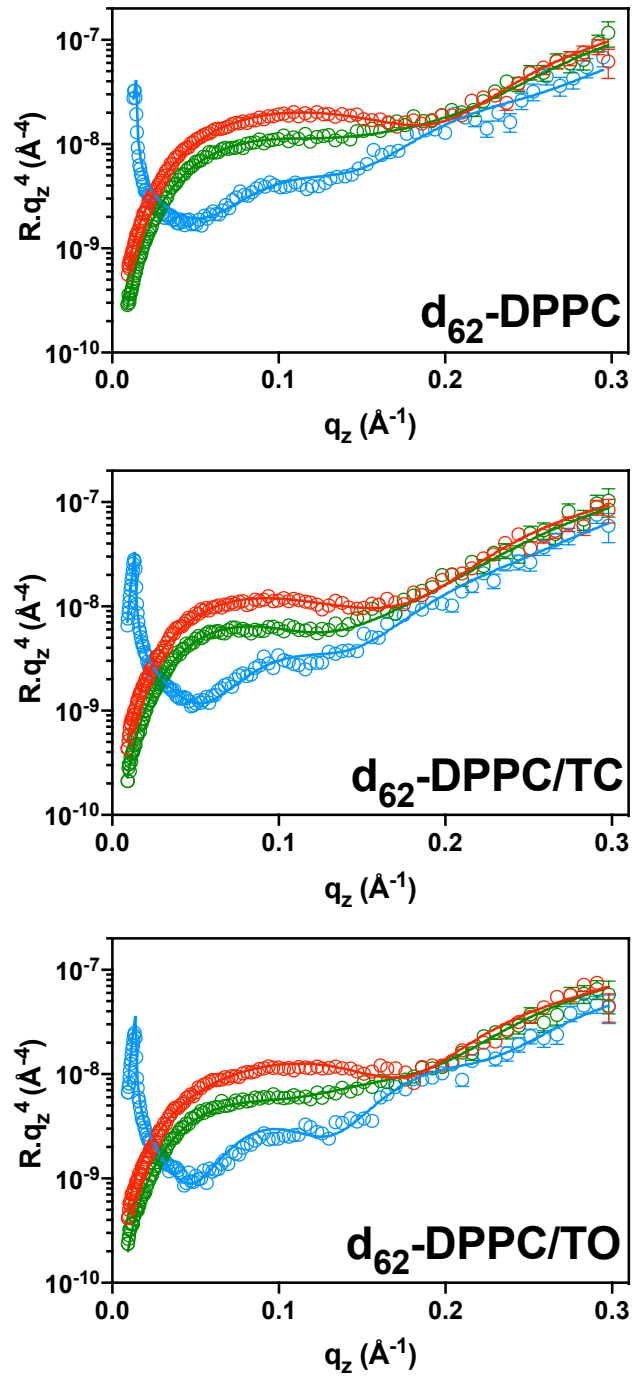


Figure 15: NR signal ($R \cdot q_z^4$ representation) of the TAG-incorporating SLB: d_{62} -DPPC, d_{62} -DPPC/TC, d_{62} -DPPC/TO, in different aqueous phases: (\circ) D_2O , (\circ) SiCMW, (\circ) H_2O , as a function of the scattering vector (q_z).

		d₆₂-DPPC	d₆₂- DPPC/TC	d₆₂- DPPC/TO
SiO₂	σ (Å)	2.0	2.0	2.0
	t (Å)	8	8	8
	SLD (×10⁶) (Å⁻²)	3.41	3.41	3.41
	f_{water}	0	0	0
Water	σ (Å)	3.0	2.1	2.0
	t (Å)	4	5	4
	SLD (×10⁶) (Å⁻²)	0	0	0
	f_{water}	1	1	1
Head group	σ (Å)	2.5	4.4	3.8
	t (Å)	5	5	10
	SLD (×10⁶) (Å⁻²)	1.88	1.88	1.88
	f_{water}	0.06	0.06	0.4
Tails	σ (Å)	2.5	4.4	3.8
	t (Å)	15	15	16
	SLD (×10⁶) (Å⁻²)	6.71	6.41	5.77
	f_{water}	0.02	0	0.06
Additional TAG layer	σ (Å)	1.0	4.4	1.0
	t (Å)	-	2	-
	SLD (×10⁶) (Å⁻²)	-	-0.35	-
	f_{water}	-	0	-
Tails	σ (Å)	-	4.4	-
	t (Å)	15	15	16
	SLD (×10⁶) (Å⁻²)	6.71	6.41	5.77
	f_{water}	0.02	0	0.06
Head group	σ (Å)	2.5	4.4	3.8
	t (Å)	5	5	10
	SLD (×10⁶) (Å⁻²)	1.88	1.88	1.88
	f_{water}	0.06	0.06	0.4
	σ (Å)	2.5	4.4	3.8

Table 9: NR parameters of each upper and lower (tails and head group) layer of the lipid (d₆₂-DPPC, d₆₂-DPPC/TC, d₆₂-DPPC/TO) bilayer: σ , the roughness, t , the thickness, SLD , the scattering length density and f_{water} , the amount of water. The parameters of the silicon oxide (SiO₂) layer and water layer between the block and the upper head group region are also given. For d₆₂-DPPC/TC, an additional layer – corresponding to the incorporation of tricaprilyn between d₆₂-DPPC tails – is present.

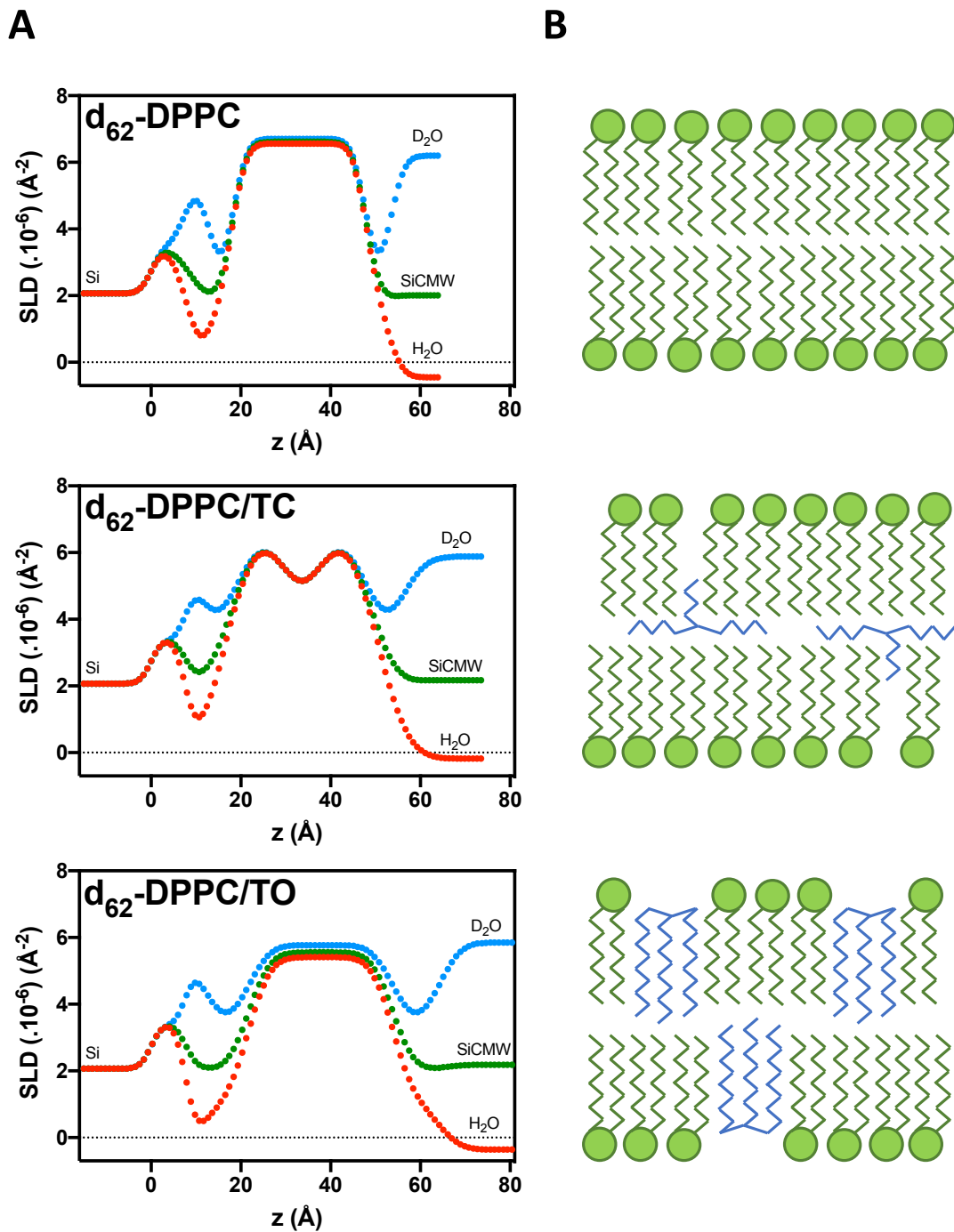


Figure 16: (A) Scattering length density (*SLD*) profile of each SLB: d_{62} -DPPC, d_{62} -DPPC/TC, d_{62} -DPPC/TO, in three different aqueous phases: (●) D_2O , (●) SiCMW, (●) H_2O , along the direction perpendicular to the surface (z), obtained from the analysis of the reflectivity curves measured at $50 \pm 2^\circ\text{C}$. Fits of the experimental data corresponding to these profiles are shown in Figure 15. (B) Schematic representation of each SLB, showing the location and organisation of each TAG (blue molecules) in the DPPC (green molecules) bilayer. Tricaprylin lies between the two tails regions of the DPPC bilayer, with two branches perpendicular to them and one parallel, whereas triolein is incorporated into the tails regions.

As expected, d_{62} -DPPC was found to form a symmetric SLB, with one homogeneous tails region and two hydrophilic head group layers (Figures 15 and 16). The latter were described by exactly the same structural parameters (t , SLD , f_{water}), while the interfacial roughness (σ) was allowed to be decoupled, because of differences likely to occur due to the different media faced by each hydrophilic layer (the solid silicon substrate for the upper layer, the aqueous phase for the lower one) (Table 9).

Several models were tested in order to reproduce the experimental reflectivity curves obtained for the d_{62} -DPPC/TC system: (i) the symmetric SLB model commonly used for pure lipids; (ii) a model in which tricaprylin would be partitioned between the hydrophobic and hydrophilic regions of the bilayer, and oriented parallel to the phospholipid acyl chains; and (iii) a model in which tricaprylin would exhibit a T shape and be localised at the centre of the bilayer, with two branches located between the two lipid tails regions (perpendicular to them) and one inserted among the tails (parallel to them). The model (iii) was the only one able to accurately fit the experimental data (Figures 15 and 16). It was possible to constrain the parameters of the head group layers to those of the pure d_{62} -DPPC SLB, while those of the tails regions and of the additional tricaprylin layer were allowed to vary during the fitting procedure (Table 9). The tricaprylin layer was described by a thickness (t) of 2 Å and SLD of -0.35×10^{-6} Å⁻². The incorporation of tricaprylin increased the interfacial roughness (σ) with respect to the one characterising the pristine d_{62} -DPPC SLB. The presence of the tricaprylin layer is particularly evident from the inspection of the SLD profiles reported in Figure 16A. Tricaprylin molecules may also display a T-shape conformation; nonetheless, these measurements do not allow the determination of the ratio between the two configurations.

Because triolein hydrophilic moiety is quite insignificant as compared to the hydrophobic region, triolein was hypothesised to insert into both lipid tails layers only (i.e., not into their head groups), as suggested elsewhere [46,73]. Data were fitted with a traditional SLB model, with the parameters of the tails regions, as well as those of the head group layers, being let free to vary, and taking into account the presence of triolein molecules within the bilayer (Table 9). Compared to the d_{62} -DPPC/TC SLB, the drop in the tails SLD was uniform, therefore indicating no formation of a central

additional layer (contrary to the less hydrophobic tricaprylin), but the insertion of hydrogenated triolein molecules into d_{62} -DPPC tails, which confirms our assumption (Figures 15 and 16). The considerable rise in both the amount of water in d_{62} -DPPC head groups (f_{water}) and in their layers thickness (t) may be explained by the presence of triolein in the tails, resulting in more solvated head group regions.

In Figure 16B, pictorial sketches depict the molecular arrangement of each TAG in the DPPC bilayer.

3.3.2. Liposomes structure

Using SANS, the morphology of the pure liposomes was analysed in the bulk aqueous phase (Figure 17). Measurements were performed at 25°C. The change in slope observed at around 0.09 \AA^{-1} is characteristic of the presence of a bilayer, thereby indicating a core/shell (or vesicles) structure. The presence of two oscillations in the scattering intensity, at around 0.009 \AA^{-1} and 0.04 \AA^{-1} , could not be reproduced using either a uni-lamellar or a multi-lamellar model. These features give an estimate of the size of the objects in solution (following this relation: $d \sim \frac{2\pi}{q}$); they correspond here to sizes of $\sim 700 \text{ \AA}$ and $\sim 160 \text{ \AA}$, respectively. For this reason, we assumed two contributions to the total scattering intensity, and the best model to use resulted to be the one described by Gerelli *et al.* [63], which considers the presence of both uni- and multi-lamellar vesicles in solution.

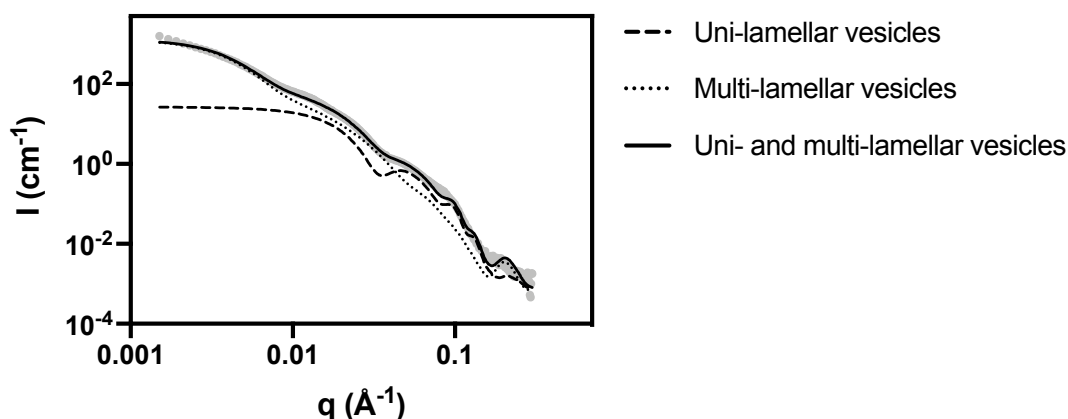


Figure 17: Scattered intensity (I) as a function of the scattering vector (q) for the pure DPPC vesicles (\bullet), measured at 25°C, by SANS. The connecting lines are the trend lines that best fit the data set using the vesicular model described by Gerelli *et al.* [63]; the contributions of both the uni- and multi-lamellar lipid vesicles are shown in this figure.

While the structure of the TAG-incorporating liposomes (DPPC/TC, DPPC/TO) cannot be resolved (uni-lamellar, multi-lamellar, uni-lamellar/uni-lamellar, multi-lamellar/multi-lamellar and uni-lamellar/multi-lamellar models were unsuccessful), the characterisation of DPPC vesicles shows the presence of both uni-lamellar liposomes (characterised by a core radius of 6.7 nm (0.3 polydispersity) and an outer single bilayer (or shell) thickness of 4.4 nm) and larger multi-lamellar liposomes (characterised by an inner core radius of 17.5 nm (0.5 polydispersity) and 4 shells of 4.4 nm thickness each (0.7 polydispersity), separated by a 2.3 nm-thick gap of water). The scattering curves of the pure DPPC/TC and DPPC/TO liposomes, which cannot be analysed, are shown in Figure 18.

3.3.3. Impact of BS on liposomes structure

Following liposomes characterisation, the ability of each BS (NaTC and NaTDC) to convert TAG-incorporating liposomes (DPPC, DPPC/TC and DPPC/TO) into mixed micelles was investigated by probing the effect of BS on lipid vesicles structure at both 25 and 37°C, with SANS (Figures 18, 19 and 20, Table 10). Visual observation was first used to identify the existence of three different phases depending on BS concentration and type: (i) from 5 to 30 mM for NaTC, and from 5 to 10 mM for NaTDC, turbidity decreases, compared to the pure lipid vesicles; (ii) at 50 mM for NaTC, and from 20 to 30 mM for NaTDC, mixtures undergo phase separation over time, giving rise to both a transparent phase and a very opaque one (samples were measured before phase separation was completed); (iii) at 100 mM for NaTC, and 50 mM for NaTDC, solutions look completely transparent. Based on these results, three BS concentrations (10, 50 and 100 mM for NaTC, and 10, 30 and 50 mM for NaTDC) – representative of each phase observed – were selected for this study.

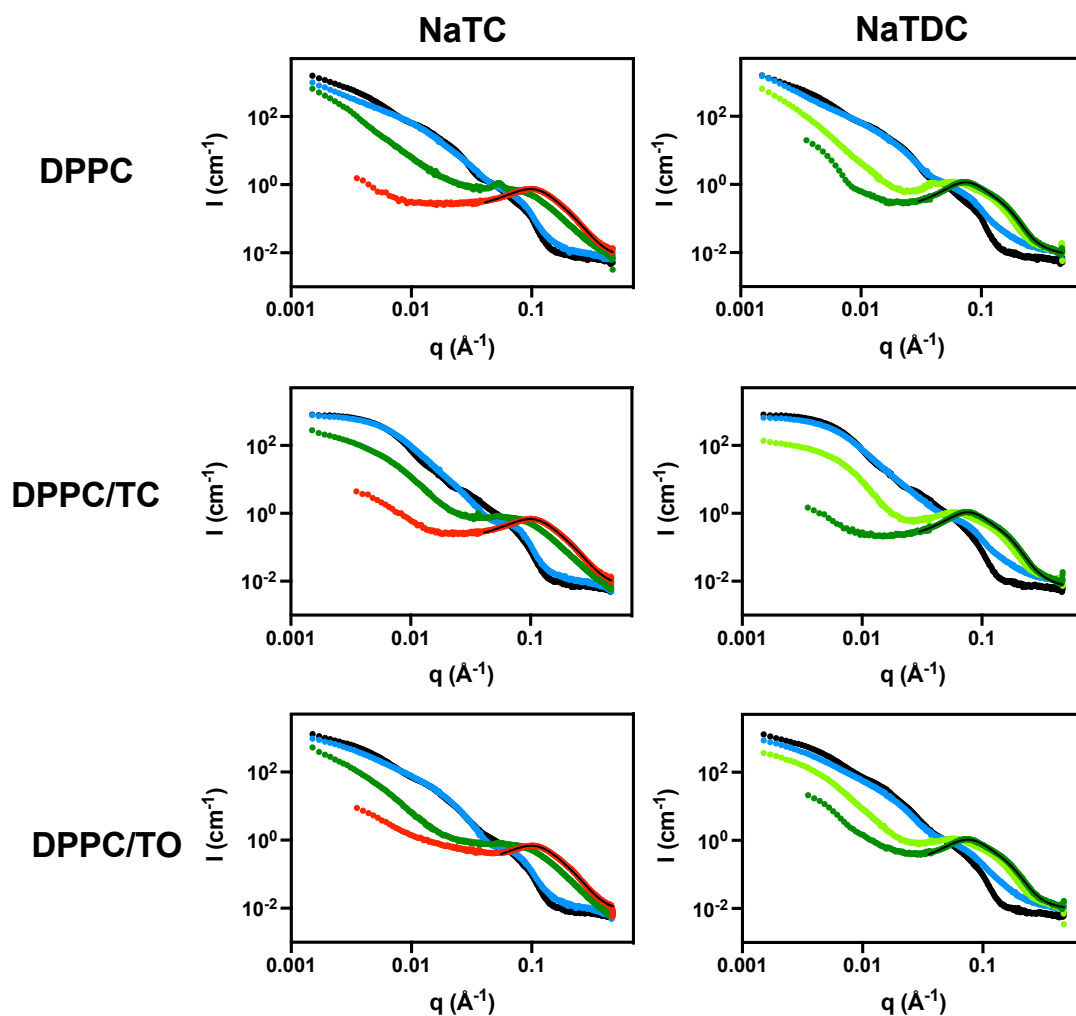


Figure 18: Scattered intensity (I) as a function of the scattering vector (q) for each TAG-incorporating lipid (DPPC, DPPC/TC, DPPC/TO) vesicle, mixed with different amounts: (●) 10 mM, (●) 30 mM, (●) 50 mM, (●) 100 mM, of BS (NaTC, NaTDC), measured at 25°C, by SANS. The scattering curve of the pure liposomes (●) is also shown for comparison. The connecting line is the trend line that best fits the data set (Equation 2).

SANS results confirm the presence of distinct structures in the three different BS concentration ranges chosen (Figure 18): (i) at low concentrations (10 mM for both NaTC and NaTDC), each liposome was found to undergo slight structural changes upon addition of BS and/or the formation of additional structures (high- q region); (ii) in the intermediate concentration range (50 mM for NaTC, 30 mM for NaTDC), the intensity decreases, suggesting solubilisation of some of the vesicles into BS micelles; (iii) at high concentrations (100 mM for NaTC, 50 mM for NaTDC), the signal originates from smaller interacting objects, likely micellar aggregates, while most of the liposomes have disintegrated.

Table 10: Amount of charges in BS mixed micelle, volume fraction fitted by the software ($\Phi_{software}$), polar (R_{Pol}) and equatorial (R_{Eq}) radii values of the (oblate) ellipsoid BS mixed micelle, volume of the BS mixed micelle core ($V_{Mixed\ micelle\ core}$), for the BS mixed micelles formed upon adding either 100 mM NaTC or 50 mM NaTDC, to the three different liposomes: DPPC, DPPC/TC, DPPC/TO. These parameters were obtained from the fitting of D33 data obtained at 25°C.

Liposomes type	Charges (e)		$\Phi_{Software}$		R_{Pol} (Å)		R_{Eq} (Å)		$V_{Mixed\ micelle\ core}$ (nm ³)	
	NaTC	NaTDC	NaTC	NaTDC	NaTC	NaTDC	NaTC	NaTDC	NaTC	NaTDC
DPPC	8	13	0.0374	0.0241	8	11	17	19	9	18
DPPC/TC	8	13	0.0365	0.0245	7	10	17	19	9	16
DPPC/TO	8	11	0.0361	0.0239	8	10	16	19	9	16

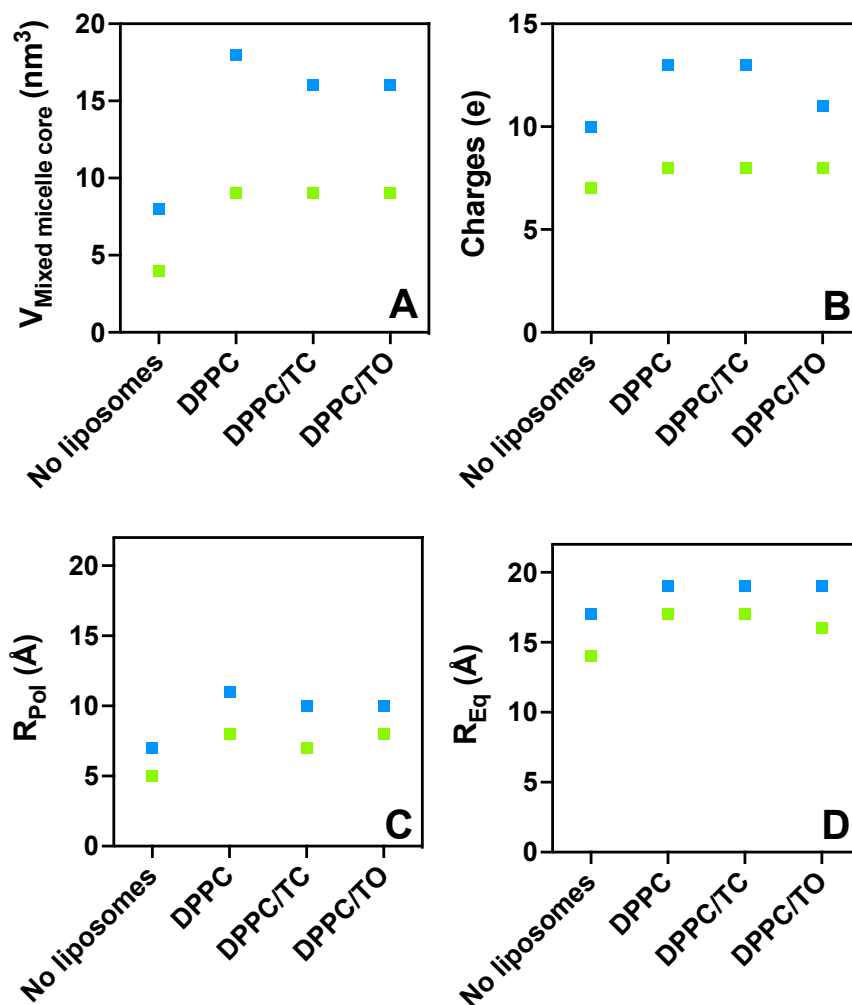


Figure 19: Evolution of (A) the volume of the BS mixed micelle core ($V_{Mixed\ micelle\ core}$), (B) the amount of charges in BS mixed micelle (charges), (C) the polar radius of the BS mixed micelle core (R_{Pol}) and (D) the equatorial radius of the BS mixed micelle core (R_{Eq}) obtained by SANS, as a function of liposome type, for DPPC, DPPC/TC and DPPC/TO vesicles, with either (■) 100 mM NaTC or (■) 50 mM NaTDC. Results obtained with pristine BS micelles, in the absence of liposomes, are also indicated for comparison.

The structures generated upon the addition of low and intermediate quantities of BS could not be analysed using data fitting, due to the presence of multiple structures over a range of length scales, on which no prior size information is available. The disruption of the liposomes morphology is likely to be due to the adsorption and/or incorporation of BS molecules onto/into the vesicles bilayers, as has been suggested elsewhere with sodium cholate [28,30,74–76], sodium deoxycholate [28,30,74] and NaTC [42] in the presence of DPPC vesicles (using various techniques, such as isothermal titration and differential scanning calorimetry,

dynamic light scattering, SANS, turbidity analysis and computer simulations), where this vesicle-to-micelle transition has already been observed.

The scattering from the aggregates formed at high BS concentrations was fitted with the same model used for both BS simple and mixed micelles. The comparison of the structure of these aggregates with the pure BS micelles described in the previous section shows that BS micelles are smaller in size in both dimensions (R_{pol} and R_{Eq}) and bear a smaller charge; the changes observed are more significant with NaTDC (Figure 19, Table 10). These results thereby demonstrate that the addition of BS to liposomes above a threshold concentration (which depends on the type of BS, NaTC vs. NaTDC) leads to the solubilisation of DPPC/TAG vesicles into BS mixed micelles. The increased charge of these aggregates suggests the incorporation of a higher amount of BS in these mixed aggregates, compared to the pure BS micelles; such a phenomenon could be explained by the decrease in BS CMC in the presence of lipids (as has already been observed, e.g., with monoolein [77]); nonetheless, these measurements do not enable the determination of the aggregates composition and organisation. Additionally, compared to NaTC, NaTDC solubilises liposomes at lower concentrations and, as observed for the pristine micelles, its mixed aggregates exhibit larger core radii and charge number.

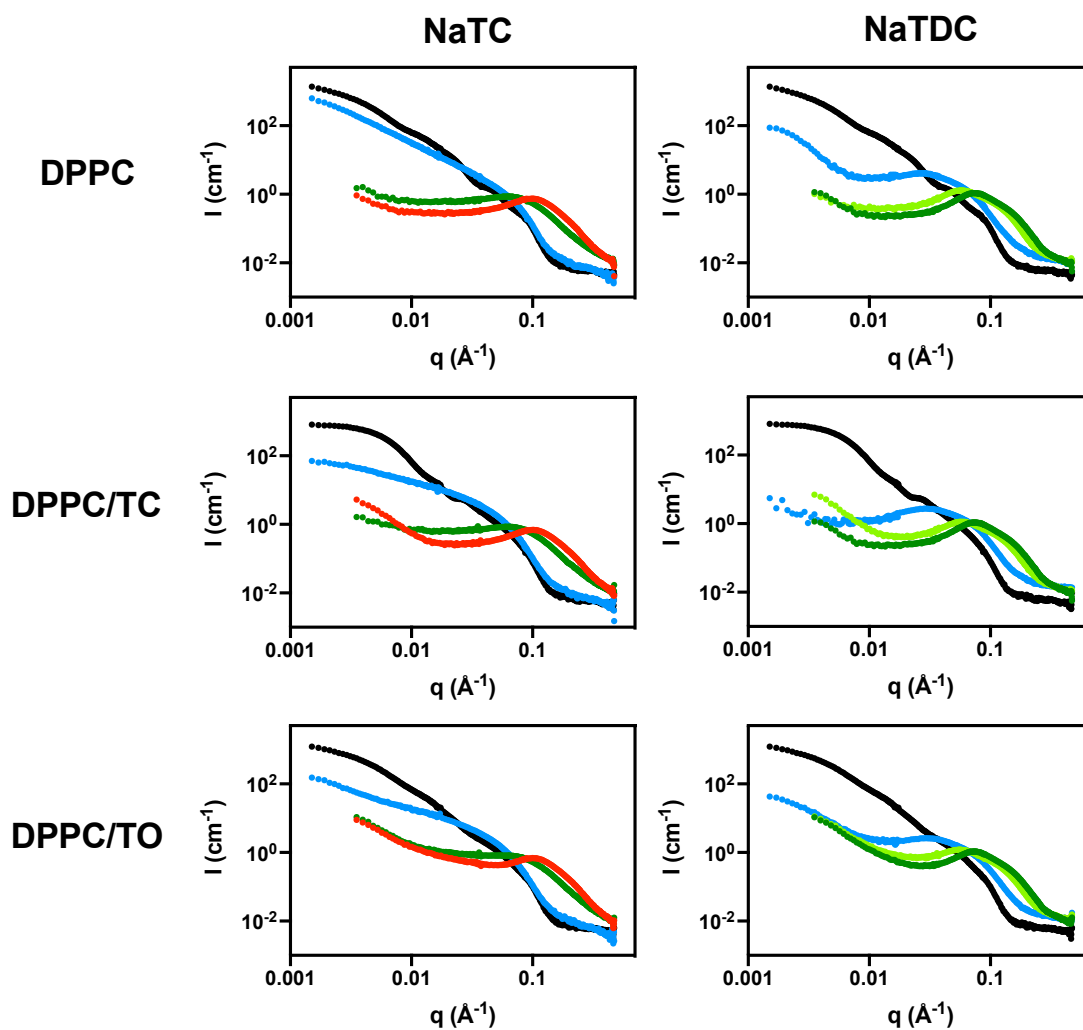


Figure 20: Scattered intensity (I) as a function of the scattering vector (q) for each TAG-incorporating lipid (DPPC, DPPC/TC, DPPC/TO) vesicle, mixed with different amounts: (●) 10 mM, (●) 30 mM, (●) 50 mM, (●) 100 mM, of BS (NaTC, NaTDC), measured at 37°C, by SANS. The scattering curve of the pure liposomes (●) obtained at 37°C, is also shown for comparison.

Interestingly, temperature was found to have a significant impact on the ability of BS to solubilise lipids into mixed micelles (Figure 20). More specifically, at physiological temperature (37°C), as compared to 25°C, liposomes solubilisation occurs at a lower BS concentration for both BS, resulting in a mixed micelles-predominant phase from 50 mM for NaTC (against 100 mM, at 25°C) and 30 mM for NaTDC (against 50 mM, at 25°C). This observation therefore demonstrates the increase in BS solubilisation efficacy with temperature.

The same phases are obtained in the same BS concentration ranges for all the liposomes used (DPPC, DPPC/TC, DPPC/TO), at both temperatures (25 and 37°C),

despite the different locations and positions of TAG in the liposomes highlighted in the NR study (Figures 18 and 20).

4. Discussion

The work presented here aimed to bring insights into the bulk aggregation process of BS, focusing on the role of their molecular architecture, which is hypothesised to control their behaviour at the lipid/water interface and, therefore, would explain their contrasting functionalities during fat digestion [1,2] (Chapters 1 and 2). For this purpose, the structure of BS micelles, as well as of the mixed micelles they form in the presence of FA and/or MAG – the main products of lipolysis –, was characterised, and the ability of BS to solubilise TAG-incorporating liposomes, mimicking ingested lipids, was evaluated. NaTC and NaTDC – two BS differing by the number of hydroxyl groups on their bile acid moiety (Figure 2) – were selected for this study based on our previous work, which had demonstrated that both display distinct adsorption/desorption properties at interfaces [1,2] (Chapters 1 and 2).

4.1. Bulk aggregation behaviour of BS, in the absence and presence of the products of lipolysis

The study of BS aggregation in water by fluorescence spectroscopy, using pyrene as a probe to detect the onset of micellisation, revealed two distinct self-assembly processes for the two BS (Figure 5, Table 6). A distinctive feature of NaTC is that, unlike NaTDC and classic surfactants, its micellisation takes place over a wide range of concentrations; overall, the *CMC* of NaTC ($CMC = 4 - 7$ mM, at 23°C) is higher than that of NaTDC ($CMC = 2$ mM), which correlates with the hydrophobicity of the two BS ($NaTC < NaTDC$) [78]. These contrasting bulk aggregation properties are linked to their interfacial behaviour. Indeed, for both BS, a common feature is that the onset of micellisation in the bulk matches the onset of desorption from phospholipid/water interfaces (which mimic food emulsion surfaces) (Chapters 1 and 2) [1]: below their *CMC*, BS free unimers are able to adsorb onto the surface, whereas the desorption process is triggered by micelle formation, thus explaining why NaTDC desorbs at low concentrations, unlike NaTC, which adsorbs over a wider concentrations range. Both SANS and SAXS measurements allowed the characterisation of the structures (shape and size) and interactions (charge) of BS aggregates over a range of concentrations (Figure 6). The structures were fitted to an oblate ellipsoid model combined with a

Hayter-Penfold structure factor to account for the charge. SAXS data analysis revealed larger (Figure 7A) and much more hydrated (Figure 7B) objects than SANS; this observation suggests that, because of a too low *SLD* contrast between the micellar hydrated shell and D₂O, neutrons are only sensitive to the micellar core, whereas X-rays may detect scattering from the whole micelle. MD simulations support the hypothesis of a 'core/shell', non-spherical micellar structure, showing in particular that BS molecules self-assemble *via* their hydrophobic steroid skeleton, their ionic chain and hydroxyl groups being in contact with the bulk water and thereby forming the outer part (or shell) of the aggregate (Figure 10). The combination of MD simulations and SANS/SAXS data suggests that the micellar shell comprises BS hydrophilic, ionic chains and a significant amount of water, while the core contains the slightly hydrated BS steroid backbones, with the hydrophilic faces (with hydroxyl groups) facing the aqueous solvent. Results from scattering studies also show that, independently of the ionic strength of the BS solution, NaTC aggregates are much smaller than NaTDC aggregates (Figure 7A). Such a size difference between cholate and deoxycholate derivatives has been reported to be due to their different hydrophobic characters. More specifically, results from nuclear magnetic resonance studies suggest that NaTC forms only primary, small aggregates *via* its hydrophobic faces, while the more hydrophobic NaTDC would predominantly associate its hydrophilic side to its hydrophobic face, through the hydrophobic effect [79–81]; the favourable shape matching between the concave hydrophilic face and convex hydrophobic face of NaTDC would therefore facilitate the formation of large aggregates. Interestingly, both BS show a transition from an ellipsoidal to a more spherical shape when increasing BS concentration – which is less marked in the presence of NaTC (Figure 8C). Computer simulations performed elsewhere have revealed similar results, which have been explained by differences in amphiphilicity: contrary to NaTC, which is thought to exhibit face-to-face arrangements due to its separated hydrophobic and hydrophilic faces, NaTDC displays a hydrophilic edge, which would allow a more curved morphology [11]. Additionally, NaTC micelles were found to extend *via* both their polar and equatorial axes, while only the polar radius of NaTDC aggregates increases, thus confirming that the two structurally distinct BS produce micelles following different self-assembly processes (Figures 8, A, B).

During the lipolysis process, products from the lipolysis (FA and MAG) accumulating at the lipid droplet interface are removed from the fat droplet surface by BS and solubilised into mixed micelles. To model how BS structure dictates their interaction with these surface-active components *in vivo* during digestion, the size and shape of systems formed at equilibrium and representing these structures were determined using SANS (Figures 11 and 12). Two types of FA (caprylic acid (C8:0) and oleic acid (C18:1)) and MAG (monocaprylin (C8:0) and monoolein (C18:1)) were employed, individually and in combination, and mixed with 100 mM of each BS.

The addition of FA and/or MAG to BS aqueous solutions was found to result in larger aggregate sizes (Figures 13A and 14, A, B) and higher charge numbers (Figures 13B and 14, C, D), as compared to BS micelles, therefore suggesting the incorporation of additives into BS aggregates, as already shown elsewhere [82,83]; moreover, because the MAG used are uncharged (contrary to the FA, which are deprotonated), the increase in charge quantities shows that further BS molecules may also incorporate into these mixed micelles, which would correlate with the decrease in BS CMC induced by the presence of lipids (as seen with monoolein [77] or sodium oleate [84]). NaTDC, which forms larger micelles than NaTC on its own, was also shown to produce larger (Figures 13A and 14, A, B) and more charged (Figures 13B and 14, C, D) mixed aggregates. With the addition of solute, BS/FA and BS/MAG mixed micelles were seen to increase in size (Figures 13A, and 14, A, B) and charge number (Figures 13B and 14, C, D), thereby showing the incorporation of further additives and/or BS molecules into the aggregates. Nevertheless, above a threshold MAG concentration, the amount of charge held by NaTDC/MAG and NaTDC/FA/MAG mixed micelles was seen to decrease, while it kept rising with the corresponding NaTC mixed aggregates, in particular in the presence of salt (Figures 14, C, D); such a result suggests that the addition of relatively high amounts of MAG induces the removal of some NaTDC molecules from these mixed micelles, but results in the increasing incorporation of NaTC molecules. Interestingly, all the changes in size (between NaTC vs. NaTDC, with vs. without salt, C8:0 vs. C18:1 additives, FA vs. MAG, and the different additives concentrations) were found to be due to changes in equatorial radius (Figures 13, C, D, and 14, E, F, G, H), which indicates that BS ellipsoidal mixed micelles elongate (or shorten) through the equatorial axis. Such a

micellar growth along the aggregate major axis has also been seen with mixed micelles of NaTDC and L-alpha-phosphatidylcholine from egg yolk, upon digestion of triolein oil [83]. This morphological change (or elongation), as well as the leaching of NaTDC molecules from BS/MAG and /FA/MAG mixed micelles, are mechanisms that are consistent with the micelle-to-vesicle transition observed elsewhere upon addition of further lipids to a lipid/BS mixed micelles system [39]. The fact that NaTDC is removed from the aggregates, while NaTC keeps being incorporated, as inferred from changes in charge (Figures 14, C, D), suggests that the process of vesicles formation starts from lower BS concentrations for the more hydrophobic NaTDC, compared with NaTC, in agreement with many studies using dihydroxy vs. trihydroxy conjugates with other polar lipids [28–30,39,74].

4.2. Solubilising capacity of BS

Following our study on BS interaction with a phospholipid (1,2-dipalmitoyl-*sn*-glycero-3-phosphocholine, DPPC) monolayer at both the air/water [1] (Chapter 1) and oil/water (Chapter 2) interfaces – used as, respectively, a preliminary and more physiologically relevant mimic of fat droplet interfaces –, we have modelled ingested lipids using TAG-incorporating liposomes and investigated their fate in the presence of BS.

The characterisation of the lipid/TAG vesicles structure by NR demonstrates that the incorporation of the TAG molecules in the liposomes depends on the TAG structure (i.e., chain length and saturation): more specifically, tricaprylin (or C8:0 TAG) was found to insert into the phospholipid vesicles by forming an additional layer between the two inner tails regions and to incorporate part of its skeleton into the lipid hydrophobic layers; instead, triolein (or C18:1 TAG) was shown to only be embedded in the lipid tails (Figure 16). While the bulk morphology of the TAG-incorporating lipid (DPPC/TC and DPPC/TO) vesicles cannot be resolved, the characterisation of pure DPPC liposomes shows the presence of a mixture of rather polydisperse uni- and multi-lamellar lipid vesicles (Figure 17).

Using SANS, BS were shown to have a substantial impact on liposomes structure, driving a transition from liposomes to mixed micelles (Figures 18 and 20). Compared to NaTC, lower amounts of NaTDC are needed to induce this transition,

leading to a mixed aggregates-predominant phase at 30 mM, compared to 50 mM for NaTC, at 37°C (Figure 20), which correlates with NaTDC higher hydrophobicity [78] and is consistent with observations made in the presence of sodium cholate vs. sodium deoxycholate [28,30,74]. Similarly, when mixing BS with FA and evaluating their solubility limits, NaTDC was found to solubilise higher amounts of FA than NaTC, thus confirming NaTDC higher solubilising efficiency (data not shown); similar observations were made when using other polar lipids, like MAG [77], phospholipids [28–30,39,74] and lecithin [33] in the presence of different dihydroxy and trihydroxy conjugates. Therefore, this study provides evidence that NaTDC exhibits a better solubilising capacity than NaTC, which supports our working hypothesis, i.e., deoxycholate-based BS are more likely to be involved in the incorporation of lipolysis products into mixed aggregates, for absorption in the gut mucosa, as compared to cholate derivatives, which, instead, may have a higher efficacy at facilitating enzymes adsorption onto the surface of fat droplets. The globular shape observed with BS/phospholipids or BS/FA and/or /MAG mixed micelles is consistent with results from numerous studies [12,26,83,85,86,33,34,36,40,41,72,76,82]. Previous computer simulations work has suggested that these small mixed micelles form with the hydrophobic region of the lipophilic component (in the case of this study, DPPC tails) in close contact with the hydrophobic face of BS (in that case, sodium cholate), while the BS hydrophilic part faces the aqueous solvent [76]; in another study, MD simulations combined with SAXS measurements have shown that these globular aggregates may exhibit a molecular organisation similar to the one observed with cylindrical mixed micelles, i.e., a hydrophobic core mainly made up of the lipids tails and a hydrophilic shell rich in BS molecules and lipids head groups [12]. SANS measurements would need to be performed using the contrast-variation method (i.e., with deuterated components) to confirm BS mixed micelles structural organisation.

5. Conclusion

Our working hypothesis is that the contrasting roles played by BS during the process of fat digestion may be explained by the architectural differences in their bile acid part; we therefore compared the aggregation properties of two BS, NaTC and NaTDC, as well as their solubilising capacity in the presence of liposomes mimicking ingested lipids.

Bulk behaviour studies show that the two structurally distinct BS follow two widely different micellisation processes, which correlate with their differences in hydrophobicity: more specifically, NaTC self-assembly occurs gradually (between 4 – 7 mM), whereas the more hydrophobic NaTDC exhibits a lower CMC (2 mM). These contrasting bulk aggregation properties – which are linked to their molecular structure – are correlated to their interfacial behaviour. The structural characterisation of BS micelles with both SANS and SAXS, combined with MD simulations, reveals that the aggregates display an ellipsoidal shape made up of a hydrophobic core containing BS steroid skeleton and a more hydrophilic shell composed of their ionic chain and water. Additionally, NaTDC was found to form more spherical and larger micelles than NaTC, and to exhibit a micellar growth along one preferential direction, contrary to NaTC, whose aggregates were seen to increase in size *via* both directions. All these results clearly confirm that the two BS selected in this study display very distinct self-assembly behaviours, which would explain their different interfacial properties and, therefore, their contrasting roles during the process of fat digestion. Nonetheless, further structural characterisations and atomistic simulations are required to obtain a clear and detailed molecular picture of the arrangement of BS molecules in their micelles.

The products of lipolysis (FA and MAG, in this study) were incorporated into BS micelles, resulting in micellar elongation, with NaTDC forming again larger mixed aggregates than NaTC. Interestingly, as inferred from changes in charge, NaTDC molecules are present in a lower quantity in NaTDC/MAG and NaTDC/FA/MAG mixed micelles, as compared with NaTDC micelles, and are further removed from the aggregates upon increasing MAG concentration; this very hypothetical result will

need to be confirmed by future SANS and/or SAXS studies using the contrast-variation method (i.e., with deuterated additives), which will enable the determination of the exact location and arrangement of the different micellar components.

The study of the interaction of BS with TAG-incorporating liposomes – which mimics a fat droplet being approached by BS molecules – shows the complete solubilisation of the vesicles into mixed micelles and highlights the better solubilising capacity of NaTDC, as compared to NaTC. A mechanistic understanding of how BS disturb these liposomes (e.g., do they incorporate into or adsorb onto the liposomes bilayer; if incorporating, do they go into the outer layer or deeper into the bilayer; do they form intermediate structures with vesicles, before generating ellipsoidal mixed micelles; etc), as well as a structural characterisation of the organisation of both BS and lipids in ellipsoidal mixed aggregates, still need to be provided. Consequently, in the future, the evolution of the bilayer morphology upon addition of BS will be studied with NR, and the contrast-variation method will be applied with SANS to give further insight into the structure of the mixed micelles formed. This information is key to unlocking the mechanisms whereby BS incorporate lipolysis products into mixed micelles, before transporting them to the gut mucosa, where they are absorbed.

References

- [1] O. Pabois, C.D. Lorenz, R.D. Harvey, I. Grillo, M.M.-L. Grundy, P.J. Wilde, Y. Gerelli, C.A. Dreiss, Molecular insights into the behaviour of bile salts at interfaces: a key to their role in lipid digestion, *J. Colloid Interface Sci.* 556 (2019) 266–277. doi:10.1016/j.jcis.2019.08.010.
- [2] R. Parker, N.M. Rigby, M.J. Ridout, A.P. Gunning, P.J. Wilde, The adsorption–desorption behaviour and structure function relationships of bile salts, *Soft Matter*. 10 (2014) 6457–6466. doi:10.1039/c4sm01093k.
- [3] L. Galantini, M.C. di Gregorio, M. Gubitosi, L. Travaglini, J.V. Tato, A. Jover, F. Meijide, V.H. Soto Tellini, N. V. Pavel, Bile salts and derivatives: rigid unconventional amphiphiles as dispersants, carriers and superstructure building blocks, *Curr. Opin. Colloid Interface Sci.* 20 (2015) 170–182. doi:10.1016/j.cocis.2015.08.004.
- [4] S.R. Euston, Molecular simulation of biosurfactants with relevance to food systems, *Curr. Opin. Colloid Interface Sci.* 28 (2017) 110–119. doi:10.1016/j.cocis.2017.04.002.
- [5] D. Madenci, S.U. Egelhaaf, Self-assembly in aqueous bile salt solutions, *Curr. Opin. Colloid Interface Sci.* 15 (2010) 109–115. doi:10.1016/j.cocis.2009.11.010.
- [6] M.C. Carey, Micelle formation by bile salts, *Arch. Intern. Med.* 130 (1972) 506–527. doi:10.1001/archinte.1972.03650040040005.
- [7] L.B. Pártay, P. Jedlovsky, M. Sega, Molecular aggregates in aqueous solutions of bile acid salts. Molecular dynamics simulation study, *J. Phys. Chem. B.* 111 (2007) 9886–9896. doi:10.1021/jp072974k.
- [8] A. Vila Verde, D. Frenkel, Kinetics of formation of bile salt micelles from coarse-grained Langevin dynamics simulations, *Soft Matter*. 12 (2016) 5172–5179. doi:10.1039/C6SM00763E.
- [9] F. Mustan, A. Ivanova, G. Madjarova, S. Tcholakova, N. Denkov, Molecular

- dynamics simulation of the aggregation patterns in aqueous solutions of bile salts at physiological conditions, *J. Phys. Chem. B.* 119 (2015) 15631–15643. doi:10.1021/acs.jpcc.5b07063.
- [10] N.A. Mazer, M.C. Carey, R.F. Kwasnick, G.B. Benedek, Quasielastic light scattering studies of aqueous biliary lipid systems. Size, shape, and thermodynamics of bile salt micelles, *Biochemistry.* 18 (1979) 3064–3075. doi:10.1021/bi00581a024.
- [11] L.B. Pártay, M. Sega, P. Jedlovszky, Morphology of bile salt micelles as studied by computer simulation methods, *Langmuir.* 23 (2007) 12322–12328. doi:10.1021/la701749u.
- [12] A.J. Clulow, A. Parrow, A. Hawley, J. Khan, A.C. Pham, P. Larsson, C.A.S. Bergström, B.J. Boyd, Characterization of solubilizing nanoaggregates present in different versions of simulated intestinal fluid, *J. Phys. Chem. B.* 121 (2017) 10869–10881. doi:10.1021/acs.jpcc.7b08622.
- [13] J. Santhanalakshmi, G.S. Lakshmi, V.K. Aswal, P.S. Goyal, Small-angle neutron scattering study of sodium cholate and sodium deoxycholate interacting micelles in aqueous medium, *J. Chem. Sci.* 113 (2001) 55–62. doi:10.1007/BF02708552.
- [14] D.B. Warren, D.K. Chalmers, K. Hutchison, W. Dang, C.W. Pouton, Molecular dynamics simulations of spontaneous bile salt aggregation, *Colloids Surfaces A Physicochem. Eng. Asp.* 280 (2006) 182–193. doi:10.1016/j.colsurfa.2006.02.009.
- [15] G. Mangiapia, G. D'Errico, F. Capuano, O. Ortona, R.K. Heenan, L. Paduano, R. Sartorio, On the interpretation of transport properties of sodium cholate and sodium deoxycholate in binary and ternary aqueous mixtures, *Phys. Chem. Chem. Phys.* 13 (2011) 15906–15917. doi:10.1039/c1cp20922a.
- [16] S. Cozzolino, L. Galantini, C. Leggio, N.V. Pavel, Correlation between small-angle X-ray scattering spectra and apparent diffusion coefficients in the study of structure and interaction of sodium taurodeoxycholate micelles, *J. Phys.*

Chem. B. 109 (2005) 6111–6120. doi:10.1021/jp044540k.

- [17] A.A. D'Archivio, L. Galantini, A. Panatta, E. Tettamanti, On the growth and shape of sodium taurodeoxycholate micellar aggregates: a spin-label and quasielastic light scattering investigation, *J. Chem. Phys.* 120 (2004) 4800–4807. doi:10.1063/1.1645513.
- [18] F. Lopez, J. Samseth, K. Mortensen, E. Rosenqvist, J. Rouch, Micro- and macrostructural studies of sodium deoxycholate micellar complexes in aqueous solutions, *Langmuir*. 12 (1996) 6188–6196. doi:10.1021/la960006v.
- [19] H. Matsuoka, J.P. Kratochvil, N. Ise, Small-angle X-ray scattering from solutions of bile salts: sodium taurodeoxycholate in aqueous electrolyte solutions, *J. Colloid Interface Sci.* 118 (1987) 387–396. doi:10.1016/0021-9797(87)90474-7.
- [20] S. Cozzolino, L. Galantini, E. Giglio, S. Hoffmann, C. Leggio, N.V. Pavel, Structure of sodium glycodeoxycholate micellar aggregates from small-angle X-ray scattering and light-scattering techniques, *J. Phys. Chem. B.* 110 (2006) 12351–12359. doi:10.1021/jp060712x.
- [21] H. Kawamura, Y. Murata, T. Yamaguchi, H. Igimi, M. Tanaka, G. Sugihara, J.P. Kratochvil, Spin-label studies of bile salt micelles, *J. Phys. Chem.* 93 (1989) 3321–3326. doi:10.1021/j100345a087.
- [22] A.R. Campanelli, S. Candeloro De Sanctis, E. Giglio, N. Viorel Pavel, C. Quagliata, From crystal to micelle: a new approach to the micellar structure, *J. Incl. Phenom. Mol. Recognit. Chem.* 7 (1989) 391–400. doi:10.1007/BF01079774.
- [23] E. Bottari, A.A. D'Archivio, M.R. Festa, L. Galantini, E. Giglio, Structure and composition of sodium taurocholate micellar aggregates, *Langmuir*. 15 (1999) 2996–2998. doi:10.1021/la9809630.
- [24] L. Galantini, E. Giglio, N.V. Pavel, F. Punzo, QELS and X-ray study of two dihydroxy bile salt aqueous solutions, *Colloids Surfaces A Physicochem. Eng. Asp.* 248 (2004) 79–84. doi:10.1016/j.colsurfa.2004.06.044.

- [25] D.M. Small, M.C. Bourgès, D.G. Dervichian, The biophysics of lipidic associations. I. The ternary systems lecithin-bile salt-water, *Biochim. Biophys. Acta.* 125 (1966) 563–580. doi:10.1016/0005-2760(66)90044-0.
- [26] J. Gustafsson, T. Nylander, M. Almgren, H. Ljusberg-Wahren, Phase behavior and aggregate structure in aqueous mixtures of sodium cholate and glycerol monooleate, *J. Colloid Interface Sci.* 211 (1999) 326–335. doi:10.1006/jcis.1998.5996.
- [27] M. Svaerd, P. Schurtenberger, K. Fontell, B. Joensson, B. Lindman, Micelles, vesicles, and liquid crystals in the monoolein-sodium taurocholate-water system: phase behavior, NMR, self-diffusion, and quasi-elastic light scattering studies, *J. Phys. Chem.* 92 (1988) 2261–2270. doi:10.1021/j100319a034.
- [28] P. Garidel, A. Hildebrand, K. Knauf, A. Blume, Membranolytic activity of bile salts: influence of biological membrane properties and composition, *Molecules.* 12 (2007) 2292–2326. doi:10.3390/12102292.
- [29] A. Hildebrand, K. Beyer, R. Neubert, P. Garidel, A. Blume, Temperature dependence of the interaction of cholate and deoxycholate with fluid model membranes and their solubilization into mixed micelles, *Colloids Surfaces B Biointerfaces.* 32 (2003) 335–351. doi:10.1016/j.colsurfb.2003.08.001.
- [30] A. Hildebrand, R. Neubert, P. Garidel, A. Blume, Bile salt induced solubilization of synthetic phosphatidylcholine vesicles studied by isothermal titration calorimetry, *Langmuir.* 18 (2002) 2836–2847. doi:10.1021/la011421c.
- [31] L. Forte, K. Andrieux, G. Keller, C. Grabielle-Madelmont, S. Lesieur, M. Paternostre, M. Ollivon, C. Bourgaux, P. Lesieur, Sodium taurocholate-induced lamellar-micellar phase transitions of DPPC, *J. Therm. Anal. Calorim.* 51 (1998) 773–782. doi:10.1007/BF03341454.
- [32] G.A. Kossena, B.J. Boyd, C.J.H. Porter, W.N. Charman, Separation and characterization of the colloidal phases produced on digestion of common formulation lipids and assessment of their impact on the apparent solubility of selected poorly water-soluble drugs, *J. Pharm. Sci.* 92 (2003) 634–648.

doi:10.1002/jps.10329.

- [33] M.A. Long, E.W. Kaler, S.P. Lee, Structural characterization of the micelle-vesicle transition in lecithin-bile salt solutions, *Biophys. J.* 67 (1994) 1733–1742. doi:10.1016/S0006-3495(94)80647-2.
- [34] R.P. Hjelm, P. Thiyagarajan, H. Alkan, A small-angle neutron scattering study of the effects of dilution on particle morphology in mixtures of glycocholate and lecithin, *J. Appl. Crystallogr.* 21 (1988) 858–863. doi:10.1107/S002188988800531X.
- [35] P. Schurtenberger, M. Svärd, E. Wehrli, B. Lindman, Vesicle formation in aqueous solutions of bile salt and monoacylglycerol, *Biochim. Biophys. Acta.* 882 (1986) 465–468. doi:10.1016/0304-4165(86)90271-0.
- [36] R.P. Hjelm, C. Schteingart, A.F. Hofmann, D.S. Sivia, Form and structure of self-assembling particles in monoolein-bile salt mixtures, *J. Phys. Chem.* 99 (1995) 16395–16406. doi:10.1021/j100044a030.
- [37] R.P. Hjelm, P. Thiyagarajan, H. Alkan-Onyuksel, Organization of phosphatidylcholine and bile salt in rodlike mixed micelles, *J. Phys. Chem.* 96 (1992) 8653–8661. doi:10.1021/j100200a080.
- [38] D. Madenci, A. Salonen, P. Schurtenberger, J.S. Pedersen, S.U. Egelhaaf, Simple model for the growth behaviour of mixed lecithin–bile salt micelles, *Phys. Chem. Chem. Phys.* 13 (2011) 3171–3178. doi:10.1039/C0CP01700K.
- [39] W.A. Birru, D.B. Warren, A. Ibrahim, H.D. Williams, H. Benameur, C.J.H. Porter, D.K. Chalmers, C.W. Pouton, Digestion of phospholipids after secretion of bile into the duodenum changes the phase behavior of bile components, *Mol. Pharm.* 11 (2014) 2825–2834. doi:10.1021/mp500193g.
- [40] A. Walter, P.K. Vinson, A. Kaplun, Y. Talmon, Intermediate structures in the cholate-phosphatidylcholine vesicle-micelle transition, *Biophys. J.* 60 (1991) 1315–1325. doi:10.1016/S0006-3495(91)82169-5.
- [41] M.A. Kiselev, M. Janich, A. Hildebrand, P. Strunz, R.H.H. Neubert, D. Lombardo,

- Structural transition in aqueous lipid/bile salt [DPPC/NaDC] supramolecular aggregates: SANS and DLS study, *Chem. Phys.* 424 (2013) 93–99. doi:10.1016/j.chemphys.2013.05.014.
- [42] K. Andrieux, L. Forte, S. Lesieur, M. Paternostre, M. Ollivon, C. Grabielle-Madelmont, Solubilisation of dipalmitoylphosphatidylcholine bilayers by sodium taurocholate: a model to study the stability of liposomes in the gastrointestinal tract and their mechanism of interaction with a model bile salt, *Eur. J. Pharm. Biopharm.* 71 (2009) 346–355. doi:10.1016/j.ejpb.2008.09.004.
- [43] A.F. Hofmann, B. Borgström, The intraluminal phase of fat digestion in man: the lipid content of the micellar and oil phases of intestinal content obtained during fat digestion and absorption, *J. Clin. Invest.* 43 (1964) 247–257. doi:10.1172/JCI104909.
- [44] K. Kalyanasundaram, J.K. Thomas, Environmental effects on vibronic band intensities in pyrene monomer fluorescence and their application in studies of micellar systems, *J. Am. Chem. Soc.* 99 (1977) 2039–2044. doi:10.1021/ja00449a004.
- [45] M. Buchweitz, P.A. Kroon, G.T. Rich, P.J. Wilde, Quercetin solubilisation in bile salts: a comparison with sodium dodecyl sulphate, *Food Chem.* 211 (2016) 356–364. doi:10.1016/j.foodchem.2016.05.034.
- [46] J.A. Hamilton, Interactions of triglycerides with phospholipids: incorporation into the bilayer structure and formation of emulsions, *Biochemistry.* 28 (1989) 2514–2520. doi:10.1021/bi00432a025.
- [47] R.J. Deckelbaum, J.A. Hamilton, A. Moser, G. Bengtsson-Olivecrona, E. Butbul, Y.A. Carpentier, A. Gutman, T. Olivecrona, Medium-chain versus long-chain triacylglycerol emulsion hydrolysis by lipoprotein lipase and hepatic lipase: implications for the mechanisms of lipase action, *Biochemistry.* 29 (1990) 1136–1142. doi:10.1021/bi00457a006.
- [48] J.A. Hamilton, D.M. Small, Solubilization and localization of triolein in

- phosphatidylcholine bilayers: a ^{13}C NMR study., *Proc. Natl. Acad. Sci.* 78 (1981) 6878–6882. doi:10.1073/pnas.78.11.6878.
- [49] C. Rojas, T. Olivecrona, G. Bengtsson-Olivecrona, Comparison of the action of lipoprotein lipase on triacylglycerols and phospholipids when presented in mixed liposomes or in emulsion droplets, *Eur. J. Biochem.* 197 (1991) 315–321. doi:10.1111/j.1432-1033.1991.tb15913.x.
- [50] D. Guard-Friar, C.-H. Chen, A.S. Engle, Deuterium isotope effect on the stability of molecules: phospholipids, *J. Phys. Chem.* 89 (1985) 1810–1813. doi:10.1021/j100255a054.
- [51] J. Webster, S. Holt, R. Dalgliesh, INTER the chemical interfaces reflectometer on target station 2 at ISIS, *Phys. B.* 385–386 (2006) 1164–1166. doi:10.1016/j.physb.2006.05.400.
- [52] O. Arnold, J.C. Bilheux, J.M. Borreguero, A. Buts, S.I. Campbell, L. Chapon, M. Doucet, N. Draper, R. Ferraz Leal, M.A. Gigg, V.E. Lynch, A. Markvardsen, D.J. Mikkelson, R.L. Mikkelson, R. Miller, K. Palmen, P. Parker, G. Passos, T.G. Perring, P.F. Peterson, S. Ren, M.A. Reuter, A.T. Savici, J.W. Taylor, R.J. Taylor, R. Tolchenov, W. Zhou, J. Zikovsky, Mantid - Data analysis and visualization package for neutron scattering and μ SR experiments, *Nucl. Instruments Methods Phys. Res. A.* 764 (2014) 156–166. doi:10.1016/j.nima.2014.07.029.
- [53] Y. Gerelli, Aurore: new software for neutron reflectivity data analysis, *J. Appl. Crystallogr.* 49 (2016) 330–339. doi:10.1107/S1600576716000108.
- [54] Y. Gerelli, Phase transitions in a single supported phospholipid bilayer: real-time determination by neutron reflectometry, *Phys. Rev. Lett.* 122 (2019) 248101-1-248101–5. doi:10.1103/PhysRevLett.122.248101.
- [55] P. Van Vaerenbergh, J. Léonardon, M. Sztucki, P. Boesecke, J. Gorini, L. Claustre, F. Sever, J. Morse, T. Narayanan, An upgrade beamline for combined wide, small and ultra small-angle x-ray scattering at the ESRF, in: *AIP Conf. Proc.*, 2016: pp. 030034-1-030034–4. doi:10.1063/1.4952857.
- [56] R.K. Heenan, S.E. Rogers, D. Turner, A.E. Terry, J. Treadgold, S.M. King, Small

- angle neutron scattering using Sans2d, *Neutron News*. 22 (2011) 19–21. doi:10.1080/10448632.2011.569531.
- [57] C.D. Dewhurst, I. Grillo, D. Honecker, M. Bonnaud, M. Jacques, C. Amrouni, A. Perillo-Marcone, G. Manzin, R. Cubitt, The small-angle neutron scattering instrument D33 at the Institut Laue-Langevin, *J. Appl. Crystallogr.* 49 (2016) 1–14. doi:10.1107/S1600576715021792.
- [58] Institut Laue-Langevin, The LAMP software application available for the ILL spectrometers, (2018). <https://www.ill.eu/fr/users/support-labs-infrastructure/software-scientific-tools/lamp/> (accessed August 23, 2018).
- [59] SasView for small angle scattering analysis, (2018). www.sasview.org (accessed August 22, 2018).
- [60] J.-P. Hansen, J.B. Hayter, A rescaled MSA structure factor for dilute charged colloidal dispersions, *Mol. Phys.* 46 (1982) 651–656. doi:10.1080/00268978200101471.
- [61] J.B. Hayter, J. Penfold, An analytic structure factor for macroion solutions, *Mol. Phys.* 42 (1981) 109–118. doi:10.1080/00268978100100091.
- [62] D. Madenci, Study of the aggregation behaviour of egg yolk lecithin/bile salt mixtures by increasing the ionic strength, The University of Edinburgh, 2009. <http://hdl.handle.net/1842/4918>.
- [63] Y. Gerelli, M.T. Di Bari, A. Deriu, L. Cantù, P. Colombo, C. Como, S. Motta, F. Sonvico, R. May, Structure and organization of phospholipid/polysaccharide nanoparticles, *J. Phys. Condens. Matter.* 20 (2008) 104211–104218. doi:10.1088/0953-8984/20/10/104211.
- [64] K. Vanommeslaeghe, E. Hatcher, C. Acharya, S. Kundu, S. Zhong, J. Shim, E. Darian, O. Guvench, P. Lopes, I. Vorobyov, A.D. Mackerell Jr., CHARMM general force field: a force field for drug-like molecules compatible with the CHARMM all-atom additive biological force fields, *J. Comput. Chem.* 31 (2010) 671–690. doi:10.1002/jcc.21367.

- [65] W.L. Jorgensen, J. Chandrasekhar, J.D. Madura, R.W. Impey, M.L. Klein, Comparison of simple potential functions for simulating liquid water, *J. Chem. Phys.* 79 (1983) 926–935. doi:10.1063/1.445869.
- [66] W.E. Reiher, *Theoretical studies of hydrogen bonding*, Harvard University, 1985.
- [67] S. Hashimoto, J.K. Thomas, Photophysical studies of pyrene in micellar sodium taurocholate at high salt concentrations, *J. Colloid Interface Sci.* 102 (1984) 152–163. doi:10.1016/0021-9797(84)90209-1.
- [68] G. Li, L.B. McGown, Model for bile salt micellization and solubilization from studies of a “polydisperse” array of fluorescent probes and molecular modeling, *J. Phys. Chem.* 98 (1994) 13711–13719. doi:10.1021/j100102a043.
- [69] K. Matsuoka, M. Maeda, Y. Moroi, Micelle formation of sodium glyco- and taurocholates and sodium glyco- and taurodeoxycholates and solubilization of cholesterol into their micelles, *Colloids Surfaces B Biointerfaces.* 32 (2003) 87–95. doi:10.1016/S0927-7765(03)00148-6.
- [70] B. Mukherjee, A.A. Dar, P.A. Bhat, S.P. Moulik, A.R. Das, Micellization and adsorption behaviour of bile salt systems, *RSC Adv.* 6 (2016) 1769–1781. doi:10.1039/C5RA20909A.
- [71] A.F. Hofmann, K.J. Mysels, Bile salts as biological surfactants, *Colloids and Surfaces.* 30 (1987) 145–173. doi:10.1016/0166-6622(87)80207-X.
- [72] S. Phan, S. Salentinig, E. Gilbert, T.A. Darwish, A. Hawley, R. Nixon-Luke, G. Bryant, B.J. Boyd, Disposition and crystallization of saturated fatty acid in mixed micelles of relevance to lipid digestion, *J. Colloid Interface Sci.* 449 (2015) 160–166. doi:10.1016/j.jcis.2014.11.026.
- [73] H. Khandelia, L. Duelund, K.I. Pakkanen, J.H. Ipsen, Triglyceride blisters in lipid bilayers: implications for lipid droplet biogenesis and the mobile lipid signal in cancer cell membranes, *PLoS One.* 5 (2010) 1–8. doi:10.1371/journal.pone.0012811.

- [74] A. Hildebrand, K. Beyer, R. Neubert, P. Garidel, A. Blume, Solubilization of negatively charged DPPC/DPPG liposomes by bile salts, *J. Colloid Interface Sci.* 279 (2004) 559–571. doi:10.1016/j.jcis.2004.06.085.
- [75] H.-J. Mögel, M. Wahab, R. Schmidt, P. Schiller, Computer simulation of the solubilization of liposomes by bile salts, *Chem. Lett.* 41 (2012) 1066–1068. doi:10.1246/cl.2012.1066.
- [76] M. Haustein, P. Schiller, M. Wahab, H.-J. Mögel, Computer simulations of the formation of bile salt micelles and bile salt/DPPC mixed micelles in aqueous solutions, *J. Solution Chem.* 43 (2014) 1755–1770. doi:10.1007/s10953-014-0239-3.
- [77] A.F. Hofmann, The function of bile salts in fat absorption. The solvent properties of dilute micellar solutions of conjugated bile salts., *Biochem. J.* 89 (1963) 57–68. doi:10.1042/bj0890057.
- [78] M.J. Armstrong, M.C. Carey, The hydrophobic-hydrophilic balance of bile salts. Inverse correlation between reverse-phase high performance liquid chromatographic mobilities and micellar cholesterol-solubilizing capacities., *J. Lipid Res.* 23 (1982) 70–80. <http://www.ncbi.nlm.nih.gov/pubmed/7057113>.
- [79] N. Funasaki, M. Fukuba, T. Hattori, S. Ishikawa, T. Okuno, S. Hirota, Micelle formation of bile salts and zwitterionic derivative as studied by two-dimensional NMR spectroscopy, *Chem. Phys. Lipids.* 142 (2006) 43–57. doi:10.1016/j.chemphyslip.2006.02.025.
- [80] N. Funasaki, M. Fukuba, T. Kitagawa, M. Nomura, S. Ishikawa, S. Hirota, S. Neya, Two-dimensional NMR study on the structures of micelles of sodium taurocholate, *J. Phys. Chem. B.* 108 (2004) 438–443. doi:10.1021/jp030899h.
- [81] K. Matsuoka, A. Yamamoto, Study on micelle formation of bile salt using nuclear magnetic resonance spectroscopy, *J. Oleo Sci.* 66 (2017) 1129–1137. doi:10.5650/jos.ess17063.
- [82] R.P. Hjelm, C.D. Scheingart, A.F. Hofmann, P. Thiyagarajan, Structure of conjugated bile salt-fatty acid-monoglyceride mixed colloids: studies by small-

- angle neutron scattering, *J. Phys. Chem. B.* 104 (2000) 197–211. doi:10.1021/jp992157n.
- [83] O. Rezhdo, S. Di Maio, P. Le, K.C. Littrell, R.L. Carrier, S.-H. Chen, Characterization of colloidal structures during intestinal lipolysis using small-angle neutron scattering, *J. Colloid Interface Sci.* 499 (2017) 189–201. doi:10.1016/j.jcis.2017.03.109.
- [84] A. Hildebrand, P. Garidel, R. Neubert, A. Blume, Thermodynamics of demicellization of mixed micelles composed of sodium oleate and bile salts, *Langmuir.* 20 (2004) 320–328. doi:10.1021/la035526m.
- [85] S. Salentinig, S. Phan, T.A. Darwish, N. Kirby, B.J. Boyd, E.P. Gilbert, pH-responsive micelles based on caprylic acid, *Langmuir.* 30 (2014) 7296–7303. doi:10.1021/la500835e.
- [86] M. Almgren, Mixed micelles and other structures in the solubilization of bilayer lipid membranes by surfactants, *Biochim. Biophys. Acta.* 1508 (2000) 146–163. doi:10.1016/S0005-2736(00)00309-6.

Chapter 4

Interactions of bile salts with a dietary fibre, methylcellulose, and impact on lipolysis

Co-authors contribution to the publication

The rheology measurements were carried out by Xi Zhao (M. Sc. student, King's College London, UK), Jasmin Omar (M. Pharm. student, King's College London, UK) and Faizah Ahmed (M. Pharm. student, King's College London, UK); the interfacial experiments by Amandine Antoine-Michard (M. Eng. student, Ecole Nationale Supérieure des Ingénieurs en Arts Chimiques et Technologiques, France), Jasmin Omar, Florian Alexis (M. Eng. student, Ecole Nationale Supérieure de Chimie de Lille, France) and I; the optical microscopy study by Amandine Antoine-Michard; the confocal microscopy observations by Xi Zhao, Faizah Ahmed and I, with the help of Dr Balazs Bajka; and the pH-stat measurements by Xi Zhao, Jasmin Omar and Faizah Ahmed. All these students (Amandine Antoine-Michard, Xi Zhao, Jasmin Omar, Faizah Ahmed and Florian Alexis) worked under my supervision.

Dr Richard D. Harvey (Institut für Pharmazie, Martin-Luther-Universität Halle-Wittenberg, Germany), Dr Myriam M.-L. Grundy (School of Agriculture, Policy and Development, University of Reading, UK), Dr Balazs Bajka (Department of Nutritional Sciences, King's College London, UK) and Prof Peter J. Wilde (Quadram Institute Bioscience, UK) provided advices and feedback as to the experimental work and manuscript.

Dr Cécile A. Dreiss (Institute of Pharmaceutical Science, King's College London, UK), Dr Yuri Gerelli (Institut Laue-Langevin, France) and Dr Isabelle Grillo (Institut Laue-Langevin, France) supervised the project.



Contents lists available at ScienceDirect

Carbohydrate Polymers

journal homepage: www.elsevier.com/locate/carbpol

Interactions of bile salts with a dietary fibre, methylcellulose, and impact on lipolysis



Olivia Paboïs^{a,b}, Amandine Antoine-Michard^a, Xi Zhao^b, Jasmin Omar^b, Faizah Ahmed^b, Florian Alexis^a, Richard D. Harvey^c, Isabelle Grillo^a, Yuri Gerelli^a, Myriam M.-L. Grundy^d, Balazs Bajka^e, Peter J. Wilde^f, Cécile A. Dreiss^{b,*}

^a Institut Laue-Langevin, Grenoble, 38000, France

^b Institute of Pharmaceutical Science, King's College London, London, SE1 9NH, United Kingdom

^c Institut für Pharmazie, Martin-Luther-Universität Halle-Wittenberg, Halle (Saale), 06099, Germany

^d School of Agriculture, Policy and Development, University of Reading, Reading, RG6 6AR, United Kingdom

^e Department of Nutritional Sciences, King's College London, London, SE1 9NH, United Kingdom

^f Quadram Institute Bioscience, Norwich Research Park, Norwich, NR4 7UA, United Kingdom

ARTICLE INFO

Keywords:

Methylcellulose

Bile salts

Rheology

Surface pressure measurements

In vitro duodenal lipolysis

ABSTRACT

Methylcellulose (MC) has a demonstrated capacity to reduce fat absorption, hypothetically through bile salt (BS) activity inhibition. We investigated MC cholesterol-lowering mechanism, and compared the influence of two BS, sodium taurocholate (NaTC) and sodium taurodeoxycholate (NaTDC), which differ slightly by their architecture and exhibit contrasting functions during lipolysis.

BS/MC bulk interactions were investigated by rheology, and BS behaviour at the MC/water interface studied with surface pressure and ellipsometry measurements. *In vitro* lipolysis studies were performed to evaluate the effect of BS on MC-stabilised emulsion droplets microstructure, with confocal microscopy, and free fatty acids release, with the pH-stat method.

Our results demonstrate that BS structure dictates their interactions with MC, which, in turn, impact lipolysis. Compared to NaTC, NaTDC alters MC viscoelasticity more significantly, which may correlate with its weaker ability to promote lipolysis, and desorbs from the interface at lower concentrations, which may explain its higher propensity to destabilise emulsions.

1. Introduction

Obesity and associated health risks (such as chronic cardiovascular diseases and type-2-diabetes mellitus) have become increasingly prevalent worldwide. In 2016, 39% of the world's adult population were classified as overweight, and 13% as obese (World Health Organization, 2019). Controlling the digestion of dietary lipids (fats) and optimising their absorption are therefore crucial to addressing this ongoing health crisis (McClements & Li, 2010b; Mei, Lindqvist, Krabisch, Rehfeld, & Erlanson-Albertsson, 2006). With their demonstrated capability to reduce food intake and aid weight loss, dietary fibres have shown great potential against obesity (Slavin, 2005). Nonetheless, a better understanding of the processes responsible for their ability to regulate calorie

uptake still needs to be provided. Due to its approved (Younes et al., 2018) and wide (The Dow Chemical Company, 2002) use in the food industry, as well as its proven capacity to diminish blood cholesterol levels (without inducing any adverse effect) (Agostoni et al., 2010), methylcellulose (MC) is an appropriate model of dietary fibre for elucidating the mechanism by which dietary fibres reduce hyperlipidaemia.

MC is a non-ionic polysaccharide belonging to the large family of cellulose ethers and containing repeating anhydroglucose units, with methyl (hydrophobic) moieties substituting hydroxyl (hydrophilic) groups (Nasatto et al., 2015b) (Fig. 1). The capacity of this dietary fibre to hinder lipolysis has been mainly attributed to its ability to induce loss of bile salts (BS) and cholesterol in faeces by (i) increasing the viscosity

* Corresponding author at: King's College London, Institute of Pharmaceutical Science, Franklin-Wilkins Building, 150 Stamford Street, SE1 9NH, London, UK.

E-mail addresses: olivia.pabois@kcl.ac.uk (O. Pabois), amandine-03@hotmail.fr (A. Antoine-Michard), xi.zhao@kcl.ac.uk (X. Zhao), jasmin.1.omar@kcl.ac.uk (J. Omar), faizah.ahmed@kcl.ac.uk (F. Ahmed), floalexis0@gmail.com (F. Alexis), richard.harvey@pharmazie.uni-halle.de (R.D. Harvey), grillo@ill.fr (I. Grillo), gerelli@ill.fr (Y. Gerelli), m.m.grundy@reading.ac.uk (M.M.-L. Grundy), balazs.bajka@kcl.ac.uk (B. Bajka), peter.wilde@quadram.ac.uk (P.J. Wilde), cecile.dreiss@kcl.ac.uk (C.A. Dreiss).

<https://doi.org/10.1016/j.carbpol.2019.115741>

Received 10 September 2019; Received in revised form 10 December 2019; Accepted 13 December 2019

Available online 16 December 2019

0144-8617/© 2019 Elsevier Ltd. All rights reserved.

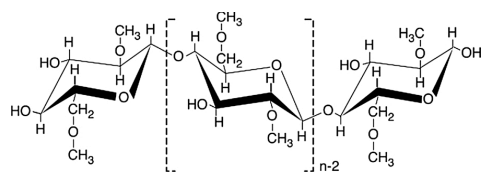


Fig. 1. Structure of methylcellulose (MC).

of the small intestine content (Reppas, Meyer, Sirois, & Dressman, 1991), which slows down fat digestion and reduces nutrients absorption (Bartley et al., 2010; Carr, Gallaher, Yang, & Hassel, 1996; Maki et al., 2009; Reppas, Swidan, Tobey, Turowski, & Dressman, 2009; van der Gronde, Hartog, van Hees, Pellikaan, & Pieters, 2016), and/or by (ii) trapping BS and/or cholesterol molecules in its network, via hydrophobic interactions occurring both in the bulk aqueous phase and at the fat droplet interface (Pilosof, 2017; Pizonos Ruiz-Henestrosa, Bellesi, Camino, & Pilosof, 2017; Torcello-Gómez & Foster, 2014; Torcello-Gómez et al., 2015). BS are biosurfactants produced in the liver and released into the small intestine (duodenum) (Hofmann & Mysels, 1987), which play key roles in lipid digestion and absorption (Maldonado-Valderrama, Wilde, Macierzanka, & Mackie, 2011; Wilde & Chu, 2011): on the one hand, they facilitate enzyme adsorption to fat droplet interfaces, thus promoting enzyme-catalysed lipolysis (Borgström, Erlanson-Albertsson, & Wieloch, 1979; Bourbon Freie, Ferrato, Carrière, & Lowe, 2006; Erlanson-Albertsson, 1983; Labourdenne, Brass, Ivanova, Cagna, & Verger, 1997); on the other, they remove the enzyme-inhibiting insoluble lipolysis products (diacylglycerols (DAG), monoacylglycerols (MAG) and free fatty acids (FFA)) present at the interface, carrying them to the gut mucosa for absorption (Hofmann & Mysels, 1987). In this work, we are focusing on the interactions between MC and BS, which have been hypothesised to explain (i) MC cholesterol-lowering effect, due to the reduction in BS reabsorption in the ileum and the subsequent increased production of BS by the liver from cholesterol, and (ii) the early signalling of satiation and lengthening of satiety feeling, by the accumulation of undigested materials in the duodenum, due to BS being entrapped and prevented from fulfilling their functions during lipolysis (Gunniss & Gidley, 2010). Recent studies have demonstrated BS inhibitory effect on MC thermally-induced structuring using microcalorimetry and rheology (Torcello-Gómez & Foster, 2014; Torcello-Gómez et al., 2015), and the competition of BS with MC for adsorption at the lipid droplet/water interface with tensiometry (Torcello-Gómez & Foster, 2014). However, there is little structural evidence for the hypothesis of entrapment of BS by MC, and a mechanistic understanding of the competitive processes leading to enzyme inhibition, delayed fat digestion and the associated health benefits, is still lacking. Therefore, further studies are required to clarify how MC interacts with BS during lipid digestion and how this, in turn, correlates to BS molecular structure and their contrasting roles.

The work presented here increases our understanding of the mechanisms underlying MC capacity to regulate fat digestion in the small intestine, with a particular focus on its ability to compete with BS for adsorption at the lipid droplet/water interface. More specifically, by combining bulk and interfacial experiments with *in vitro* lipolysis studies, we examined the interactions between MC and BS in bulk water, at the MC/water interface, and at the oil/water interface of fat droplets mimicking food colloids. It has been hypothesised that BS structural diversity is responsible for the different functions they carry out in fat digestion; to explore this postulate, two BS, sodium taurocholate (NaTC) and sodium taurodeoxycholate (NaTDC) (Fig. 2), were selected, as they display contrasting adsorption/desorption dynamics, which are thought to reflect their different roles in the gut (Pabois et al., 2019; Parker, Rigby, Ridout, Gunning, & Wilde, 2014). Since BS are expected to interact with MC both in the bulk aqueous phase and at the surface of MC-stabilised emulsion droplets, we assessed the impact of BS on MC

rheological properties, using oscillatory shear rheology, and BS/MC interfacial behaviour at the air/water interface, through surface pressure measurements in a Langmuir trough set-up and ellipsometry. We then investigated how these interactions affect the lipolysis of an MC-stabilised emulsion, by monitoring the structure of emulsion droplets after addition of BS and enzymes, with different optical microscopy techniques, and by measuring the amount of FFA released throughout *in vitro* lipid digestion, with the pH-stat method.

2. Experimental section

2.1. Materials

Methocel™ SG A7C (solution viscosity: 700 mPa.s at 2% w/w at 20 °C; methoxyl degree of substitution: 1.8; molecular weight: 400–500 kDa) (Fig. 1) was kindly supplied by Dow Wolff Cellulosics GmbH (Bomlitz, Germany). Chloroform (CHCl₃) was purchased from Fisher Scientific (Loughborough, UK). NaTC (P97.0% TLC) (Fig. 2A), NaTDC (P95.0% TLC) (Fig. 2B), paraffin oil, ethanol (EtOH, P99.8% GC), orlistat (P98.0%), Nile red, fluorescent brightener 28 (calcofluor), dimethyl sulfoxide anhydrous (P99.9%), sunflower seed oil from *Helianthus annuus*, pancreatin from porcine pancreas (or pancreatic lipase/co-lipase; activity: 40 U/mg of solid, based on lipase activity using tributyrin as a substrate), sodium phosphate monobasic dihydrate (NaH₂PO₄, P99.0% T), sodium phosphate dibasic dihydrate (Na₂HPO₄, P99.0% T), sodium chloride (NaCl, P99.8%), calcium chloride dihydrate (CaCl₂, P99.0%) and sodium hydroxide (NaOH, 0.1 M) were all obtained from Sigma-Aldrich (Gillingham, UK). Ultrapure water, or MilliQ-grade water (H₂O, 18.2 MΩ.cm, Merck Millipore, Molsheim, France), was used in all experiments. Phosphate buffer (10 mM, pH = 7.04 at 21 °C) was prepared by mixing 0.01% wt NaH₂PO₄ with 0.01% wt Na₂HPO₄, in ultrapure water. All reagents were used as supplied.

2.2. Methods

2.2.1. Bulk and interfacial studies

2.2.1.1. Preparation of MC and MC/BS aqueous solutions. MC aqueous solution was prepared using the “hot/cold” method (The Dow Chemical Company, 2002, 2013). Solid MC was first dispersed into one third of the required mass of ultrapure water heated to 80 °C (for around 15 min), until complete wetting of particles; then, the dispersion was transferred into an ice bath, and the remaining two thirds of cold ultrapure water (4 °C) were added progressively into the stirred solution, which was finally left to stir overnight at 4 °C, to ensure complete solubilisation. MC/BS solutions were prepared simply by mixing both components together at the required concentrations.

2.2.1.2. Rheology measurements. Rheology experiments were performed with a strain-controlled rheometer (ARES, TA instruments, Inc, Borehamwood, UK), fitted with a 25 mm diameter titanium parallel plate and equipped with a temperature-controlled Peltier system (with a ± 0.1 °C temperature stability at thermal equilibrium). Each sample was loaded onto the lower plate, and the upper plate was adjusted to a gap size of 0.8 ± 0.3 mm. A thin layer of low viscosity paraffin oil was deposited around the edges of the sample exposed to air to prevent sample drying and evaporation throughout the measurement.

Dynamic temperature sweeps were performed at a fixed angular frequency of 6.28 rad/s and strain of 1%, from 20 °C to 80 °C, with a heating rate of 2 °C/min, to measure the evolution of the storage (G') and loss (G'') moduli as a function of temperature, in the absence and presence of BS. Dynamic frequency sweeps were performed over an angular frequency range of 0.1–100 rad/s, at a fixed strain of 1%, and a fixed temperature of 60 °C (above MC transition temperature (T_c), which is the point where a break in the slope of G' is detected in the dynamic temperature sweep curves). The strain of 1% was chosen

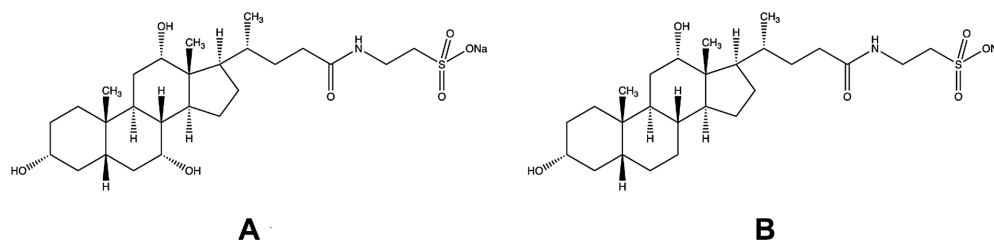


Fig. 2. Structures of sodium taurocholate (NaTC) (A) and sodium taurodeoxycholate (NaTDC) (B).

within the linear viscoelastic regime, which was established by performing dynamic strain amplitude sweeps on MC and MC/BS solutions, over a strain range of 0.01–100%, at a constant angular frequency of 6.28 rad/s and a temperature of 60 °C. Each test was repeated at least twice to confirm reproducibility; representative curves (rather than averages) are shown in the manuscript.

2.2.1.3. Langmuir trough measurements. Interfacial tension measurements were performed in a 50 mm diameter perfluoroalkoxy Petri dish (19.6 cm² surface area and 20 mL volume of subphase), to study the adsorption of MC and its interaction with BS at the air/water interface. All experiments were carried out under constant stirring, at a fixed area, and at a temperature of 23 ± 2 °C (room temperature). The surface pressure (π) was measured by a Wilhelmy plate made of chromatographic paper (Whatman International Ltd, Maidstone, UK) of 2.3 × 1.0 cm (length x width) and attached to a calibrated Nima PS4 microbalance (Nima Technology Ltd, Coventry, UK). Prior to any measurement, the trough was thoroughly cleaned with EtOH and CHCl₃ to remove organic impurities, and then filled with ultrapure water (subphase). Surface-active contaminants, dust and bubbles were all removed from the subphase by suction with a pump, and the subphase was considered as clean when changes in surface pressure did not exceed ± 0.2 mN/m over approximately two minutes.

2.2.1.3.1. MC adsorption at the air/water interface. Using a 1 mL syringe (Becton Dickinson, Madrid, Spain) fitted with a 19 G x 1 ½ in. needle (Becton Dickinson, Madrid, Spain), a specific amount of pure MC solution in ultrapure water was injected into the subphase, under constant stirring. Surface pressure (π) was measured over time until it reached a plateau. Each experiment was repeated at least twice; either a representative curve or an average measurement is shown.

2.2.1.3.2. BS interaction with a MC layer at the air/water interface. A MC layer was first formed at the air/water interface, by addition of a specific amount of MC aqueous solution into the clean and stirred water ($\pi_{MC} = 21 \pm 1$ mN/m with 0.5% w/w, and $\pi_{MC} = 18 \pm 2$ mN/m with 0.5 × 10⁻²% w/w). After film equilibration (ca. 1–2 hours), a specific amount of pure BS aqueous solution was injected beneath the MC layer. The corresponding changes in surface pressure (π) were recorded over time. Each experiment was repeated at least twice; either a representative curve or the average measurement is shown.

2.2.1.4. Ellipsometry. MC adsorption and interaction with BS at the air/water interface was further investigated by ellipsometry (Beaglehole Instruments, Wellington, New Zealand). Time-dependent measurements were performed with a 632.8 nm-wavelength laser hitting the surface at an incident angle of 50°. In this configuration, changes in the polarisation of light reflected by the interface are measured over the 1 mm² area and ~1 µm depth probed by the laser beam; these changes can be correlated to the amount of material adsorbed at this interface over time. The polarisation state of the incident light is composed of an *s*- and *p*-component (where the *s*-component is oscillating parallel to the sample surface, and the *p*-component parallel to the plane of incidence). The ratio of the reflectivity of these two components (r_s for the *s*-component and r_p for the *p*-component)

characterises the polarisation change and is expressed by the following equation:

$$\frac{r_p}{r_s} = \tan \Psi. e^{i\Delta} \quad (1)$$

where Ψ is the amplitude change and Δ the phase shift. In the thin film limit at the air/water interface (*i.e.*, film thickness << laser wavelength), Δ is found to be much more sensitive to changes in the amount adsorbed at the interface than Ψ (Motschmann & Teppner, 2001). Therefore, time-dependent changes in phase shift ($\Delta\Delta$) were measured, with $\Delta\Delta(t) = \Delta(t) - \Delta(t_0)$, where $\Delta(t_0)$ is the phase shift at the beginning of a given experiment, namely, the phase shift of the bare air/water interface (Δ_0) for MC adsorption and interaction with BS, at the air/water interface. Changes in the phase shift are directly proportional to the amount of material adsorbed at the interface (Motschmann & Teppner, 2001). In order to measure simultaneously the surface pressure and phase shift for the same surface, the instrument was mounted on top of the Petri dish, used as a Langmuir trough. Data were acquired at a rate of 0.2 Hz, using the Igor Pro software.

2.2.2. In vitro lipolysis studies

2.2.2.1. Preparation of MC-stabilised emulsion. MC (0.5% w/w) was dispersed into sunflower oil (15% w/w). Cold phosphate buffer (84.5% w/w, at $T < T_{dissolution} = 10$ °C) was added to the oil phase and the mixture stirred for a few minutes. The dispersion was then pre-emulsified at 11,000 rpm for 1 min, using a high-shear mixer (T25 digital Ultra-Turrax, IKA®-Werke GmbH & Co. KG, Staufen, Germany). This pre-emulsion was transferred into a 10 mL volume beaker in an ice bath and was sonicated at a frequency of 20 kHz and amplitude of 70% for 5 min with a tip sonicator (SONOPULS HD 3100 ultrasonic homogeniser, microtip model: MS 73, BANDELIN electronic GmbH & Co. KG, Berlin, Germany).

2.2.2.2. Simulation of the duodenal lipolysis environment. For each *in vitro* lipolysis experiment, the following model (Grundy, Wilde, Butterworth, Gray, & Ellis, 2015) was employed to simulate the duodenum (small intestine) environment: 19 mL of MC-stabilised emulsion was added to a thermostatically-controlled and mechanically-stirred reaction vessel at 37 °C, followed by 15 mL of a BS aqueous solution (NaTC, NaTDC; 2.5, 25, 125 mM, in phosphate buffer). Then, 1 mL of NaCl (4.9 M, in ultrapure water) and 1 mL of CaCl₂ (0.37 M, in ultrapure water) were added to the mixture, under continuous stirring. Finally, 1.5 mL of either phosphate buffer (for the blank assay, used as a control) or freshly prepared pancreatic lipase/colipase suspension (17 mg/mL, in phosphate buffer) (for the lipolysis assay) were added. The final system was made up of 7.6% w/w lipid, 1, 10, or 50 mM BS, 130 mM NaCl, 10 mM CaCl₂, and 0.68 mg/mL pancreatic lipase/colipase.

2.2.2.3. Optical microscopy. The structural changes induced on an MC-stabilised emulsion upon duodenal digestion, were monitored over time by brightfield optical (Olympus BX61 microscope, Olympus France S.A.S., Rungis, France) and confocal (Leica TCS SP2, DMIRE2 inverted,

Leica Microsystems UK Ltd, Milton Keynes, UK) microscopy. Prior to *in vitro* lipolysis studies, the pure emulsion was characterised; then, the mixture modelling the duodenal environment was added to the emulsion and samples measured at different time points ($t = 5, 15, 30$ and 60 min), to analyse the evolution of emulsion droplet microstructure from the beginning to the end of duodenal lipolysis. The influence of each component (NaTC, NaTDC, NaCl and CaCl_2) used individually and together was assessed to better understand their impact on duodenal lipolysis. A blank assay was also measured as a control to monitor changes over time in the absence of enzymes.

For confocal microscopy, prior to visualisation, samples were mixed with 1 mg/mL orlistat (prepared in dimethyl sulfoxide) to stop lipolysis, and then stained with $10 \text{ }\mu\text{g/mL}$ Nile red (prepared in dimethyl sulfoxide) and $20 \text{ }\mu\text{g/mL}$ calcofluor (prepared in ultrapure water), to detect lipids (red fluorescence) and MC (blue fluorescence), respectively. Samples were excited at 488 nm (for Nile red) and 405 nm (for calcofluor), and the fluorescence emitted by the samples was detected between $510\text{--}650 \text{ nm}$ (for Nile red) and $410\text{--}480 \text{ nm}$ (for calcofluor). Images were captured using objective lenses of $10\times$, $20\times$ or $63\times$, and micrographs were compiled with the Olympus image analysis software (for optical microscopy, Olympus France S.A.S., Rungis, France) and Fiji software ("Fiji", 2019) (for confocal microscopy).

2.2.2.4. pH-stat measurements. The rate and extent of lipolysis were evaluated by titrating the amount of FFA released from an MC-stabilised emulsion with 0.1 M NaOH, at 37°C and $\text{pH } 7.0$, in conditions mimicking the duodenal (small intestine) environment. Each assay was carried out over 1 hour of digestion, using a pH-stat titration unit (848 Titrino plus, Metrohm AG, Herisau, Switzerland). The blank experiment was performed as a control, to measure pH fluctuation in the absence of enzymes; the volume of NaOH released during this assay was then subtracted from the data recorded in the presence of pancreatic lipase/co-lipase (lipolysis assay). Each blank and lipolysis experiment was repeated at least six times.

The volume of NaOH released during MC-stabilised emulsion digestion was converted into the percentage of FFA produced, using this equation:

$$\% \text{FFA}(t) = 100 \times \frac{V_{\text{NaOH}}(t) \cdot [\text{NaOH}] \cdot M_{\text{Lipid}}}{2 \cdot m_{\text{Lipid}}} \quad (2)$$

where V_{NaOH} is the volume of NaOH required to neutralise the FFA produced over time, $[\text{NaOH}]$ the concentration of the NaOH solution used, M_{Lipid} the molecular weight of the oil employed in this experiment (in our case, $M_{\text{Sunflower oil}} = 876 \text{ g/mol}$ (Sánchez, Maceiras, Cancela, & Rodríguez, 2012)), and m_{Lipid} the mass of triacylglycerol (TAG) initially present in the digestion vessel. This equation has been established considering the ideal case where the hydrolysis of one molecule of TAG leads to the formation of one molecule of MAG and two molecules of FFA. The results are shown as the proportion of FFA release as a function of time.

The pH-stat data were analysed with the GraphPad Prism software ("GraphPad Prism," 2019); statistical analysis was carried out using the two-way analysis of variance (ANOVA), followed by the Tukey post-test, with a 95% confidence level, meaning that differences were considered as statistically significant when $P < 0.05$.

3. Results

3.1. BS interaction with MC in the bulk

3.1.1. MC viscoelastic behavior

The temperature-dependence of MC rheological properties was investigated by performing dynamic temperature sweep measurements on MC solutions prepared at concentrations ranging between 0.1 and 2.0% w/w (Fig. S1).

At all the MC concentrations studied, a relatively flat region is observed for the storage modulus (G') in the lower temperature range ($ca. 20\text{--}40^\circ\text{C}$), followed by a steep increase beyond a transition temperature (T_t) and a final plateau at high temperatures. As MC concentration increases, the transition temperature from which G' starts to level off shifts towards lower values (from 55°C at 0.1% w/w, to 37°C at 2.0% w/w). Below and above T_t , MC behaves as a predominantly solid-like material over the whole range of temperatures studied (G' dominates over G'' over the range of frequencies measured), and above T_t , both moduli increase and are still independent of frequency (data not shown) (Funami et al., 2007; Li et al., 2001; Li, 2002); the transition temperature thereby corresponds to a weak-to-strong gel transition. The increase in MC concentration also induces a relatively weak change in MC elastic properties (G') at low temperatures, and a much more significant one in the high temperature region, in agreement with previous studies (Nasatto et al., 2015a).

The gelation of MC – whose chains are arranged as ‘bundles’ at room temperature (or packed ‘strands’ held together by packing of unsubstituted regions and the hydrophobically-driven aggregation of methyl groups in regions of denser substitution) – has been postulated to follow two steps (Desbrières, Hirrien, & Rinaudo, 1998; Funami et al., 2007; Haque & Morris, 1993; Hirrien, Chevillard, Desbrières, Axelos, & Rinaudo, 1998; Isa Ziembowicz et al., 2019; Kobayashi, Huang, & Lodge, 1999; Li et al., 2001, 2002; Li, 2002; Li, Wang, & Xu, 2003; Nasatto et al., 2015a; Sarkar, 1995; Torcello-Gómez & Foster, 2014; Torcello-Gómez et al., 2015): upon heating, MC strands separate, allowing intermolecular associations to form between MC hydrophobic (methyl) groups, therefore inducing the formation of a strong, physical gel network; at low temperatures, these hydrophobic polymer-polymer interactions take place to a much lower extent because of water molecules surrounding MC methyl moieties (via hydrogen bonds), thus resulting in the swelling of ‘bundles’ and the formation of a softer, weaker gel. The effect of MC concentration on its rheological properties is therefore attributed to the increase in the number of methyl groups in solution, resulting in a larger number of hydrophobic interactions from lower temperatures.

3.1.2. Effect of BS on MC viscoelastic behaviour

The impact of the two BS on MC rheological properties was assessed by following the dynamic moduli (G' , G'') of a 1.0% w/w MC solution over a range of temperatures and frequencies (Fig. 3). The evolution of the transition temperature (T_t , from which the increase in G' becomes steeper) and of both dynamic moduli (G' , G'') are shown as a function of BS concentration in Fig. 4A and B, respectively.

In the presence of BS, the dynamic temperature sweeps of MC solutions show a similar profile as the pure MC solution, namely, a moderate increase in G' followed by a sharp rise (Fig. 3A, B). However, BS have a significant impact on MC rheological properties, leading to a notable, and gradual increase in the transition temperature from around 50°C , in the absence of BS, to 53°C with 500 mmol/kg NaTC and 58°C with 500 mmol/kg NaTDC (Fig. 4A). In addition, both BS (from the lowest concentration studied of 1 mmol/kg) induce a drop in MC viscoelasticity (G') at all temperatures studied, most visibly at high temperatures (Fig. 3A, B). At physiological temperature (37°C), a decrease from $G' = 10 \text{ Pa}$ in the absence of BS, to $G' = 5$ and 2 Pa in the presence of 1 mmol/kg of, respectively, NaTC and NaTDC, is observed. Dynamic frequency sweeps performed at 60°C , where MC forms a strong gel and changes caused by BS are most visible (Fig. 3C, D), reveal a 10-fold decrease in G' , from $ca. 280 \text{ Pa}$ in the absence of BS, to $ca. 20 \text{ Pa}$ with the highest concentration of BS studied, at a frequency of 1 rad/s (Fig. 4B). In addition, G' shows an increasing dependence on frequency with the addition of BS, more notably so with NaTDC. Overall therefore, the presence of the BS converts MC gel into a less solid-like material. Comparing the two BS, it is clear that NaTDC has a much stronger impact; for instance, only 10 mmol/kg of NaTDC are needed to significantly reduce the value of the storage modulus (G')

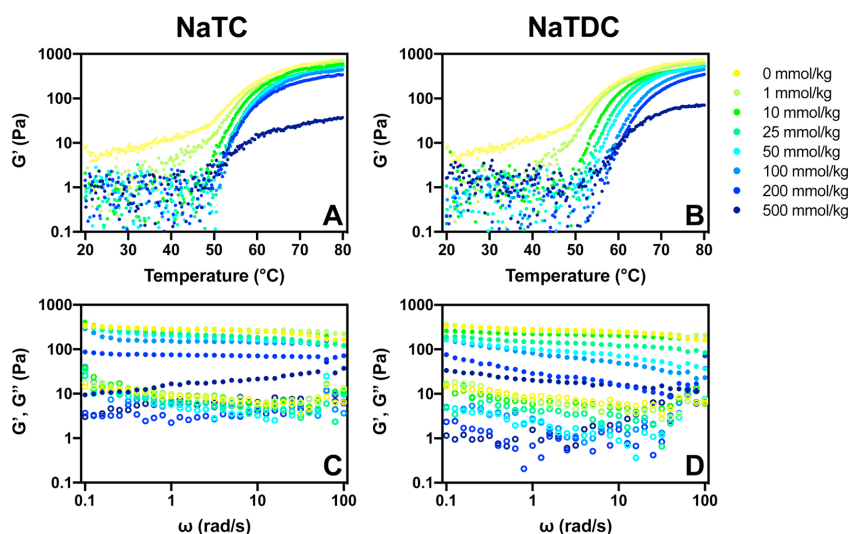


Fig. 3. (A, B) Temperature-dependent evolution of the storage modulus (G') obtained from dynamic temperature sweeps, and (C, D) angular frequency-dependent evolution of the dynamic moduli: (●) G' , the storage modulus, (○) G'' , the loss modulus, obtained from dynamic frequency sweeps performed at a constant temperature of 60 °C, on a 1.0% w/w MC aqueous solution containing increasing amounts (1, 10, 25, 50, 100, 200, 500 mmol/kg) of BS: (A, C) NaTC, (B, D) NaTDC. The curves obtained in the absence of BS are also shown for comparison.

(Figs. 3D and 4 B), while 25 mmol/kg of NaTC are required to induce the same effect (Figs. 3C and 4 B). Similar observations have been reported elsewhere (Torcello-Gómez et al., 2015).

Overall, over the whole temperature range studied, MC behaves as a gel whose strength increases with temperature. The addition of BS induces a transition to a softer material (lower elastic modulus (G')), both above and below MC transition temperature (T_t); in addition, this transition occurs at lower concentrations of NaTDC, compared to NaTC.

3.2. BS interfacial properties in the presence of MC

3.2.1. MC adsorption dynamics at the air/water interface

MC behaviour at the bare air/water interface was studied using both a Langmuir trough and ellipsometer, by monitoring the time-dependent evolution of the surface pressure (π) and phase shift ($\Delta\Delta$), respectively, upon injection into the water subphase of either successive quantities of MC (0.5×10^{-1} , 0.25 and 0.5% w/w (Fig. S2); 0.5×10^{-2} , 0.25×10^{-1} and 0.5×10^{-1} % w/w (Fig. S3)), or fixed amounts over a longer period of time (0.5×10^{-3} , 0.5×10^{-2} , 0.5×10^{-1} or 0.5% w/w) (Fig. S4).

Upon addition of 0.5×10^{-1} % w/w MC into the aqueous subphase, the surface pressure increases until reaching a near-plateau at $\pi = 19 \pm 1$ mN/m, which stays relatively constant with following injections ($\pi = 19 \pm 1$ mN/m at 0.25% w/w, and $\pi = 18 \pm 3$ mN/m at

0.5% w/w) (Fig. S2A). With the same injection sequence, the ellipsometry phase shift, which is measured at the same time as the surface pressure and relates to the amount of material adsorbed at the interface (Motschmann & Teppner, 2001), exhibits the same trend as the surface pressure (Fig. S2B): it reaches a value of $\Delta\Delta = 0.033^\circ$, which then slightly increases to $\Delta\Delta = 0.035^\circ$ at 0.25% w/w and $\Delta\Delta = 0.036^\circ$ at 0.5% w/w. Both measurements thus show that MC adsorbs at the air/water interface up to a saturation point, independently of its concentration in the bulk. The two experiments differ, nevertheless, by the presence of peaks of surface pressure visible straight after BS injection, not detected in the phase shifts, which could be explained by an initial strong adsorption, followed by a relaxation process as the polymer rearranges at the air/water interface, changing conformation (Graham & Phillips, 1979). These transient surface pressure peaks were also observed in a previous study with BS injected under the air/water interface (Pabois et al., 2019). The trends in surface pressure (Fig. S3A) and phase shift (Fig. S3B) are reproduced with lower amounts of MC (0.5×10^{-2} , 0.25×10^{-1} , and 0.5×10^{-1} % w/w) injected into water.

In order to study the kinetics of adsorption of MC molecules at the air/water interface, surface pressure measurements were performed over longer periods of time (Fig. S4). Results show that, above 0.5×10^{-2} % w/w, the same equilibrium surface pressure ($\pi = 17 \pm 1$ mN/m) is always reached, irrespective of MC concentration, whereas a much lower value is obtained at the lowest

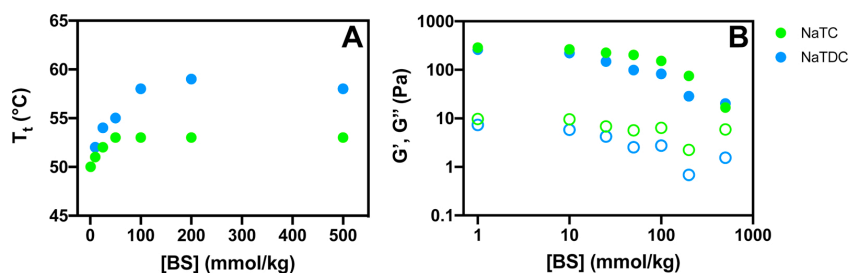


Fig. 4. Evolution of MC transition temperature (T_t) (A) and dynamic moduli: (●) G' , the storage modulus, (○) G'' , the loss modulus, obtained at an angular frequency of 1 rad/s (B), as a function of the concentration in BS: NaTC, NaTDC. The transition temperature (T_t) is the temperature from which G' starts changing. These data are extracted from, respectively, (A) dynamic temperature sweeps performed over a temperature range of 20 – 80 °C (Fig. 3A, B), and (B) dynamic frequency sweeps performed over an angular frequency range of 0.1 – 100 rad/s, at a constant temperature of 60 °C (Fig. 3C, D).

concentration studied of $0.5 \times 10^{-3}\%$ w/w ($\pi = 10 \pm 0.4$ mN/m). Arboleya and Wilde (Arboleya & Wilde, 2005) also observed a saturation point from a similar MC concentration (i.e., $1 \times 10^{-2}\%$ w/w), and obtained comparable interfacial tension values. Furthermore, as MC concentration decreases, the surface pressure rises at a slower rate: a change in surface pressure is immediately observed after injection of both 0.5×10^{-1} and 0.5% w/w, while a lag period of about 3 and 40 min is seen with solutions containing 0.5×10^{-2} and $0.5 \times 10^{-3}\%$ w/w MC, respectively. The amount injected into the aqueous subphase thus affects MC adsorption rate and extent, such that the lower the concentration, the slower the adsorption process and the lower the quantity of material adsorbed, therefore indicating a diffusion-controlled adsorption mechanism, as already observed elsewhere with hydroxypropyl MC (Avranas & Tasopoulos, 2000; Camino, Pérez, Sanchez, Rodríguez Patino, & Pilosof, 2009; Pérez, Sánchez, Pilosof, & Rodríguez Patino, 2008; Wollenweber, Makievski, Miller, & Daniels, 2000). In the literature, MC adsorption has been suggested to occur in three stages: MC first slowly diffuses from the bulk phase to the sub-surface region and then adsorbs at the air/water interface, while undergoing conformational changes (Arboleya & Wilde, 2005).

All these results are consistent with data reported elsewhere (Nasatto et al., 2014; Pizonés et al., 2017).

3.2.2. BS interaction with a MC layer at the air/water interface

The interfacial behaviour of the two selected BS (NaTC and NaTDC) in the presence of a MC film at the air/water interface was then evaluated, by injecting BS below the polysaccharide layer. Measurements were carried out either by adding increasing amounts of BS every hour (2, 4, 6, 8 and 10 mM) (Figs. 5 and S5) or by injecting fixed concentrations and measuring over longer times (1, 5 or 10 mM) (Figs. 6 and S6). These BS concentrations were selected to be below, around, and above their critical micelle concentration (CMC), which is 4–7 mM for NaTC (gradual micellisation process) and 2 mM for NaTDC in ultrapure water (data not shown) (Matsuoka, Maeda, & Moroi, 2003). Prior to BS injection, a saturated film of MC at the interface was formed by injecting it into the water subphase, at either 0.5% w/w (Figs. 5, 6 and S6) or $0.5 \cdot 10^{-2}\%$ w/w (Fig. S5).

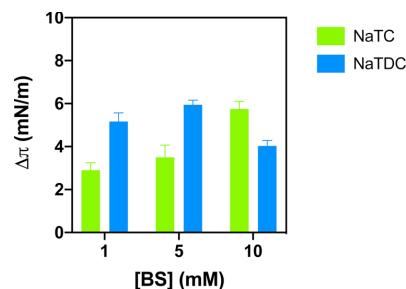


Fig. 6. Evolution of the surface pressure ($\Delta\pi = \pi_{\text{Equilibrium}} - \pi_{\text{MC}}$) as a function of BS concentration, measured in a Langmuir trough, upon injection of fixed concentrations (1, 5, 10 mM) of BS (NaTC, NaTDC) into the aqueous subphase (at $23 \pm 2^\circ\text{C}$). 0.5% w/w MC were injected into water to form a layer at the air/water interface, at $\pi_{\text{MC}} = 21 \pm 1$ mN/m. These data were extracted from individual BS injections measurements (Figure S6). Each experiment was reproduced at least twice, and the average measurement was selected for each BS at each concentration.

The evolution of the surface pressure is quite different for the two BS (Fig. 5A, B): while the successive injections of NaTC lead to a continuous increase in surface pressure (up to $\pi = 23 \pm 0.5$ mN/m at 10 mM) (Fig. 5A), with NaTDC, a steep rise to $\pi = 25 \pm 1$ mN/m (at 2 mM), followed by a gradual drop to $\pi = 22 \pm 1$ mN/m (at 10 mM), is observed (Fig. 5B). These trends are also obtained with a lower amount of MC at the air/water interface (Fig. S5). The ellipsometry phase shift obtained in parallel follows the same trends (Fig. 5C, D): with NaTC, it gradually increases up to $\Delta\Delta = 0.045 \pm 0.003^\circ$ upon successive additions of BS into the subphase (Fig. 5C); instead, the injection of 2 mM NaTDC into the water induces a sharp increase to $\Delta\Delta = 0.047 \pm 0.003^\circ$, followed by a decrease to $\Delta\Delta = 0.042 \pm 0.001^\circ$ from 4 mM (Fig. 5D). As observed with successive injections of MC, temporary surface pressure peaks are also present after each addition of BS; here again, these peaks could be attributed to MC film compression and subsequent relaxation, induced by BS adsorption (Graham & Phillips, 1979).

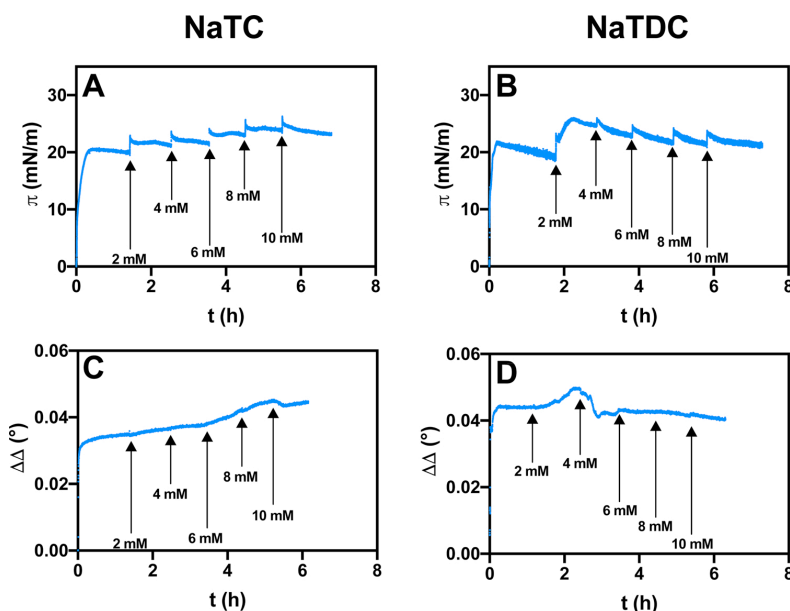


Fig. 5. Time-dependent evolution of (A, B) the surface pressure (π) measured in a Langmuir trough, and (C, D) phase shift ($\Delta\Delta(t) = \Delta(t) - \Delta_0$) measured by ellipsometry, upon successive injections of either (A, C) NaTC or (B, D) NaTDC into the aqueous subphase (at $23 \pm 2^\circ\text{C}$). The first increase in surface pressure corresponds to the adsorption of MC at the air/water interface, which was added into water at a concentration of 0.5% w/w ($\pi_{\text{MC}} = 21 \pm 1$ mN/m, $\Delta\Delta_{\text{MC}} = 0.039 \pm 0.005^\circ$). Each addition of BS is shown by an arrow, together with the corresponding BS concentration achieved in the subphase. Each experiment was reproduced twice, and a representative measurement was selected for each experiment.

Upon injection of fixed BS concentrations, the surface pressure increases sharply over time until reaching a plateau value, independently of the BS type and concentration (Fig. S6). The surface pressure values achieved at equilibrium are summarised in Fig. 6, showing $\Delta\pi = \pi_{\text{Equilibrium}} - \pi_{\text{MC}}$, where π_{MC} is the initial MC layer surface pressure ($\pi_{\text{MC}} = 21 \pm 1 \text{ mN/m}$). The surface pressure changes induced by the two BS are relatively small, in agreement with previous studies performed on the interaction of a hydroxypropyl MC layer with bile extract (Pizones Ruiz-Henestrosa et al., 2017). At 1 and 5 mM, NaTDC induces a higher increase in surface pressure ($\Delta\pi = 5 \pm 0.4 \text{ mN/m}$ at 1 mM, and $\Delta\pi = 6 \pm 0.2 \text{ mN/m}$ at 5 mM), compared to NaTC ($\Delta\pi = 3 \pm 0.3 \text{ mN/m}$ at 1 mM, and $\Delta\pi = 4 \pm 1 \text{ mN/m}$ at 5 mM); at high BS concentration (10 mM), the opposite trend is observed ($\Delta\pi = 6 \pm 0.4 \text{ mN/m}$ for NaTC, and $\Delta\pi = 4 \pm 0.3 \text{ mN/m}$ for NaTDC).

3.3. Effect of BS structure and concentration on the duodenal digestion of an MC-stabilised emulsion

A range of *in vitro* duodenal lipolysis studies was carried out on a sunflower oil emulsion stabilised by MC. Before reaching the small intestine, ingested fat droplets pass through simulated oral and gastric digestion, where their physicochemical and structural properties are significantly affected; however, because our main aim is to understand BS roles during lipolysis, the work performed here focuses on the duodenum part of the lipolysis process, where BS are acting.

3.3.1. Evolution of emulsion droplets microstructure

The structure of the pure MC-stabilised emulsion droplets was first characterised using both optical and confocal microscopy (Fig. S7). Optical microscopy demonstrates that emulsion droplets are uniformly dispersed with a size ranging between 2 and 5 μm , and with a small number of larger droplets around 10 μm (Fig. S7A). Confocal microscopy highlights the presence of a MC network (stained in blue with calcofluor) in the bulk and at the interface of emulsion droplets (stained in red with Nile red) (Fig. S7B).

In vitro lipolysis studies were performed on the emulsion by adding the digestive medium and monitoring the structural changes of the emulsion droplets by microscopy (Figs. 7, S8 and S9). Using brightfield optical microscopy, the influence of both BS type and concentration on the structure of MC-stabilised emulsion droplets was assessed in control assays (no enzyme), as well as the effect of enzymes (lipolysis assays) (Fig. 7). In the absence of enzymes (blank assays), the emulsion droplets microstructure is affected by the digestive fluid, as revealed by the occurrence of droplets flocculation, and some – limited – coalescence, which is more visible with NaTDC, and particularly evident for both BS at high concentration (10 mM). Upon the addition of enzymes (lipolysis assays), flocculation occurs to a higher extent, and droplet coalescence (size increase) is observed in all samples, to a larger extent, again, with NaTDC. To further elucidate the mechanism of digestion of an MC-stabilised emulsion, the influence of the different components of the digestive fluid (NaCl, CaCl_2 and BS) on droplet stability was also evaluated (Figs. S8 and S9). Brightfield optical micrographs show that extensive flocculation occurs when both BS and salts are present, which suggests that the association of BS with the different salts (NaCl, CaCl_2) is responsible for the droplet aggregation observed in Fig. 7.

This *in vitro* lipolysis study was complemented with micro-structural assessment of the emulsion droplets with confocal microscopy, to determine the localisation of MC throughout the emulsion and its evolution during lipid digestion (Figs. 8 and 9). Based on our pH-stat results (see the following section), 50 mM BS was used here, as it shows the higher extent of FFA release. The images obtained suggest that the addition of digestive fluid not only breaks down the network of MC, but also displaces it from the lipid/water interface (Fig. 8); interestingly, MC bulk network is disrupted to a higher extent in the presence of NaTDC, compared to NaTC. Additionally, the lipid droplets become non-spherical with “rough” surfaces, compared to the initial emulsion

(Figs. 8 and 9). This demonstrates coalescence and may be an indication of fats being digested by enzymes; in particular, small oil droplets were seen to flocculate or coalesce onto the surface of larger droplets (Fig. 9A) and areas with an undefined oil/water interface suggest the presence of digestion products (Fig. 9B).

3.3.2. Quantification of FFA release from the MC-stabilised emulsion

The ability of NaTC and NaTDC to promote or inhibit the duodenal digestion of an MC-stabilised emulsion was compared by monitoring the release of FFA (%FFA) over time with the pH-stat method (Li, Hu, & McClements, 2011) (Fig. 10). The effect of BS concentration on the rate of lipolysis and its extent was also evaluated using the two BS at both 10 and 50 mM.

Independently of the BS type and concentration, the proportion of FFA generated during lipolysis increases steeply after the addition of enzymes (Fig. 10A); this rapid initial rate of lipolysis, already observed elsewhere (Bellesi, Martinez, Pizones Ruiz-Henestrosa, & Piloosof, 2016; McClements & Li, 2010a), can be attributed to the immediate adsorption of lipase/co-lipase onto fat droplets surfaces, which then triggers TAG break-down and thus lipid digestion. After a certain time ($t = 0.07 \text{ h}$ with both BS at 10 mM, $t = 0.18 \text{ h}$ with 50 mM NaTDC and $t = 0.24 \text{ h}$ with 50 mM NaTC), the release of FFA starts slowing down, until it reaches a near-plateau. This decrease in the rate of lipolysis can be explained by the accumulation of lipolysis products at the oil/water interface during the process of fat digestion (Patton & Carey, 1979; Reis, Holmberg, Watzke, Leser, & Miller, 2009; Reis, Miller et al., 2008; Reis, Raab et al., 2008), which then leads to the inhibition of enzymes binding to the substrate, as previously demonstrated (Bellesi et al., 2016; Borel et al., 1994). Increasing BS concentration from 10 to 50 mM leads to a significant increase in the percentage of FFA produced, for both BS ($P_{\text{NaTC}} < 0.0001$ and $P_{\text{NaTDC}} < 0.0001$) (Fig. 10B); more specifically, a 14% and 9% increase is obtained with, respectively, NaTC and NaTDC. This can be attributed to the larger amount of BS micelles, which can solubilise a larger amount of FFA released, thereby preventing droplets surface saturation by these products (Wilde & Chu, 2011). While no significant differences are observed between the two BS at the lowest concentration (10 mM) (%FFA $_{t=1\text{h}} = 6 \pm 1\%$ for both NaTC and NaTDC; $P_{10\text{mM}} = 0.4$), a significant difference is seen at high concentration (50 mM), with NaTC inducing a higher extent of lipolysis (%FFA $_{t=1\text{h}} = 20 \pm 1\%$ and $14 \pm 1\%$ for, respectively, NaTC and NaTDC; $P_{50\text{mM}} < 0.0001$).

4. Discussion

The objective of this study was to investigate the interactions of MC with BS, in particular the ability of MC to inhibit BS activity, and thus to shed light on the mechanism of lipid digestion regulation by MC – a dietary fibre with a proven potential to lower cholesterol levels (Agostoni et al., 2010). Bulk (rheology) and interfacial (surface pressure measurements and ellipsometry) studies were carried out to characterise the interactions between these two components in the bulk and at the interface, while *in vitro* lipolysis (microscopy, pH-stat) experiments were performed to link these interactions to the lipid digestion of an MC-stabilised emulsion. The two BS, which differ by the presence (NaTC) or absence (NaTDC) of a hydroxyl group on their steroid skeleton (Fig. 2) and constitute 20% of human bile (Staggers, Hernell, Stafford, & Carey, 1990), were chosen for this study, as they have been reported to exhibit different interfacial behaviours, hypothesised to explain the contrasting roles they play during the process of lipolysis (Pabois et al., 2019; Parker et al., 2014).

4.1. Interaction between MC and BS in the bulk and at the interface

The impact of BS on MC rheological properties was investigated to explore the interaction of BS with MC in the bulk, where MC is present in excess. Increasing the amount of BS in solution led to a notable shift

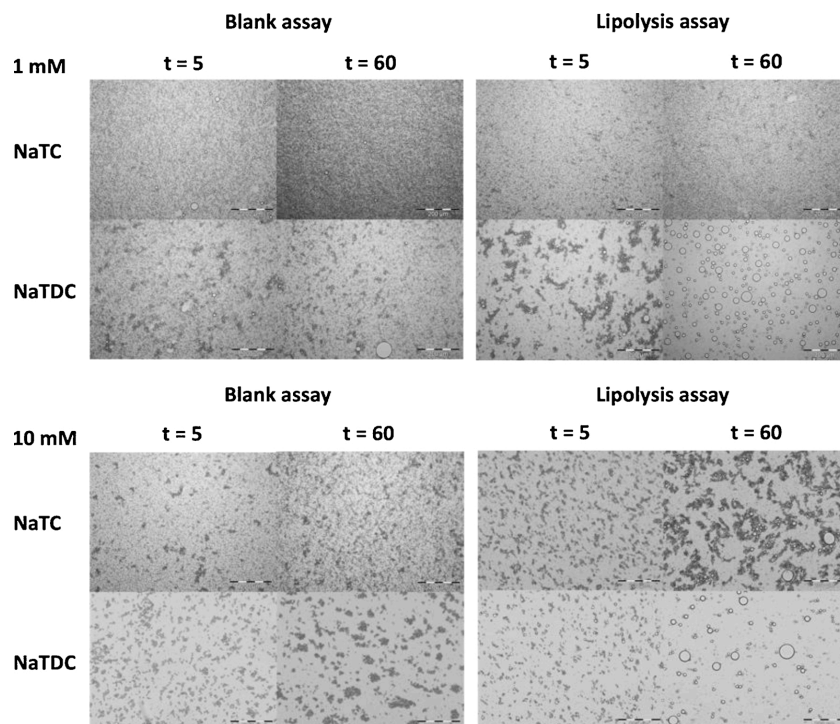


Fig. 7. Time-dependent evolution of the microstructure of MC-stabilised emulsion droplets in the presence of BS: NaTC, NaTDC, used at 1 and 10 mM, under duodenal digestion conditions (at 37 °C). MC-stabilised emulsion was made up of 0.5% MC and 15% sunflower oil. Both blank (without enzymes) and lipolysis (with enzymes) assays were performed to assess, respectively, the effect of BS type and concentration on the droplets stability, and of enzymes on the droplets microstructure. Microscopy observations were made at $t = 5$ and 60 min. The scale bar is 200 μm .

in the transition temperature (T_g) to higher values, as well as a gradual drop in viscoelastic properties, which were more substantial with NaTDC (Figs. 3 and 4). In particular, MC – which presents predominantly solid-like properties in the absence of BS – turned into a softer gel above a threshold concentration of BS (25 mmol/kg for NaTC vs. 10 mmol/kg for NaTDC, at 60 °C) (Figs. 3C, D and 4 B). MC gelation

occurs *via* the association of the hydrophobic (methyl) moieties (Desbrières et al., 1998; Funami et al., 2007; Haque & Morris, 1993; Hirrien et al., 1998; Isa Ziembowicz et al., 2019; Kobayashi et al., 1999; Li et al., 2001, 2002; Li, 2002; Li et al., 2003; Nasatto et al., 2015a; Sarkar, 1995; Torcello-Gómez & Foster, 2014; Torcello-Gómez et al., 2015). The presence of BS and its association with MC may thus prevent

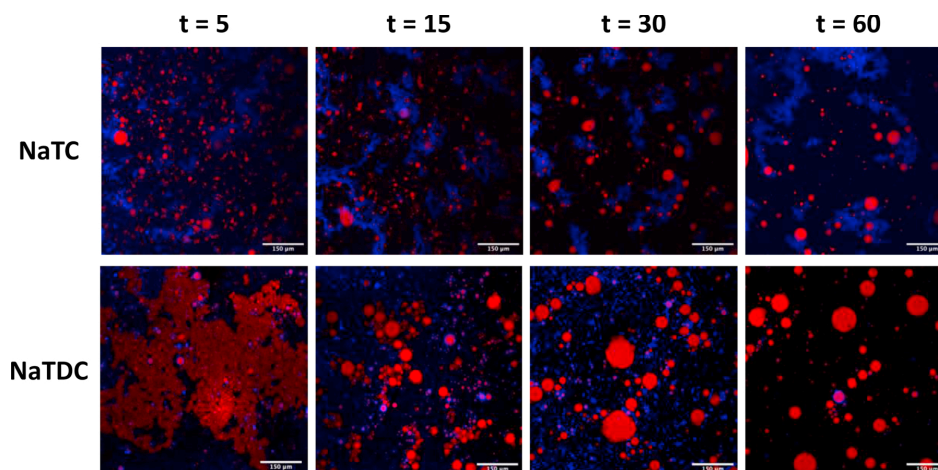


Fig. 8. Time-dependent evolution of the microstructure of MC-stabilised emulsion droplets in the presence of 50 mM BS: NaTC, NaTDC, under duodenal digestion conditions (at 37 °C). MC-stabilised emulsion was made up of 0.5% MC and 15% sunflower oil. The lipid droplets are stained in red (with Nile red), while MC is stained in blue (with calcofluor). Microscopy observations were made at $t = 5, 15, 30$ and 60 min, to compare the structural changes occurring during digestion; at each time point, orlistat was used to inhibit lipolysis. The scale bar is 150 μm . (For interpretation of the references to colour in this figure legend, the reader is referred to the web version of this article).

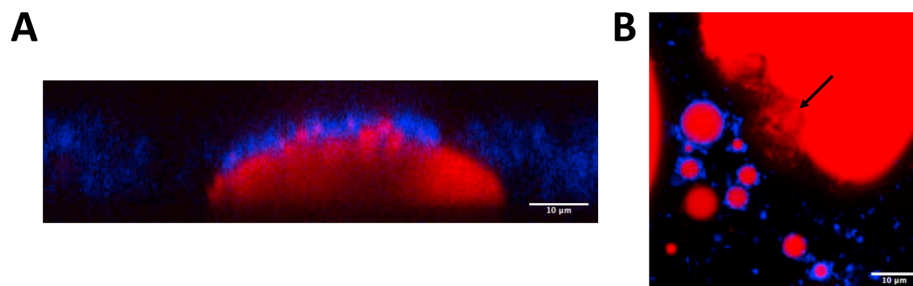


Fig. 9. (A) Cross-section confocal image of MC-stabilised emulsion droplets in the presence of 50 mM NaTC, under duodenal digestion conditions (at 37 °C). The microscopy observation was made at $t = 15$ min. (B) MC-stabilised emulsion droplets in the presence of 50 mM NaTDC, under duodenal digestion conditions (at 37 °C). Insoluble lipolysis products seem to be presumably present at the fat droplet interface (see the arrow). MC-stabilised emulsion was made up of 0.5% MC and 15% sunflower oil. The lipid droplets are stained in red (with Nile red), while MC is stained in blue (with calcofluor). The scale bar is 10 μm . (For interpretation of the references to colour in this figure legend, the reader is referred to the web version of this article).

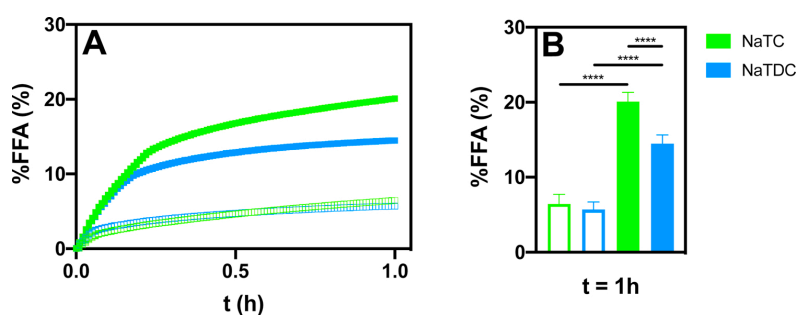


Fig. 10. (A) Proportion of FFA released (% FFA) over time from an MC-stabilised emulsion, using two different BS: NaTC, NaTDC, at two different concentrations: (□) 10 and (■) 50 mM, under duodenal digestion conditions (at 37 °C). (B) Proportion of FFA released (% FFA) after 1 hour of digestion of an MC-stabilised emulsion, using the two BS, at 10 and 50 mM, under duodenal digestion conditions (at 37 °C). Statistical significance was determined using the two-way ANOVA, followed by the Tukey post-test (**** indicates $P < 0.0001$, i.e., differences are extremely significant). MC-stabilised emulsion was made up of 0.5% MC and 15% sunflower oil.

hydrophobic groups from assembling with each other, thus weakening the gels or hindering gelation altogether. The stronger effect observed with NaTDC may be attributed to its higher hydrophobicity (Armstrong & Carey, 1982), which may result in a more efficient connection between BS and MC hydrophobic regions (Torcello-Gómez et al., 2015). Overall, these rheological measurements reveal the presence of strong interactions between BS and the dietary fibre, which have a substantial impact on MC viscosity; the presence (NaTC) or absence (NaTDC) of a hydroxyl group on BS steroid backbone impacts this behaviour considerably.

The interfacial properties of BS in the presence of a MC layer formed at the air/water interface were then studied to determine the interactions occurring when a BS molecule approaches a fat droplet stabilised by MC. Studies with a Langmuir trough set-up (Figs. 5A, B, S5, 6 and S6) combined to ellipsometry (Fig. 5C, D) demonstrate that the two BS behave quite differently when injected beneath an almost-saturated MC film: NaTC was shown to gradually adsorb at the interface with increasing concentration, whereas NaTDC first adsorbed at low concentrations (up to 2–3 mM) and then desorbed above 4–5 mM. This contrasting interfacial behaviour correlates with their micellisation behaviour, which occurs over 4–7 mM for NaTC and at 2 mM for NaTDC. Similar differences have been observed when BS were injected below a phospholipid monolayer (Pabois et al., 2019). Nevertheless, BS were found to adsorb and/or desorb to a much lower extent in the presence of a MC film, compared to the phospholipid monolayer (surface pressures changes as high as 30 mN/m were monitored in the presence of the lipid film, whereas an increase of up to 10 mN/m was observed with the MC layer). This may in part be explained by the likely presence of MC excess in the bulk, which could interact with BS and therefore limit their adsorption at the interface.

4.2. Impact of BS/MC interactions on fat digestion

Next, we performed *in vitro* lipolysis studies by following the evolution of the structure of an MC-stabilised emulsion with optical and confocal microscopy, to compare the effect of the two BS on the droplets (Figs. S7A and 7) and shed light on the behaviour of MC during emulsion digestion (Figs. S7B). The characterisation of the MC-stabilised emulsion by confocal microscopy clearly demonstrates that fat droplets are entrapped in a network of MC present in excess in the bulk, which may be responsible for the stabilisation of the emulsion against droplets flocculation or coalescence (Fig. S7B). Optical microscopy images (Fig. 7) demonstrate that, even in the absence of digestive enzymes, the presence of both BS destabilises the emulsion, inducing some flocculation; upon the addition of lipases, droplets destabilisation (namely, flocculation and coalescence) was found to occur to a large extent, and more markedly with NaTDC, compared to NaTC. Confocal microscopy images (Fig. 8) suggest that flocculation and coalescence observed during lipolysis are due to the MC network being broken down and removed from the lipid/water interface. The better ability of NaTDC to induce coalescence could therefore be explained by its higher capacity to disturb MC bulk network (as observed by confocal microscopy observations), which, in turn, could be attributed to its stronger interactions with MC (as seen from rheology measurements) and higher propensity to desorb from the interface at lower concentrations (as detected by interfacial measurements). While the displacement of MC from the interface by BS may facilitate the access of BS and enzymes to the lipid droplets surface, the network of MC remaining in the bulk may also trap BS (via hydrophobic interactions) and thus prevent them from removing insoluble lipolysis products, which could explain how MC hinders lipase activity. Emulsion droplets coalescence (and thus the

decrease in droplets surface area), which occurs under duodenal digestion conditions, could also explain the slowing down of lipolysis.

The capacity of the two BS to promote or inhibit MC-stabilised emulsion digestion was then explored with the pH-stat method and revealed that NaTC favoured FFA release to a higher extent than NaTDC (at 50 mM) (Fig. 10). The lower proportion of FFA release obtained with NaTDC can be explained by its higher efficiency at binding to MC network (as suggested by rheology measurements), which may result in this BS becoming trapped in the bulk and therefore not contributing to the lipolysis process.

5. Conclusion

The demonstrated potential of MC, a dietary fibre, to regulate lipolysis is thought to be due to its ability to reduce BS activity by sequestration; the objective of this work was to compare the interactions of two structurally different BS, NaTC and NaTDC, with MC, and to determine their impact on the digestion of an emulsion stabilised by this polysaccharide. These findings are key to establishing a molecular-level, mechanistic understanding of the ability of MC to lower fat absorption.

Both BS were found to decrease the elasticity of MC gels, and to shift the transition temperature (T_g) to stiffer gels to higher temperatures, to a higher extent with NaTDC. When injected below a MC film at the air/water interface, NaTC remained adsorbed at the interface over a wider concentration range, compared to NaTDC, which desorbed at a lower concentration, correlating with the onset of micellisation in the bulk (between 4–7 mM for NaTC and at 2 mM for NaTDC). The small difference in the two BS molecular structure, specifically their bile acid portion, is responsible for their contrasting behaviour, and explains the different results obtained during *in vitro* lipid digestion: (i) NaTDC has a higher propensity to disrupt MC network in the bulk and interfacial layer, and thus induces more extensive emulsion destabilisation (as seen from optical and confocal microscopy); (ii) the release of FFA is lower with NaTDC, which can be linked to its higher capacity to bind MC in the bulk, resulting in BS being unable to access the oil/water interface. Overall, it is clear that BS architectural diversity – whose importance is often neglected – plays a key role in their functionalities during fat digestion.

This work is a first step towards unlocking the mechanism of lipid digestion regulation by MC. Additional structural studies, in particular with techniques such as small-angle neutron scattering and neutron reflectometry, should bring significant knowledge to the area, in particular to examine the structure of MC in the presence of BS and the evolution of the fat droplet interface during digestion; this is the focus of current work. Building upon these results, the next challenge will be to engineer MC-stabilised lipid emulsions with appetite-suppressing or satiety-enhancing properties and evaluate their effect on cholesterol levels.

Declaration of Competing Interest

None.

Acknowledgements

The Institut Laue-Langevin (ILL, Grenoble, France) is acknowledged for the provision of a PhD studentship (OP). The authors acknowledge the Partnership for Soft Condensed Matter (PSCM) for access to sample preparation facilities and the use of the Langmuir trough, ellipsometer and optical microscope. Prof Peter Ellis is thanked for many useful discussions and access to laboratory facilities. OP also thanks Dr Angélique Pabois for her kind help with the statistical analysis of pH-stat data, and Taniya Akhtar for her contribution to the project. PJW and MM-LG gratefully acknowledge the support of the Biotechnology and Biological Sciences Research Council (BBSRC) through the BBSRC

Institute Strategic Programme Food Innovation and Health BB/R012512/1 and its constituent project BBS/E/F/000PR10345. Dr Isabelle Grillo, one of our co-authors and OP's PhD co-supervisor, sadly passed away during the writing-up of this manuscript; we dedicate this to her memory.

Appendix A. Supplementary data

Supplementary material related to this article can be found, in the online version, at doi:<https://doi.org/10.1016/j.carbpol.2019.115741>.

References

- Agostoni, C., Bresson, J.-L., Fairweather-Tait, S., Flynn, A., Golly, I., Korhonen, H., ... Verhagen, H. (2010). Scientific opinion on the substantiation of health claims related to hydroxypropyl methylcellulose (HPMC) and maintenance of normal bowel function (ID 812), reduction of post-prandial glycaemic responses (ID 814), maintenance of normal blood cholesterol c. *EFSA Journal*, 8(10), 1739. <https://doi.org/10.2903/j.efsa.2010.1739>.
- Arbolea, J.-C., & Wilde, P. J. (2005). Competitive adsorption of proteins with methylcellulose and hydroxypropyl methylcellulose. *Food Hydrocolloids*, 19(3), 485–491. <https://doi.org/10.1016/j.foodhyd.2004.10.013>.
- Armstrong, M. J., & Carey, M. C. (1982). The hydrophobic-hydrophilic balance of bile salts. Inverse correlation between reverse-phase high performance liquid chromatographic mobilities and micellar cholesterol-solubilizing capacities. *Journal of Lipid Research*, 23(1), 70–80. Retrieved from <http://www.ncbi.nlm.nih.gov/pubmed/7057113>.
- Avranas, A., & Tasopoulos, V. (2000). Aqueous solutions of sodium deoxycholate and hydroxypropylmethylcellulose: Dynamic surface tension measurements. *Journal of Colloid and Interface Science*, 221(2), 223–229. <https://doi.org/10.1006/jcis.1999.6574>.
- Bartley, G. E., Yokoyama, W., Young, S. A., Anderson, W. H. K., Hung, S.-C., Albers, D. R., ... Kim, H. (2010). Hypocholesterolemic effects of hydroxypropyl methylcellulose are mediated by altered gene expression in hepatic bile and cholesterol pathways of male hamsters. *The Journal of Nutrition*, 140(7), 1255–1260. <https://doi.org/10.3945/jn.109.118349>.
- Bellesi, F. A., Martínez, M. J., Pizonas Ruiz-Henestrosa, V. M., & Pilosof, A. M. R. (2016). Comparative behavior of protein or polysaccharide stabilized emulsion under *in vitro* gastrointestinal conditions. *Food Hydrocolloids*, 52, 47–56. <https://doi.org/10.1016/j.foodhyd.2015.06.007>.
- Borel, P., Armand, M., Ythier, P., Dutot, G., Melin, C., Senf, M., ... Lairon, D. (1994). Hydrolysis of emulsions with different triglycerides and droplet sizes by gastric lipase *in vitro*. Effect on pancreatic lipase activity. *The Journal of Nutritional Biochemistry*, 5(3), 124–133. [https://doi.org/10.1016/0955-2863\(94\)90083-3](https://doi.org/10.1016/0955-2863(94)90083-3).
- Borgström, B., Erlanson-Albertsson, C., & Wieloch, T. (1979). Pancreatic colipase: Chemistry and physiology. *Journal of Lipid Research*, 20(7), 805–816. Retrieved from <http://www.ncbi.nlm.nih.gov/pubmed/385801>.
- Bourbon Freie, A., Ferrato, F., Carrière, F., & Lowe, M. E. (2006). Val-407 and Ile-408 in the $\beta 5'$ -loop of pancreatic lipase mediate lipase-colipase interactions in the presence of bile salt micelles. *The Journal of Biological Chemistry*, 281(12), 7793–7800. <https://doi.org/10.1074/jbc.M512984200>.
- Camino, N. A., Pérez, O. E., Sanchez, C. C., Rodriguez Patino, J. M., & Pilosof, A. M. R. (2009). Hydroxypropylmethylcellulose surface activity at equilibrium and adsorption dynamics at the air–water and oil–water interfaces. *Food Hydrocolloids*, 23(8), 2359–2368. <https://doi.org/10.1016/j.foodhyd.2009.06.013>.
- Carr, T. P., Gallaher, D. D., Yang, C.-H., & Hassel, C. A. (1996). Increased intestinal contents viscosity reduces cholesterol absorption efficiency in hamsters fed hydroxypropyl methylcellulose. *The Journal of Nutrition*, 126(5), 1463–1469. <https://doi.org/10.1093/jn/126.5.1463>.
- Desbrières, J., Hirrien, M., & Rinaudo, M. (1998). A calorimetric study of methylcellulose gelation. *Carbohydrate Polymers*, 37, 145–152.
- Erlanson-Albertsson, C. (1983). The interaction between pancreatic lipase and colipase: A protein-protein interaction regulated by a lipid. *FEBS Letters*, 162(2), 225–229. [https://doi.org/10.1016/0014-5793\(83\)80760-1](https://doi.org/10.1016/0014-5793(83)80760-1).
- Fiji. (2019). Retrieved July 29, 2019, from <https://fiji.sc/>.
- Funami, T., Kataoka, Y., Hiroe, M., Asai, I., Takahashi, R., & Nishinari, K. (2007). Thermal aggregation of methylcellulose with different molecular weights. *Food Hydrocolloids*, 21(1), 46–58. <https://doi.org/10.1016/j.foodhyd.2006.01.008>.
- Graham, D. E., & Phillips, M. C. (1979). Proteins at liquid interfaces. I. Kinetics of adsorption and surface denaturation. *Journal of Colloid and Interface Science*, 70(3), 403–414. [https://doi.org/10.1016/0021-9797\(79\)90048-1](https://doi.org/10.1016/0021-9797(79)90048-1).
- GraphPad Prism, 2019. Retrieved June 28, 2019, from <https://www.graphpad.com/scientific-software/prism/>.
- Grundy, M. M. L., Wilde, P. J., Butterworth, P. J., Gray, R., & Ellis, P. R. (2015). Impact of cell wall encapsulation of almonds on *in vitro* duodenal lipolysis. *Food Chemistry*, 185, 405–412. <https://doi.org/10.1016/j.foodchem.2015.04.013>.
- Gunness, P., & Gidley, M. J. (2010). Mechanisms underlying the cholesterol-lowering properties of soluble dietary fibre polysaccharides. *Food & Function*, 1(2), 149–155. <https://doi.org/10.1039/c0fo00080a>.
- Haque, A., & Morris, E. R. (1993). Thermogelation of methylcellulose. Part I: Molecular structures and processes. *Carbohydrate Polymers*, 22(3), 161–173. [https://doi.org/10.1016/0144-8617\(93\)90137-S](https://doi.org/10.1016/0144-8617(93)90137-S).

- Hirrien, M., Chevillard, C., Desbrières, J., Axelos, M. A. V., & Rinaudo, M. (1998). Thermogelation of methylcelluloses: New evidence for understanding the gelation mechanism. *Polymer*, 39(25), 6251–6259. [https://doi.org/10.1016/S0032-3861\(98\)00142-6](https://doi.org/10.1016/S0032-3861(98)00142-6).
- Hofmann, A. F., & Mysels, K. J. (1987). Bile salts as biological surfactants. *Colloids and Surfaces*, 30(1), 145–173. [https://doi.org/10.1016/0166-6622\(87\)80207-X](https://doi.org/10.1016/0166-6622(87)80207-X).
- Isa Ziembowicz, F., de Freitas, D. V., Bender, C. R., dos Santos Salbego, P. R., Piccinin Frizzo, C., Pinto Martins, M. A., ... Villetti, M. A. (2019). Effect of mono- and dicationic ionic liquids on the viscosity and thermogelation of methylcellulose in the semi-diluted regime. *Carbohydrate Polymers*, 214, 174–185. <https://doi.org/10.1016/j.carbpol.2019.02.095>.
- Kobayashi, K., Huang, C., & Lodge, T. P. (1999). Thermoreversible gelation of aqueous methylcellulose solutions. *Macromolecules*, 32(21), 7070–7077. <https://doi.org/10.1021/ma990242n>.
- Labourdenne, S., Brass, O., Ivanova, M., Cagna, A., & Verger, R. (1997). Effects of colipase and bile salts on the catalytic activity of human pancreatic lipase. A study using the oil drop tensiometer. *Biochemistry*, 36(12), 3423–3429. <https://doi.org/10.1021/bj961331k>.
- Li, L., Shan, H., Yue, C. Y., Lam, Y. C., Tam, K. C., & Hu, X. (2002). Thermally induced association and dissociation of methylcellulose in aqueous solutions. *Langmuir*, 18(20), 7291–7298. <https://doi.org/10.1021/la020029b>.
- Li, L., Thangamathesvaran, P. M., Yue, C. Y., Tam, K. C., Hu, X., & Lam, Y. C. (2001). Gel network structure of methylcellulose in water. *Langmuir*, 17(26), 8062–8068. <https://doi.org/10.1021/la010917r>.
- Li, L. (2002). Thermal gelation of methylcellulose in water: Scaling and thermoreversibility. *Macromolecules*, 35(15), 5990–5998. <https://doi.org/10.1021/ma0201781>.
- Li, L., Wang, Q., & Xu, Y. (2003). Thermoreversible association and gelation of methylcellulose in aqueous solutions. *Nihon Reoroji Gakkaiishi*, 31(5), 287–296. <https://doi.org/10.1678/rheology.31.287>.
- Li, Y., Hu, M., & McClements, D. J. (2011). Factors affecting lipase digestibility of emulsified lipids using an in vitro digestion model: Proposal for a standardised pH-stat method. *Food Chemistry*, 126(2), 498–505. <https://doi.org/10.1016/j.foodchem.2010.11.027>.
- Maki, K. C., Carson, M. L., Kerr Anderson, W. H., Geohas, J., Reeves, M. S., Farmer, M. V., ... Rains, T. M. (2009). Lipid-altering effects of different formulations of hydroxypropylmethylcellulose. *Journal of Clinical Lipidology*, 3(3), 159–166. <https://doi.org/10.1016/j.jacl.2009.04.053>.
- Maldonado-Valderrama, J., Wilde, P., Macierzanka, A., & Mackie, A. (2011). The role of bile salts in digestion. *Advances in Colloid and Interface Science*, 165(1), 36–46. <https://doi.org/10.1016/j.cis.2010.12.002>.
- Matsuoka, K., Maeda, M., & Moroi, Y. (2003). Micelle formation of sodium glyco- and taurocholates and sodium glyco- and taurodeoxycholates and solubilization of cholesterol into their micelles. *Colloids and Surfaces B, Biointerfaces*, 32(2), 87–95. [https://doi.org/10.1016/S0927-7765\(03\)00148-6](https://doi.org/10.1016/S0927-7765(03)00148-6).
- McClements, D. J., & Li, Y. (2010a). Review of in vitro digestion models for rapid screening of emulsion-based systems. *Food & Function*, 1, 32–59. <https://doi.org/10.1039/c0fo00111b>.
- McClements, D. J., & Li, Y. (2010b). Structured emulsion-based delivery systems: Controlling the digestion and release of lipophilic food components. *Advances in Colloid and Interface Science*, 159(2), 213–228. <https://doi.org/10.1016/j.cis.2010.06.010>.
- Mei, J., Lindqvist, A., Krabisch, L., Rehfeld, J. F., & Erlanson-Albertsson, C. (2006). Appetite suppression through delayed fat digestion. *Physiology & Behavior*, 89(4), 563–568. <https://doi.org/10.1016/j.physbeh.2006.07.020>.
- Motschmann, H., & Teppner, R. (2001). Ellipsometry in interface science. In D. Möbius, & R. Miller (Eds.), *Studies in interface science - Novel methods to study interfacial layers* (pp. 1–42). (1st ed.). Amsterdam: Elsevier Science B.V.
- Nasatto, P. L., Pignon, F., Silveira, J. L. M., Duarte, M. E. R., Nosedá, M. D., & Rinaudo, M. (2014). Interfacial properties of methylcelluloses: The influence of molar mass. *Polymers*, 6(12), 2961–2973. <https://doi.org/10.3390/polym6122961>.
- Nasatto, P. L., Pignon, F., Silveira, J. L. M., Duarte, M. E. R., Nosedá, M. D., & Rinaudo, M. (2015a). Influence of molar mass and concentration on the thermogelation of methylcelluloses. *International Journal of Polymer Analysis and Characterization*, 20(2), 110–118. <https://doi.org/10.1080/1023666X.2015.973155>.
- Nasatto, P. L., Pignon, F., Silveira, J. L. M., Duarte, M. E. R., Nosedá, M. D., & Rinaudo, M. (2015b). Methylcellulose, a cellulose derivative with original physical properties and extended applications. *Polymers*, 7(5), 777–803. <https://doi.org/10.3390/polym7050777>.
- Pabois, O., Lorenz, C. D., Harvey, R. D., Grillo, I., Grundy, M. M.-L., Wilde, P. J., ... Dreiss, C. A. (2019). Molecular insights into the behaviour of bile salts at interfaces: A key to their role in lipid digestion. *Journal of Colloid and Interface Science*, 556, 266–277. <https://doi.org/10.1016/j.jcis.2019.08.010>.
- Parker, R., Rigby, N. M., Ridout, M. J., Gunning, A. P., & Wilde, P. J. (2014). The adsorption-desorption behaviour and structure function relationships of bile salts. *Soft Matter*, 10(34), 6457–6466. <https://doi.org/10.1039/c4sm01093k>.
- Patton, J., & Carey, M. (1979). Watching fat digestion. *Science*, 204(4389), 145–148. <https://doi.org/10.1126/science.432636>.
- Pérez, O. E., Sánchez, C. C., Pilosof, A. M. R., & Rodríguez Patino, J. M. (2008). Dynamics of adsorption of hydroxypropyl methylcellulose at the air-water interface. *Food Hydrocolloids*, 22(3), 387–402. <https://doi.org/10.1016/j.foodhyd.2006.12.005>.
- Pilosof, A. M. R. (2017). Potential impact of interfacial composition of proteins and polysaccharides stabilized emulsions on the modulation of lipolysis. The role of bile salts. *Food Hydrocolloids*, 68, 178–185. <https://doi.org/10.1016/j.foodhyd.2016.08.030>.
- Pizonés Ruiz-Henestrosa, V. M., Bellesi, F. A., Camino, N. A., & Pilosof, A. M. R. (2017). The impact of HPMC structure in the modulation of in vitro lipolysis: The role of bile salts. *Food Hydrocolloids*, 62, 251–261. <https://doi.org/10.1016/j.foodhyd.2016.08.002>.
- Reis, P., Holmberg, K., Watzke, H., Leser, M. E., & Miller, R. (2009). Lipases at interfaces: A review. *Advances in Colloid and Interface Science*, 147–148, 237–250. <https://doi.org/10.1016/j.cis.2008.06.001>.
- Reis, P. M., Raab, T. W., Chuat, J. Y., Leser, M. E., Miller, R., Watzke, H. J., ... Holmberg, K. (2008). Influence of surfactants on lipase fat digestion in a model gastro-intestinal system. *Food Biophysics*, 3(4), 370–381. <https://doi.org/10.1007/s11483-008-9091-6>.
- Reis, P., Miller, R., Leser, M., Watzke, H., Fainerman, V. B., & Holmberg, K. (2008). Adsorption of polar lipids at the water-oil interface. *Langmuir*, 24(11), 5781–5786. <https://doi.org/10.1021/la704043g>.
- Reppas, C., Swidan, S. Z., Tobey, S. W., Turowski, M., & Dressman, J. B. (2009). Hydroxypropylmethylcellulose significantly lowers blood cholesterol in mildly hypercholesterolemic human subjects. *European Journal of Clinical Nutrition*, 63(1), 71–77. <https://doi.org/10.1038/sj.ejcn.1602903>.
- Reppas, C., Meyer, J. H., Sirois, P. J., & Dressman, J. B. (1991). Effect of hydroxypropylmethylcellulose on gastrointestinal transit and luminal Viscosity in dogs. *Gastroenterology*, 100(5), 1217–1223. [https://doi.org/10.1016/0016-5085\(91\)70007-K](https://doi.org/10.1016/0016-5085(91)70007-K).
- Sánchez, A., Maceiras, R., Cancela, A., & Rodríguez, M. (2012). Influence of n-hexane on situ transesterification of marine macroalgae. *Energies*, 5(2), 243–257. <https://doi.org/10.3390/en5020243>.
- Sarkar, N. (1995). Kinetics of thermal gelation of methylcellulose and hydroxypropylmethylcellulose in aqueous solutions. *Carbohydrate Polymers*, 26(3), 195–203. [https://doi.org/10.1016/0144-8617\(94\)00107-5](https://doi.org/10.1016/0144-8617(94)00107-5).
- Slavin, J. L. (2005). Dietary fiber and body weight. *Nutrition*, 21(3), 411–418. <https://doi.org/10.1016/j.nut.2004.08.018>.
- Staggers, J. E., Hernel, O., Stafford, R. J., & Carey, M. C. (1990). Physical-chemical behavior of dietary and biliary lipids during intestinal digestion and absorption. 1. Phase behavior and aggregation states of model lipid systems patterned after aqueous duodenal contents of healthy adult human beings. *Biochemistry*, 29(8), 2028–2040. <https://doi.org/10.1021/bi00460a011>.
- The Dow Chemical Company (2002). *METHOCEL cellulose ethers - Technical handbook*. (192-01062-0902 AMS). 1–32.
- The Dow Chemical Company (2013). *Chemistry of METHOCEL™: cellulose ethers - a technical review. METHOCEL™ - Technical Bulletin, (198-02289-10/13 EST)*. Retrieved from 1–16. http://msdssearch.dow.com/PublishedLiteratureDOWCOM/dh_08e5/0901b803808e5f58.pdf?filepath=dowwolff/pdfs/noreg/198-02289.pdf&fromPage=GetDoc.
- Torcello-Gómez, A., Fernández Fraguas, C., Ridout, M. J., Woodward, N. C., Wilde, P. J., & Foster, T. J. (2015). Effect of substituent pattern and molecular weight of cellulose ethers on interactions with different bile salts. *Food & Function*, 6(3), 730–739. <https://doi.org/10.1039/c5fo00099h>.
- Torcello-Gómez, A., & Foster, T. J. (2014). Interactions between cellulose ethers and a bile salt in the control of lipid digestion of lipid-based systems. *Carbohydrate Polymers*, 113, 53–61. <https://doi.org/10.1016/j.carbpol.2014.06.070>.
- van der Gronde, T., Hartog, A., van Hees, C., Pellikaan, H., & Pieters, T. (2016). Systematic review of the mechanisms and evidence behind the hypocholesterolaemic effects of HPMC, pectin and chitosan in animal trials. *Food Chemistry*, 199, 746–759. <https://doi.org/10.1016/j.foodchem.2015.12.050>.
- Wilde, P. J., & Chu, B. S. (2011). Interfacial & colloidal aspects of lipid digestion. *Advances in Colloid and Interface Science*, 165(1), 14–22. <https://doi.org/10.1016/j.cis.2011.02.004>.
- Wollenweber, C., Makievski, A. V., Miller, R., & Daniels, R. (2000). Adsorption of hydroxypropyl methylcellulose at the liquid/liquid interface and the effect on emulsion stability. *Colloids and Surfaces A, Physicochemical and Engineering Aspects*, 172(1–3), 91–101. [https://doi.org/10.1016/S0927-7757\(00\)00569-0](https://doi.org/10.1016/S0927-7757(00)00569-0).
- World Health Organization (2019). *Obesity and overweight*. Retrieved June 26, 2019, from <http://www.who.int/mediacentre/factsheets/fs311/en/>.
- Younes, M., Aggett, P., Aguilar, F., Crebelli, R., Di Domenico, A., Dusemund, B., ... Woutersen, R. A. (2018). Re-evaluation of celluloses E 460(i), E 460(ii), E 461, E 462, E 463, E 464, E 465, E 466, E 468 and E 469 as food additives. *EFSA Journal*, 16(1), 1–104. <https://doi.org/10.2903/j.efsa.2018.5047>.

Supporting information

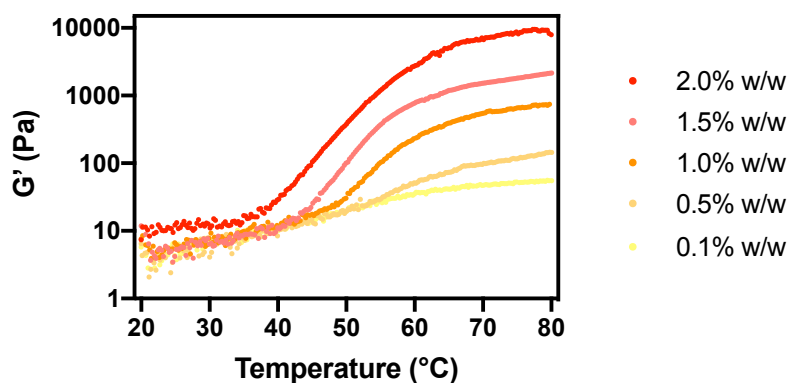


Figure S1: Temperature-dependent evolution of the storage modulus (G') obtained from dynamic temperature sweeps, on MC aqueous solutions prepared at different concentrations (0.1, 0.5, 1.0, 1.5 and 2.0% w/w). G' dominates over G'' at all concentrations and temperatures; G'' was therefore omitted for clarity.

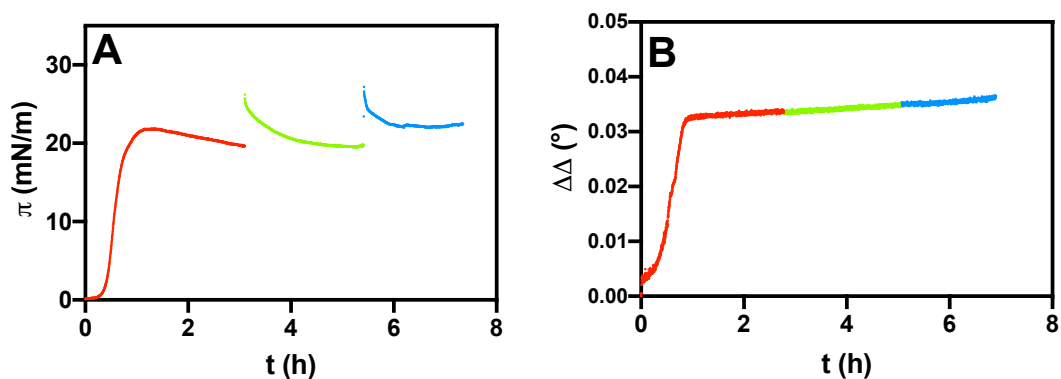


Figure S2: Time-dependent evolution of (A) the surface pressure (π) measured in a Langmuir trough, and (B) phase shift ($\Delta\Delta(t) = \Delta(t) - \Delta_0$) measured by ellipsometry, upon successive injections of MC: (—) 0.5 $\times 10^{-1}\%$ w/w, (—) 0.25 $\%$ w/w, (—) 0.5% w/w, into the aqueous subphase (at $23 \pm 2^{\circ}\text{C}$).

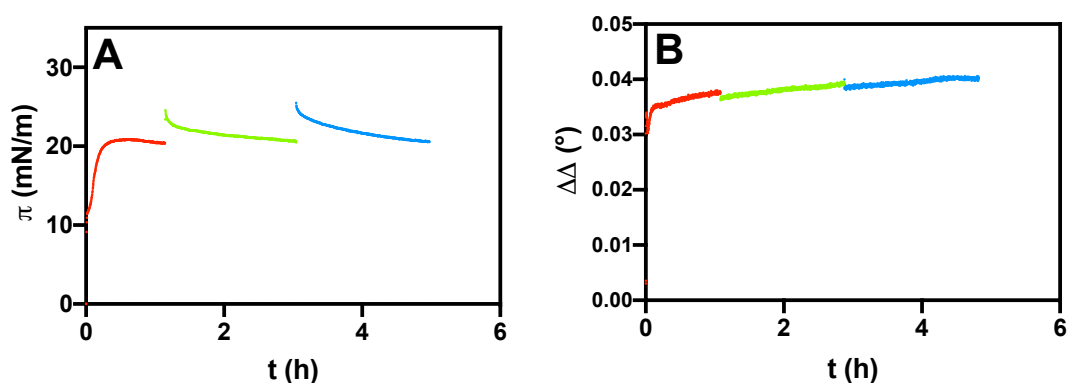


Figure S3: Time-dependent evolution of (A) the surface pressure (π) measured in a Langmuir trough, and (B) phase shift ($\Delta\Delta(t) = \Delta(t) - \Delta_0$) measured by ellipsometry, upon successive injections of MC: (—) 0.5 $\times 10^{-2}\%$ w/w, (—) 0.25 $\times 10^{-1}\%$ w/w, (—) 0.5 $\times 10^{-1}\%$ w/w, into the aqueous subphase (at $23 \pm 2^{\circ}\text{C}$).

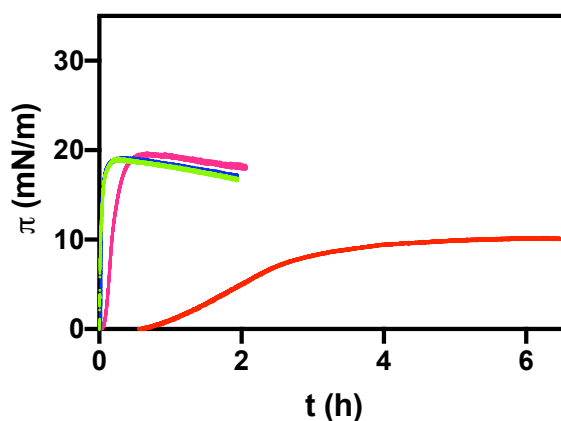


Figure S4: Time-dependent evolution of the surface pressure (π) measured in a Langmuir trough, upon injection of MC into the aqueous subphase, at varying concentrations: (—) $0.5 \times 10^{-3}\text{‰}$ w/w, (—) $0.5 \times 10^{-2}\text{‰}$ w/w, (—) $0.5 \times 10^{-1}\text{‰}$ w/w, (—) 0.5‰ w/w (at $23 \pm 2^\circ\text{C}$). Each experiment was reproduced twice, and the average measurement was selected for each BS at each concentration.

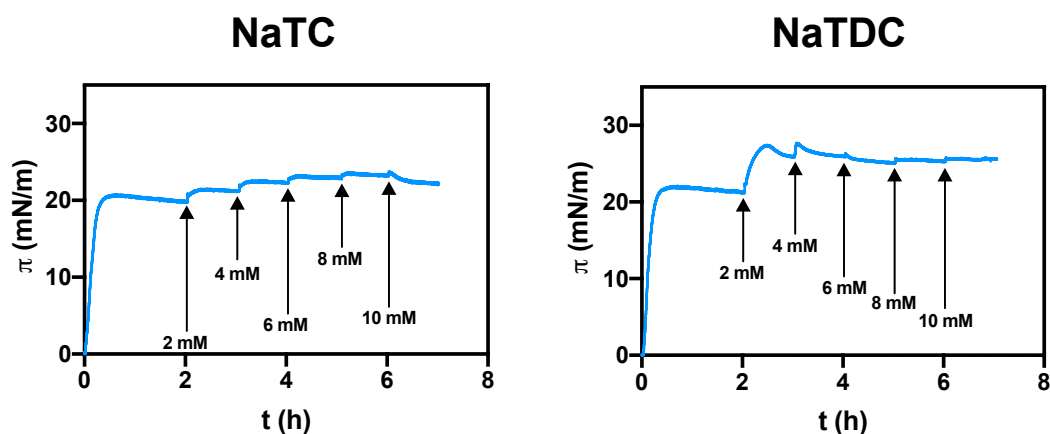


Figure S5: Time-dependent evolution of the surface pressure (π) measured in a Langmuir trough, upon successive injections of BS into the aqueous subphase: NaTC, NaTDC (at $23 \pm 2^\circ\text{C}$). The first increase in surface pressure corresponds to the adsorption of MC at the air/water interface, which was added into water at a concentration of $0.5 \times 10^{-2}\text{‰}$ w/w ($\pi_{\text{MC}} = 18 \pm 2$ mN/m). Each addition of BS is shown by an arrow, together with the corresponding BS concentration achieved in the subphase. Each experiment was reproduced twice, and a representative measurement was selected for each experiment.

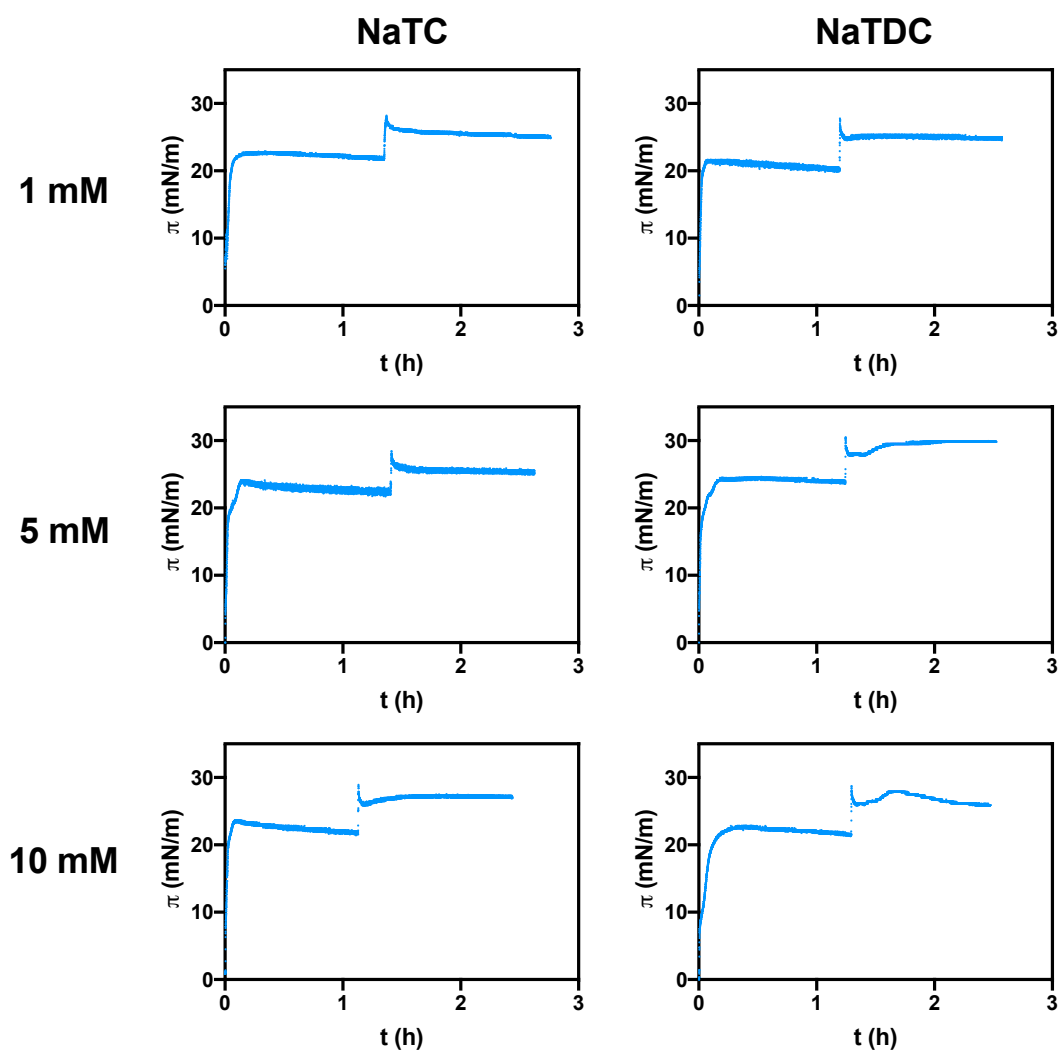


Figure S6: Time-dependent evolution of the surface pressure (π) measured in a Langmuir trough, upon injection of varying concentrations: 1, 5, 10 mM, of BS: NaTC, NaTDC, into the aqueous subphase (at $23 \pm 2^\circ\text{C}$). The first increase in surface pressure corresponds to the adsorption of MC at the air/water interface, which was added into water at a concentration of 0.5% w/w ($\pi_{\text{MC}} = 21 \pm 1$ mN/m). Each experiment was reproduced at least twice, and a representative measurement was selected for each BS at each concentration.

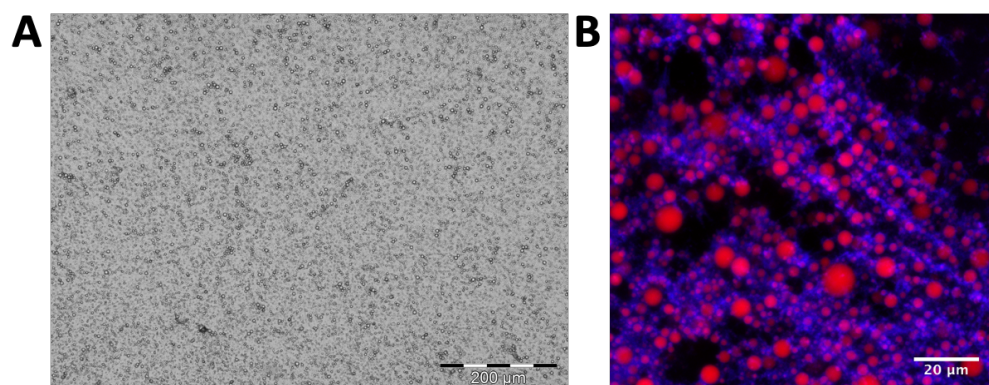


Figure S7: Characterisation of MC-stabilised emulsion droplets microstructure by (A) optical (scale bar: 200 μm) and (B) confocal (scale bar: 20 μm) microscopy. MC-stabilised emulsion was made up of 0.5% MC and 15%

sunflower oil. The confocal micrograph shows the lipid droplets (stained in red with Nile red) surrounded by MC (stained in blue with calcofluor) present as a network in the bulk (B).

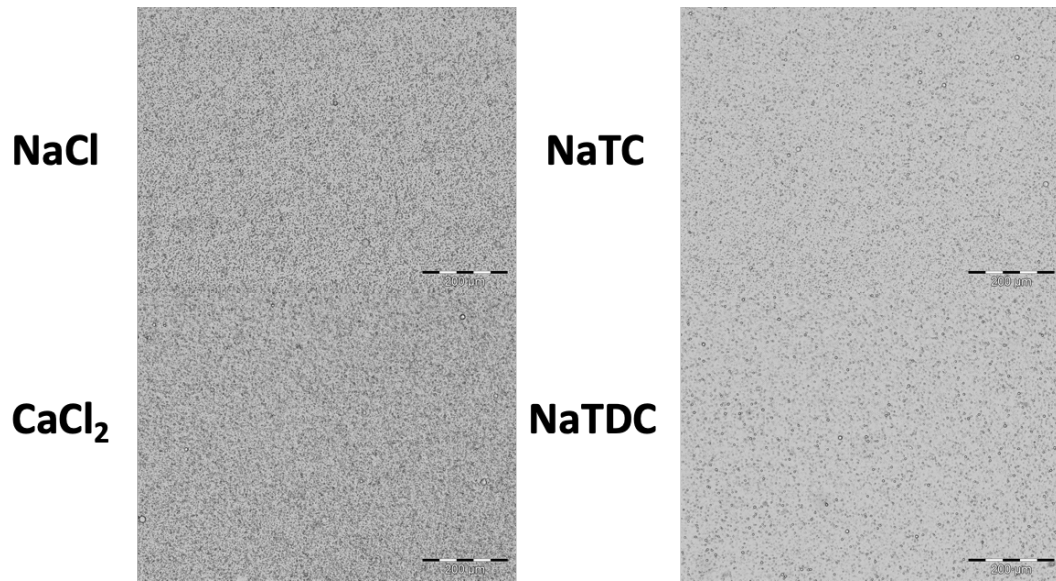


Figure S8: Impact of the different digestive fluid components: NaCl, CaCl₂ and BS (NaTC, NaTDC) (used individually), on the microstructure of MC-stabilised emulsion droplets, 60 min after mixing (at 37°C). MC-stabilised emulsion was made up of 0.5% MC and 15% sunflower oil. The scale bar is 200 µm.

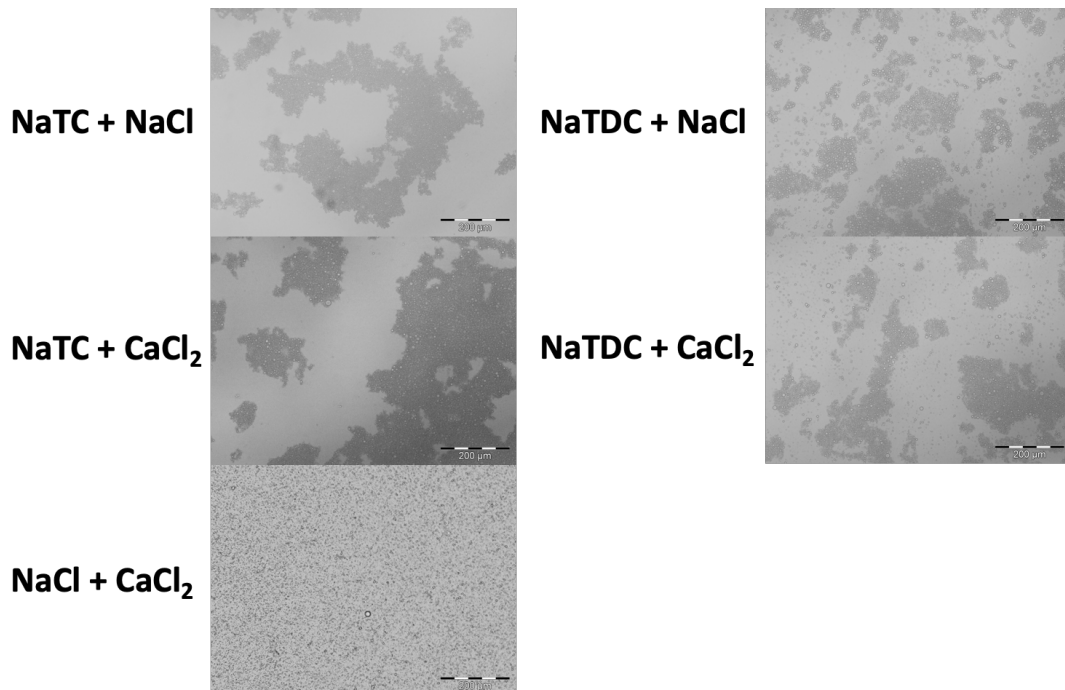


Figure S9: Impact of the different digestive fluid components: NaCl, CaCl₂ and BS (NaTC, NaTDC) (used in combination), on the microstructure of MC-stabilised emulsion droplets, 60 min after mixing (at 37°C). MC-stabilised emulsion was made up of 0.5% MC and 15% sunflower oil. The scale bar is 200 µm.

References

- [1] World Health Organization, Obesity and overweight, (2019). <http://www.who.int/mediacentre/factsheets/fs311/en/> (accessed June 26, 2019).
- [2] J. Mei, A. Lindqvist, L. Krabisch, J.F. Rehfeld, C. Erlanson-Albertsson, Appetite suppression through delayed fat digestion, *Physiol. Behav.* 89 (2006) 563–568. doi:10.1016/j.physbeh.2006.07.020.
- [3] D.J. McClements, Y. Li, Structured emulsion-based delivery systems: controlling the digestion and release of lipophilic food components, *Adv. Colloid Interface Sci.* 159 (2010) 213–228. doi:10.1016/j.cis.2010.06.010.
- [4] J.L. Slavin, Dietary fiber and body weight, *Nutrition.* 21 (2005) 411–418. doi:10.1016/j.nut.2004.08.018.
- [5] M. Younes, P. Aggett, F. Aguilar, R. Crebelli, A. Di Domenico, B. Dusemund, M. Filipič, M. Jose Frutos, P. Galtier, D. Gott, U. Gundert-Remy, G. Georg Kuhnle, C. Lambré, J. Leblanc, I.T. Lillegaard, P. Moldeus, A. Mortensen, A. Oskarsson, I. Stankovic, P. Tobback, I. Waalkens-Berendsen, M. Wright, A. Tard, S. Tasiopoulou, R.A. Woutersen, Re-evaluation of celluloses E 460(i), E 460(ii), E 461, E 462, E 463, E 464, E 465, E 466, E 468 and E 469 as food additives, *EFSA J.* 16 (2018) 1–104. doi:10.2903/j.efsa.2018.5047.
- [6] The Dow Chemical Company, METHOCEL cellulose ethers - Technical handbook, (2002) 1–32.
- [7] C. Agostoni, J.-L. Bresson, S. Fairweather-Tait, A. Flynn, I. Golly, H. Korhonen, P. Lagiou, M. Løvik, R. Marchelli, A. Martin, B. Moseley, M. Neuhäuser-Berthold, H. Przyrembel, S. Salminen, Y. Sanz, S.J.J. Strain, S. Strobel, I. Tetens, D. Tomé, H. van Loveren, H. Verhagen, Scientific opinion on the substantiation of health claims related to hydroxypropyl methylcellulose (HPMC) and maintenance of normal bowel function (ID 812), reduction of post-prandial glycaemic responses (ID 814), maintenance of normal blood cholesterol

concentrations (ID 815) and increase in satiety leading to a reduction in energy intake (ID 2933) pursuant to Article 13(1) of Regulation (EC) No 1924/2006, EFSA J. 8 (2010) 1739. doi:10.2903/j.efsa.2010.1739.

- [8] P.L. Nasatto, F. Pignon, J.L.M. Silveira, M.E.R. Duarte, M.D. Nosedá, M. Rinaudo, Methylcellulose, a cellulose derivative with original physical properties and extended applications, *Polymers (Basel)*. 7 (2015) 777–803. doi:10.3390/polym7050777.
- [9] C. Reppas, J.H. Meyer, P.J. Sirois, J.B. Dressman, Effect of hydroxypropylmethylcellulose on gastrointestinal transit and luminal viscosity in dogs, *Gastroenterology*. 100 (1991) 1217–1223. doi:10.1016/0016-5085(91)70007-K.
- [10] K.C. Maki, M.L. Carson, W.H. Kerr Anderson, J. Geohas, M.S. Reeves, M. V. Farmer, M. Turowski, M. Miller, V.N. Kaden, M.R. Dicklin, T.M. Rains, Lipid-altering effects of different formulations of hydroxypropylmethylcellulose, *J. Clin. Lipidol.* 3 (2009) 159–166. doi:10.1016/j.jacl.2009.04.053.
- [11] C. Reppas, S.Z. Swidan, S.W. Tobey, M. Turowski, J.B. Dressman, Hydroxypropylmethylcellulose significantly lowers blood cholesterol in mildly hypercholesterolemic human subjects, *Eur. J. Clin. Nutr.* 63 (2009) 71–77. doi:10.1038/sj.ejcn.1602903.
- [12] G.E. Bartley, W. Yokoyama, S.A. Young, W.H.K. Anderson, S.-C. Hung, D.R. Albers, M.L. Langhorst, H. Kim, Hypocholesterolemic effects of hydroxypropyl methylcellulose are mediated by altered gene expression in hepatic bile and cholesterol pathways of male hamsters, *J. Nutr.* 140 (2010) 1255–1260. doi:10.3945/jn.109.118349.
- [13] T. van der Gonde, A. Hartog, C. van Hees, H. Pellikaan, T. Pieters, Systematic review of the mechanisms and evidence behind the hypocholesterolaemic effects of HPMC, pectin and chitosan in animal trials, *Food Chem.* 199 (2016) 746–759. doi:10.1016/j.foodchem.2015.12.050.

- [14] T.P. Carr, D.D. Gallaher, C.-H. Yang, C.A. Hassel, Increased intestinal contents viscosity reduces cholesterol absorption efficiency in hamsters fed hydroxypropyl methylcellulose, *J. Nutr.* 126 (1996) 1463–1469. doi:10.1093/jn/126.5.1463.
- [15] A. Torcello-Gómez, T.J. Foster, Interactions between cellulose ethers and a bile salt in the control of lipid digestion of lipid-based systems, *Carbohydr. Polym.* 113 (2014) 53–61. doi:10.1016/j.carbpol.2014.06.070.
- [16] A. Torcello-Gómez, C. Fernández Fraguas, M.J. Ridout, N.C. Woodward, P.J. Wilde, T.J. Foster, Effect of substituent pattern and molecular weight of cellulose ethers on interactions with different bile salts, *Food Funct.* 6 (2015) 730–739. doi:10.1039/c5fo00099h.
- [17] V.M. Pizones Ruiz-Henestrosa, F.A. Bellesi, N.A. Camino, A.M.R. Pilosof, The impact of HPMC structure in the modulation of in vitro lipolysis: the role of bile salts, *Food Hydrocoll.* 62 (2017) 251–261. doi:10.1016/j.foodhyd.2016.08.002.
- [18] A.M.R. Pilosof, Potential impact of interfacial composition of proteins and polysaccharides stabilized emulsions on the modulation of lipolysis. The role of bile salts., *Food Hydrocoll.* 68 (2017) 178–185. doi:10.1016/j.foodhyd.2016.08.030.
- [19] A.F. Hofmann, K.J. Mysels, Bile salts as biological surfactants, *Colloids and Surfaces.* 30 (1987) 145–173. doi:10.1016/0166-6622(87)80207-X.
- [20] J. Maldonado-Valderrama, P. Wilde, A. Macierzanka, A. Mackie, The role of bile salts in digestion, *Adv. Colloid Interface Sci.* 165 (2011) 36–46. doi:10.1016/j.cis.2010.12.002.
- [21] P.J. Wilde, B.S. Chu, Interfacial & colloidal aspects of lipid digestion, *Adv. Colloid Interface Sci.* 165 (2011) 14–22. doi:10.1016/j.cis.2011.02.004.
- [22] B. Borgström, C. Erlanson-Albertsson, T. Wieloch, Pancreatic colipase: chemistry and physiology., *J. Lipid Res.* 20 (1979) 805–816.

<http://www.ncbi.nlm.nih.gov/pubmed/385801>.

- [23] C. Erlanson-Albertsson, The interaction between pancreatic lipase and colipase: a protein-protein interaction regulated by a lipid, *FEBS Lett.* 162 (1983) 225–229. doi:10.1016/0014-5793(83)80760-1.
- [24] A. Bourbon Freie, F. Ferrato, F. Carrière, M.E. Lowe, Val-407 and Ile-408 in the β 5'-loop of pancreatic lipase mediate lipase-colipase interactions in the presence of bile salt micelles, *J. Biol. Chem.* 281 (2006) 7793–7800. doi:10.1074/jbc.M512984200.
- [25] S. Labourdenne, O. Brass, M. Ivanova, A. Cagna, R. Verger, Effects of colipase and bile salts on the catalytic activity of human pancreatic lipase. A study using the oil drop tensiometer, *Biochemistry.* 36 (1997) 3423–3429. doi:10.1021/bi961331k.
- [26] P. Gunness, M.J. Gidley, Mechanisms underlying the cholesterol-lowering properties of soluble dietary fibre polysaccharides, *Food Funct.* 1 (2010) 149–155. doi:10.1039/c0fo00080a.
- [27] R. Parker, N.M. Rigby, M.J. Ridout, A.P. Gunning, P.J. Wilde, The adsorption–desorption behaviour and structure function relationships of bile salts, *Soft Matter.* 10 (2014) 6457–6466. doi:10.1039/c4sm01093k.
- [28] O. Pabois, C.D. Lorenz, R.D. Harvey, I. Grillo, M.M.-L. Grundy, P.J. Wilde, Y. Gerelli, C.A. Dreiss, Molecular insights into the behaviour of bile salts at interfaces: a key to their role in lipid digestion, *J. Colloid Interface Sci.* 556 (2019) 266–277. doi:10.1016/j.jcis.2019.08.010.
- [29] The Dow Chemical Company, Chemistry of METHOCEL™: cellulose ethers - a technical review, METHOCEL™ - Tech. Bull. (2013) 1–16. http://msdssearch.dow.com/PublishedLiteratureDOWCOM/dh_08e5/0901b803808e5f58.pdf?filepath=dowwolff/pdfs/noreg/198-02289.pdf&fromPage=GetDoc.

- [30] H. Motschmann, R. Teppner, Ellipsometry in interface science, in: D. Möbius, R. Miller (Eds.), *Stud. Interface Sci. - Nov. Methods to Study Interfacial Layers*, 1st ed., Elsevier Science B. V., Amsterdam, 2001: pp. 1–42.
- [31] M.M.L. Grundy, P.J. Wilde, P.J. Butterworth, R. Gray, P.R. Ellis, Impact of cell wall encapsulation of almonds on in vitro duodenal lipolysis, *Food Chem.* 185 (2015) 405–412. doi:10.1016/j.foodchem.2015.04.013.
- [32] Fiji, (2019). <https://fiji.sc/> (accessed July 29, 2019).
- [33] A. Sánchez, R. Maceiras, A. Cancela, M. Rodríguez, Influence of n-hexane on in situ transesterification of marine macroalgae, *Energies.* 5 (2012) 243–257. doi:10.3390/en5020243.
- [34] GraphPad Prism, (2019). <https://www.graphpad.com/scientific-software/prism/> (accessed June 28, 2019).
- [35] L. Li, P.M. Thangamathesvaran, C.Y. Yue, K.C. Tam, X. Hu, Y.C. Lam, Gel network structure of methylcellulose in water, *Langmuir.* 17 (2001) 8062–8068. doi:10.1021/la010917r.
- [36] L. Li, Thermal gelation of methylcellulose in water: scaling and thermoreversibility, *Macromolecules.* 35 (2002) 5990–5998. doi:10.1021/ma0201781.
- [37] T. Funami, Y. Kataoka, M. Hiroe, I. Asai, R. Takahashi, K. Nishinari, Thermal aggregation of methylcellulose with different molecular weights, *Food Hydrocoll.* 21 (2007) 46–58. doi:10.1016/j.foodhyd.2006.01.008.
- [38] P.L. Nasatto, F. Pignon, J.L.M. Silveira, M.E.R. Duarte, M.D. Nosedá, M. Rinaudo, Influence of molar mass and concentration on the thermogelation of methylcelluloses, *Int. J. Polym. Anal. Charact.* 20 (2015) 110–118. doi:10.1080/1023666X.2015.973155.
- [39] N. Sarkar, Kinetics of thermal gelation of methylcellulose and hydroxypropylmethylcellulose in aqueous solutions, *Carbohydr. Polym.* 26

- (1995) 195–203. doi:10.1016/0144-8617(94)00107-5.
- [40] J. Desbrières, M. Hirrien, M. Rinaudo, A calorimetric study of methylcellulose gelation, *Carbohydr. Polym.* 37 (1998) 145–152.
- [41] M. Hirrien, C. Chevillard, J. Desbrières, M.A. V Axelos, M. Rinaudo, Thermogelation of methylcelluloses: new evidence for understanding the gelation mechanism, *Polymer (Guildf)*. 39 (1998) 6251–6259. doi:10.1016/S0032-3861(98)00142-6.
- [42] K. Kobayashi, C. Huang, T.P. Lodge, Thermoreversible gelation of aqueous methylcellulose solutions, *Macromolecules*. 32 (1999) 7070–7077. doi:10.1021/ma990242n.
- [43] L. Li, H. Shan, C.Y. Yue, Y.C. Lam, K.C. Tam, X. Hu, Thermally induced association and dissociation of methylcellulose in aqueous solutions, *Langmuir*. 18 (2002) 7291–7298. doi:10.1021/la020029b.
- [44] L. Li, Q. Wang, Y. Xu, Thermoreversible association and gelation of methylcellulose in aqueous solutions, *Nihon Reoroji Gakkaishi*. 31 (2003) 287–296. doi:10.1678/rheology.31.287.
- [45] F. Isa Ziembowicz, D.V. de Freitas, C.R. Bender, P.R. dos Santos Salbego, C. Piccinin Frizzo, M.A. Pinto Martins, J.M. Reichert, I.T. Santos Garcia, C.L. Kloster, M.A. Villetti, Effect of mono- and dicationic ionic liquids on the viscosity and thermogelation of methylcellulose in the semi-diluted regime, *Carbohydr. Polym.* 214 (2019) 174–185. doi:10.1016/j.carbpol.2019.02.095.
- [46] A. Haque, E.R. Morris, Thermogelation of methylcellulose. Part I: molecular structures and processes, *Carbohydr. Polym.* 22 (1993) 161–173. doi:10.1016/0144-8617(93)90137-S.
- [47] D.E. Graham, M.C. Phillips, Proteins at liquid interfaces. I. Kinetics of adsorption and surface denaturation, *J. Colloid Interface Sci.* 70 (1979) 403–414. doi:10.1016/0021-9797(79)90048-1.

- [48] J.-C. Arboleya, P.J. Wilde, Competitive adsorption of proteins with methylcellulose and hydroxypropyl methylcellulose, *Food Hydrocoll.* 19 (2005) 485–491. doi:10.1016/j.foodhyd.2004.10.013.
- [49] O.E. Pérez, C.C. Sánchez, A.M.R. Pilosof, J.M. Rodríguez Patino, Dynamics of adsorption of hydroxypropyl methylcellulose at the air–water interface, *Food Hydrocoll.* 22 (2008) 387–402. doi:10.1016/j.foodhyd.2006.12.005.
- [50] N.A. Camino, O.E. Pérez, C.C. Sanchez, J.M. Rodriguez Patino, A.M.R. Pilosof, Hydroxypropylmethylcellulose surface activity at equilibrium and adsorption dynamics at the air–water and oil–water interfaces, *Food Hydrocoll.* 23 (2009) 2359–2368. doi:10.1016/j.foodhyd.2009.06.013.
- [51] C. Wollenweber, A. V. Makievski, R. Miller, R. Daniels, Adsorption of hydroxypropyl methylcellulose at the liquid/liquid interface and the effect on emulsion stability, *Colloids Surfaces A Physicochem. Eng. Asp.* 172 (2000) 91–101. doi:10.1016/S0927-7757(00)00569-0.
- [52] A. Avranas, V. Tasopoulos, Aqueous solutions of sodium deoxycholate and hydroxypropylmethylcellulose: dynamic surface tension measurements, *J. Colloid Interface Sci.* 221 (2000) 223–229. doi:10.1006/jcis.1999.6574.
- [53] P.L. Nasatto, F. Pignon, J.L.M. Silveira, M.E.R. Duarte, M.D. Nosedá, M. Rinaudo, Interfacial properties of methylcelluloses: the influence of molar mass, *Polymers (Basel)*. 6 (2014) 2961–2973. doi:10.3390/polym6122961.
- [54] K. Matsuoka, M. Maeda, Y. Moroi, Micelle formation of sodium glyco- and taurocholates and sodium glyco- and taurodeoxycholates and solubilization of cholesterol into their micelles, *Colloids Surfaces B Biointerfaces*. 32 (2003) 87–95. doi:10.1016/S0927-7765(03)00148-6.
- [55] Y. Li, M. Hu, D.J. McClements, Factors affecting lipase digestibility of emulsified lipids using an in vitro digestion model: proposal for a standardised pH-stat method, *Food Chem.* 126 (2011) 498–505. doi:10.1016/j.foodchem.2010.11.027.

- [56] F.A. Bellesi, M.J. Martinez, V.M. Pizones Ruiz-Henestrosa, A.M.R. Pilosof, Comparative behavior of protein or polysaccharide stabilized emulsion under in vitro gastrointestinal conditions, *Food Hydrocoll.* 52 (2016) 47–56. doi:10.1016/j.foodhyd.2015.06.007.
- [57] D.J. McClements, Y. Li, Review of in vitro digestion models for rapid screening of emulsion-based systems, *Food Funct.* 1 (2010) 32–59. doi:10.1039/c0fo00111b.
- [58] P. Reis, R. Miller, M. Leser, H. Watzke, V.B. Fainerman, K. Holmberg, Adsorption of polar lipids at the water–oil interface, *Langmuir.* 24 (2008) 5781–5786. doi:10.1021/la704043g.
- [59] J. Patton, M. Carey, Watching fat digestion, *Science* (80-.). 204 (1979) 145–148. doi:10.1126/science.432636.
- [60] P. Reis, K. Holmberg, H. Watzke, M.E. Leser, R. Miller, Lipases at interfaces: a review, *Adv. Colloid Interface Sci.* 147–148 (2009) 237–250. doi:10.1016/j.cis.2008.06.001.
- [61] P.M. Reis, T.W. Raab, J.Y. Chuat, M.E. Leser, R. Miller, H.J. Watzke, K. Holmberg, Influence of surfactants on lipase fat digestion in a model gastrointestinal system, *Food Biophys.* 3 (2008) 370–381. doi:10.1007/s11483-008-9091-6.
- [62] P. Borel, M. Armand, P. Ythier, G. Dutot, C. Melin, M. Senft, H. Lafont, D. Lairon, Hydrolysis of emulsions with different triglycerides and droplet sizes by gastric lipase in vitro. Effect on pancreatic lipase activity., *J. Nutr. Biochem.* 5 (1994) 124–133. doi:10.1016/0955-2863(94)90083-3.
- [63] J.E. Staggers, O. Hernell, R.J. Stafford, M.C. Carey, Physical-chemical behavior of dietary and biliary lipids during intestinal digestion and absorption. 1. Phase behavior and aggregation states of model lipid systems patterned after aqueous duodenal contents of healthy adult human beings, *Biochemistry.* 29 (1990) 2028–2040. doi:10.1021/bi00460a011.

- [64] M.J. Armstrong, M.C. Carey, The hydrophobic-hydrophilic balance of bile salts. Inverse correlation between reverse-phase high performance liquid chromatographic mobilities and micellar cholesterol-solubilizing capacities., *J. Lipid Res.* 23 (1982) 70–80. <http://www.ncbi.nlm.nih.gov/pubmed/7057113>.

General conclusion

Conclusion

The first objective of this PhD thesis was to understand the interfacial (Chapters 1 and 2) and bulk (Chapter 3) behaviour of BS, which underlies their role in fat (lipid) digestion. Our working hypothesis was that small variations in BS bile acid portion are responsible for the different biological functions they fulfil; this explains why we have selected for this project NaTC and NaTDC, two BS that differ by the presence of an additional hydroxyl group on NaTC skeleton and display contrasting adsorption/desorption behaviours at interfaces, which may therefore lead to different functions in the process of lipolysis

The study of BS adsorption/desorption dynamics at the bare and lipid-dense air/water (Chapter 1) and oil/water (Chapter 2) interfaces with a LT (surface pressure measurements), ellipsometer and pendant drop instrument, as well as of their interfacial morphology with BAM, XRR and NR, confirmed the significance – so far largely neglected in the literature – of BS structural variability in their behaviour at these interfaces. A similar observation was made at an air/water interface stabilised by a polysaccharide, namely, MC (Chapter 4). More specifically, despite its higher hydrophilicity, NaTC was found to adsorb more efficiently at the air/water interface, both in the absence (Chapter 1) and presence of a lipid (Chapter 1) or polysaccharide (Chapter 4) stabiliser, compared to NaTDC, which showed a higher propensity for desorption; at the pristine oil/water interface, NaTDC – the more hydrophobic BS – displayed a better stabilising capacity and, at the phospholipid-stabilised oil/water interface, the two structurally distinct BS were found to exhibit different interfacial behaviours, which nonetheless still need to be clarified (Chapter 2). In particular, NR structural studies at the air/water interface stabilised by a phospholipid monolayer (using neutron contrast-variation method, through isotopic substitution) enabled us to establish the molecular-level organisation of each BS/lipid film (Chapter 1). Both BS were shown to disorganise the lipid film below which they were injected; nonetheless, contrary to NaTC, which penetrated deeply into the phospholipid head group layer, NaTDC induced the formation of a diffuse layer beneath the lipid film, at the head group/water interface. NR also revealed that NaTDC displaced lipid molecules from the interface, and therefore induced lipid solubilisation, to a much

higher extent than NaTC. The better solubilising capacity of NaTDC was also observed in the presence of TAG-incorporating liposomes, used as a preliminary mimic of fat droplets being approached by BS molecules. Indeed, a vesicle-to-micelle transition occurred at a lower BS concentration in the presence of NaTDC, compared to NaTC (e.g., from 30 mM for NaTDC vs. 50 mM for NaTC, at 37°C) (Chapter 3). All these differences between the two BS support our hypothesis that NaTC may be more efficient at facilitating enzymes adsorption at the fat droplet interface, whereas NaTDC may be more prone to remove insoluble lipolysis products from the interface *via* dynamic exchange, through their incorporation into mixed micelles.

The bulk study on BS micellisation process with fluorescence spectroscopy, using pyrene as a probe, demonstrated that the contrasting interfacial behaviour displayed by the two BS correlates with their bulk aggregation process: the adsorption of NaTC at interfaces over a wider range of concentrations correlates with a later onset of micellisation (4–7 mM), while desorption of NaTDC occurring at low concentrations correlates with a lower CMC value (ca. 2 mM) (Chapter 3). BS adsorption/desorption behaviour at the interface is therefore linked to processes taking place in the bulk, which, in turn, are dictated by BS chemical structure. MD simulations, as well as SANS and SAXS measurements, were performed in order to provide a molecular picture of BS micelles (Chapter 3). While both BS were shown to associate with each other *via* their steroid backbone, with their ionic chain and hydroxyl groups forming a more hydrophilic shell, clear differences were obtained between the two BS in terms of micellar size and shape; in particular, NaTDC was demonstrated to form larger aggregates than NaTC. Similar observations were made with the self-assembled aggregates formed by BS in the presence of the products of lipolysis (i.e., MAG and FA) (Chapter 3). All these results highlight the distinct behaviours of the two structurally and hydrophobically different BS in the bulk, which may explain their contrasting interfacial properties. Finally, SANS was used to monitor the fate of TAG-incorporating liposomes, mimicking food colloidal structures found in the gut, upon interaction with the two selected BS (Chapter 3). Both BS converted these lipid vesicles into mixed micelles, with the more hydrophobic NaTDC exhibiting a better solubilising capacity. Consequently, as already suggested by interfacial studies, NaTDC seemed to be more prone to remove lipolysis products

from the interface and to incorporate them into mixed micelles, before transporting them towards the gut mucosa, where they are absorbed.

The last part of this thesis explored the role of dietary fibres and their interactions with BS. MC is a dietary fibre, whose efficiency to lower cholesterol levels is thought to be due to its ability to entrap BS molecules and thereby to prevent them from fulfilling their functionalities. To explore this postulate, the interactions occurring between MC and the two selected BS, NaTC and NaTDC, were compared, and their impact on the digestion of an emulsion stabilised by this polysaccharide assessed (Chapter 4).

BS are expected to interact with MC both in the bulk aqueous phase and at the surface of MC-stabilised emulsion droplets. Oscillatory shear rheology measurements were therefore carried out to measure the effect of BS on MC viscoelastic properties, and interfacial studies to characterise BS adsorption/desorption dynamics in the presence of a MC film at the air/water interface. Results demonstrated that both BS affected MC rheological behaviour, by decreasing its elastic modulus (G') and by shifting its weak-to-strong gel transition point (T_t) to higher temperatures, NaTDC having a more notable impact than NaTC. NaTDC higher ability to inhibit MC gelation behaviour may be attributed to its higher hydrophobicity, which may be responsible for its higher efficacy at binding to MC hydrophobic chains and therefore at preventing their self-association. Upon successive injections of BS below a MC film formed at the air/water interface, NaTC was found to gradually adsorb at the interface, whereas NaTDC showed desorption from a relatively low concentration (2-3 mM). In order to link BS/MC interactions with the behaviour of MC upon lipid digestion, *in vitro* lipolysis studies were also performed with optical/confocal microscopy techniques and the pH-stat method. Microscopy observations demonstrated that both flocculation and coalescence occurred upon emulsion digestion, to a higher extent in the presence of NaTDC, as compared to NaTC. Complementary confocal images suggested that these destabilisation phenomena were due to the breaking down of the MC network stabilising the droplets and to the removal of MC from the fat droplets surface; additionally, NaTDC showed a better ability to disturb and displace MC bulk network,

which may be attributed to its higher propensity for binding to MC and for desorbing from a MC/water interface. The titration of FFA released upon emulsion digestion (pH-stat method) clearly demonstrated that NaTC was more efficient at promoting lipolysis than NaTDC (when used at 50 mM); the inhibition of NaTDC activity may be due to NaTDC higher efficacy at interacting with MC, resulting in the BS molecules being entrapped in the MC network and therefore prevented from performing their role. Overall, it is clear that the structure of BS dictates their interactions with MC, which, in turn, have a notable effect on lipolysis.

Future work

Because all the interfacial experiments described in this thesis have been performed in the presence of BS only, the work presented here should first be complemented by interfacial studies in the presence of both BS and enzymes, to better mimic the action of the digestive fluid. More specifically, following-up our study with the newly developed NR liquid/liquid cell at the ILL, which consisted in probing the effect of BS on the interfacial structure, *in vitro* lipolysis studies could be carried out with the same technique and set-up, to monitor structural changes occurring at a lipid-dense oil/water interface, upon adsorption of both BS and pancreatic lipase/co-lipase. These measurements would enable the determination of the impact of BS structure on enzymes activity and help confirm our hypothesis that BS bile acid moiety is responsible for their different roles during fat digestion.

The second objective would be to employ a more physiologically relevant system, following-up directly our SANS study on the effect of BS on the structure of liposomes mimicking ingested food. Emulsions with well-defined, monodisperse droplets stabilised by BS alone would be a model of choice, as they would allow performing *in vitro* lipolysis studies (with the pH-stat method and small-angle scattering technique, for instance) in the absence of an exogeneous stabiliser, whose presence may have an impact on the pristine roles of BS during digestion. A microfluidic device could be designed in order to produce emulsion droplets of narrow size distribution and thereby facilitate the analysis and description of small-angle scattering data (since structures evolve upon digestion, giving rise to multiple, complex systems over a range of length scales, starting from a monodisperse, well-defined system would help the analysis).

Investigating the interfacial and bulk properties of the four other main BS would also be of considerable interest as it would help confirm our assumption that the position and number of hydroxyl groups on BS (rather than the type of conjugating group, e.g., tauro or glyco) are responsible for the distinct functions they fulfil during fat digestion. These measurements could also be extended to mixtures of BS, which would be more representative of the actual composition of the human bile, to assess synergic effects.

As part of the second objective of this PhD project, which was to determine the processes by which MC – a dietary fibre capable of lowering cholesterol levels – inhibits BS (and thus enzymes) activity and, as a result, slows down fat digestion, structural characterisation could be carried out using SANS; more precisely, the effect of BS on MC structural properties could be investigated, as well as on MC-stabilised emulsion interfacial structure, in the presence of enzymes mimicking digestion conditions (*in vitro* lipolysis study). Additionally, similar interfacial measurements as those performed at a phospholipid-stabilised interface could be performed with NR, to relate MC/BS interfacial interaction to that in the bulk, and ultimately elucidate how these interactions control lipid digestion.

Appendixes

Appendix 1

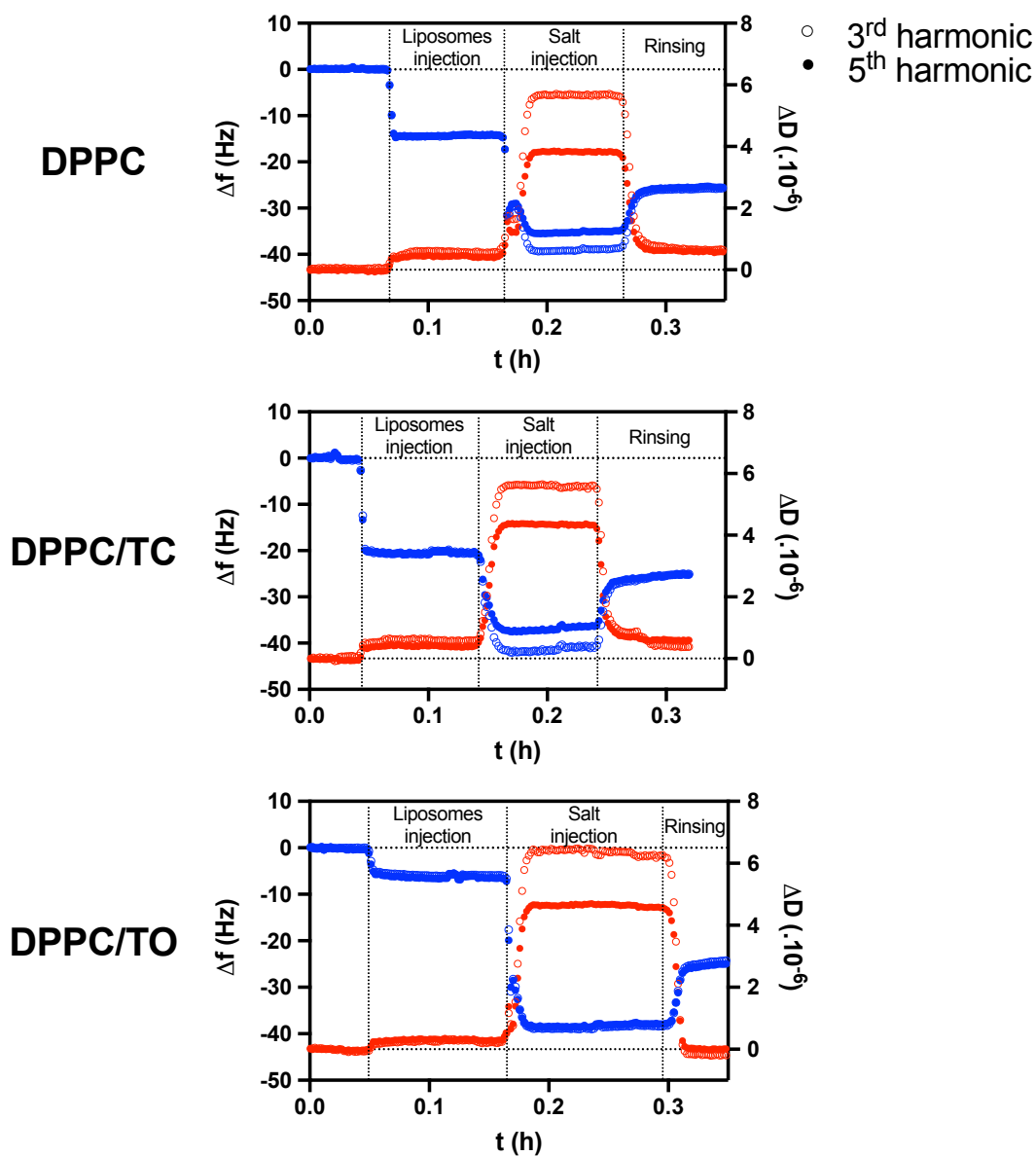


Figure A1: Time-dependent evolution of the (●) resonance frequency (Δf) and (●) energy dissipation factor (ΔD) measured by quartz-crystal microbalance with dissipation monitoring (QCM-D) [1], upon formation of a SLB: DPPC, DPPC/TC, DPPC/TO, in ultrapure water, through liposomes fusion (at $50 \pm 2^\circ\text{C}$). Liposomes, followed by salt (0.5 M NaCl), were injected into the chamber, which was finally rinsed with ultrapure water to remove the lipid vesicles remaining intact at the interface and in the bulk. For readability purposes, resonance frequencies and energy dissipation factors obtained for the 3rd and 5th harmonics only are shown here. A frequency shift of around -25 Hz typically denotes the effective formation of a stable lipid membrane [2]. Each experiment was reproduced twice, and a representative measurement was selected for each SLB.

Quartz-crystal microbalance with dissipation monitoring (QCM-D) measurements [1] were performed prior to NR experiments in order to define the protocol of formation

of the SLB described in the “Neutron reflectometry (NR)” method section. Changes in resonance frequency (Δf), which correlates with the adsorbed mass [3], and energy dissipation factor (ΔD) were recorded simultaneously over time. For each composition, the injection of liposomes leads to a first decrease in resonance frequency (and, to a lower extent, to an increase in energy dissipation factor), indicating lipid vesicles adsorption onto the quartz-coated support (Figure A1). The addition of salt results in a second, much higher decrease in resonance frequency (and in an increase in energy dissipation factor), which implies the formation of the SLB. Upon rinsing, surface-adsorbed liposomes are removed, thus leading to a rise to around $\Delta f = -25$ Hz and to a drop to less than $\Delta D = 1 \times 10^{-6}$ for, respectively, the resonance frequency and energy dissipation factor – which are values characteristic of the formation of a homogeneous and rigid SLB [2].

Appendix 2

Scattering data analysis applied to BS micelles and mixed micelles (with FA and/or MAG)

The (oblate) ellipsoid model used with SasView [4] fits the experimental data according to this equation (which is equivalent to Equation 3 of Chapter 3, in the case of BS micelles):

$$I(q) = \Phi_{Micelles} (SLD_{Micelle} - SLD_{Water})^2 P_{Ellipsoid}(q) S_{H-P}(q) \quad (A1)$$

where $\Phi_{Micelles}$ is the micellar volume fraction, $SLD_{Micelle}$ and SLD_{Water} the SLD of the BS micelle or mixed micelle and water, respectively, $P_{Ellipsoid}(q)$ the form factor for ellipsoids, and $S_{H-P}(q)$ the Hayter-Penfold structure factor, which describes the interactions between charged micelles [5,6].

For the measurement of BS micelles, knowing that:

$$\Phi_{Micelles} = \Phi_{BS} + \Phi_{Water} = \frac{\Phi_{BS}}{1 - x_{Water}} \quad (A2)$$

and:

$$\begin{aligned} SLD_{Micelle} - SLD_{Water} &= (1 - x_{Water})SLD_{BS} + x_{Water} SLD_{Water} - SLD_{Water} \\ &= (1 - x_{Water})(SLD_{BS} - SLD_{Water}) \quad (A3) \end{aligned}$$

where Φ_{BS} and Φ_{Water} are the volume fractions of, respectively, BS and water in the micelles, x_{Water} , or $\frac{\Phi_{Water}}{\Phi_{Micelles}}$, the proportion of water in the micelles, and SLD_{BS} the SLD of BS, Equation A1 can be rewritten as follows:

$$I(q) = \Phi_{BS} (1 - x_{Water}) (SLD_{BS} - SLD_{Water})^2 P_{Ellipsoid}(q) S_{H-P}(q) \quad (A4)$$

where $\Phi_{BS} (1 - x_{Water})$ corresponds to the volume fraction parameter returned by the software (referred to as $\Phi_{software}$), when fixing the SLD of BS and water in the software to their calculated value (Tables 1 and 2). Φ_{BS} is calculated by considering the presence of free monomers in the solution:

$$\Phi_{BS} = \frac{([BS]_{total} - CMC_{BS}) M_{BS}}{\rho_{BS}} \quad (A5)$$

where $[BS]_{total}$ is the total BS concentration in the solution, CMC_{BS} the BS critical micelle concentration, M_{BS} the BS molecular weight, and ρ_{BS} the BS density. The degree of hydration of BS micelles (x_{Water}) is then estimated from the volume fraction fitted. It is worth noting that for the measurement of BS micelles with SANS, x_{Water} actually corresponds to the extent of hydration of the micellar core, as this technique was found to resolve this part of the micelle only.

References

- [1] M.C. Dixon, Quartz crystal microbalance with dissipation monitoring: enabling real-time characterization of biological materials and their interactions., *J. Biomol. Tech.* 19 (2008) 151–158. <http://www.ncbi.nlm.nih.gov/pubmed/19137101>.
- [2] Y. Jing, H. Trefna, M. Persson, B. Kasemo, S. Svedhem, Formation of supported lipid bilayers on silica: relation to lipid phase transition temperature and liposome size, *Soft Matter*. 10 (2014) 187–195. doi:10.1039/C3SM50947H.
- [3] M. Rodahl, F. Höök, A. Krozer, P. Brzezinski, B. Kasemo, Quartz crystal microbalance setup for frequency and Q-factor measurements in gaseous and liquid environments, *Rev. Sci. Instrum.* 66 (1995) 3924–3930. doi:10.1063/1.1145396.
- [4] SasView for small angle scattering analysis, (2018). www.sasview.org (accessed August 22, 2018).
- [5] J.-P. Hansen, J.B. Hayter, A rescaled MSA structure factor for dilute charged colloidal dispersions, *Mol. Phys.* 46 (1982) 651–656. doi:10.1080/00268978200101471.
- [6] J.B. Hayter, J. Penfold, An analytic structure factor for macroion solutions, *Mol. Phys.* 42 (1981) 109–118. doi:10.1080/00268978100100091.